Bragg-Grating-Based Rare-Earth-Ion-Doped Channel Waveguide Lasers And Their Applications

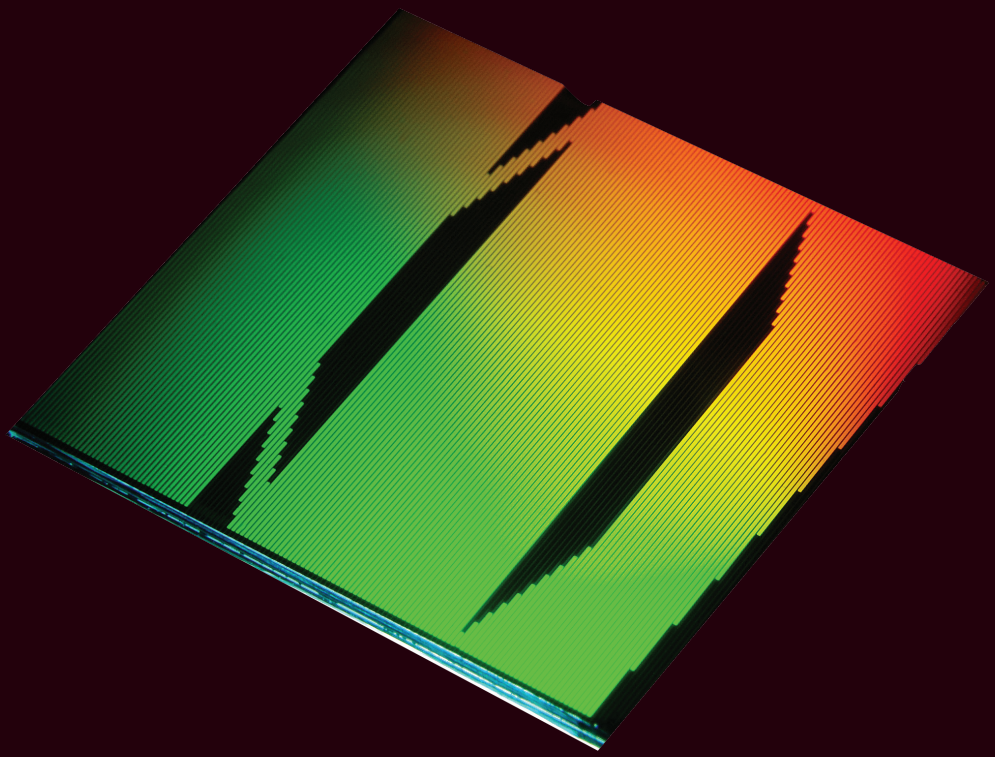

Edward H. Bernhardi

Bragg-Grating-Based Rare-Earth-Ion-Doped Channel Waveguide Lasers And Their Applications

Edward H. Bernhardi

Graduation committee:

Chairman and Secretary:

Prof. Dr. Ir. A. J. Mouthaan	University of Twente

Promoter:

Prof. Dr. M. Pollnau	University of Twente

Assistant Promoter:

Dr. K. Wörhoff	University of Twente

Members:

Prof. Dr. K. J. Boller	University of Twente
Prof. Dr. J. E. Broquin	Grenoble Institute of Technology
Prof. Dr. V. Subramaniam	University of Twente
Dr. B. H. Verbeek	IOP Photonic Devices

The research described in this thesis was performed at the Integrated Optical MicroSystems (IOMS) group, Faculty of Electrical Engineering, Mathematics and Computer Science, MESA+ Institute for Nanotechnology, University of Twente, PO Box 217, 7500 AE Enschede, The Netherlands.

This research was financially supported by the Smartmix Memphis programme of the Dutch Ministry of Economic Affairs.

Front cover: Photograph of various integrated distributed feedback and distributed Bragg reflector cavities in Al_2O_3. The bright colours are from light being diffracted by the Bragg gratings. (*Photograph by Henk van Wolferen*)

Printed by Wöhrmann Print Service, Zutphen, The Netherlands

ISBN: 978-90-365-3450-5
DOI: 10.3990./1.9789036534505
URL: http://dx.doi.org/10.3990/1.9789036534505

Bragg-Grating-Based Rare-Earth-Ion-Doped Channel Waveguide Lasers And Their Applications

DISSERTATION

to obtain
the degree of doctor at the University of Twente,
on the authority of the rector magnificus,
prof. dr. H. Brinksma,
on account of the decision of the graduation committee,
to be publicly defended
on Thursday the 22nd of November 2012 at 14h45

by

Edward Harold Bernhardi

born on the 5th of April 1982
in Kempton Park, South Africa

This dissertation is approved by:

The promoter: Prof. Dr. M. Pollnau

The assistant promoter: Dr. K. Wörhoff

Contents

Abstract

The research presented in this thesis concerns the investigation and development of Bragg-grating-based integrated cavities for the rare-earth-ion-doped Al_2O_3 (aluminium oxide) waveguide platform, both from a theoretical and an experimental point of view, with the primary purpose of realizing narrow-linewidth, monolithic channel waveguide lasers.

To determine the optimum design parameters and for understanding the operation principles of Bragg-grating-based rare-earth-ion-doped channel waveguide lasers, a mathematical model of such a laser is implemented. The mathematical description consists of laser rate equations, which describe the population dynamics of rare-earth ions, as well as coupled mode equations, which describe the operation of waveguide Bragg gratings.

Making use of reactive co-sputtering from high purity metallic targets, rare-earth-ion-doped Al_2O_3 waveguide layers are deposited onto thermally-oxidized silicon substrates, after which channel waveguides are etched using a chlorine-based reactive ion etching process. A high-resolution lithography technique, known as laser interference lithography is used to define the Bragg-grating structures, which are finally etched via reactive ion etching into a SiO_2 cladding layer on top of the waveguides.

Optimized waveguide and grating geometries allowed various rare-earth-ion-doped integrated channel waveguide lasers to be demonstrated. These include an erbium-doped Al_2O_3 distributed feedback channel waveguide laser having a linewidth of 1.7 kHz, as well as highly efficient ytterbium-doped Al_2O_3 distributed feedback and distributed Bragg reflector lasers with slope efficiencies as high as 67%.

The use of two local phase shifts in a distributed-feedback structure enables the demonstration of a dual-wavelength distributed feedback channel waveguide laser. This device is used for the photonic generation of a microwave signal via the heterodyne detection of the two optical waves emitted by the laser. By varying the values of the respective phase shifts, various laser cavities producing microwave signals with frequencies ranging between 12.43 GHz and 23.2 GHz are demonstrated. The stability performance and narrow-linewidth of these free-running lasers show the great potential of using rare-earth-ion-doped monolithic waveguide lasers for the photonic generation of stable microwave signals in novel applications such as phased array antennas.

Another innovative application of the photonic generation of stable microwave signals is the demonstration of an integrated intra-laser-cavity micro-particle optical sensor based on a dual-wavelength distributed-feedback channel waveguide laser. Real-time detection and accurate size measurement of single micro-particles with diameters ranging between 1 μm and 20 μm is achieved. This represents the typical size of many fungal and bacterial

pathogens as well as a large variety of human cells. A limit of detection of $\sim$ 500 nm is deduced. The sensing principle relies on measuring changes in the frequency difference between the two longitudinal laser modes as the evanescent field of the dual-wavelength laser interacts with micro-sized particles on the surface of the waveguide.

Samenvatting

Het onderzoek in dit proefschrift betreft het onderzoek naar en de ontwikkeling van Bragg-rooster gebaseerde geïntegreerde resonatoren voor het zeldzame-aard-ion-gedoteerd Al_2O_3 (aluminium oxide) golfgeleider-platform, zowel vanuit een theoretisch als wel als een experimenteel oogpunt, met als primair doel het realiseren van lasers met een smalle lijnbreedte gebaseerd op monolithische zeldzame aard-ion-gedoteerde kanaal golfgeleiders.

Voor het bepalen van de optimale ontwerpparameters en voor het theoretische begrip van de zeldzame-aard-ion-gedoteerde Bragg-rooster kanaal golfgeleider lasers is een wiskundig model van een dergelijke laser opgesteld. De wiskundige beschrijving omvat een set differentiaalvergelijkingen die de energietoestand van de ionen beschrijven, gecombineerd met gekoppelde-mode vergelijking die de spatiale foton distributie binnen de Bragg-rooster reflector beschrijven.

Zeldzame-aard-ion-gedoteerde Al_2O_3 waveguide lagen worden door middel van een reactief co-sputtering proces op thermisch geoxideerd silicium substraten gedeponeerd, met gebruikmaking van metalen met een hoge zuiverheid, waarna kanaal golfgeleiders worden geëtst met een op chloor gebaseerd reactief ionen ets proces. Een hoge resolutie lithografie techniek, bekend als laser interferentie lithografie, wordt gebruikt om de Bragg-rooster reflectoren te definiëren op de golfgeleiders. Deze worden vervolgens door middel van een reactief ionen ets proces geëtst in een SiO_2 toplaag bovenop de golfgeleiders.

Het resultaat van het optimaliseren van de golfgeleiders en Bragg reflectoren is een scala van verschillende kanaal golfgeleider lasers. Deze omvatten een erbium gedoteerde Al_2O_3 continue Bragg rooster reflector laser (een zgn. *gedistribueerde-feedback* laser) met een lijnbreedte van 1.7 kHz, en zeer efficiënt ytterbium gedoteerde Al_2O_3 continue Bragg rooster lasers en discontinue Bragg rooster lasers met efficiëntie tot 67% van het opgenomen pomp vermogen.

Het gebruik van twee lokale faseverschuivingen in een gedistribueerde-feedback laser heeft geleid tot de demonstratie van een dual-golflengte golfgeleider laser. Deze laser wordt gebruikt voor het genereren van een microgolf signaal via heterodyne detectie van de twee frequenties van de laser. Door het variëren van de sterkte van de twee faseverschuivingen in een reeks lasers werden frequenties tussen 12.43 GHz en 23.2 GHz gegenereerd. De stabiliteit en smalle lijnbreedte van deze *free-running* lasers tonen het grote potentieel van het gebruik van zeldzame-aarde-ion-gedoteerde monolithische golfgeleider lasers voor het genereren van stabiele microgolf signalen door middel van fotonica in nieuwe toepassingen zoals *phased array* antennes.

Een andere innovatieve toepassing van de fotonische generatie van stabiele micro-

golf signalen is de demonstratie van een geïntegreerde optische sensor van micro-deeltjes binnen de laser resonator, gebaseerd op een dual-golflengte *distributed-feedback* kanaal golfgeleider laser. Real-time detectie van enkele micro-deeltjes met een diameter tussen 1 μm en 20 μm is gedemonstreerd, wat de grootte is van vele schimmel- en bacteriële pathogenen evenals een grote verscheidenheid aan menselijke cellen. Bij de detectie kon onderscheid worden gemaakt tussen de grootte van de deeltjes, waarbij een detectielimiet van $\sim$ 500 nm geldt als de ondergrens wat betreft de grootte van detecteerbare deeltjes. Het detectieprincipe berust op het meten van veranderingen in het frequentieverschil tussen de twee longitudinale lasermodi ten gevolge van de interactie van de deeltjes met het evanescente veld van de dual-golflengte laser.

1

Introduction

The operation of a laser is governed by the way in which electromagnetic radiation interacts with matter. The specific process which produces laser light is known as stimulated emission. It is from this interaction process between light and matter where the term **LASER** has its origin. It is an acronym for **L**ight **A**mplification by **S**timulated **E**mission of **R**adiation. The concept of stimulated emission was first introduced by EINSTEIN in 1917 in his work on the emission and absorption of light by atoms and molecules [1]. In their classical paper of 1958, SCHAWLOW and TOWNES proposed a device for the generation of monochromatic infrared radiation by using a potassium vapor as the gain medium [2]. Two years after the work of SCHAWLOW and TOWNES, the first operation of a laser was demonstrated by MAIMAN in the form of a solid-state ruby laser [3].

Nowadays a great variety of laser sources are available, with emission wavelengths ranging from x-rays, through the visible region, all the way to the far-infrared part of the electromagnetic spectrum. Lasers produce radiation which is spatially and temporally highly coherent compared to conventional light sources such as lamps. These unique attributes have ensured that lasers have found numerous applications in the scientific, military, industrial, medical and telecommunication fields. The growing demand in laser applications ensures that the development of lasers remains an active area of research.

The work presented in this thesis concerns the development of optically pumped rare-earth-ion-doped dielectric channel waveguide lasers in particular. Due to its versatility and favorable emission properties, this specific type of laser is of great interest for many integrated optical applications, which include the generation of stable microwave signals for telecommunication purposes as well as the realization of highly sensitive integrated optical sensors.

1.1 Integrated Optics

Over the last few decades there has been an ever-increasing demand for high speed internet access and broadband data communication services. This has ensured that the development of optical technologies has become ever more important since they are able to provide a more efficient alternative to electrical communication systems. Single-mode silica fibers were particularly successful in the realization of efficient and inexpensive long-haul communication systems, due to the fact that they enable optical data transmission with losses as low as 0.2 dB/km in the third telecommunication transmission window, or C-band, which spans the wavelength range from 1525 nm to 1565 nm. Since the optical emission of erbium coincides with wavelengths in this low-loss silica transmission window, the invention of the erbium-doped fiber amplifier (EDFA) further provided the possibility for all-optical amplification of multi-wavelength signals that are used in dense wavelength division multiplexing communication systems which operate within the C-band.

The advances in fiber-optic communication systems have encouraged the continual research towards more compact and reliable optical components. As a consequence, integrated optics has been a continuously expanding field along-side the growth of fiber-optic communications. While fiber-optic components are relatively large and bulky, the aim of integrated optics is to reduce the size and cost of optical systems. This is achieved by realizing devices with high functionality on a single chip by making use of guiding structures based on planar and channel waveguides. An optical waveguide basically consists of a high-refractive-index guiding layer which is embedded between two lower-index cladding layers, so that the optical signal is confined to the guiding layer by means of total internal reflection. In the case of a planar, or slab waveguide, the propagating light is confined only in the vertical direction, while in a channel waveguide the light is confined in both horizontal and vertical directions. Due to the large refractive-index contrast between waveguide and cladding which can be achieved in thin-film waveguide platforms, smaller waveguide cross-sections and bending radii are possible as compared to optical fibers. This allows a high integration density of complex photonic circuits on a single chip.

Integrated optical devices can be classified into two main categories according to their particular functionality. Firstly there are *passive* devices which generally facilitates the guiding and directing of light in applications such as filters, splitters, couplers, and multiplexers. Secondly there are *active* devices which concerns the generation or amplification of light on a chip. This second category of integrated optical devices has seen the establishment of the erbium-doped waveguide amplifier (EDWA) as an alternative to the EDFA for certain applications. Since EDWAs are typically much shorter, have smaller waveguide cross-sections and produce higher gain per unit length than their fiber-optic counterparts, they are more useful in terms of their compactness and pump power requirements, while also being cost-effective due to the wafer-scale fabrication potential. Over the last two decades EDWAs have been investigated extensively for their application in integrated amplifiers and on-chip waveguide laser sources.

1.2 Waveguide Lasers

As opposed to optical amplifiers which concern the amplification of existing optical signals, lasers are used for the generation of new optical signals. In its most basic form, a laser cavity consists of two optical feedback elements with an optical gain medium placed in between them. In the case of a waveguide laser, a planar or channel waveguide is fabricated in an optical gain medium, while the optical feedback is usually provided by means of butt-coupled or end-deposited mirrors, ring resonators, or Bragg gratings. Since the gain medium and optical feedback elements can be fabricated from the same material and on a common substrate, waveguide lasers allow for a monolithic design which facilitates stable operation. Another key advantage of waveguide lasers is the fact that there is basically no beam divergence inside the cavity, so that extremely high optical intensities can be maintained over long lengths. This makes it possible to achieve high pump rates, resulting in low-threshold laser operation. Monolithic rare-earth-ion-doped dielectric waveguide lasers have already been demonstrated in various cavity configurations in a variety of dielectric materials, including silica [4], ion-exchanged [5, 6] and femtosecond-laser-written [7, 8] phosphate glass waveguides, as well as lithium niobate [9–11] and other crystalline hosts such as potassium double tungstate [12–14].

The waveguide lasers presented in this thesis are all based on optically pumped rare-earth-ion-doped dielectric channel waveguides, which have been integrated with distributed feedback (DFB) or distributed Bragg reflector (DBR) cavities. Due to the inherent stability provided by the monolithic nature of waveguide lasers, they are particularly suitable to realize narrow-linewidth, single-frequency light sources.

1.3 Narrow-Linewidth Lasers

A laser which operates on only a single longitudinal-mode is often referred to as a *single-frequency laser*. These light sources typically have a high spectral purity, or narrow emission linewidth. Single-longitudinal-mode laser operation is typically achieved when the frequency spacing (free spectral range) of the resonator modes is larger than the gain bandwidth of the laser gain medium. In some cases, e.g. microchip lasers [15], it is possible to reduce the cavity length sufficiently to obtain a cavity mode spacing which exceeds the material gain bandwidth in order to facilitate single-frequency operation. However, it is still possible to obtain single-longitudinal-mode operation even if the frequency spacing of the resonator modes is smaller than the gain bandwidth, although the use of additional intra-cavity filters is then required [16]. Alternatively, novel resonator configurations such as quarter-wavelength phase shifted DFB cavities can be used to force the laser oscillation to operate only on a single longitudinal-mode. The operating principles of these DFB and other Bragg-grating-based devices are discussed in detail in Chapter 2. Narrow-linewidth single-longitudinal-mode lasers have been realized in a variety of semiconductor materials, as well as rare-earth-ion-doped fiber, bulk, and waveguide configurations.

1.3.1 Semiconductor Lasers

Standard semiconductor DFB and DBR lasers typically have linewidths that are on the order of a few to tens of MHz [17–23]. The relatively wide emission linewidth in semiconductor lasers is mainly because of the change of refractive index with carrier density due to spontaneous emission, which induces phase changes in the laser field [24]. Longitudinal spatial hole burning is also a limiting factor, particularly in DFB lasers, when carriers are depleted by the nonuniform photon distribution. This induces a refractive-index change, which results in a decreased grating reflectivity and, consequently, linewidth broadening [18]. It is possible to realize sub-MHz semiconductor lasers, but this usually requires highly complex structures such as corrugation-pitch-modulated multiple-quantum-well cavities [25–27], vertical-cavity surface-emitting lasers (VCSEL) whose linewidths are minimized by optical feedback [28], impractical external cavity devices which can be as long as 10 cm [29], or discrete mode laser diodes which require a sophisticated design procedure [30, 31]. The linewidth performance of a selection of these narrow-linewidth free-running semiconductor lasers is given in Table 1.1.

Material	Cavity	Wavelength	Linewidth	Ref.
InGaAsP	DFB	1550 nm	170 kHz	[25]
GaInAs/InGaAsP	DBR	1540 nm	85 kHz	[26]
InGaAsP	DFB	1543 nm	3.6 kHz	[27]
InGaAs/AlGaAs	External cavity	940 nm	20 kHz	[29]
InGaAs/GaAs	DBR	1058 nm	25 kHz	[32]
AlGaAsGaAs	DBR	853 nm	30 kHz	[33]
InGaAlAs	Fabry-Pérot	1545 nm	100 kHz	[34]
GaAs Quantum-well	VCSEL	853 nm	190 kHz	[28]

Table 1.1: A selection of free-running, narrow-linewidth semiconductor lasers in the literature.

1.3.2 Rare-Earth-Ion-Doped Lasers

Since rare-earth-ion-doped dielectric materials do not exhibit an amplitude-phase coupling mechanism as large as that observed in semiconductor lasers, these materials can be used to realize ultra-narrow-linewith lasers, which are not attainable with standard semiconductor lasers. Furthermore, the high gain in semiconductor lasers makes it difficult to maintain single-longitudinal-mode operation for Bragg-grating-based cavities with relatively strong gratings, since the achievable gain in the cavity also supports the operation of higher order longitudinal modes. In rare-earth-ion-doped lasers, however, single-longitudinal-mode operation is typically possible even for cavities with strong gratings, which allows high-quality cavities to be demonstrated due to the high grating reflectivity. Since the minimum attainable laser linewidth (according to the Schawlow-Townes equation [2]) scales quadratically with the passive cavity linewidth, Bragg-

Platform	Material	Cavity	Wavelength	Linewidth	Ref.
Fiber	Silica (Er)	Ring	1550 nm	1.4 kHz	[36]
	Glass (Er)	DBR	1548 nm	47 kHz	[37]
	Phosphosilicate (Er/Yb)	DFB	1535 nm	18 kHz	[38]
	Phosphate glass (Er/Yb)	DBR	1560 nm	2 kHz	[39]
	Unspecified (Er/Yb)	DFB	1552 nm	3 kHz	[40]
	Unspecified (Er)	DBR	1550 nm	10 kHz	[41]
	Unspecified (Er)	DBR	1550 nm	0.22 kHz	[42]
Bulk	YAG (Nd)	Ring	1060 nm	5 kHz	[43]
	Phosphate glass (Er/Yb)	Fabry-Pérot	1535 nm	1 kHz	[44]
Waveguide	Lithium niobate (Er)	DBR	1561 nm	8 kHz	[45]
	Phosphate glass (Er/Yb)	DBR	1536 nm	500 kHz	[46]
	Phosphate glass (Er/Yb)	DFB	1538 nm	3 kHz	[6]
	Al_2O_3 (Er)	**DFB**	**1545 nm**	**1.7 kHz**	**This work**
	Al_2O_3 (Yb)	**DFB**	**1020 nm**	**4.5 kHz**	**This work**
Other	Glass (Er)	Toroid	1550 nm	11 kHz	[47]
	Sol-gel silica (Er)	Toroid	1550 nm	4 Hz	[48]

Table 1.2: A selection of free-running, narrow-linewidth rare-earth-ion-doped lasers in literature.

grating-based rare-earth-ion-doped dielectric cavities can be used to realize ultra-narrow-linewidth single-longitudinal-mode lasers. Table 1.2 shows the linewidth performance of a selection of these narrow-linewidth free-running rare-earth-ion-doped lasers in fiber, bulk, and waveguide configurations. The monolithic, compact, and stable nature of waveguide lasers, as discussed in Section 1.2, together with the ultra-narrow-linewidth potential of rare-earth-ion-doped gain media, suggest that these lasers could provide a versatile solution to the stringent requirements posed by some ultra-narrow-linewidth laser applications.

In this thesis, erbium- and ytterbium-doped waveguide lasers are considered in particular. Erbium has become a widely used ion, especially in the telecommunication industry, since the transition from the first excited state to the ground state coincides with the wavelength of lowest loss and lowest dispersion in silica optical fibers that are used in optical telecommunication transmission systems. Ytterbium is a more suitable rare-earth dopant than erbium for a variety of active biosensing applications, since the absorption coefficient of water is ~ 0.2 cm^{-1} at 1020 nm (ytterbium emission) compared to ~ 10 cm^{-1} at 1550 nm (erbium emission) [35].

1.3.3 Applications

Although there are numerous applications for narrow-linewidth lasers, in this work particular attention will be given to two of these applications.

Photonic generation of microwave or millimeter wave signals

Microwave photonics has recently attracted much research interest due to its great application potential in satellite communication [49] and phased array antenna systems [50], as well as broadband wireless and radio-over-fiber networks, radar, and sensor devices [51]. Microwave signals are conventionally generated with complex and expensive electronic circuits, after which they are distributed along electrical distribution lines, such as coaxial cables, which intrinsically have high propagation losses. Compared with the electronic solutions, photonic generation of microwaves has many advantages, such as high-speed operation, low power consumption, low cost, and the distribution of the optical carrier signals via low loss, inexpensive optical fibers over large distances [52]. One particularly successful method of generating microwave signals in the optical domain is to make use of two narrow-linewidth lasers (or a single dual-wavelength laser), with the two laser wavelengths separated by the desired microwave frequency. An electrical beat signal is then generated at the output of a photodetector, with a frequency corresponding to the wavelength spacing of the two optical waves.

The work presented in this thesis was performed within the Smartmix MEMPHIS (**M**erging **E**lectronics and **M**icro and Nano-**PH**otonics in **I**ntegrated **S**ystems) program of the Dutch Ministry of Economic Affairs, where the primary goal of the particular work-package (C11-Optical (de)mux of radio signals) was to develop monolithic, narrow-linewidth lasers to be used in novel phased array antenna systems. These electronically-steered antennas form a key technology for novel avionic communication systems used in broadband aircraft-to-satellite communication. The purpose of the narrow-linewidth lasers is to generate a stable on-chip microwave signal ($9.75 - 10.6$ GHz), which can be used as a local oscillator in order to down-convert the $10.7 - 12.75$ GHz radio frequency (RF) signal received by the antenna for further on-chip signal processing.

Optical sensing

There is an ever-increasing demand for compact and reliable label-free biosensors which are able to detect DNA, bacteria, as well as other micro- and nano-sized biological specimens. As a consequence, integrated optical sensors have become a very active and relevant area of research in which a variety of novel sensors have been demonstrated [53–57]. The majority of these optical sensors make use of passive resonant cavities, where the sensing principle is based on the interaction between the optical field in the cavity and the micro- or nano-sized particles in the vicinity of the cavity, which induces a perturbation of the resonance condition of the cavity [58]. This perturbation is usually observed in the form of a shift in the resonance frequency of the cavity. The sensitivity of such a sensor is determined by the passive cavity linewidth. A narrower optical resonance linewidth allows one to observe smaller shifts in the cavity resonance, suggesting that smaller particles can potentially be detected. A narrow resonance linewidth implies a long cavity photon lifetime, which increases the interaction probability between the photons in the cavity and the micro- or nanoparticle. In this thesis, on-chip single microparticle detection and sizing are demonstrated by using a narrow-linewidth dual-wavelength DFB channel waveguide

laser. This integrated narrow-linewidth-laser-based particle sensor provides a convenient, real-time and high-resolution sensor readout signal.

1.4 Al_2O_3 Waveguide Platform

Monolithic, single-frequency, waveguide lasers have been demonstrated in the form of DFB and DBR cavities in a variety of rare-earth-ion-doped dielectric materials, including silica [4], lithium niobate [9–11], as well as ion-exchanged [5, 6] and femtosecond-laser-written [7, 8] phosphate glass waveguides. During the last few years, rare-earth-ion-doped amorphous aluminum oxide (a-Al_2O_3 or simply Al_2O_3, as opposed to its crystalline counterpart which is known as sapphire) has been extensively investigated and developed as a waveguide platform at the Integrated Optical MicroSystems group (IOMS) at the University of Twente. Al_2O_3 offers several advantages compared to these previously mentioned materials. When doped with rare-earth ions, Al_2O_3 has a larger emission bandwidth than silica, which provides greater potential for wavelength tunability [59]. In the case of erbium, a gain bandwidth of > 80 nm has previously been achieved in Al_2O_3:Er^{3+} layers [60], as compared to erbium-implanted SiO_2 films with a photoluminescence spectrum of 11 nm wide [61]. The relatively high refractive index of 1.65 and, hence, high refractive-index contrast Δn, between waveguide and cladding (SiO_2), allow for the fabrication of more compact integrated optical structures and smaller waveguide cross-sections in Al_2O_3 ($\Delta n = 2 \times 10^{-1}$) as compared to ion-exchanged ($\Delta n \leq 1 \times 10^{-1}$) [5, 6] or femtosecond-laser-written ($\Delta n \leq 2.3 \times 10^{-3}$) [7, 8] phosphate glass waveguides. Al_2O_3:Er^{3+} can be deposited on a number of substrates, including thermally oxidized silicon, which allows for integration with any existing silicon compatible passive platform. Some of the Al_2O_3 devices which have previously been demonstrated by the IOMS group include the following:

- Reactive cosputtering of Al_2O_3 planar waveguides and reactive ion etching of channel waveguides with propagation losses as low as 0.11 dB/cm [62] and 0.21 dB/cm [60], respectively.
- Erbium-doped aluminum oxide (Al_2O_3:Er^{3+}) waveguides with an internal net gain over a wavelength range of 80 nm ($1500 - 1580$ nm), with a peak gain of 2.0 dB/cm at 1533 nm [60]
- Monolithic integration of Al_2O_3:Er^{3+} amplifiers with passive silicon-on-insulator waveguides, where a signal enhancement of more than 7 dB at 1533 nm wavelength was obtained [63].
- Signal transmission experiments were performed up to a rate of 170 Gbit/s in an integrated Al_2O_3:Er^{3+} waveguide amplifier to demonstrate its potential in high-speed integrated photonic applications [64].
- A lossless planar power splitter, obtained by monolithically integrating an optical amplifier and a 1×2 power splitter in Al_2O_3:Er^{3+} [65].

- An Al_2O_3:Er^{3+} integrated laser in a ring resonator geometry has been shown to operate on several wavelengths in the range 1530 − 1557 nm [66].
- Neodymium-doped aluminum oxide (Al_2O_3:Nd^{3+}) channel waveguide amplifiers operating at signal wavelengths of 880 nm, 1064 nm, and 1330 nm, with a small-signal gain of 1.57 dB/cm, 6.30 dB/cm, and 1.93 dB/cm, respectively [67].
- An integrated optical backplane amplifier operating at 880 nm, where a maximum 0.21 dB net gain was demonstrated in a structure in which an Al_2O_3:Nd^{3+} waveguide was coupled between two polymer waveguides [68].

The diversity and performance of these devices are evidence that Al_2O_3 is a promising host for rare-earth-ions and that it is an excellent choice for a waveguide gain platform in order to realize monolithic narrow-linewidth lasers.

1.5 Thesis Outline

This thesis concerns the design, fabrication, and characterization of high-quality, narrow-linewidth active and passive Bragg-grating-based monolithic cavities realized in rare-earth-ion-doped Al_2O_3 channel waveguides. The thesis is organized as follows.

In Chapter 2 the theoretical background required for the modelling of Bragg-grating-based rare-earth-ion-doped channel waveguides is presented. This chapter consists of three main parts: laser rate equations which describe the population dynamics of rare-earth ions, coupled mode equations used to describe the operation of waveguide Bragg gratings, and a discussion regarding the linewidth and stability of a typical waveguide laser.

An optimized waveguide and grating geometry are derived in Chapter 3. The rest of this chapter is devoted to a description of the relevant fabrication processes, which include the deposition and structuring of Al_2O_3 waveguides, as well as the fabrication of surface corrugated Bragg gratings.

Making use of the fabrication processes described in Chapter 3, a variety of uniform Bragg gratings, distributed Bragg reflector cavities and distributed feedback cavities are demonstrated and characterized in Chapter 4, where particular attention is given to the high quality factors of these cavities.

Various monolithic Bragg-grating-based channel waveguide lasers are demonstrated and characterized in Chapter 5, including an Al_2O_3:Er^{3+} distributed feedback laser, as well distributed feedback and distributed Bragg reflector lasers in Al_2O_3:Yb^{3+}.

Chapter 6 demonstrates the use of dual-phase-shift, dual-wavelength distributed feedback lasers for the generation of microwave signals. One of the dual-wavelength lasers is used to realize an integrated, ultra-sensitive intra-laser-cavity microparticle sensor.

In Chapter 7 general conclusions based on the work presented in this thesis are outlined, after which a future outlook and recommendations are given.

2

Theoretical Analysis

Due to the increasing complexity and sophistication of integrated optical devices, it has become vital to develop accurate theoretical models and simulations, which allow the rapid design and optimization of integrated optical circuits and components. Effective theoretical models essentially eliminate the need for experimental trial-and-error optimization of optical devices and structures, which can be extremely expensive and time consuming. An accurate theoretical model also expedites the interpretation and improvement of experimental results.

In this chapter the general theoretical background of optically pumped rare-earth-ion-doped dielectric waveguide lasers is described. Particular attention is given to Bragg-grating-based erbium- and ytterbium-doped waveguide lasers. The mathematical description of such a laser consists of two main parts. The first part concerns the laser rate equations, which describe the population dynamics and interaction between the laser gain medium and the propagating light fields. The second part of the mathematical description makes use of coupled-mode theory to describe the distributed feedback nature of the Bragg grating which forms the laser cavity.

2.1 Laser Dynamics

2.1.1 Rare-Earth Elements

The particular rare-earth elements which are of interest for the work presented in this thesis are the lanthanides, a group of 14 elements with atomic number 57 - 71 in the periodic table of elements. Due to their favorable electronic and optical properties, many rare-earth ions are extensively used in the realization of optical amplifiers and lasers. When these elements are pumped at a suitable wavelength, ions are excited to a higher

Rare-earth ion	Emission wavelength
Nd^{3+}	880, 1060, 1330 nm
Eu^{3+}	615 nm
Ho^{3+}	2100 nm
Tm^{3+}	1900 nm
Er^{3+}	1550 nm
Yb^{3+}	1020 nm

Table 2.1: Most common emission wavelengths of several rare-earth ions.

energy level, which produces a large number of possible transitions, producing optical emission at characteristic wavelengths as shown in Table 2.1.

The electronic structure of erbium (atomic number 68) and ytterbium (atomic number 70) are are $[Xe]4f^{12}6s^2$ and $[Xe]4f^{14}6s^2$, respectively. However, when they are included into a dielectric host, they usually exist in their trivalent charge states Er^{3+} and Yb^{3+}, with electronic configurations of $[Xe]4f^{11}$ and $[Xe]4f^{13}$, respectively. These particular electronic configurations are such that they are composed of incompletely filled 4f shells which are shielded from the surrounding host matrix by two closed 5s and 5p shells. Due to the shielding effect of the outer shells, the exact energies of the 4f states, and consequently absorption and emission wavelengths, differ only slightly for different hosts in which the ions are incorporated [69]. Each energy level can be represented by the Russell-Saunders notation $^{2S+1}L_J$, where the spin angular momentum is represented by S, while the multiplicity is given by $2S + 1$. L represents the orbital angular momentum and J the total angular momentum. Despite the shielding effect of the outer 5s and 5p shells, the influence of the local electric field of the host material around the ion removes the degeneracy of the 4f levels, resulting in a Stark splitting of the energy levels into a total of $2J + 1$ Stark sub-levels when J is an integer or $J + \frac{1}{2}$ Stark sub-levels otherwise.

Rare-earth-ion-doped lasers are generally classified as three-, four-, or quasi-three-level systems, depending on the number and configuration of the energy levels which are involved in the optical pumping and lasing processes, as shown in Figure 2.1.

Three-Level System

Absorption of incident pump radiation causes the rare-earth ions (or atoms) to be excited into an appropriate higher energy level, from where they can undergo a rapid radiative or non-radiative transfer to the upper laser level. The laser action depopulates ions from the upper laser level back to the ground state via the process of stimulated emission. More than half of the ions have to be pumped into the upper laser level in order to reach a population inversion, which is needed to obtain optical gain. Since the lower laser level is in fact the ground level, it is possible for ions in the ground level to absorb laser photons. The reabsorption of laser light introduces a loss of laser photons in the system. Due to the reabsorption loss in three-level lasers, they require relatively high pump intensities as compared to four-level lasers. The first ever demonstrated laser was a three-level ruby

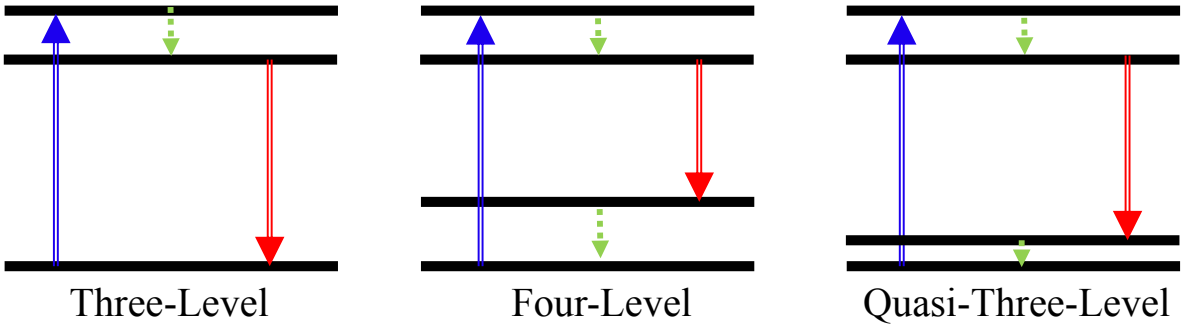

Figure 2.1: Energy level diagrams of different laser systems. Pump absorption is indicated by the blue arrows, while stimulated emission on the laser transition is indicated by the red arrows. The green arrows indicate rapid non-radiative transitions.

laser [3].

Four-Level System

Pump radiation excites ions from the ground level into a higher energy level, from where a rapid non-radiative transition populates the upper laser level. From here the laser action occurs via stimulated emission to a lower laser level which is well above the ground state. From the lower laser level, another fast non-radiative transition occurs to the ground state so that no significant population density of the lower laser level occurs. Consequently, reabsorption of the laser radiation is avoided with such an energy level scheme. Neodymium-doped lasers which are pumped at $\sim$ 800 nm and emit at $\sim$ 1060 nm are good examples of a four-level system.

Quasi-Three-Level System

This type of laser level scheme provides a situation which is in-between the idealized three- and four-level laser models. In this case the laser transition terminates on a level which is so close to the ground state that a substantial portion of the active ions occupy this lower laser level, as given by a Boltzmann distribution at the temperature of the gain medium. Typically, the lower laser level and the ground state are different Stark levels from the same multiplet. In this type of laser level scheme, the unpumped regions of the gain medium causes some additional reabsorption loss at the laser wavelength, with similar consequences to that of a three-level laser. In the limit where the temperature of the gain medium goes to zero, the population density of the lower laser level will also go to zero, so that the device will operate as a four-level laser. It should also be noted that prominent three-level behavior is inevitable for gain media with a very small quantum defect, due to the small energy difference between the lower laser level and the ground state, so that the thermal population at room temperature of the lower laser level is significant. The quantum defect refers to the difference in energy between a pump photon and a laser photon. Both erbium- and ytterbium-doped lasers which are considered in this work are

good examples of quasi-three-level lasers at room temperature. Particular attention is given to the population dynamics of these two rare-earth elements.

2.1.2 Population Dynamics of the Yb^{3+} Ion

Energy Transitions

Compared to other rare-earth elements, Yb^{3+} has a rather simple energy level structure which consists of two energy manifolds. The upper manifold labeled $^2F_{5/2}$ contains three Stark levels, while the $^2F_{7/2}$ ground state contains four Stark levels (Figure 2.2). The Stark splitting of the two manifolds is on the order of 10^2 cm^{-1} while the energy gap between the two manifolds is approximately 10^4 cm^{-1}. Since the Yb^{3+} ion has only two energy manifolds, there are no parasitic processes such as upconversion or excited state absorption (ESA) [70], which could be detrimental to the performance of lasers and amplifiers. Despite the fact that there are only two energy manifolds, the strong Stark splitting makes is possible to invert the Yb^{3+} system, and thus to obtain the gain necessary for optical amplification or laser action. Due to the Stark splitting, the operation of the Yb^{3+} ion can be considered as a quasi-three level system.

The relevant transitions for laser action are shown in Figure 2.2. Via absorption of pump light at a wavelength around 980 nm (976 nm absorption peak), the ions are excited from the ground manifold to the $^2F_{5/2}$ manifold. The luminescence lifetime of the excited state in Al_2O_3 is 740 μs [70]. Stimulated emission at $\sim$ 1020 nm then transfers the excited ions back to the high-lying Stark levels of the $^2F_{7/2}$ manifold, from where a fast thermal relaxation transfers them to a lower Stark level in the same manifold. Spontaneous emission from the $^2F_{5/2}$ to the $^2F_{7/2}$ manifold is also considered. Figure 2.3 shows the absorption and emission cross-sections of the Yb^{3+} ion in an Al_2O_3 waveguide.

Rate Equations

From the transitions between the respective energy levels, rate equations are derived which describe the population dynamics of the Yb^{3+} ions. For the purpose of the rate equation model, the Yb^{3+} ion can be considered as a two level system with a ground state population density N_0, excited state population density N_1, and total doping concentration N_T. The rate equation describing the population density of the first excited energy manifold is given by

$$\frac{dN_1(x,y,z)}{dt} = R_{01}(x,y,z)N_0(x,y,z) - R_{10}(x,y,z)N_1(x,y,z) \tag{2.1}$$

where x, y and z represent spatial coordinates. R_{01} is the total rate at which Yb^{3+} ions are pumped from the $^2F_{7/2}$ ground state to the $^2F_{5/2}$ excited state by means of absorption (at pump and laser wavelengths), while R_{10} is the total rate at which ions are transferred from the excited state back to the ground state by means of stimulated emission and

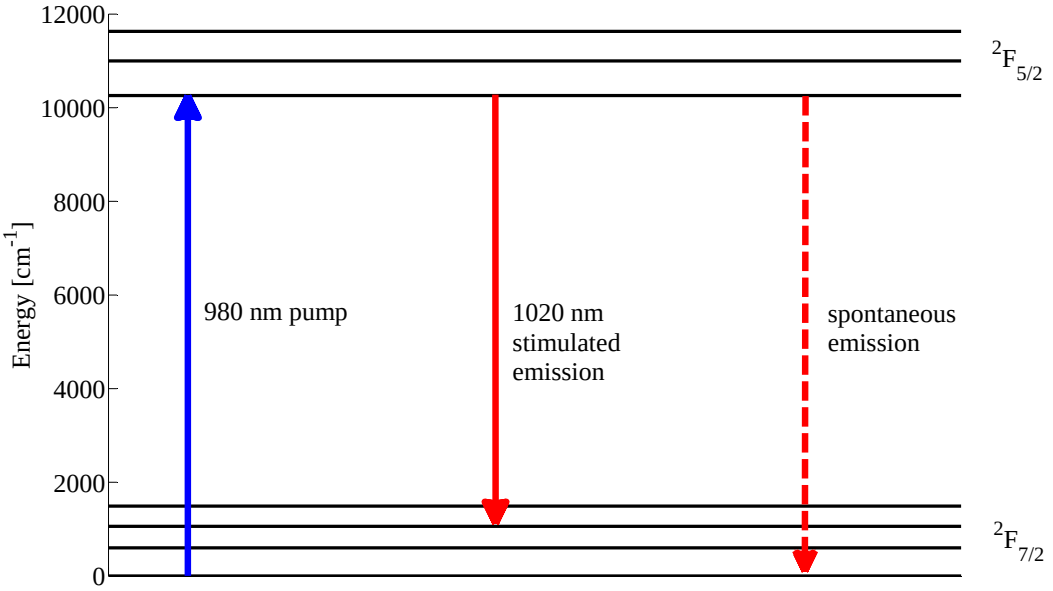

Figure 2.2: Schematic of the energy levels (with an indication of the Stark splitting) in the Yb^{3+} ion along with the selected transitions which are considered in this work. (Adapted from [71].)

spontaneous emission so that

$$R_{01}(x,y,z) = \frac{P_{\mathrm{P}}(z)\phi_{\mathrm{P}}(x,y)}{h\nu_{\mathrm{P}}}\sigma_{\mathrm{P}}^{\mathrm{abs}} + \frac{P_{\mathrm{L}}(z)\phi_{\mathrm{L}}(x,y)}{h\nu_{\mathrm{L}}}\sigma_{\mathrm{L}}^{\mathrm{abs}} \tag{2.2}$$

$$R_{10}(x,y,z) = \frac{P_{\mathrm{P}}(z)\phi_{\mathrm{P}}(x,y)}{h\nu_{\mathrm{P}}}\sigma_{\mathrm{P}}^{\mathrm{em}} + \frac{P_{\mathrm{L}}(z)\phi_{\mathrm{L}}(x,y)}{h\nu_{\mathrm{L}}}\sigma_{\mathrm{L}}^{\mathrm{em}} + \frac{1}{\tau} \tag{2.3}$$

P is the total optical power at position z along the cavity, subscripts P and L denote pump and laser, respectively, and $\phi(x,y)$ is a normalized transverse intensity distribution, such that

$$\int_{-\infty}^{\infty}\int_{-\infty}^{\infty}\phi(x,y)\,\mathrm{d}x\,\mathrm{d}y = 1 \tag{2.4}$$

h is Planck's constant, ν is the optical frequency, τ is the luminescence lifetime of the $^2\mathrm{F}_{5/2}$ excited state, while σ^{abs} and σ^{em} represent the effective absorption and emission cross-sections, respectively (Figure 2.3). It is assumed that the following boundary condition is true

$$N_0(x,y,z) = N_{\mathrm{T}} - N_1(x,y,z) \tag{2.5}$$

where N_{T} is the total density of active ions. By using Equation 2.5 and the fact that Equation 2.1 is equal to zero during steady state operation, it follows that

$$N_1(x,y,z) = N_{\mathrm{T}}\frac{R_{01}(x,y,z)}{R_{01}(x,y,z) + R_{10}(x,y,z)} \tag{2.6}$$

In Section 2.1.4, Equations 2.5 and 2.6 are combined with the propagation of the pump and signal (laser) fields to form an optical gain model for an ytterbium-doped waveguide.

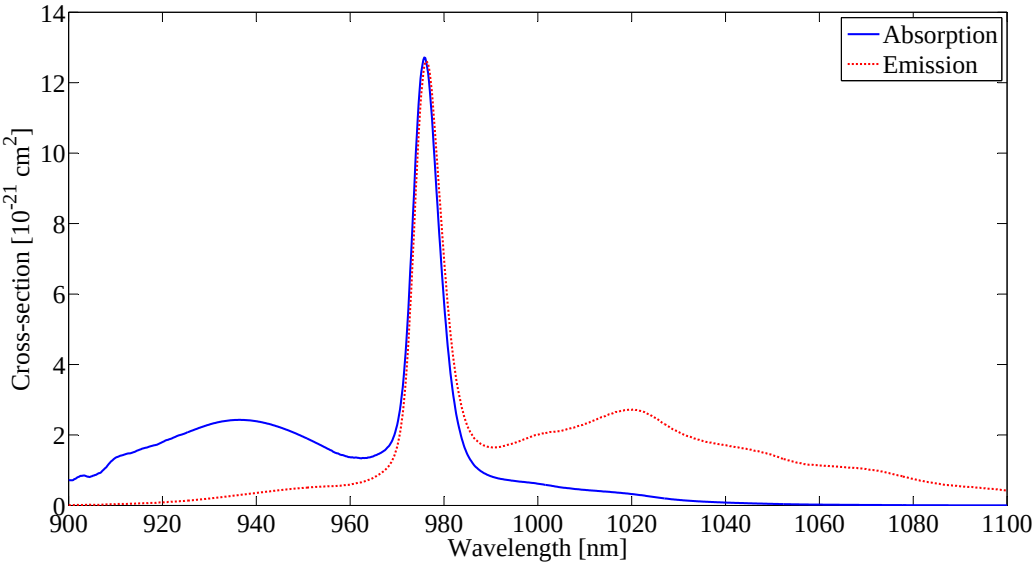

Figure 2.3: Effective absorption and emission cross-sections of Al_2O_3:Yb^{3+}. (Adapted from [70].)

2.1.3 Population Dynamics of the Er^{3+} Ion

Energy Transitions

The Er^{3+} ion has a much more complicated energy level scheme than Yb^{3+}. Its electron configuration is such that it gives rise to a number of possible states, which introduces the possibility of excited state absorption (ESA) and energy transfer upconversion (ETU). Figure 2.4 shows a schematic representation of the lower-lying energy levels of Er^{3+}, starting from the ground state and continuing up to the $^4F_{7/2}$ level. Also displayed in the figure are the wavelengths corresponding to the ground-state transitions from each manifold and the approximate energy in cm^{-1} relative to the ground state for each level. The Stark splitting of the multiplets and non-radiative transitions are not depicted in Figure 2.4 for the sake of simplicity.

The waveguide lasers which are considered in this work operate based on stimulated emission at $\sim$ 1533 nm from the first excited $^4I_{13/2}$ manifold to the $^4I_{15/2}$ ground state. The metastable $^4I_{13/2}$ level has a long lifetime of several milliseconds, which can be used to create a population inversion with respect to the ground state. Pump light at a wavelength of 980 nm or 1480 nm can be used to populate the $^4I_{13/2}$ level. Pumping at 1480 nm will excite ions from the $^4I_{15/2}$ ground state to the upper Stark levels of the $^4I_{13/2}$ first excited state. Alternatively, an indirect pumping of the $^4I_{13/2}$ level can be achieved with a 980 nm pump, where the ions are first pumped from the ground state to the $^4I_{11/2}$ level, followed by rapid non-radiative decay to the $^4I_{13/2}$ level. Spontaneous emission processes from the first and second excited states to the ground state are also considered.

As opposed to ground state absorption where an ion in the ground state absorbs a pump photon to be elevated to a excited state, ESA relates to the absorption of a pump

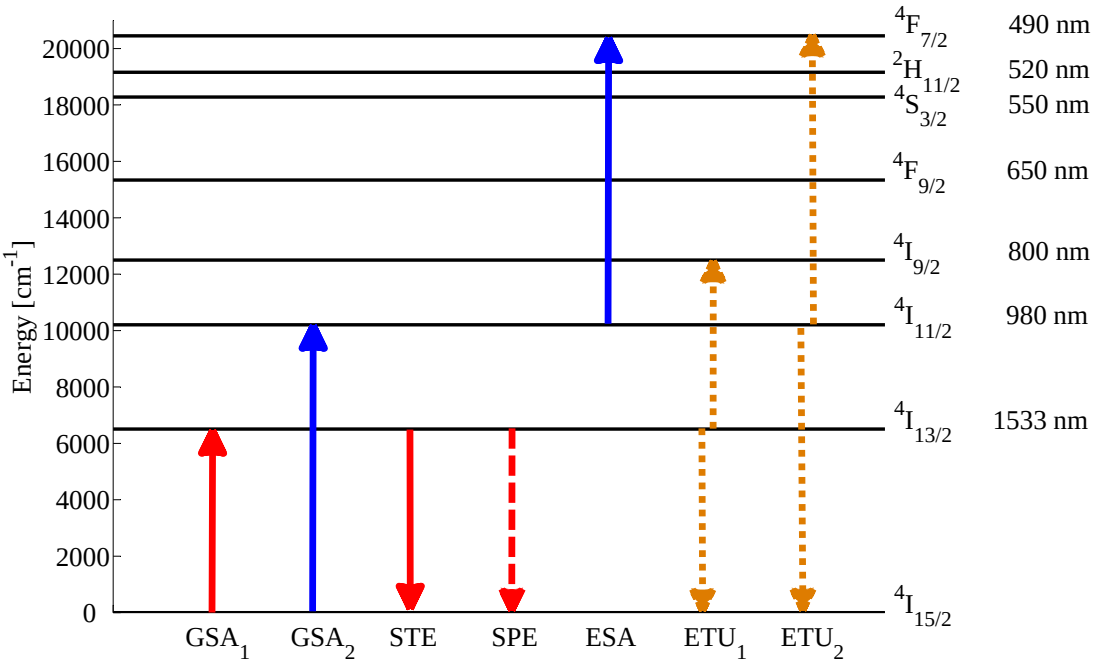

Figure 2.4: Schematic of the energy levels in the Er^{3+} ion. The energy in cm^{-1} relative to the ground state and the wavelength corresponding to a photon of this energy are also indicated. ((Adapted from [72].)
GSA_1: Ground state absorption (1480 nm) to the upper Stark levels of the $^4I_{13/2}$ manifold.
GSA_2: Ground state absorption (980 nm) to the $^4I_{11/2}$ manifold.
STE : Stimulated emission from the first excited state to the ground state.
SPE : Spontaneous emission from the first excited state to the ground state.
ESA : Excited state absorption (980 nm) from the $^4I_{11/2}$ to $^4F_{7/2}$ manifold.
ETU_1: Energy transfer upconversion between two neighboring ions in the $^4I_{13/2}$ manifold.
ETU_2: Energy transfer upconversion between two neighboring ions in the $^4I_{11/2}$ manifold.

photon by an ion which is already in an excited state, in order to be excited to an even higher energy state. In the Er^{3+} system, ESA occurs when ions in the $^4I_{11/2}$ level absorb 980 nm pump light to be excited to the $^4F_{7/2}$ level.

Due to the limited length of erbium-doped waveguides as compared to fibers, a high erbium concentration is required to have sufficiently short pump absorption lengths in order to obtain the desired performance. However, as the doping concentration is increased, the average distance between Er^{3+} ions is decreased. ETU is a dipole-dipole interaction between two Er^{3+} ions and can have a significant impact on the performance of Er-doped lasers and amplifiers. Since ETU has a R^{-6} dependence on the inter-ionic radius R, the effect of ETU becomes more pronounced at high erbium concentrations. Two different ETU processes are considered in this work. The first one involves energy transfer between two ions in the $^4I_{13/2}$ level resulting in promotion of one ion to the $^4I_{9/2}$ state and de-excitation of the other to the ground state. This process decreases the number of ions in the $^4I_{13/2}$ state available for stimulated emission. The second ETU process involves

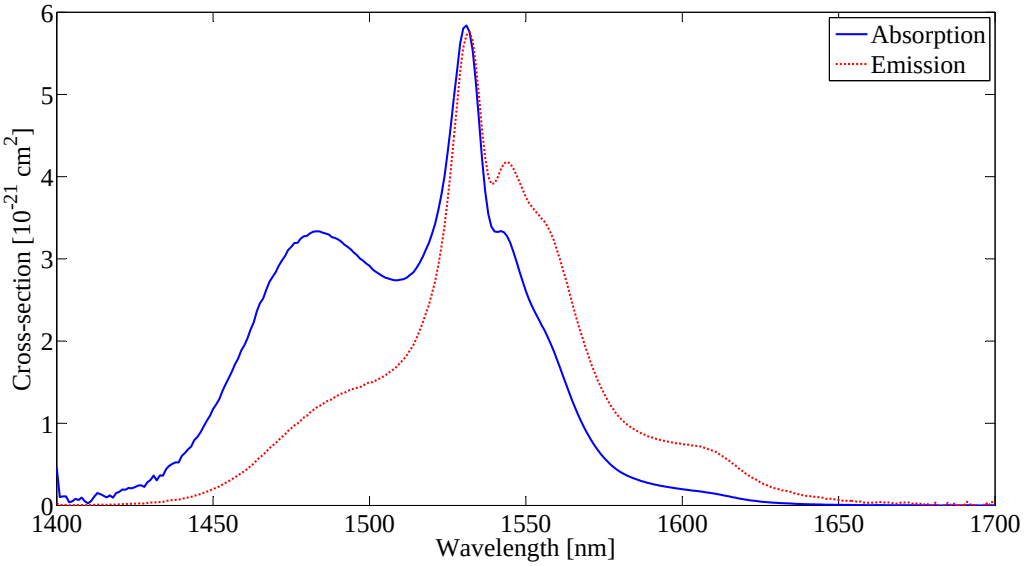

Figure 2.5: Effective absorption and emission cross-sections of Al_2O_3:Er^{3+}. (Adapted from [60].)

energy transfer between two ions in the $^4I_{11/2}$ state and excitation of one of the ions to higher-lying levels and de-excitation of the other to the ground state.

The effective absorption and emission cross-sections of Al_2O_3:Er^{3+} are shown in Figure 2.5. From the emission cross-sections it is clear that Al_2O_3:Er^{3+} has a wide emission bandwidth and has the ability to emit photons at wavelengths which span the entire telecom C-band, ranging from 1525 nm to 1565 nm. In order to obtain the optimum performance from optical amplifiers and lasers operating in this wavelength range, careful consideration should be given as to which pump wavelength should be used for the particular device. In this work, 980 nm and 1480 nm pump configurations are considered. To understand how the underlying population dynamics influence the performance of such a device, two different rate equation models are used, each considering the relevant dynamics associated with the particular pump wavelength.

Rate Equations (980 nm Pumping)

For the purpose of the rate equation model, the Er^{3+} ions being pumped at a wavelength of 980 nm are described using three energy levels which include the $^4I_{15/2}$ ground state (N_0), the $^4I_{13/2}$ first excited level (N_1), the $^4I_{11/2}$ pump excitation level (N_2), and a total doping concentration N_T. Since the $^4I_{11/2}$ population density is small due to a relatively short lifetime and rapid non-radiative relaxation to the $^4I_{13/2}$ level as well as the fact that energy migration was observed to be significantly slower in the $^4I_{11/2}$ second excited state as compared to the $^4I_{13/2}$ first excited state [70], the influence of ETU from this second excited level into the higher-lying $^4F_{7/2}$ level was excluded from the model. Further it is assumed that ESA from the $^4I_{11/2}$ level only contributes to the reduction of pump power but does not affect the population dynamics in any other way, since excitation to higher-

lying levels will result in rapid non-radiative relaxation back to the $^4I_{11/2}$ level. The rate equations describing the population densities of the first two energy manifolds are given by

$$\frac{dN_2}{dt} = R_{02}N_0 - R_{20}N_2 - R_{21}N_2 + W_{\mathrm{ETU}}N_1^2 \tag{2.7}$$

$$\frac{dN_1}{dt} = R_{01}N_0 - R_{10}N_1 + R_{21}N_2 - 2W_{\mathrm{ETU}}N_1^2 \tag{2.8}$$

W_{ETU} is the macroscopic material-dependent ETU parameter, which represents the probability of the ETU process occurring from the first excited $^4I_{13/2}$ level. R_{02} and R_{01} are the rates at which ions are transferred from the ground state to the first and second excited states, respectively, by means of the absorption of radiation. In the case of R_{02} it concerns the absorption of 980 nm pump radiation, while R_{01} describes the absorption of $\sim$ 1533 nm laser radiation. R_{20} is the rate at which ions are de-excited from the second excited state back to the ground state via stimulated emission of 980 nm pump radiation, while R_{10} is the rate at which ions are de-excited from the first excited state back to the ground state via stimulated and spontaneous emission. R_{21} is the rate at which ions are transferred from the second to the first excited state by means of a rapid non-radiative transition. Note that the population densities and respective transition rates in Equations 2.7 and 2.8 are spatially dependent, as in the case of Equations 2.1 to 2.3. However, here the spatial coordinates are omitted for the sake of readability. The respective rates are defined by

$$R_{02} = \frac{P_{\mathrm{P}}(z)\phi_{\mathrm{P}}(x,y)}{h\nu_{\mathrm{P}}}\sigma_{\mathrm{P}}^{\mathrm{abs}} \tag{2.9}$$

$$R_{20} = \frac{P_{\mathrm{P}}(z)\phi_{\mathrm{P}}(x,y)}{h\nu_{\mathrm{P}}}\sigma_{\mathrm{P}}^{\mathrm{em}} \tag{2.10}$$

$$R_{21} = \frac{1}{\tau_2} \tag{2.11}$$

$$R_{01} = \frac{P_{\mathrm{L}}(z)\phi_{\mathrm{L}}(x,y)}{h\nu_{\mathrm{L}}}\sigma_{\mathrm{L}}^{\mathrm{abs}} \tag{2.12}$$

$$R_{10} = \frac{P_{\mathrm{L}}(z)\phi_{\mathrm{L}}(x,y)}{h\nu_{\mathrm{L}}}\sigma_{\mathrm{L}}^{\mathrm{em}} + \frac{1}{\tau_1} \tag{2.13}$$

where τ_1 and τ_2 represent the luminescence lifetime of the first and second excited states, respectively. The other parameters have the same definitions as in Section 2.1.2. It is assumed that the following boundary condition is true

$$N_0 = N_{\mathrm{T}} - (N_1 + N_2) \tag{2.14}$$

In the case of a continuous-wave laser, the population densities of the respective energy levels are in a steady state, so that Equations 2.7 and 2.8 are equal to zero. From this assumption it follows that

$$N_2 = \frac{R_{02}(N_{\mathrm{T}} - N_1) + W_{\mathrm{ETU}}N_1^2}{R_{02} + R_{20} + R_{21}} \tag{2.15}$$

$$N_1 = \frac{\sqrt{B^2 - 4AC} - B}{2A} \tag{2.16}$$

where A, B, and C are given by

$$A = W_{\mathrm{ETU}} \left(2 + \frac{R_{01} - R_{21}}{R_{02} + R_{20} + R_{21}} \right) \tag{2.17}$$

$$B = R_{01} + R_{10} + \frac{R_{02} \left(R_{21} - R_{01} \right)}{R_{02} + R_{20} + R_{21}} \tag{2.18}$$

$$C = - \left(R_{01} N_{\mathrm{T}} + \frac{R_{02} N_{\mathrm{T}} \left(R_{21} - R_{01} \right)}{R_{02} + R_{20} + R_{21}} \right) \tag{2.19}$$

In Section 2.1.4, Equations 2.14 to 2.16 are combined with the propagation of the pump and signal (laser) fields to form an optical gain model for an erbium-doped waveguide pumped at a wavelength of 980 nm.

Rate Equations (1480 nm Pumping)

The rate equation model in this section describes the population dynamics of the Er^{3+} ion being pumped at a wavelength of 1480 nm. As in the case of 980 nm pumping, the system is described using three energy levels which include the $^4I_{15/2}$ ground state (N_0), the $^4I_{13/2}$ first excited level (N_1), the $^4I_{11/2}$ pump excitation level (N_2), and a total doping concentration N_{T}. The main difference as compared to the 980 nm rate equation model is that the 1480 nm pump absorption excites ions to the $^4I_{13/2}$ first excited state instead of the $^4I_{11/2}$ second excited state as with 980 nm pump radiation. The rate equations describing the population densities of the first two energy manifolds are given by

$$\frac{dN_2}{dt} = W_{\mathrm{ETU}} N_1^2 - R_{21} N_2 \tag{2.20}$$

$$\frac{dN_1}{dt} = R_{01} N_0 - R_{10} N_1 + R_{21} N_2 - 2 W_{\mathrm{ETU}} N_1^2 \tag{2.21}$$

R_{01} is the total rate at which ions are pumped from the ground state to the first excited state by means of absorption of 1480 nm pump and $\sim$ 1533 nm laser radiation. R_{10} is the rate at which ions are de-excited from the first excited state back to the ground state via stimulated emission, at the pump and laser wavelengths, as well as spontaneous emission. As before, R_{21} is the rate at which ions are transferred from the second to the first excited state by means of a rapid non-radiative transition. The respective rates are defined by

$$R_{21} = \frac{1}{\tau_2} \tag{2.22}$$

$$R_{01} = \frac{P_{\mathrm{P}}(z) \phi_{\mathrm{P}}(x,y)}{h \nu_{\mathrm{P}}} \sigma_{\mathrm{P}}^{\mathrm{abs}} + \frac{P_{\mathrm{L}}(z) \phi_{\mathrm{L}}(x,y)}{h \nu_{\mathrm{L}}} \sigma_{\mathrm{L}}^{\mathrm{abs}} \tag{2.23}$$

$$R_{10} = \frac{P_{\mathrm{P}}(z) \phi_{\mathrm{P}}(x,y)}{h \nu_{\mathrm{P}}} \sigma_{\mathrm{P}}^{\mathrm{em}} + \frac{P_{\mathrm{L}}(z) \phi_{\mathrm{L}}(x,y)}{h \nu_{\mathrm{L}}} \sigma_{\mathrm{L}}^{\mathrm{em}} + \frac{1}{\tau_1} \tag{2.24}$$

It is assumed that the following boundary condition is true

$$N_0 = N_{\mathrm{T}} - (N_1 + N_2) \tag{2.25}$$

In the case of a continuous-wave laser, the population densities of the respective energy levels are in a steady state, so that Equations 2.20 and 2.21 are equal to zero. From this assumption it follows that

$$N_2 = \frac{W_{\mathrm{ETU}} N_1^2}{R_{21}} \tag{2.26}$$

$$N_1 = \frac{\sqrt{B^2 - 4AC} - B}{2A} \tag{2.27}$$

where A, B, and C are given by

$$A = W_{\mathrm{ETU}} \left(1 + \frac{R_{01}}{R_{21}}\right) \tag{2.28}$$

$$B = R_{01} + R_{10} \tag{2.29}$$

$$C = -R_{01} N_{\mathrm{T}} \tag{2.30}$$

In Section 2.1.4, Equations 2.25 to 2.27 are combined with the propagation of the pump and signal (laser) fields to form an optical gain model for an erbium-doped waveguide pumped at a wavelength of 1480 nm.

2.1.4 Absorption and Gain Coefficients

The rate equations which were derived in the previous section describe how the population densities in the rare-earth ions change as the ions interact with pump and laser radiation. However, it is also necessary to consider the change in the radiation due to the interaction with the rare-earth ions, primarily via the processes of absorption and stimulated emission. The Lambert-Beer law for absorption and emission defines the longitudinal propagation of an optical signal with power P and wavelength λ, along the length of the active waveguide as

$$\frac{\mathrm{d}P_\lambda(z)}{\mathrm{d}z} = \gamma(\lambda, z) P_\lambda(z) \tag{2.31}$$

γ is a coefficient which determines whether the optical signal will be attenuated or amplified as it propagates through the waveguide. When $\gamma < 0$ it is referred to as the absorption coefficient α and implies that the optical signal will be attenuated, while $\gamma > 0$ is termed the gain coefficient g and results in the optical signal being amplified. In this work, α is usually associated with the pump wavelength λ_{P}, while g is related to the laser wavelength λ_{L}. When γ is constant as a function of z, it is possible to solve Equation 2.31 analytically. However, in reality γ has a z-dependence so that Equation 2.31 has to be solved with numerical methods. In Section 2.2.1, α and g are used in combination with coupled mode theory in order to simulate the operation of rare-earth-ion-doped DFB and DBR waveguide lasers. Although α and g traditionally do not consider propagation losses, in this work I do include the propagation losses in the definition of α and g, respectively.

Ytterbium

In the case of ytterbium, α and g are given by

$$\alpha(\lambda_{\mathrm{P}}, z) = \int_{-\infty}^{\infty}\int_{-\infty}^{\infty} \phi_{\mathrm{P}}(x,y)\left(\sigma_{\mathrm{P}}^{\mathrm{em}}(\lambda_{\mathrm{P}})N_1 - \sigma_{\mathrm{P}}^{\mathrm{abs}}(\lambda_{\mathrm{P}})N_0\right)\mathrm{d}x\mathrm{d}y - \alpha_{\mathrm{P}}^{\mathrm{loss}} \tag{2.32}$$

$$g(\lambda_{\mathrm{L}}, z) = \int_{-\infty}^{\infty}\int_{-\infty}^{\infty} \phi_{\mathrm{L}}(x,y)\left(\sigma_{\mathrm{L}}^{\mathrm{em}}(\lambda_{\mathrm{L}})N_1 - \sigma_{\mathrm{L}}^{\mathrm{abs}}(\lambda_{\mathrm{L}})N_0\right)\mathrm{d}x\mathrm{d}y - \alpha_{\mathrm{L}}^{\mathrm{loss}} \tag{2.33}$$

where $\alpha_{\mathrm{P}}^{\mathrm{loss}}$ and $\alpha_{\mathrm{L}}^{\mathrm{loss}}$ represent the propagation loss at the pump and laser wavelengths, respectively, expressed in dimensions of m^{-1}. N_0 and N_1 are the population densities of the $^2\mathrm{F}_{7/2}$ ground state and $^2\mathrm{F}_{5/2}$ excited state of the Yb^{3+} ion which are calculated from Equations 2.5 and 2.6.

Erbium (980 nm Pumping)

For an erbium-doped waveguide being pumped at a wavelength of 980 nm, α and g are given by

$$\alpha(\lambda_{\mathrm{P}}, z) = \int_{-\infty}^{\infty}\int_{-\infty}^{\infty} \phi_{\mathrm{P}}(x,y)\left(\sigma_{\mathrm{P}}^{\mathrm{em}}(\lambda_{\mathrm{P}})N_2 - \sigma_{\mathrm{P}}^{\mathrm{abs}}(\lambda_{\mathrm{P}})N_0 - \sigma_{\mathrm{P}}^{\mathrm{ESA}}(\lambda_{\mathrm{P}})N_2\right)\mathrm{d}x\mathrm{d}y - \alpha_{\mathrm{P}}^{\mathrm{loss}} \tag{2.34}$$

$$g(\lambda_{\mathrm{L}}, z) = \int_{-\infty}^{\infty}\int_{-\infty}^{\infty} \phi_{\mathrm{L}}(x,y)\left(\sigma_{\mathrm{L}}^{\mathrm{em}}(\lambda_{\mathrm{L}})N_1 - \sigma_{\mathrm{L}}^{\mathrm{abs}}(\lambda_{\mathrm{L}})N_0\right)\mathrm{d}x\mathrm{d}y - \alpha_{\mathrm{L}}^{\mathrm{loss}} \tag{2.35}$$

N_0, N_1 and N_2 are the population densities of the $^4\mathrm{I}_{15/2}$ ground state, $^4\mathrm{I}_{13/2}$ first excited state, and the $^4\mathrm{I}_{11/2}$ second excited state of the Er^{3+} ion and are calculated from Equations 2.14 to 2.16. $\sigma_{\mathrm{P}}^{\mathrm{ESA}}$ is the ESA cross-section which contributes to the attenuation of pump power via the absorption of pump radiation by ions in the $^4\mathrm{I}_{11/2}$ second excited state.

Erbium (1480 nm Pumping)

For an erbium-doped waveguide being pumped at a wavelength of 1480 nm, α and g are given by

$$\alpha(\lambda_{\mathrm{P}}, z) = \int_{-\infty}^{\infty}\int_{-\infty}^{\infty} \phi_{\mathrm{P}}(x,y)\left(\sigma_{\mathrm{P}}^{\mathrm{em}}(\lambda_{\mathrm{P}})N_1 - \sigma_{\mathrm{P}}^{\mathrm{abs}}(\lambda_{\mathrm{P}})N_0\right)\mathrm{d}x\mathrm{d}y - \alpha_{\mathrm{P}}^{\mathrm{loss}} \tag{2.36}$$

$$g(\lambda_{\mathrm{L}}, z) = \int_{-\infty}^{\infty}\int_{-\infty}^{\infty} \phi_{\mathrm{L}}(x,y)\left(\sigma_{\mathrm{L}}^{\mathrm{em}}(\lambda_{\mathrm{L}})N_1 - \sigma_{\mathrm{L}}^{\mathrm{abs}}(\lambda_{\mathrm{L}})N_0\right)\mathrm{d}x\mathrm{d}y - \alpha_{\mathrm{L}}^{\mathrm{loss}} \tag{2.37}$$

Here, N_0, N_1 and N_2 are also the population densities of the $^4\mathrm{I}_{15/2}$ ground state, $^4\mathrm{I}_{13/2}$ first excited state, and the $^4\mathrm{I}_{11/2}$ second excitation state of the Er^{3+} ion and are calculated from Equations 2.25 to 2.27.

2.2 Bragg Gratings

In the context of integrated optics, a Bragg grating is a periodic perturbation of the guided structure which results in a periodic perturbation of the effective refractive index n_{eff} of the guided mode. Such a structure acts as a one-dimensional diffraction grating which has the ability to diffract radiation from a forward-propagating guided mode into a backward-propagating mode. In order to have efficient diffraction of a guided mode, with free-space wavelength λ_0, into a backward-propagating mode, the reflections from the individual periods in the grating should interfere constructively. This requires that the grating period Λ obeys the following relation

$$\Lambda = \frac{m\lambda_0}{2n_{\text{eff}}} \tag{2.38}$$

where m is a positive integer which denotes the order of the grating. This condition is know as Bragg's law, and the wavelength for which this condition holds is referred to as the Bragg wavelength λ_{B}.

The ability to integrate Bragg grating structures with optical waveguides provides the opportunity to realize a variety of compact monolithic optical devices such as DFB lasers [6], DBR lasers [4], optical add-drop multiplexers [73], and dispersion compensators [74], which are widely used in telecommunication systems and integrated optical sensors. Several fabrication techniques have been used to realize Bragg gratings in channel waveguides. These include UV-photo-induced [75], femtosecond laser-written [76], and physically corrugated Bragg gratings [6].

The Bragg grating which are considered in this work are first order ($m = 1$) physically corrugated gratings. The most common method to simulate the performance of such a Bragg grating structure is to make use of coupled mode theory.

2.2.1 Coupled Mode Theory

In this section the operation of a Bragg grating structure is described mathematically by using coupled mode theory (CMT), in which the Bragg grating is considered as a perturbation in the waveguide [77–79]. Because of its mathematical simplicity and physical intuitiveness, CMT has been applied extensively in integrated optics as a mathematical tool to analyze the propagation and interaction of electromagnetic waves [80]. Since the model is versatile enough to allow for easy integration with a gain model which describes the population dynamics of the rare-earth ions, it provides a very efficient tool for the modelling of distribute feedback (DFB) and distributed Bragg reflector (DBR) waveguide lasers.

Instead of considering the optical reflections from each of the individual grating periods, the grating is rather considered as a distributed reflector in which power is transferred between the forward- and backward propagating modes. In the case of a uniform Bragg grating, the coupling between the two counter-propagating modes of wavelength λ is

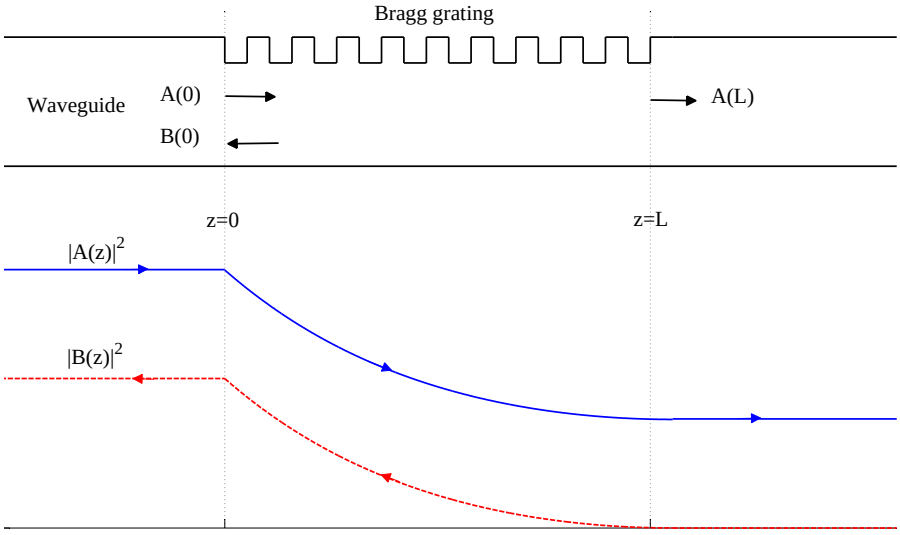

Figure 2.6: Surface-corrugated Bragg grating in a section of a dielectric waveguide showing the incident (blue) and reflected (red) fields for $\Delta\beta = 0$.

described by the following set of differential equations [79, 81–84]

$$\frac{\mathrm{d}A(z)}{\mathrm{d}z} = -i\kappa B(z)e^{(i2\Delta\beta z)} + \frac{\gamma}{2}A(z) \tag{2.39}$$

$$\frac{\mathrm{d}B(z)}{\mathrm{d}z} = i\kappa A(z)e^{(-i2\Delta\beta z)} - \frac{\gamma}{2}B(z) \tag{2.40}$$

where $A(z)$ and $B(z)$ are the amplitudes of the forward- and backward propagating modes, respectively, i is the imaginary unit, and γ is the power gain or absorption per unit length as defined in Section 2.1.4. Equations 2.39 and 2.40 provide a valid approximation for gratings with a weak perturbation. The coupling coefficient between the forward and backward waves is denoted by κ, which is expressed in units of m^{-1}. $\Delta\beta$ is a measure of the deviation from the Bragg condition given by

$$\begin{aligned}\Delta\beta &= \beta - \beta_{\mathrm{B}} \\ &= \frac{2\pi}{\lambda}n_{\mathrm{eff}} - \frac{\pi}{\Lambda}\end{aligned} \tag{2.41}$$

where β and β_{B} are the propagation constants of the modes with wavelength λ and λ_{B}, respectively. A schematic showing a uniform surface-corrugated Bragg grating of length L in a section of a dielectric waveguide along with the forward- and backward traveling waves at the Bragg wavelength ($\Delta\beta = 0$) is depicted in Figure 2.6. The power of the forward- and backward traveling modes are proportional to $|A(z)|^2$ and $|B(z)|^2$, respectively. A wave with an amplitude $A(0)$ is assumed to be incident from the left on the corrugated section. The power of the incident mode decreases exponentially along the length of the grating. This behavior is not due to absorption, but due to reflection into the backward traveling mode B(z).

Transfer Matrix Method

Assuming the continuity conditions of forward and backward waves at the interfaces of $z = 0$ and $z = L$ (Figure 2.6), the solution to the coupled mode Equations 2.39 and 2.40 can be written in matrix form as [82, 83, 85]

$$\begin{bmatrix} A(0) \\ B(0) \end{bmatrix} = \begin{bmatrix} F_{11} & F_{12} \\ F_{21} & F_{22} \end{bmatrix} \begin{bmatrix} A(L) \\ B(L) \end{bmatrix} \tag{2.42}$$

The elements of the transfer matrix F are given by

$$F_{11} = \cosh(\rho L) + i\frac{\delta}{\rho}\sinh(\rho L) \tag{2.43}$$

$$F_{12} = i\frac{\kappa}{\rho}\sinh(\rho L) \tag{2.44}$$

$$F_{21} = -i\frac{\kappa}{\rho}\sinh(\rho L) \tag{2.45}$$

$$F_{22} = \cosh(\rho L) - i\frac{\delta}{\rho}\sinh(\rho L) \tag{2.46}$$

where the following definitions have been used

$$\delta = \Delta\beta + i\frac{\gamma}{2} \tag{2.47}$$

$$\rho^2 = \kappa^2 - \delta^2 \tag{2.48}$$

Note that the determinant of the transfer matrix is unity, so that F is invertible. If it is assumed that an external field is incident only from the left on the Bragg grating, then the entire backward propagating field originates from within the Bragg grating region, which implies that there is no backward propagating field at the right boundary of the Bragg grating (i.e. $B(L) = 0$). With this assumption, it follows directly from Equation 2.42 that the amplitude reflection and transmission coefficients of such a uniform Bragg grating are given, respectively, by

$$r = \frac{B(0)}{A(0)} = \frac{F_{21}}{F_{11}} = \frac{-i\kappa\tanh(\rho L)}{\rho + i\delta\tanh(\rho L)} \tag{2.49}$$

$$t = \frac{A(L)}{A(0)} = \frac{1}{F_{11}} = \frac{\rho\,\mathrm{sech}(\rho L)}{\rho + i\delta\tanh(\rho L)} \tag{2.50}$$

It follows from Equations 2.49 and 2.50 that the power reflection and transmission coefficients of a uniform Bragg grating can be written as

$$R = |r|^2 = \left|\frac{-i\kappa\tanh(\rho L)}{\rho + i\delta\tanh(\rho L)}\right|^2 \tag{2.51}$$

$$T = |t|^2 = \left|\frac{\rho\,\mathrm{sech}(\rho L)}{\rho + i\delta\tanh(\rho L)}\right|^2 \tag{2.52}$$

Although Equations 2.51 and 2.52 give the optical response of the Bragg grating in terms of its wavelength dependent reflection and transmission at the input ($z = 0$) and output

($z = L$) positions of the grating, respectively, they do not provide any insight about the internal field distribution of a light wave propagating through the grating structure. However, once the forward- and backward propagating fields at the input ($A(0)$ and $B(0)$) and output ($A(L)$ and $B(L)$) of the grating are known, the field amplitudes can be determined for any arbitrary position z_p inside the grating with $0 < z_\mathrm{p} < L$. The transfer matrix P from the grating input at $z = 0$ to the point $z = z_\mathrm{p}$ is defined as

$$\begin{bmatrix} A(0) \\ B(0) \end{bmatrix} = \begin{bmatrix} P_{11} & P_{12} \\ P_{21} & P_{22} \end{bmatrix} \begin{bmatrix} A(z_\mathrm{p}) \\ B(z_\mathrm{p}) \end{bmatrix} \tag{2.53}$$

The distribution of the forward- and backward propagating fields inside the Bragg grating are then calculated using [86]

$$A(z_\mathrm{p}) = \frac{A(0)}{|P|} \left(P_{22} - P_{12} r\right) \tag{2.54}$$

$$B(z_\mathrm{p}) = \frac{A(0)}{|P|} \left(-P_{21} + P_{11} r\right) \tag{2.55}$$

where $|P|$ is the determinant of the transfer matrix P and r is the amplitude reflection coefficient of the entire grating structure as given by Equation 2.49.

Non-uniform gratings can be modelled with the transfer matrix method by dividing the entire grating structure into N small segments so that the grating parameters for each individual segment are assumed to be constant [82]. With the transfer matrix for the k^{th} segment denoted by F^k, the transfer matrix of the entire grating structure is determined by a multiplication of all the individual F^k matrices as follows

$$F = \prod_{\mathrm{k}=1}^{N} F^\mathrm{k} \tag{2.56}$$

This approach is valid under the assumption that $\Lambda^\mathrm{k} \ll L^\mathrm{k}$, where Λ^k and L^k are the grating period and length of the k^{th} segment, respectively.

In the case of a DFB or DBR laser structure operating at the Bragg wavelength, the assumed boundary conditions are different from a passive Bragg grating in the sense that there is no incident laser field, i.e. $A(0) = \sqrt{P_\mathrm{L}^\mathrm{A}(0)} = 0$ and $B(L) = \sqrt{P_\mathrm{L}^\mathrm{B}(L)} = 0$, where $P_\mathrm{L}^\mathrm{A}(z)$ and $P_\mathrm{L}^\mathrm{B}(z)$ are the laser powers traveling to the right and left, respectively. In other words, the device acts as a self-sustained oscillator where the entire laser signal is generated inside the device.

Since the grating parameters (such as grating period and optical gain) are generally not constant along the length of the waveguide, the laser structure is divided into a number of segments (typically a few hundred), where the grating parameters for each individual segment are assumed to be constant. An iterative procedure is used, where for a given pump power first an output laser power $P_\mathrm{L}^\mathrm{B}(0)$ is assumed. For each segment, first the pump attenuation and the laser gain are calculated, and then the transfer matrix of that section. Calculating through all segments, this leads to a remaining pump power $P_\mathrm{P}(L)$ and generally an (unphysical) nonzero input power $P_\mathrm{L}^\mathrm{B}(L)$. The assumed output

power $P_{\mathrm{L}}^{\mathrm{B}}(0)$ is then iteratively adjusted in such a way that the boundary condition $P_{\mathrm{L}}^{\mathrm{B}}(L) = 0$ is better approximated, until the error is smaller than a predetermined value. Alternatively, the fields in a DFB or DBR laser structure can also be determined by using numerical integration methods to solve Equations 2.39 and 2.40 with the same boundary conditions as mentioned above. All calculations performed in this work were implemented in MATLAB[1]. An example of the Matlab code used for the calculations of a DFB waveguide laser is given in the Appendix.

Grating Coupling Coefficient

For a surface-corrugated Bragg grating with a rectangular corrugation profile, as the devices which are considered in this work, the coupling coefficient, expressed in units of m^{-1}, is given by [87]

$$\kappa = \frac{\Gamma(n_{\mathrm{h}}^2 - n_{\mathrm{l}}^2)}{\lambda_{\mathrm{B}} n_{\mathrm{eff}}} \sin(\pi D) \tag{2.57}$$

where n_{h} and n_{l} are the alternating high and low refractive indices of the two materials inside the grating region. The grating duty cycle D is defined as the fraction of a single grating period which is occupied by the high-index material n_h, while the overlap between the guided mode and the grating region is given by

$$\Gamma = \iint\limits_{grating} \phi_{\mathrm{B}}(x, y)\mathrm{d}x\mathrm{d}y \tag{2.58}$$

where ϕ_{B} is a normalized transverse intensity distribution of the guided mode with wavelength λ_{B}. From Equation 2.57 it can be deduced that the coupling coefficient of a surface-corrugated Bragg grating is mainly determined by three factors: the difference between n_{h} and n_{l}, the overlap between the guided mode and the grating region, and the duty cycle of the grating structure. The width of the Bragg grating stopband $\Delta\lambda$, centered around λ_{B}, is directly proportional to κ according to [87]

$$\Delta\lambda = \frac{\kappa\lambda_{\mathrm{B}}^2}{\pi n_{\mathrm{eff}}} \tag{2.59}$$

For wavelengths inside this stopband, the counter-propagating field amplitudes grow and decay exponentially along the length of the (uniform) grating, while they evolve sinusoidally for wavelengths outside the stopband [88].

The grating strength is often expressed in terms of the dimensionless quantity κL. Note that the spectral characteristics of a Bragg grating are not completely determined by the value of κL, since a long weak grating has a much narrower reflection spectrum than a short strong one, although their peak reflectivities are equal. Semiconductor DFB lasers typically have grating strengths of $\kappa L \approx 1$ [89, 90], while the rare-earth-ion-doped lasers considered in this work have $4 < \kappa L < 7$. This difference in grating strength between the two laser types is largely due to the difference in the maximum achievable gain. Due to the

[1]Matlab version R2010b (www.mathworks.com)

high gain in semiconductor lasers, single-longitudinal-mode operation generally becomes difficult to achieve for cavities with $\kappa L > 1$, even for quarter-wavelength phase shifted cavities, since there is enough gain available for the cavity to also support higher order longitudinal modes. For rare-earth-ion-doped lasers, single-longitudinal-mode operation is typically possible even for cavities with larger κL values.

2.2.2 Uniform Bragg Gratings

In this section the calculated spectral response and internal field distribution of a typical uniform Bragg grating are shown in order to demonstrate the implementation of the coupled mode theory and transfer matrix method which have been discussed in the previous section. Figure 2.7 shows the calculated reflection and transmission spectra for a 1-cm-long uniform lossless Bragg grating for various values of κL, using Equations 2.51 and 2.52, where $R + T = 1$. For wavelengths near the Bragg wavelength, the reflections from the individual corrugations in the grating build up in phase, resulting in a peak in the reflection spectrum. For the typical grating lengths which are considered in this work (few mm to a cm), gratings with $\kappa L \gg 1$ result in a reflection peak with a plateau-like shape close to the Bragg wavelength, as can be seen in Figure 2.7 for $\kappa L = 4$. On either sides of the main reflection peak, the spectral response shows a series of ripples or sidelobes. These sidelobes quickly decay as the wavelength moves away from the Bragg condition until the structure is effectively transparent. For a fixed grating length, the reflectivity increases as a function of κ, while the width of the reflection peak also increases as predicted by Equation 2.59. In the case of a lossless grating, the reflectivity R and transmission T at the Bragg wavelength can be deduced from Equations 2.51 and 2.52 as

$$R = \tanh^2(\kappa L) \tag{2.60a}$$

$$T = \operatorname{sech}^2(\kappa L) \tag{2.60b}$$

For certain applications such as optical filters, it is usually sufficient to know the spectral response of the Bragg grating. However, for DFB and DBR laser applications where the intra-laser-cavity optical fields are crucial for the performance of the device, it is important to have knowledge of the internal field distributions in order to avoid instabilities caused by higher order longitudinal modes [91]. By making use of Equations 2.54 and 2.55, the total optical power ($|A(z)|^2 + |B(z)|^2$) inside a lossless 1-cm-long uniform Bragg grating was calculated for various values of κL (Figure 2.8).

It can clearly be seen how the width of the grating stopband increases with increasing values of κ. A number of resonances that exhibit a sinusoidal dependence on their position along the Bragg grating are visible for wavelengths outside the stopband. These resonances, or longitudinal modes, become more pronounced for stronger gratings and their spectral width becomes narrower for larger values of κL. The spatial dependence of the first three resonances are shown for $\kappa L = 4$ (Figure 2.9). Note that the spatial distribution of the m^{th} resonance has m peaks and that the resonance amplitude decreases with increasing mode number. As with the spectral response of a uniform Bragg grating, the internal field distributions and resonances are symmetrical with respect to the Bragg

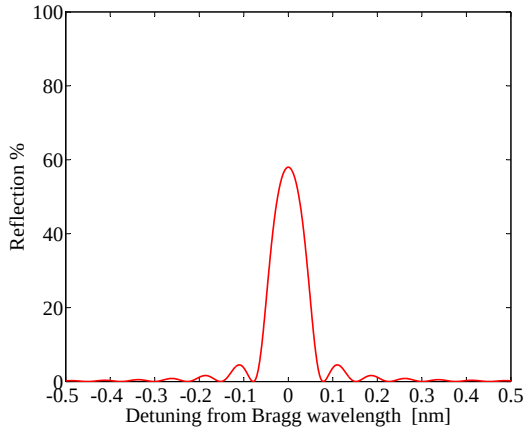

(a) Reflection spectrum for $\kappa L = 1.0$.

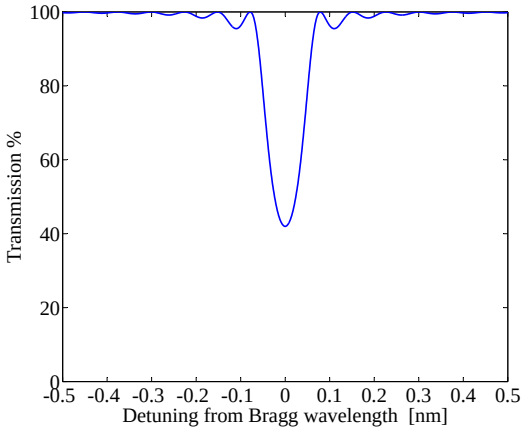

(b) Transmission spectrum for $\kappa L = 1.0$.

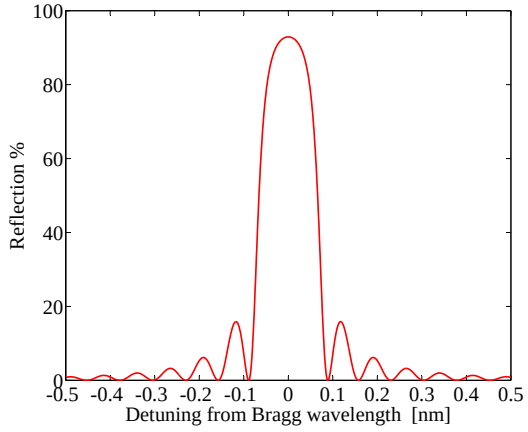

(c) Reflection spectrum for $\kappa L = 2.0$.

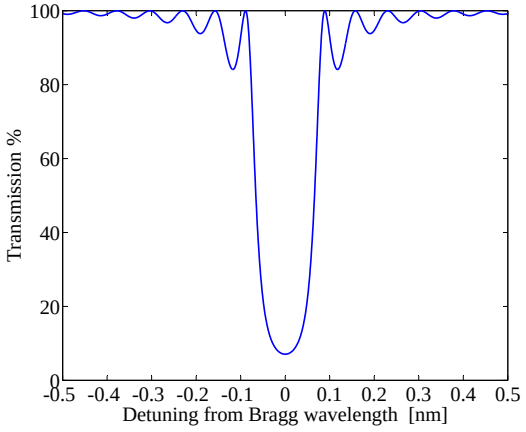

(d) Transmission spectrum for $\kappa L = 2.0$.

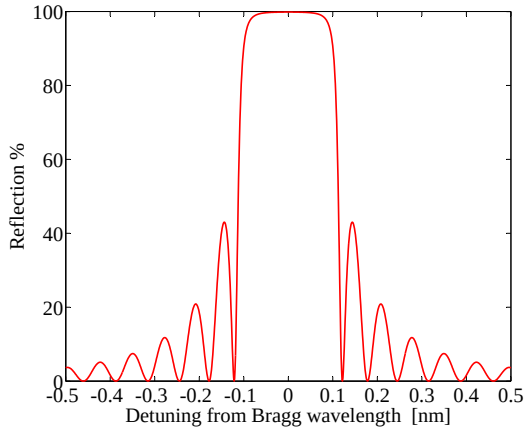

(e) Reflection spectrum for $\kappa L = 4.0$.

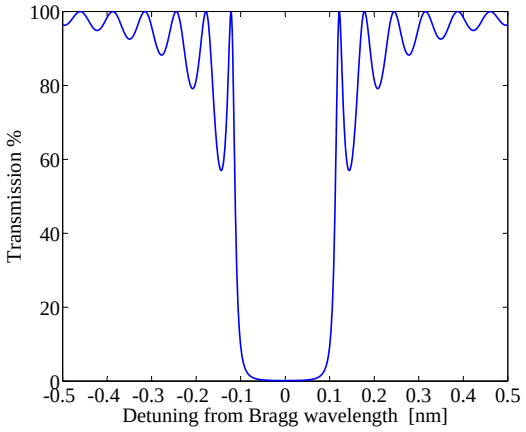

(f) Transmission spectrum for $\kappa L = 4.0$.

Figure 2.7: Reflection and transmission spectra for a $1-$cm$-$long uniform Bragg grating ($\lambda_B = 1550$ nm and $n_{eff} = 1.6$) for different values of κL.

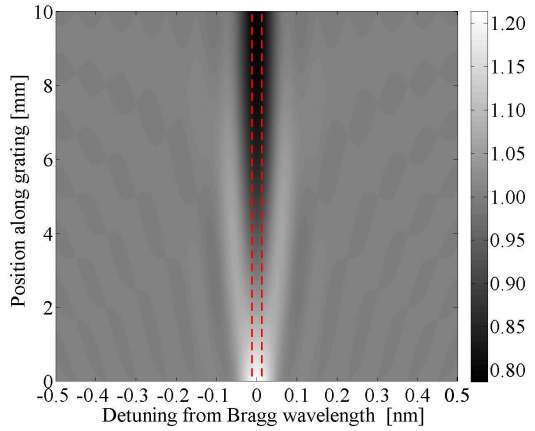

(a) $\kappa L = 0.5$.

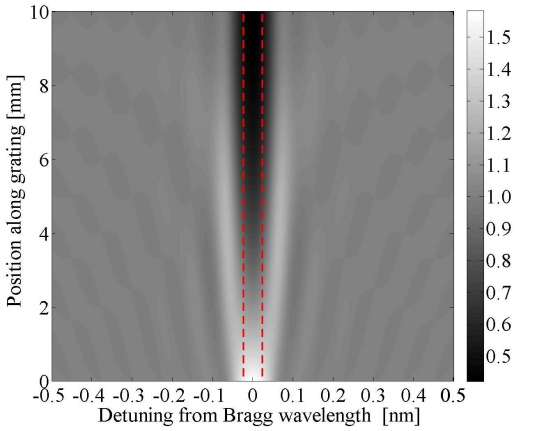

(b) $\kappa L = 1.0$.

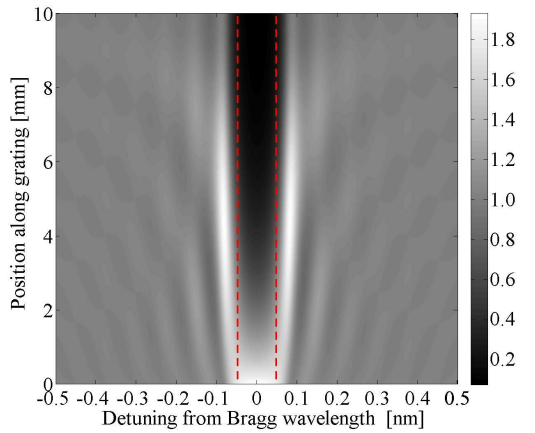

(c) $\kappa L = 2.0$.

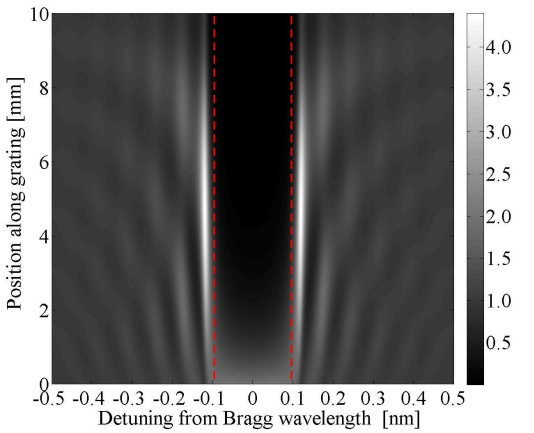

(d) $\kappa L = 4.0$.

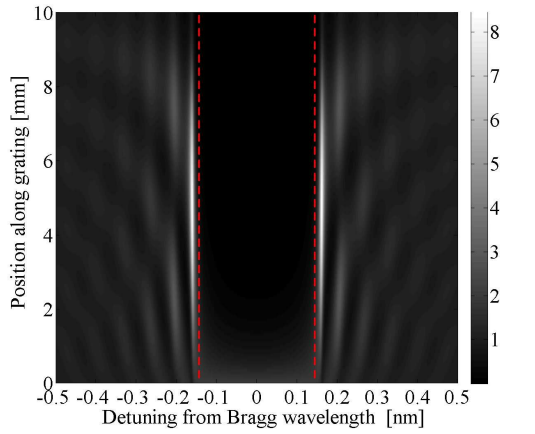

(e) $\kappa L = 6.0$.

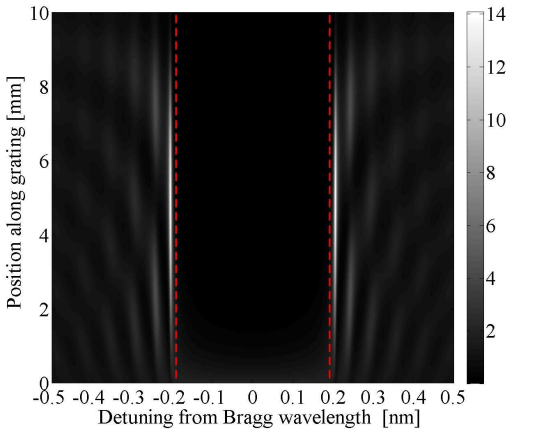

(f) $\kappa L = 8.0$.

Figure 2.8: Total optical power (normalized with respect to the incident power) inside a 1−cm−long uniform Bragg grating ($\lambda_B = 1550$ nm and $n_{eff} = 1.6$) for various values of κL. The region between the vertical red lines indicate the grating stopband according to Equation 2.59.

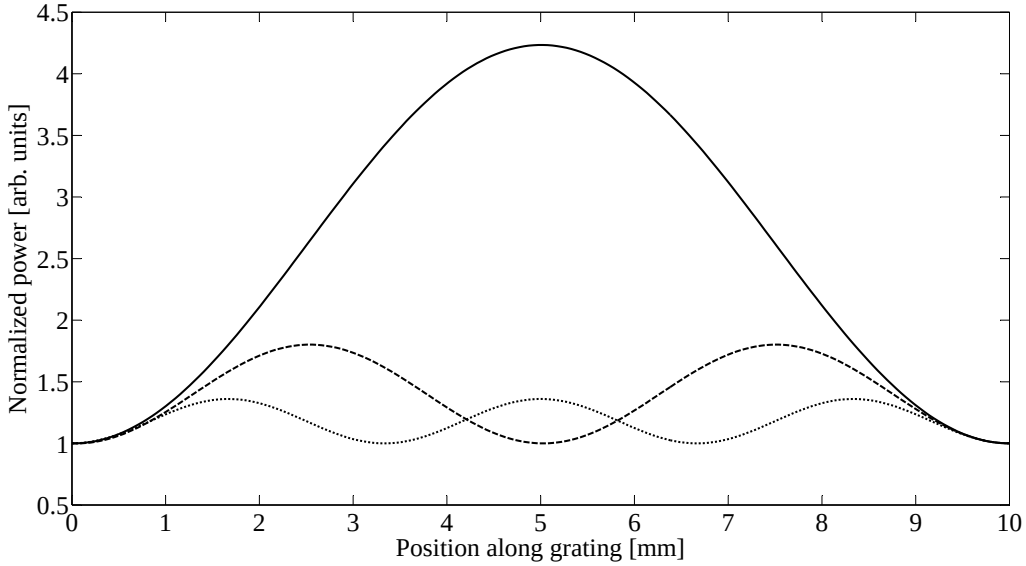

Figure 2.9: Spatial dependence of the first three longitudinal resonances in a $1-$cm$-$long uniform Bragg grating with $\kappa L = 4$.

wavelength. A single uniform Bragg grating is not useful for the realization of single-longitudinal-mode lasers, since the first resonances on either side of the stopband will reach laser threshold simultaneously. For the purpose of realizing single-longitudinal-mode lasers, Bragg gratings are used in DFB and DBR configurations to facilitate stable and narrow-linewidth performance. In the context of this thesis, the definition of distributed feedback (DFB) is used to refer to integrated cavities which are formed by introducing a quarter-wavelength phase shift in the center region of a uniform waveguide Bragg grating.

2.2.3 Distributed Bragg Reflector Cavities

A distributed Bragg reflector cavity can be considered analogous to a Fabry-Pérot cavity. However, instead of forming a cavity using two dielectric coatings, which strongly reflect the light within a few periods of the alternating layers in the coating, two Bragg gratings, or Bragg reflectors, which are monolithically integrated with the waveguide, are used to reflect the light over a much larger number of grating periods instead (Figure 2.10). Consequently, the light in a DBR cavity is reflected in a distributed manner along the length of the Bragg reflectors. A key advantage of such a monolithic DBR structure over a Fabry-Pérot cavity formed by dielectric coatings, is that the Bragg gratings in a monolithic DBR cavity provide a much narrower reflection bandwidth as compared to the strong Bragg gratings which are used in dielectric coatings. This makes it more favorable for single-longitudinal-mode operation. In the context of semiconductor lasers, the Bragg reflectors of a DBR laser are located outside the gain region so that these regions do not contribute to the amplification of the laser signal. In rare-earth-ion-doped lasers, however, the Bragg reflectors are very often part of the gain region due to the need for a longer gain section because of the smaller gain per unit length. The distance between the two

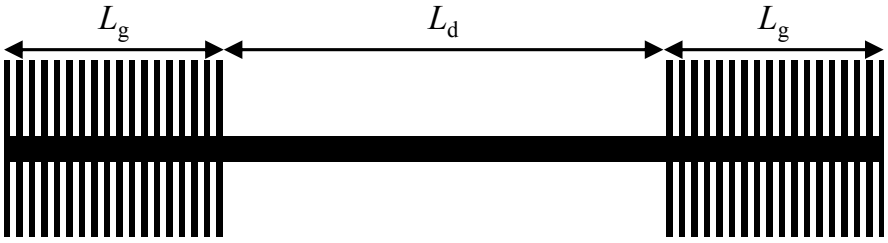

Figure 2.10: Schematic of a DBR cavity.

Bragg reflectors plus the depth to which the light penetrates into each of the two Bragg reflectors form the effective cavity length. For a uniform Bragg grating of length L with $\gamma \ll \kappa$, the penetration depth at the Bragg wavelength is given by [92]

$$L_{\text{pen}} = \frac{\tanh(\kappa L)}{2\kappa} \tag{2.61}$$

When the effective cavity length is such that its free spectral range (FSR) is smaller than the spectral width of the stopband of the two Bragg reflectors, several Fabry-Pérot resonances can be supported by the DBR cavity. As an example of a DBR cavity which supports a few Fabry-Pérot resonances, consider two identical 2.5-mm-long uniform Bragg gratings ($\kappa = 0.4$ mm^{-1}) which are separated by a distance of 5 mm. The reflection and transmission spectra of such a device are shown in Figures 2.11(a) and 2.11(b), respectively. In this case the DBR cavity supports three longitudinal modes which are visible inside the stopband of the Bragg reflectors. The region between the two vertical black dashed lines in the Figures 2.11(a) and 2.11(b) denote the grating stopband according the Equation 2.59. The wavelength-dependent optical power distribution inside the DBR cavity is shown in Figure 2.11(c), where the five longitudinal modes can be seen. The majority of the power of each of these supported longitudinal modes is located in the region between the two Bragg reflectors, with the power decaying exponentially into the two Bragg reflectors (Figure 2.11(d)). The wavelength spacing between the respective cavity resonances is given by

$$\Delta\lambda_{\text{FSR}} = \frac{\lambda_{\text{B}}^2}{2n_{\text{eff}}L_{\text{eff}}} \tag{2.62}$$

where L_{eff} is the effective cavity length defined as

$$L_{\text{eff}} = L_{\text{d}} + 2L_{\text{pen}} \tag{2.63}$$

with L_{d} the distance between the two Bragg reflectors. From Equations 2.59 and 2.61-2.63, it follows that the requirement for the DBR structure to support only a single longitudinal mode inside the stopband of the identical Bragg reflectors is given by

$$L_{\text{d}} < \frac{\pi - 2\tanh(\kappa L_{\text{g}})}{2\kappa} \tag{2.64}$$

where L_{g} is the length of each of the two Bragg reflectors. However, for many applications L_{d} cannot be made sufficiently short to satisfy the single-longitudinal-mode requirement

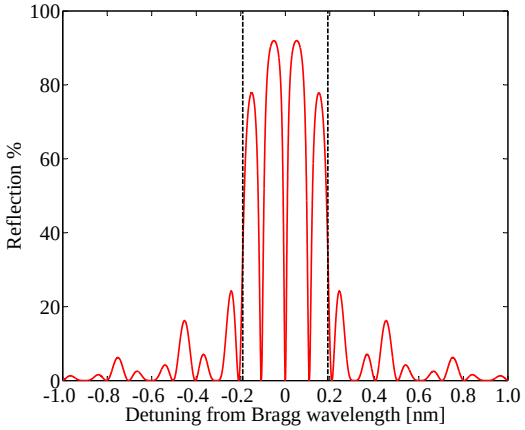

(a) Reflection spectrum.

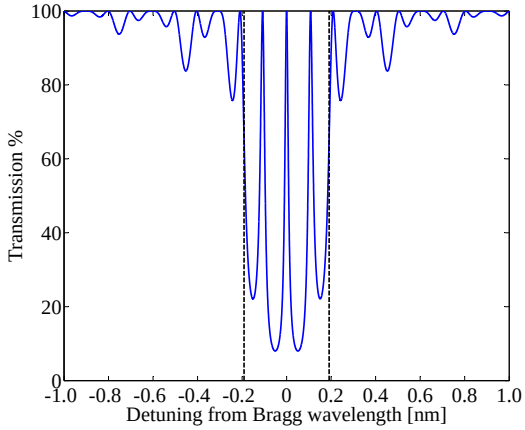

(b) Transmission spectrum.

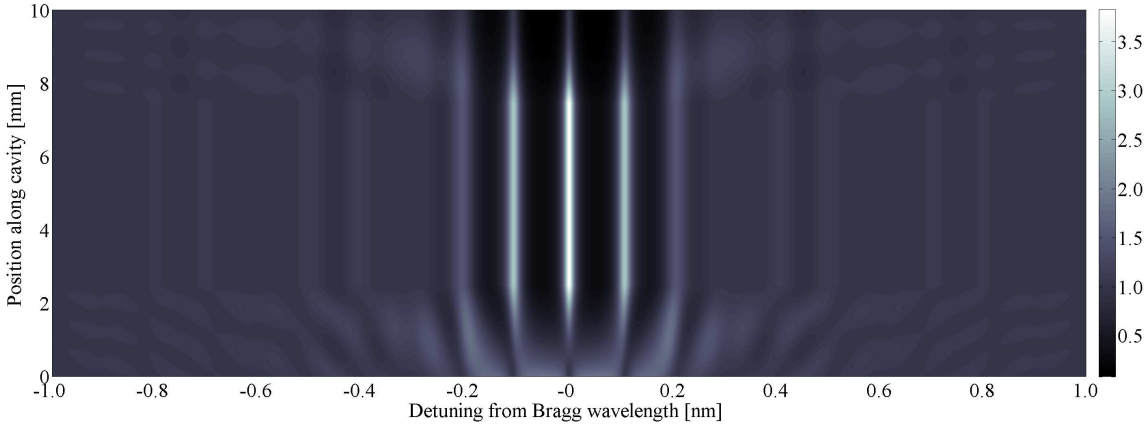

(c) Wavelength-dependent spatial distribution of optical power (normalized with respect to the incident power) inside the DBR cavity.

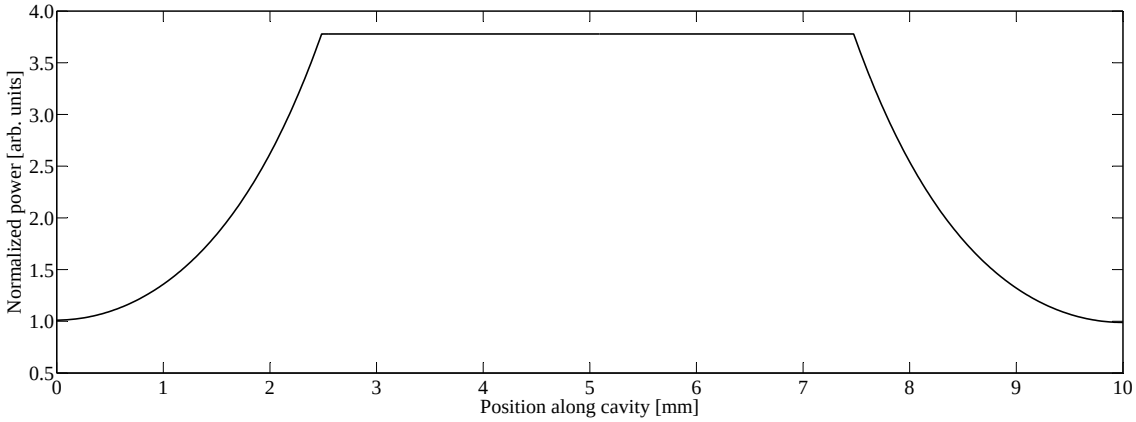

(d) Spatial distribution of the longitudinal mode operating at the Bragg wavelength.

Figure 2.11: Spectral characteristics of a DBR cavity formed by two identical 2.5-mm-long uniform Bragg gratings ($\kappa = 0.4$ mm^{-1}, $\lambda_B = 1550$ nm and $n_{eff} = 1.6$) which are separated by a distance of 5 mm.

of Equation 2.64. In rare-earth-ion-doped waveguide lasers, the absorption length of the pump light poses a lower limit to how short the DBR cavity (and thus L_{d}) can be made, while still absorbing sufficient pump radiation to reach laser threshold. As an example, consider a typical value of $\kappa = 0.4$ mm^{-1} and 2.5-mm-long Bragg reflectors which, according to Equation 2.64, requires $L_{\mathrm{d}} < 2$ mm to support only a single longitudinal mode, while the absorption length of erbium at a pump wavelength of 1480 nm is approximately 10 mm (assuming an absorption cross-section of 3.3×10^{-21} cm^2 [93], and a doping concentration of 3.0×10^{20} cm^{-3}). For the purpose of realizing single-longitudinal-mode lasers, distributed feedback cavities are generally more suitable alternatives to DBR cavities.

2.2.4 Distributed Feedback Cavities

As mentioned in Section 2.2.2, the spectral response of a uniform Bragg grating is symmetrical with respect to the Bragg wavelength. As a result, such a device has two lowest order resonances on either side of the stopband, which will reach laser threshold simultaneously if the structure has sufficient optical gain. To understand the spectral response of Bragg gratings in general, it is necessary to consider the optical phase of the wave reflected by the grating. The amplitude reflection coefficient of a Bragg grating structure as measured at the input ($z = 0$) can be written in the following form

$$r = \sqrt{R}e^{i\theta} \tag{2.65}$$

where θ is the optical phase, and r and R are the amplitude and power reflection coefficients which are calculated from Equations 2.49 and 2.51, respectively. As an example, consider the calculated round trip optical phase $2 \times \theta$ of a 1-cm-long uniform Bragg grating with $\kappa = 4$ cm^{-1} (Figure 2.12). Note that at the Bragg wavelength the round trip optical phase is $2 \times \theta = \pi$. Since this round trip phase is not an integer multiple of 2π as required for constructive interference in a cavity, no cavity resonance is possible at the Bragg wavelength. However, the resonance condition is satisfied for a number of wavelengths on either side of the stopband. The two resonant wavelengths nearest to the stopband are the two lowest order resonances.

In order to achieve a single resonance exactly at the Bragg wavelength, an additional round trip phase of $2 \times \psi = \pi$ should be added to the structure in order to fulfill the resonance condition [94]. The additional required phase shift of $\psi = \frac{\pi}{2}$ corresponds to exactly one quarter of the Bragg wavelength. From the Bragg condition given by Equation 2.38, this is equivalent to a change in the grating structure of half a period. The reflection coefficient of such a quarter-wavelength-shifted Bragg grating of length L, where the phase shift is located in the center of the Bragg grating, is given by [95]

$$R = |r|^2 = \left| \frac{2\kappa\delta \sinh^2\left(\rho\frac{L}{2}\right)}{\kappa^2 - \delta^2\cosh(\rho L) + i\rho\delta\sinh(\rho L)} \right|^2 \tag{2.66}$$

From Equations 2.65 and 2.66, the calculated round trip phase change for such a quarter-wavelength-shifted Bragg grating is shown in Figure 2.13. There are still a number of

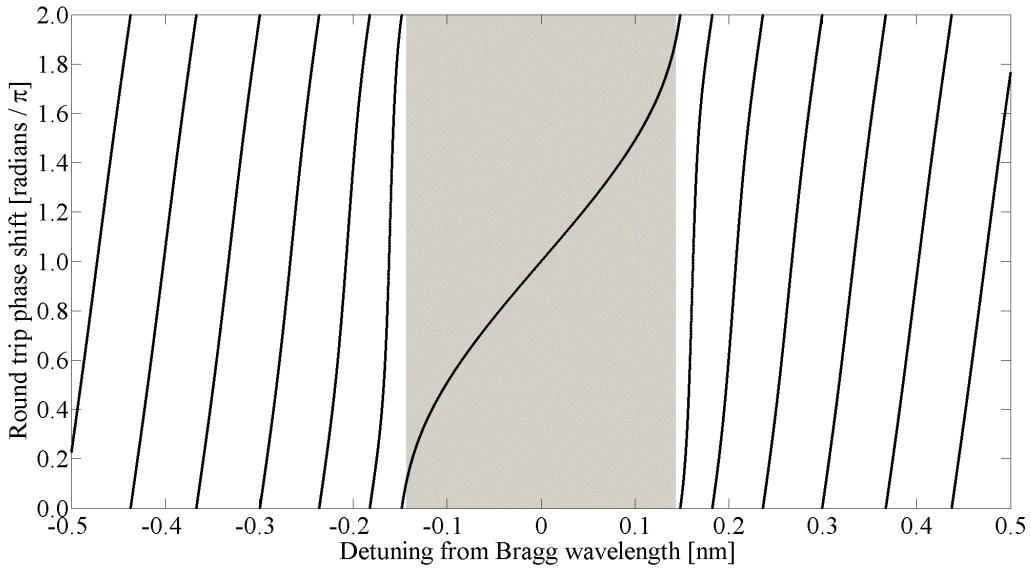

Figure 2.12: Round trip optical phase shift of a 1−cm−long uniform Bragg grating ($\kappa = 4$ cm^{-1}, $\lambda_B = 1550$ nm and $n_{eff} = 1.6$). The shaded gray region indicates the stopband.

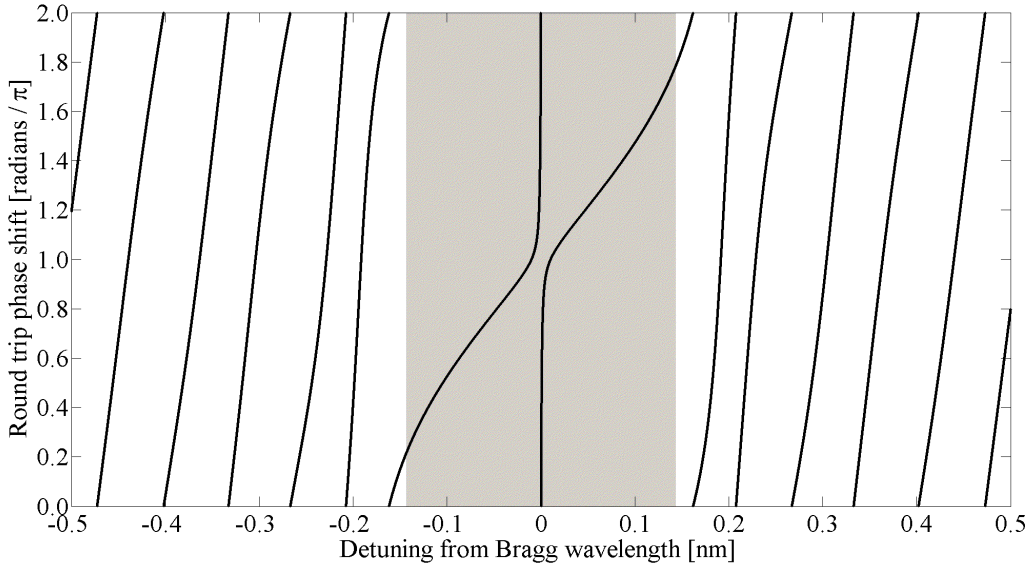

Figure 2.13: Round trip optical phase shift of a 1−cm−long Bragg grating ($\kappa = 4$ cm^{-1}, $\lambda_B = 1550$ nm and $n_{eff} = 1.6$) with a quarter-wavelength phase shift in the center. The shaded gray region indicates the stopband.

wavelengths outside the stopband for which the resonance condition is met. However, the key difference from the uniform Bragg grating is the fact that the resonance condition is now also fulfilled at the Bragg wavelength. Consequently, the optical response of such a quarter-wavelength-shifted Bragg grating is altered such that there appears an extremely narrow resonance inside the center of the stopband (Figures 2.14(a)-2.14(c)). This narrow resonance is confined around the phase shift region from where the power decays exponentially into the Bragg grating on either side (Figure 2.14(d)). Since the resonant mode at the Bragg wavelength experiences the strongest optical feedback (highest reflectivity), it has the lowest required threshold gain when this structure is used as a laser. In other words, the modal degeneracy of a uniform Bragg grating is removed by introducing a quarter-wavelength phase shift to the cavity [96].

Distributed Phase Shift

There are basically two different methods to realize a quarter-wavelength-shifted Bragg grating. The first is to change the phase of the surface corrugation itself. This requires that half a period of the grating is added or removed somewhere in the center region of the cavity in order to induce the quarter-wavelength phase shift. The realization of such a device with the required accuracy is not a trivial task and often demands rather complicated fabrication techniques and additional post processing steps [97]. The second method is to induce the phase shift by locally changing the waveguide dimensions, particularly the waveguide width, while the surface corrugation of the grating remains unaltered [96]. In this case, the phase shift does not occur in a discrete point as with the former method, but it is rather accumulated along the length of the localized perturbed region of the waveguide. Such a distributed phase shift provides a more elegant solution, since the phase shift region can be defined in the same lithographic step in which the waveguide is defined. To reduce additional scattering losses, the transition from the unperturbed waveguide to the phase shift region should be sufficiently adiabatic. For this purpose, it is beneficial to choose a perturbation with a smooth transition region, like in the case of a $\sin^2$ shape (Figure 2.15) [96], instead of a discrete change, or step, in the waveguide width. Inside such a $\sin^2$ distributed phase shift region with length L_{ps}, the accumulated phase shift is

$$\begin{aligned}\theta &= \int_0^{L_{\mathrm{ps}}} (\beta_{\mathrm{ps}} - \beta_{\mathrm{B}})\mathrm{d}z \\ &= \frac{2\pi\Delta n}{\lambda_{\mathrm{B}}} \int_0^{L_{\mathrm{ps}}} \sin^2\left(\frac{\pi z}{L_{\mathrm{ps}}}\right)\mathrm{d}z \\ &= \frac{\pi\Delta n L_{\mathrm{ps}}}{\lambda_{\mathrm{B}}}\end{aligned} \tag{2.67}$$

where $\Delta n = n_{\mathrm{eff}}^{\mathrm{ps}} - n_{\mathrm{eff}}$, with $n_{\mathrm{eff}}^{\mathrm{ps}}$ being the effective refractive index in the widest part of the $\sin^2$ distributed phase shift region and n_{eff} the effective refractive index of the waveguide without the phase shift. β_{ps} and β_{B} are the propagation constants of the modes at the Bragg wavelength, inside and outside the distributed phase shift region, respectively. In

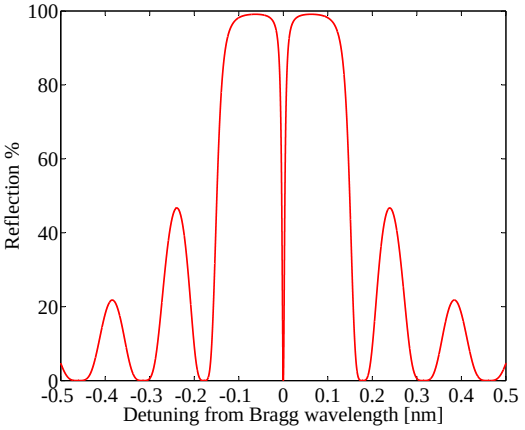

(a) Reflection spectrum.

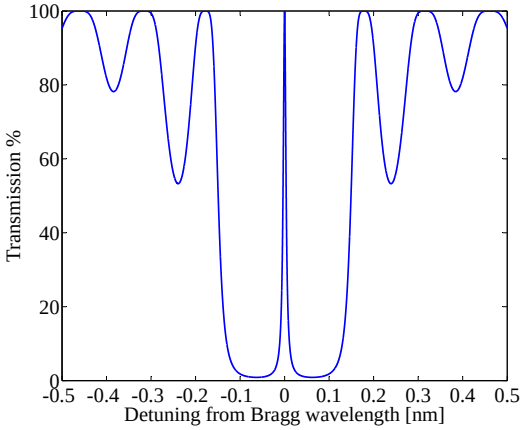

(b) Transmission spectrum.

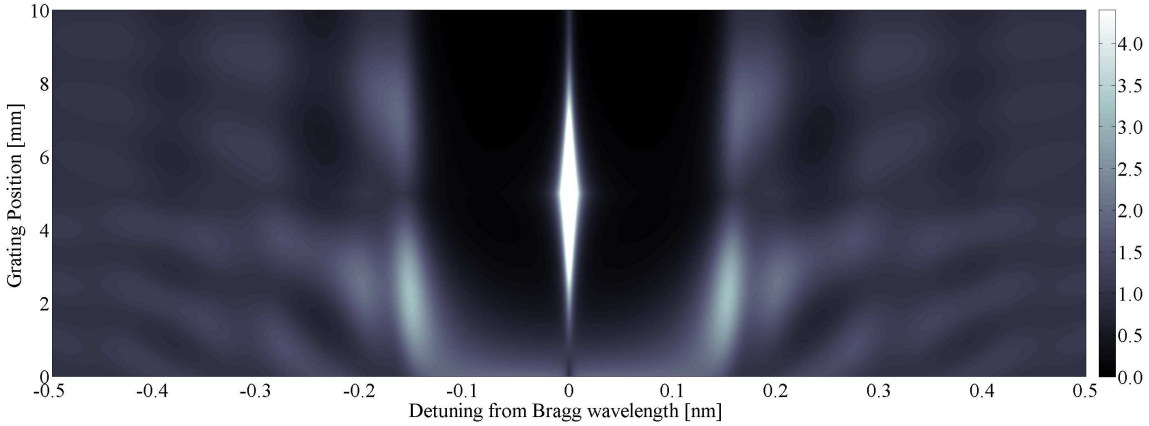

(c) Wavelength-dependent spatial distribution of optical power (normalized with respect to the incident power) inside the DFB cavity.

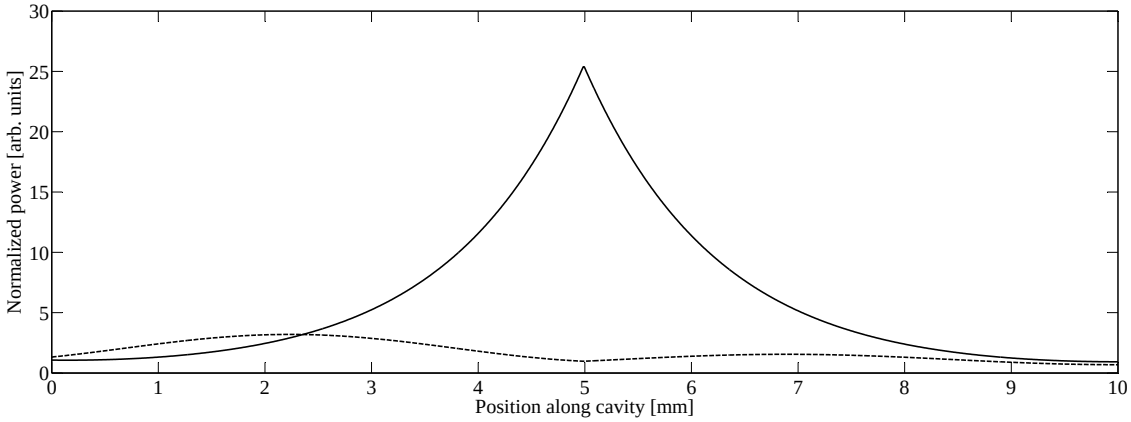

(d) Spatial distributions of the longitudinal mode operating at the Bragg wavelength (solid line) and the first higher order modes on either side of the stopband (dashed line).

Figure 2.14: Spectral characteristics of a 1−cm−long Bragg grating $\kappa = 4$ cm^{-1}, $\lambda_B =$ 1550 nm and $n_{\text{eff}} = 1.6$) with a discrete quarter-wavelength phase shift in the center of the grating.

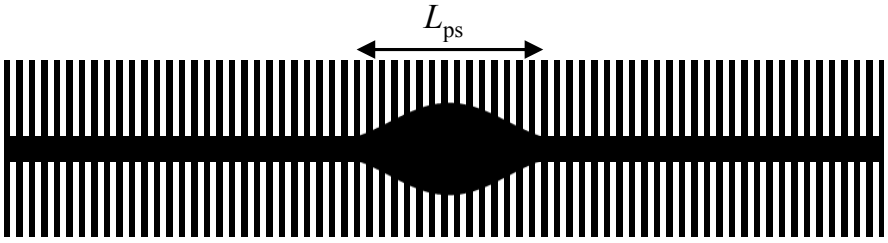

Figure 2.15: Schematic of the distributed phase shift region via a local widening of the waveguide.

order to induce a quarter-wavelength phase shift, it follows from Equation 2.67 that the length of the $\sin^2$ phase shift region should be chosen such that

$$L_{ps} = \frac{\lambda_B}{2\Delta n} \tag{2.68}$$

Note that the required length of the $\sin^2$-shaped distributed phase shift region is twice as long as that of a rectangular-shaped distributed phase shift region for the same amount of induced phase shift (assuming the same Δn value for both phase shifts). Although a rectangular-shaped distributed phase shift region is shorter, it will come at the expense of larger additional scattering losses.

2.3 Laser Linewidth

The linewidth of a single-longitudinal-mode laser, expressed as the full width at half maximum (FWHM) of the optical emission spectrum, is fundamentally limited due to spontaneous emission in the cavity. Spontaneously emitted photons have random directions and random phases and each spontaneous emission event which is coupled into the laser mode produces, depending on its phase relative to the coherent photons in the cavity, a phase and intensity fluctuation in the intra-laser-cavity optical field. The spontaneously emitted radiation has an intrinsic Lorentzian frequency distribution, so that it sets a lower limit to the laser linewidth which can be achieved. This fundamental linewidth limit is theoretically expressed by the well known Schawlow-Townes equation [2]

$$\Delta\nu_L = \frac{2\pi h\nu_L(\Delta\nu_c)^2}{P_{out}} \tag{2.69}$$

where h is Planck's constant, while ν_L and P_{out} are the optical frequency and output power of the laser, respectively. The passive cavity linewidth is given by $\Delta\nu_c$. As the laser power increases, and consequently the number of stimulated emitted photons in the cavity, each spontaneous emitted photon which is coupled to the laser mode will have a less pronounced effect on the perturbation of the laser emission. This is the reason for the inverse power dependence of the linewidth limit. It should be noted that Equation 2.69 is only valid for an ideal four-level laser with no intrinsic resonator losses and no external

noise sources. If one assumes that the intensity fluctuations are damped out by relaxation oscillations, the SCHAWLOW-TOWNES linewidth is reduced by a factor of two [98, 99].

The generalized SCHAWLOW-TOWNES linewidth, which accounts for possible intrinsic cavity losses as well as reabsorption losses which occur in three-level lasers, is given by [100]

$$\Delta\nu_{\mathrm{L}} = \frac{2\pi h\nu_{\mathrm{L}}(\Delta\nu_{\mathrm{c}})^2}{P_{\mathrm{out}}}\left[1-\frac{\tau_{\mathrm{c}}}{\tau_{\mathrm{loss}}}\right]\left[1-\frac{\sigma_{\mathrm{L}}^{\mathrm{abs}}(c\tau_{\mathrm{c}}\sigma_{\mathrm{L}}^{\mathrm{em}}N_{\mathrm{T}}-1)}{\sigma_{\mathrm{L}}^{\mathrm{em}}(c\tau_{\mathrm{c}}\sigma_{\mathrm{L}}^{\mathrm{abs}}N_{\mathrm{T}}+1)}\right]^{-1} \tag{2.70}$$

where c is the speed of light in a vacuum, $\sigma_{\mathrm{L}}^{\mathrm{abs}}$ and $\sigma_{\mathrm{L}}^{\mathrm{em}}$, respectively, are the effective absorption and emission cross-sections at the laser wavelength, and N_{T} is the rare-earth-ion doping concentration. The photon decay time τ_{c}, loss decay time τ_{loss}, and outcoupling decay time τ_{out} of the cavity are defined as

$$\frac{1}{\tau_{\mathrm{c}}} = \frac{1}{\tau_{\mathrm{loss}}} + \frac{1}{\tau_{\mathrm{out}}} = 2\pi\Delta\nu_{\mathrm{c}} \tag{2.71}$$

$$\frac{1}{\tau_{\mathrm{loss}}} = -\frac{c}{2l_{\mathrm{opt}}}\ln(1-l) \tag{2.72}$$

$$\frac{1}{\tau_{\mathrm{out}}} = -\frac{c}{2l_{\mathrm{opt}}}\ln(R_{\mathrm{out}}) \tag{2.73}$$

with l_{opt} the optical length of the cavity, l the intrinsic round-trip loss in the cavity, and R_{out} the outcoupling reflectivity. Compared to the SCHAWLOW-TOWNES linewidth of Equation 2.69, the first correction term of Equation 2.70 arises due to intrinsic resonator losses, while the second correction term represents the reabsorption losses which occur in three-level lasers. From Equation 2.70 it is evident that the values of the effective absorption and emission cross-sections as well as the doping concentration have a significant influence on the fundamental laser linewidth limit. However, it is not immediately obvious which typical rare-earth-ion laser transitions have the most suitable cross-sections for the realization of narrow laser linewidths. Since in rare-earth-ion-doped lasers the cross-sections are orders of magnitude smaller than in semiconductor lasers, the dopant concentration and inverted fraction must be accordingly higher. Equation 2.70 was used to determine whether the typical 1550 nm laser transition in Al_2O_3:Er^{3+} or the 1020 nm laser transition in Al_2O_3:Yb^{3+} are most suitable for narrow laser linewidth operation. Aside from ν_{L} and the effective cross-sections which are different for the two respective laser transitions, the other DFB parameters (Table 2.2) were fixed for both lasers, in order to see the influence of the cross-sections on the fundamental linewidth. The effective cross-sections as shown in Figures 2.3 and 2.5 were used for the calculations. The effective cavity length was calculated as the sum of the penetration depth (Equation 2.59) of the laser light into both 0.5-cm-long Bragg reflectors on either side of a discrete quarter-wavelength phase shift in the center of a 1-cm-long Bragg grating. The round-trip cavity loss was calculated based on a propagation loss value of 0.2 dB/cm over the effective round-trip cavity length. Based on these parameters, the calculated fundamental laser linewidths for the two transitions are shown in Figures 2.16(a) and 2.16(b). Since ν_{L} for the Al_2O_3:Yb^{3+} laser operating at 1020 nm is ~ 1.5 times larger than that of the Al_2O_3:Er^{3+} laser operating at 1550 nm, one might intuitively deduce from Equation 2.70

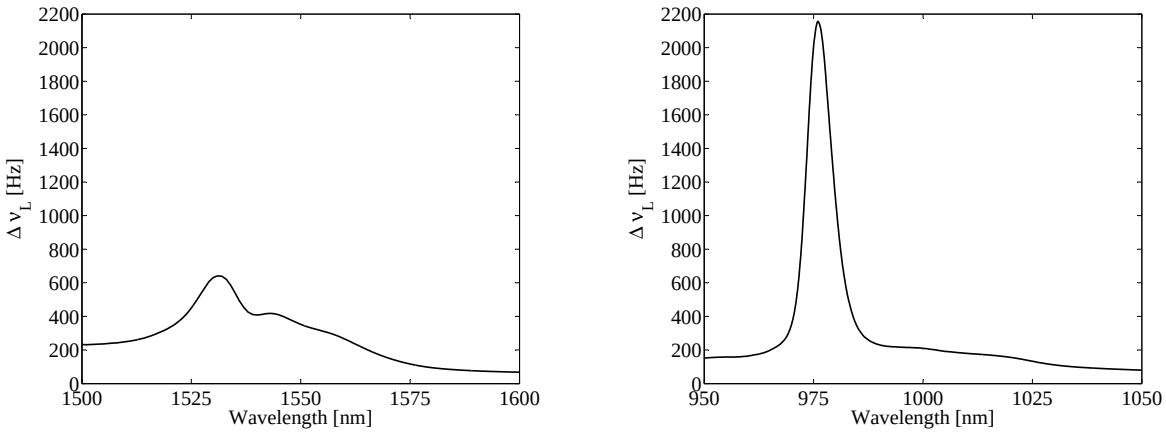

(a) Al_2O_3:Er^{3+}. (b) Al_2O_3:Yb^{3+}.

Figure 2.16: Fundamental laser linewidths according to Equation 2.70 based on the parameters listed in Table 2.2.

that the Al_2O_3:Yb^{3+} laser will probably have the larger fundamental linewidth. However, from Figures 2.16(a) and 2.16(b) it can be seen that the 1020 nm Al_2O_3:Yb^{3+} laser has a fundamental linewidth which is ~ 2 times narrower than that of the Al_2O_3:Er^{3+} laser operating at 1550 nm, the reason being the influence of the effective absorption cross-section, where the absorption cross-section at 1020 nm for the Al_2O_3:Yb^{3+} laser is ~ 8 times smaller than that of the 1550 nm Al_2O_3:Er^{3+} laser. The dependence of the fundamental linewidth on the absorption cross-section is clear from the calculated linewidths, which have a similar wavelength dependence than the absorption cross-sections, suggesting that it is better to operate the lasers on the longer wavelengths of the respective laser transitions where the absorption cross-sections are smaller. With the same parameters listed in Table 2.2, the 1064 nm and 1330 nm four-level laser transitions in Al_2O_3:Nd^{3+} result in a fundamental linewidth of ~ 50 Hz.

Semiconductor lasers generally have linewidths which are larger than what is predicted by the Schawlow-Townes limit. The enhanced linewidth is attributed to the varia-

Parameter	Value	Parameter	Value
$\Delta\nu_c$	320 MHz	l_{opt}	2.65 mm
P_{out}	1 mW	l	0.015
N_T	3×10^{20} cm^{-3}	R_{out}	0.98
κ	6.0 cm^{-1}	τ_c	0.50 ns
Total grating length	1.0 cm	τ_{loss}	1.16 ns
Effective cavity length	1.66 mm	τ_{out}	0.90 ns
n_{eff}	1.6		

Table 2.2: Parameters used to calculate the fundamental laser linewidth for a number of typical rare-earth-ion laser transitions in Al_2O_3.

tion of the refractive index with carrier density [24]. Spontaneous emission induces phase and intensity changes in the laser field. The restoration of the laser to its steady-state intensity results in changes in the carrier density and gain in the cavity. These changes are accompanied by changes in the refractive index, which cause additional phase fluctuations and linewidth broadening. In principle the same happens in rare-earth-ion-doped materials, since the Kramers-Kronig relation [101, 102] is universally valid, i.e., any absorption or gain is accompanied with an according change of the real part of the refractive index. However, since the cross-sections are orders of magnitude smaller in rare-earth-ion-doped materials, the refractive-index change is accordingly smaller. This is partly compensated by the higher dopant concentration and excitation density required in rare-earth-ion-doped materials. HENRY introduced the linewidth enhancement factor α to quantify this amplitude-phase coupling, where α is the ratio between the real and imaginary components of the carrier-induced variation of the refractive index. He showed that semiconductor lasers have a linewidth which is larger by a factor of $(1+\alpha^2)$ as compared with the SCHAWLOW-TOWNES limit, where α is typically in the range 3-7 [103].

2.4 Laser Stability

In the preceding section the laser linewidth in the absence of external noise sources was discussed. However, in reality the laser cavity is susceptible to a variety of noise sources which ultimately affect the power and frequency stability as well as linewidth of the laser.

2.4.1 Environmental and Fundamental Thermal Noise

Mechanical vibrations, acoustic noise and temperature fluctuations cause perturbations of the cavity resonance frequency, which consequently cause fluctuations in the laser frequency and linewidth. In the case of a monolithic Bragg-grating-based waveguide cavity, ambient temperature fluctuations induce changes in the refractive index (of the respective layers which form the waveguide) via the thermo-optic effect, while linear thermal expansion of the cavity and Bragg grating period also occurs. From Equation 2.38, it follows that any change in the effective refractive index of the guided mode or change in the grating period will influence the Bragg wavelength. In addition to ambient temperature fluctuations, acoustic noises induce additional temperature fluctuations. As the air pressure varies inside an acoustic wave, the work done to compress and decompress the air leads to temporal temperature variations [104]. The sensitivity of the laser to these environmental noise sources can to some extent be reduced by proper packaging. Self-heating from non-radiative transitions and temperature changes due to fluctuations in the pump power also contribute to the total amount of temperature fluctuation which the laser experiences.

In addition to the environmental temperature fluctuations, there is also fundamental thermal noise, caused by random temperature fluctuations within the laser cavity [105]. Even if the laser cavity is in perfect thermal equilibrium with its surroundings, this fundamental thermal noise floor exists due to random diffusion of thermal energy in and out

of the laser mode volume [103]. The fundamental temperature fluctuation noise spectrum is given by [106]

$$S_{\mathrm{T}}(f) = \frac{k_{\mathrm{B}}T^2}{2\pi k_{\mathrm{T}} L_{\mathrm{eff}}} \mathrm{Re}\left[e^{\left(\frac{ik_1^2a^2}{2}\right)} E_1\left(\frac{ik_1^2a^2}{2}\right)\right] \tag{2.74}$$

where the following definitions have been used

$$E_1(x) = \int_x^\infty \frac{e^{-t}}{t}\mathrm{d}t \tag{2.75}$$

$$k_1(f) = \sqrt{\frac{\pi f c_{\mathrm{v}}}{k_{\mathrm{T}}}} \tag{2.76}$$

with k_{B} the Boltzmann constant, T the temperature, L_{eff} the effective cavity length, a the guided mode radius where the intensity has decreased to e^{-2} of its maximum (assuming a Gaussian transverse distribution), while c_{v} and k_{T} are the specific-heat capacity (per unit volume) and thermal conductivity of the waveguide, respectively. $S_{\mathrm{T}}(f)$ has units of $\mathrm{K}^2.\mathrm{Hz}^{-1}$ and physically represents the mean squared temperature fluctuation within a 1 Hz bandwidth centered at fluctuation frequency f. Although Equation 2.74 was derived assuming an optical fiber with infinite cladding [105], it serves as a good starting point for general theoretical considerations in monolithic channel waveguide lasers. The frequency noise spectrum $S_\nu(f)$ is derived directly from the thermal noise spectrum $S_{\mathrm{T}}(f)$ and in the case of a DFB laser is given by [105]

$$S_\nu(f) = \frac{1}{2}\nu_{\mathrm{L}}^2 q^2 S_{\mathrm{T}}(f) \tag{2.77}$$

where ν_{L} is the laser optical frequency and q the thermo-optic coefficient of the waveguide given by

$$q = \frac{\mathrm{d}n}{n\mathrm{d}T} + \alpha_{\mathrm{TEC}} \tag{2.78}$$

with n the refractive index and α_{TEC} the thermal expansion coefficient of the waveguide. $S_\nu(f)$ corresponds to the mean squared frequency deviation within a 1 Hz band centered at (fluctuation) frequency f and has units of $\mathrm{Hz}^2.\mathrm{Hz}^{-1}$. It was recently shown that the FWHM laser linewidth $\Delta\nu_{\mathrm{L}}$ can be determined directly from the frequency noise spectrum $S_\nu(f)$ by using [107]

$$\Delta\nu_{\mathrm{L}} = \sqrt{8\ln(2)A} \tag{2.79}$$

where A is defined as

$$A = \int_{\frac{1}{t_{\mathrm{o}}}}^\infty H\left(S_\nu(f) - \frac{8\ln(2)}{\pi^2}f\right) S_\nu(f)\mathrm{d}f \tag{2.80}$$

$H(x)$ is the Heaviside step function with $H(x) = 0$ if $x < 0$ and $H(x) = 1$ if $x \geq 0$. The linewidth observation time t_{o} determines the lower cut-off frequency, since the linewidth cannot contain contributions from fluctuations at frequencies lower than $1/t_{\mathrm{o}}$. It should be noted that Equation 2.79 is valid, independent of the noise source and for any shape of the frequency noise spectrum.

2.4.2 Optical Feedback

External optical back-reflections are known to cause excess frequency noise or even self-pulsing in narrow-linewidth semiconductor lasers [108]. These optical back-reflections mainly occur due to Fresnel reflections in fiber pigtails and in optical fiber connectors; these optical feedback effects have been studied extensively for semiconductor lasers [109–114]. However, in the literature there are very few investigations concerning optical feedback effects in rare-earth-ion-doped lasers [115, 116]. Since rare-earth-ion-doped lasers are fundamentally different from semiconductor lasers, very few conclusions can be drawn about the laser stability from existing work on semiconductor lasers. The laser- and cavity linewidth, mirror reflectivity, cavity lifetime, cavity dimensions, refractive index, optical gain and relaxation oscillation frequency are but a few of the laser parameters which are significantly different for rare-earth-ion-doped lasers as compared to semiconductor lasers.

When the laser light is reflected back into the laser cavity, it induces a change in the intra-cavity gain g. The degree to which the gain is influenced depends on the phase of the reflected light resulting in [108]

$$g = g_0 - \frac{2T\sqrt{f_{\text{ext}}}}{L_{\text{eff}}}\cos(\phi_{\text{ext}}) \tag{2.81}$$

where L_{eff} is the effective length of the laser cavity, g_0 is the threshold gain in the cavity in the absence of any back-reflections, f_{ext} is the power fraction of emitted laser light which re-enters the laser cavity, and T is the power transmission coefficient from the laser to the external cavity, which can be determined with Equation 2.60b. In the case of a DFB cavity, the length of the cavity used in the calculation of Equation 2.60b is taken as the distance from the end-facet where the fiber is connected to the quarter-wavelength phase shift. The phase of the reflected light is $\phi_{\text{ext}} = 2\pi\nu\tau_{\text{ext}}$, with the optical frequency ν and the external round-trip delay time τ_{ext}. When ϕ_{ext} is an integer multiple of 2π it will interfere constructively with the intra-cavity laser field, resulting in a slightly increased intra-cavity laser field and consequently, increased stimulated emission so that the population inversion or gain is decreased. However, when ϕ_{ext} is an odd multiple of π, destructive interference with the intra-cavity laser field leads to a decreased intra-cavity laser field and stimulated emission so that the population inversion or gain is increased.

Consider the case where the external optical back-reflection of a DFB waveguide laser operating at a wavelength of 1550 nm originates from the 3.4% Fresnel-reflection at the end-facet of a standard silica fiber which is connected to the chip with a fiber-to-chip coupling efficiency of 30%. Assume the rest of the laser parameters to be the same as in Table 2.2. The calculated intra-cavity laser gain as a function of ϕ_{ext} using Equation 2.81 is shown in Figure 2.17, where a propagation loss of $\alpha_{\text{loss}} = 0.2$ dB/cm was assumed and $g_0 = \alpha_{\text{loss}} - \ln(R_{\text{out}})/(2L_{\text{eff}})$ with R_{out}, the outcoupling reflectivity. For this particular example, it is evident that depending on the phase of the Fresnel back-reflection, a total variation of about 12% is induced in the intra-cavity laser gain. Since only slight changes in ϕ_{ext} result in significant changes in the intra-cavity laser gain, and since the external cavity generally supports a multitude of longitudinal modes, the optical back-reflections

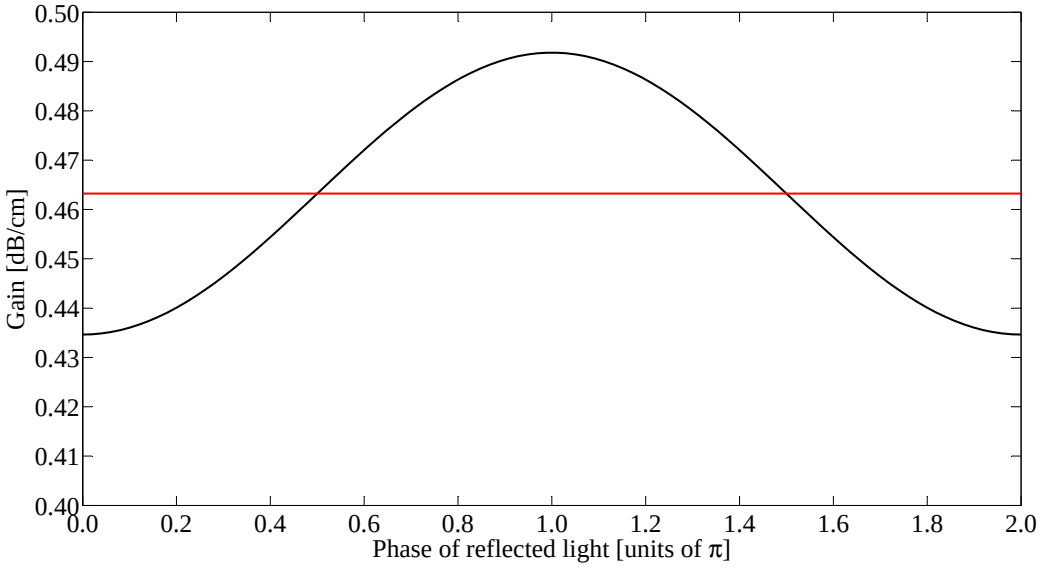

Figure 2.17: Laser gain g (solid black line) under the influence of external optical back-reflections. The solid red line represents g_0.

may lead to mode-hopping between external cavity modes, even in the case of single-longitudinal-mode lasers.

The change in the round-trip phase of the laser due to the external feedback can be written as [108]

$$\Delta\phi = \frac{\tau_{\mathrm{L}}}{\tau_{\mathrm{ext}}}[2\pi\tau_{\mathrm{ext}}(\nu - \nu_0)) + C\sin(2\pi\nu\tau_{\mathrm{ext}} + \arctan(\alpha)] \tag{2.82}$$

where τ_{L} is the round-trip time inside the laser cavity, ν_0 is the laser frequency, and α is the linewidth enhancement factor of the laser. C is a dimensionless parameter known as the feedback parameter and is given by [108, 117]

$$C = \zeta\tau_{\mathrm{ext}}\sqrt{1+\alpha^2} \tag{2.83}$$

where the feedback rate is

$$\zeta = \frac{2T\sqrt{f_{\mathrm{ext}}}}{\tau_{\mathrm{L}}}. \tag{2.84}$$

In the case of a quarter-wavelength phase shifted DFB laser, ζ can be approximated with

$$\zeta = \frac{\kappa c\,\mathrm{sech}^2(\kappa L_{\mathrm{p}})\sqrt{f_{\mathrm{ext}}}}{n_{\mathrm{eff}}} \tag{2.85}$$

with n_{eff}, the effective refractive index of the laser cavity, c the speed of light in vacuum, and L_{p}, the distance from the quarter-wavelength phase shift to the end-facet from where the external back-reflections enter the laser cavity.

The degree of coupling between the laser and external cavity as well as the strength and phase of the back-reflection determines its effect on the laser emission characteristics. The feedback parameter C was derived in order to characterize the different operating

regimes of a semiconductor laser with external feedback. Based on the value of C, Tkach has identified five distinct optical feedback regimes (listed in order of increasing amount of feedback) [111]:

Feedback Regime I

Very weak external optical feedback is represented by $C < 1$, and in this regime the laser will continue to operate on a single longitudinal mode. However, despite the low levels of feedback in this regime, the laser linewidth $\Delta\nu_{\mathrm{L}}$ will be influenced according to [108]

$$\Delta\nu_{\mathrm{L}} = \frac{\Delta\nu_0}{[1 + C\cos(\phi_{\mathrm{ext}} + \arctan(\alpha))]^2} \tag{2.86}$$

where $\Delta\nu_0$ is the laser linewidth in the absence of optical feedback. Note that, depending on the phase of the back-reflected light, the laser linewidth can be narrowed [118], or broadened in this regime. For semiconductor lasers effects on the linewidth was already observed at values of $f_{\mathrm{ext}} = -80$ dB [111]. It should be mentioned that rare-earth-ion-doped lasers seem to become unstable even for $C < 1$ [115].

Feedback Regime II

When the feedback level is increased to the point where $1 < C < 2$, an apparent split of the laser linewidth will arise due to the rapid mode-hopping between different external cavity modes [108, 110]. The external cavity modes arise due to the round-trip phase condition ($\Delta\phi = 0$) in Equation 2.82, having multiple solutions when $C > 1$.

Feedback Regime III

With a further increase of feedback as compared to regime II, the laser tends to lock onto the external cavity mode with the best phase stability, resulting in a single and relatively stable narrow linewidth mode. This mode has the largest value of $\mathrm{d}(\Delta\phi)/\mathrm{d}\nu$, and is also referred to as the minimum linewidth mode [108]. For semiconductor lasers, the onset of this stable behavior occurs at $f_{\mathrm{ext}} = -45$ dB (independent on the distance to the reflection), and is related to the increase of the feedback-induced gain difference between the split modes of regime II [111]. This stable regime is quite small, and for semiconductor lasers it was observed to span an optical feedback range of only about 6 dB [111].

Feedback Regime IV

This feedback regime is the most detrimental for the laser emission, and has also been termed the *coherence collapse* regime [110]. The onset of this regime is also independent on the distance to the external reflector and complete coherence collapse is preceded by the appearance of side modes separated from the main peak by the relaxation oscillation frequency [111]. The amplitudes of the side modes grow as the optical feedback increases until, at the onset of coherence collapse, the laser linewidth suddenly increases by a few orders of magnitude, so that it cannot be distinguished from the side modes anymore

[110]. This event is also associated with a drastic increase in the relative intensity noise of the laser and low-frequency pulsations [108]. It was suggested that coherence collapse occurs when [119]

$$\zeta\sqrt{1+\alpha^2} \geq \omega_\mathrm{r} \tag{2.87}$$

with ω_r being the relaxation oscillation frequency of the laser. Since, in the case of rare-earth-ion-doped lasers, the relaxation oscillation frequency is proportional to the square root of the pump rate, it suggests that the laser will become more tolerable to optical back-reflection at high pump powers. Schunk and Petermann describe the unstable behavior of coherence collapse as being a consequence of the competition between the lasing mode with lowest threshold and the mode with the best phase stability (narrow linewidth mode) [120]. It follows from Equations 2.81 and 2.82 that if $\alpha = 0$, then these are the same mode and no coherence collapse occurs [108]. The relaxation oscillation frequency of a three-level laser is given by [121]

$$\omega_\mathrm{r}^2 = \frac{R_\mathrm{p} - R_\mathrm{th}}{R_\mathrm{th}\tau\tau_\mathrm{c}}\left(1 + \frac{c}{n_\mathrm{eff}}\sigma_\mathrm{L}^\mathrm{abs} N_\mathrm{T}\tau_\mathrm{c}\right) \tag{2.88}$$

where R_p is the pump rate, R_th the threshold pump rate, τ the lifetime of the upper laser level, τ_c the cavity lifetime given by Equation 2.71, $\sigma_\mathrm{L}^\mathrm{abs}$ the effective absorption cross-section at the laser wavelength, and N_T the rare-earth-ion doping concentration. By combining Equations 2.87 and 2.88, it is found that the following condition has to be fulfilled in order for the external optical feedback rate to be low enough for the DFB laser not to enter the coherence collapse regime

$$\xi > \frac{\tau\tau_\mathrm{c} f_\mathrm{ext}(1+\alpha^2)}{N_\mathrm{T} c\sigma_\mathrm{L}^\mathrm{abs}\tau_\mathrm{c} n_\mathrm{eff} + n_\mathrm{eff}^2}[\kappa c\,\mathrm{sech}^2(\kappa L_\mathrm{p})]^2 + 1 \tag{2.89}$$

with ξ being the ratio of the pump rate to the threshold pump rate. This relation is particularly useful since it gives an estimate of how far above threshold the laser should be operated in order to prevent the parasitic effects which are associated with coherence collapse.

Feedback Regime V

At the highest levels of feedback (typically $f_\mathrm{ext} > -10$ dB for a semiconductor laser) the laser operates as a long cavity laser with a short active region [111]. With sufficient wavelength selectivity in the extended cavity, the device will operate on a single longitudinal mode with a narrow emission linewidth. In this regime of operation, the laser is relatively insensitive to additional external optical back-reflections.

3

Design and Fabrication

Now that the theoretical background has been established in the previous chapter, the criteria for designing an optimized waveguide geometry and Bragg grating structure are presented in this chapter. After the optimum waveguide and grating geometries have been calculated, the necessary fabrication steps are discussed, where particular consideration is given to the deposition and etching of the rare-earth-ion-doped Al_2O_3 waveguide layers, along with fabrication of the surface corrugated Bragg gratings.

3.1 Design

In order to have optimized performance from the rare-earth-ion-doped Al_2O_3 waveguide lasers the optimum waveguide and grating geometries were calculated within the constraints of the fabrication techniques. These constrains include the 800 nm minimum channel width that can be defined using standard lithography in the MESA+ cleanroom as well as the maximum uniform grating length of ~ 1 cm, which can be fabricated using the laser interference lithography setup. In the case of the DFB and DBR cavities, the Bragg grating coupling coefficient is considered to be the most important design parameter along with the waveguide geometry.

3.1.1 Waveguides

The two main considerations for the design of a suitable waveguide geometry were single-transverse-mode operation at pump and laser wavelengths and high confinement of the guided mode inside the rare-earth-ion-doped Al_2O_3 layer in order to have a strong interaction between the light fields and the rare-earth ions. Since only straight DFB and DBR cavities are considered in this work, the minimum waveguide bend radius was not

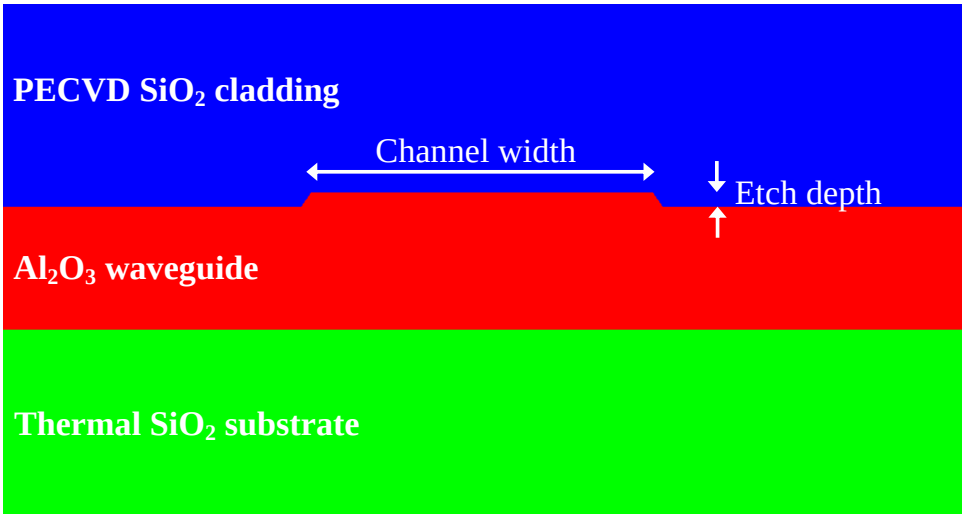

Figure 3.1: Schematic of the Al_2O_3 waveguide layer stack.

Layer	Refractive Index			
	980 nm	1020 nm	1480 nm	1550 nm
PECVD SiO_2 cladding	1.468	1.468	1.465	1.464
Al_2O_3 waveguide	1.648	1.647	1.640	1.640
Thermal SiO_2	1.450	1.449	1.446	1.446

Table 3.1: Refractive indices used in the mode calculations.

identified as an important parameter for this particular application. The layer stack which forms the waveguide consists of an 8-μm-thick thermally-oxidized silicon substrate layer (thermal SiO_2). The Al_2O_3 waveguide core layer is deposited onto this thermal SiO_2 layer, after which channel waveguides are etched using reactive ion etching. Finally, a SiO_2 cladding layer is deposited on top of the Al_2O_3 waveguide core layer by means of plasma enhanced chemical vapour deposition (PECVD). A schematic of the layer stack is shown in Figure 3.1.

A commercial modesolver software package[1] was used to perform the optical waveguide simulations. The mode simulations were carried out using the refractive indices as listed in 3.1. The refractive index of undoped Al_2O_3 layers were used in the calculations. Although the refractive index of the undoped Al_2O_3 layers are slightly lower than that of rare-earth-ion-doped Al_2O_3 layers, it does not make a significant difference in the calculation of the optimum waveguide geometry. The refractive indices of the undoped Al_2O_3 layers used in the calculations were interpolated between measured values taken from [93], while that of the cladding and substrate layers were measured with a Woollam M44 spectroscopic ellipsometer. To achieve the high mode confinement which is required, the Al_2O_3 layer thickness was chosen to be 1 μm in the calculations, while the channel etch depth and channel width were varied to determine the optimum channel waveguide dimensions. The colored regions in Figure 3.2 indicate the parameter range for which the waveguide is

[1] PhoeniX FieldDesigner (www.phoenixbv.com)

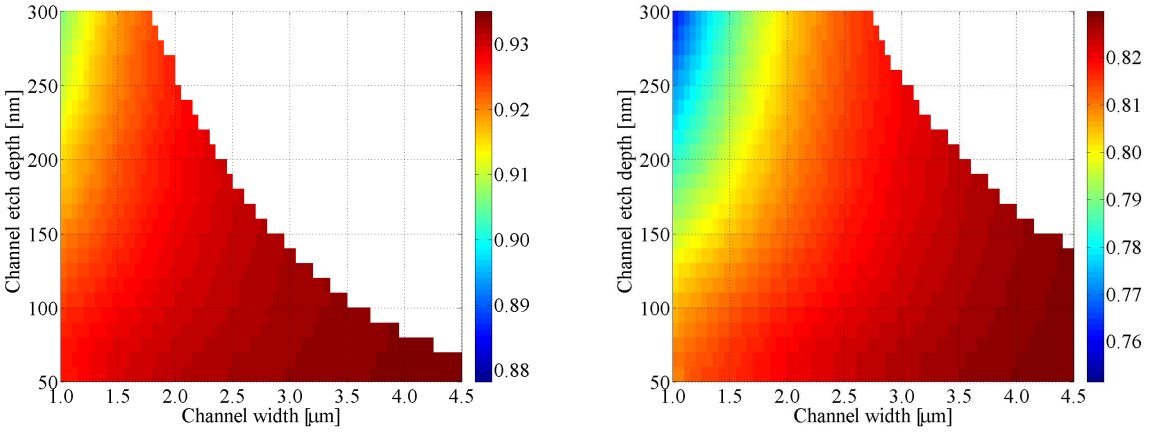

(a) 980 nm wavelength.

(b) 1550 nm wavelength.

Figure 3.2: Confinement factor inside the 1-μm-thick Al_2O_3 waveguide layer. The colored regions indicate the parameter range where single-transverse mode operation occurs, while the white regions indicate multi-mode behavior.

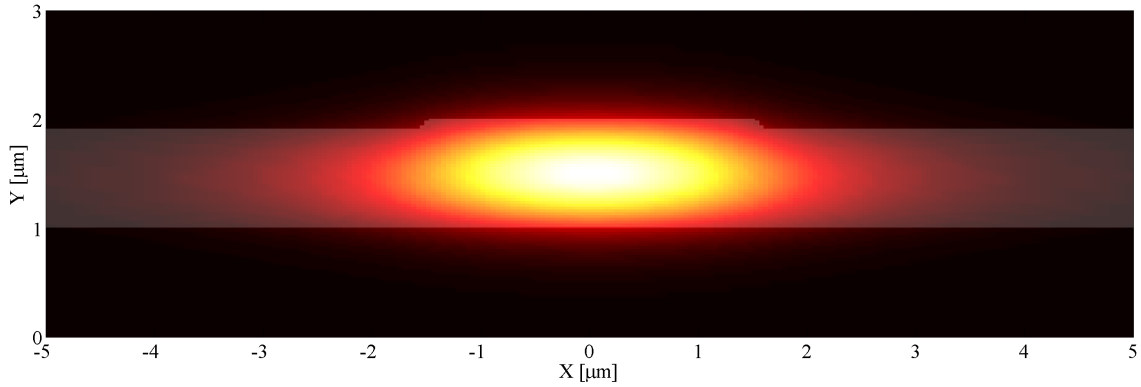

Figure 3.3: Calculated TE mode at a wavelength of 1550 nm for the optimized waveguide geometry. For the TE mode shown in this waveguide cross-section, the electric field is along the X-direction, while the magnetic field is along the Y-direction.

single-transverse-mode for the respective wavelengths. It can be seen that an etch depth of 100 nm provides single mode waveguides for channel widths ranging from 1 μm to at least 4.5 μm. The optimum waveguide width was chosen to be 2.5 - 3.0 μm with an etch depth of 100 nm, resulting in a mode confinement of at least 80% for wavelengths between 980 nm and 1550 nm. These two wavelengths, respectively, represent the upper- and lower limits of the wavelength range which is of interest for the work in this thesis. Since the optical modes supported by these shallow ridge waveguides in Al_2O_3 have similar characteristics for both transverse-electric (TE) and transverse-magnetic (TM) polarization [60], only the TE-polarization calculations are considered. Figure 3.3 shows the calculated TE-mode at a wavelength of 1550 nm for the optimized waveguide geometry.

3.1.2 Grating Coupling Coefficient

Once the optimum waveguide geometry has been calculated, it is necessary to determine the optimum Bragg grating coupling coefficient for the best laser performance. Based on Equation 2.66 which describes the reflectivity of a quarter-wavelength phase shifted DFB cavity, it is possible to evaluate the laser threshold gain of the device (under the assumption of spatially uniform gain). Recall from Equation 2.49 that the reflectivity of the grating is also expressed as

$$R = \left| \frac{B(0)}{A(0)} \right|^2 \tag{3.1}$$

with $B(0)$ and $A(0)$, respectively, the complex amplitudes of the reflected and incident fields at the input of the grating. For certain discrete values of wavelength and gain, the denominator in Equation 2.66 will equal zero, implying a theoretical reflectivity of infinity. At the particular wavelength and gain values at which these singularities occur, the device will act as a self-sustained oscillator since it yields a finite output field $B(0)$ with no input field $A(0)$ [79]. Figure 3.4 shows the calculated reflectivity, according to Equation 2.66, as a function of wavelength and optical gain, for a DFB cavity length of 1 cm and a grating coupling coefficient of $\kappa = 6$ cm^{-1}. In this figure the singularities which represent the possible longitudinal laser modes are clearly visible. As expected, the lowest threshold gain occurs for the mode operating at the Bragg wavelength, with multiple higher order modes (which have significantly higher threshold gain) on either side of the Bragg grating stopband. The optimum grating coupling coefficient is derived by performing a threshold analysis as presented in Figure 3.4, but for a range of different grating coupling coefficients.

The highest small-signal gain which has previously been demonstrated in Al_2O_3:Er^{3+} is 2 dB/cm [60]. It is thus a requirement that the grating coupling coefficient, and consequently the grating reflectivity, are sufficiently high so that the threshold gain of the DFB structure is less than the maximum achievable gain of 2 dB/cm. However, if the grating is made too strong, the threshold gain of the higher order modes will be reduced to a value below 2 dB/cm, so that they can reach threshold along with the fundamental mode so that single-longitudinal-mode operation is no longer possible. A strong grating will also induce additional scattering losses, which should be avoided. In other words, the

optimum grating coupling coefficient range is defined such that the threshold gain of the fundamental mode is below 2 dB/cm, while that of the higher order modes remain higher than 2 dB/cm. These requirements are illustrated in Figure 3.5, where the threshold gain for the fundamental and first order modes are shown as a function of grating coupling coefficient for a 1-cm-long DFB cavity. The 1-cm-long cavity length is assumed since this represents the upper limit of the current grating fabrication technique as discussed in Section 3.2.2. The yellow region represents a grating which is too weak for the fundamental mode to have a sufficiently low threshold gain (< 2 dB/cm), while the red region represents a grating which is so strong that the first higher order modes will have sufficient gain to reach threshold. The green region shows the range of suitable grating coupling coefficients for Al_2O_3:Er^{3+} ranging from ~ 3.5 cm^{-1} to ~ 10.5 cm^{-1}. Since the expected optical gain of ~ 2.5 dB/cm in Al_2O_3:Yb^{3+} is slightly higher than that of Al_2O_3:Er^{3+}, a grating coupling coefficient between 4.0 cm^{-1} and 8.0 cm^{-1} was chosen as the optimum for the devices to be fabricated. In the case of a 1-cm-long DFB cavity, these grating coupling coefficients correspond to reflectivities, of the Bragg reflectors on either side of the centered quarter-wavelength phase shift, which exceed 93%.

The approach which was taken in order to realize a Bragg grating with the particular desired coupling coefficient, was to fabricate a surface corrugated Bragg grating on the top surface of the PECVD SiO_2 cladding (Figure 3.6). By fixing the depth of the surface corrugation, the coupling coefficient of the grating is determined by the thickness of the PECVD SiO_2 cladding, since it determines the overlap between the Bragg grating and the guided mode. With a fixed grating corrugation depth of 100 nm, which is chosen as a typical grating etch depth based on initial grating fabrication experiments, Figure 3.7 shows the calculated grating coupling coefficient according to Equation 2.57, as a function

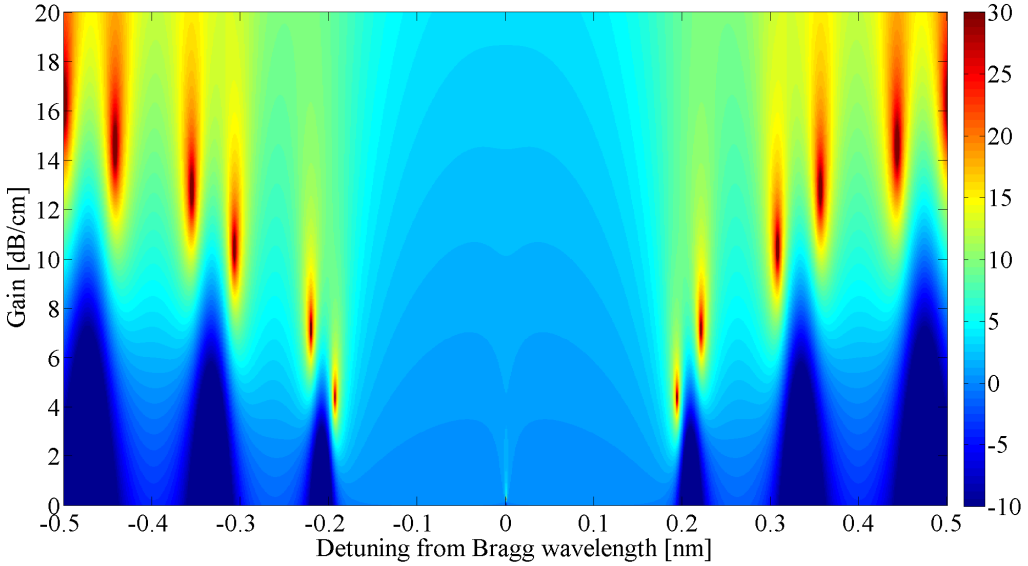

Figure 3.4: Calculated reflection spectrum (in dB) of a 1-cm-long DFB cavity as a function of gain for $\kappa = 6$ cm^{-1}.

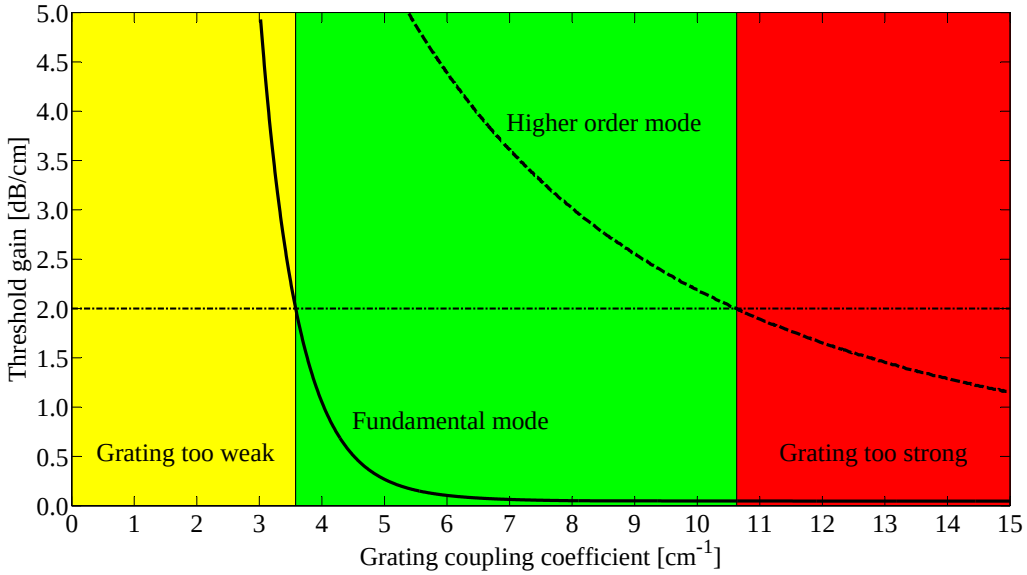

Figure 3.5: Threshold gain as a function of grating coupling coefficient for the fundamental and first order longitudinal modes of a 1-cm-long DFB cavity.

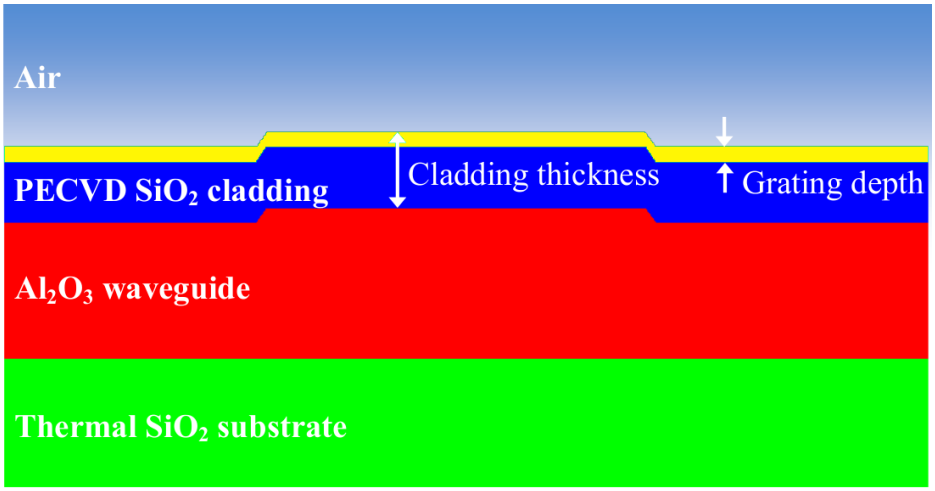

Figure 3.6: Schematic of the waveguide along with the surface corrugated Bragg grating etched in the top surface of the PECVD SiO_2 cladding.

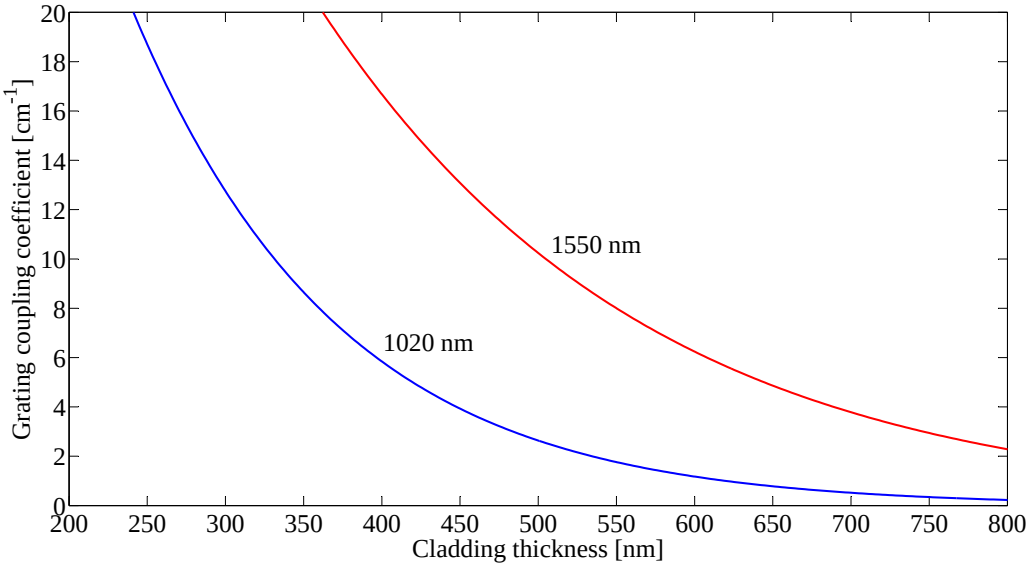

Figure 3.7: Grating coupling coefficient of a 100-nm-deep surface corrugation as a function of the PECVD SiO_2 cladding thickness, for a guided mode at 1020 nm (Al_2O_3:Yb^{3+} laser wavelength) and 1550 nm (Al_2O_3:Er^{3+} laser wavelength), respectively. The waveguide width was chosen to be 2.5 μm, with a channel etch depth of 100 nm.

of the PECVD SiO_2 cladding thickness for a guided mode at 1020 nm (Al_2O_3:Yb^{3+} laser wavelength) and 1550 nm (Al_2O_3:Er^{3+} laser wavelength), respectively. The waveguide width was chosen to be 2.5 μm, with a channel etch depth of 100 nm. Since a guided mode at a wavelength of 1020 nm is more confined to the waveguide core as compared to a 1550 nm guided mode, the grating coupling coefficient, which is determined by the modal overlap with the grating region, is always less as compared to a 1550 nm mode for the same SiO_2 cladding thickness.

3.2 Fabrication

The optimum waveguide and grating geometries for laser operation have been determined in the previous section. This section will be devoted to discussing the waveguide fabrication processes, as well as the use of laser interference lithography and reactive ion etching to define the Bragg grating structures. The use of reactive ion etching to structure the surface-corrugated Bragg gratings is also discussed.

3.2.1 Waveguides

The reactive co-sputtering process which has been used to deposit the rare-earth-ion-doped Al_2O_3 thin films has primarily been developed and optimized by Dr. K. Wörhoff [62], while the lithography and etching of the Al_2O_3 channel waveguides were mostly developed by Dr. J.D.B. Bradley [122]. An overview of the above-mentioned technology

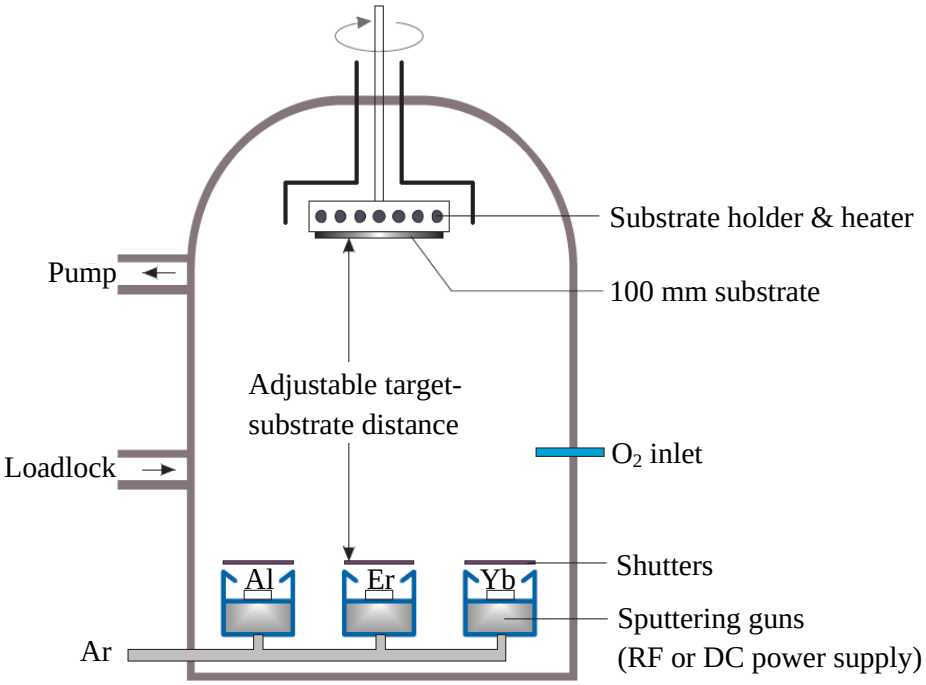

Figure 3.8: Schematic illustration of the reactive co-sputtering system used for the Al_2O_3, Al_2O_3:Er^{3+} and Al_2O_3:Yb^{3+} thin film growth. (Illustration adapted from [93].)

and relevant parameters is given in this section.

Deposition

An AJA ATC 1500 sputtering system which have been equipped with three sputtering guns was used for the deposition of the Al_2O_3 waveguide films. A schematic illustration of this sputtering system is displayed in Figure 3.8. Thermally oxidized silicon wafers, with a diameter of 100 mm, were fixed in a bottom-up configuration on the substrate holder. The substrate holder allows the mounted substrate to be rotated and heated up to a maximum temperature of 800°C, with an accuracy of ±3°C. It is possible to pump the deposition chamber to a background pressure of 10^{-7} mTorr, which is essential in order to reach a negligible OH^- level in the deposition process. For devices based on rare-earth-ion transitions, an OH^--free deposition process is required, since these bonds induce strong luminescence quenching and greatly reduce the achievable optical gain [62]. The three sputtering guns are designed for 2-inch sputtering targets and can each be driven individually by either RF or DC power supplies, having a maximum range of 500 W with an accuracy of ±1 W. In order to achieve the minimum optical loss of the deposited layers layers, RF sputtering was chosen and its process parameters were optimized. High purity aluminum (99.999% purity), erbium (99.95% purity) and ytterbium (99.95% purity) metallic targets were sputtered separately using argon guns, while oxygen was added to the deposition process through a flow-controlled gas inlet in the chamber wall. After the substrate is placed in the holder, it is heated up to the deposition temperature of

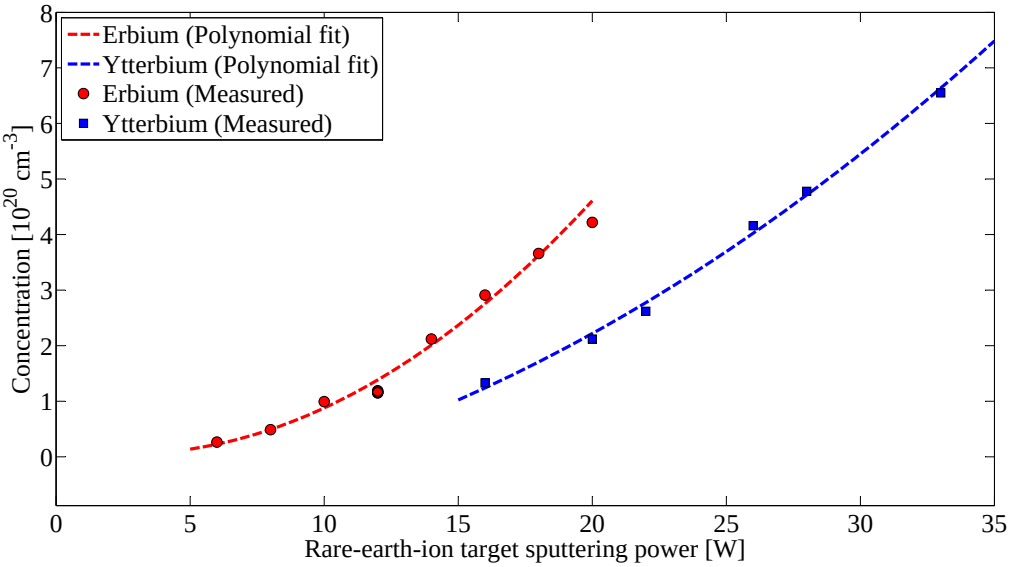

Figure 3.9: Erbium and ytterbium concentration in the deposited Al_2O_3 thin films as a function of target sputtering power.

Parameter	Value
Substrate temperature [°C]	650
Chamber pressure [mTorr]	3.5
Power on aluminum target [W]	200
Power on erbium target [W]	5 - 20
Power on ytterbium target [W]	15 - 35
Total gas flow [sccm]	31.5
O_2 flow percentage [%]	5

Table 3.2: Optimized deposition processing parameters for Al_2O_3 layers deposited by reactive co-sputtering [62, 93]

.

650°C followed by a temperature stabilization of 15 minutes. After the gas flows and the chamber pressure were adjusted to their process set-points, the sputtering power applied to the aluminum target was held constant at 200 W, while the power on the rare-earth-ion metallic targets was varied in order to adjust the rare-earth-ion doping concentration. The power on the target was varied over a range of 5 - 20 W for erbium, and 15 - 35 W for ytterbium. The rare-earth-ion doping concentration in the Al_2O_3 layers was determined by Rutherford backscattering spectroscopy measurements. Figure 3.9 shows the resulting Er^{3+} and Yb^{3+} concentration in the Al_2O_3 thin film versus sputtering power applied to the respective erbium and ytterbium targets. The typical deposition rate of Al_2O_3 layers deposited by RF sputtering is 3 - 5 nm/min. A summary of the optimized deposition process parameters is given in Table 3.2.

Lithography and Etching

To define channel waveguides in the Al_2O_3 layers, an inductively-coupled plasma (ICP) reactive ion etching process which was developed by Bradley has been used [93, 122]. Bradley compared a variety of possible mask materials and reactive gas chemistries, including CF_4/O_2, BCl_3, BCl_3/HBr and Cl_2, in order to find a suitable etch rate and selectivity of the Al_2O_3 layer. Based on these criteria, a BCl_3/HBr plasma with a gas ratio of 5:2 was used along with an OiR 097-17 resist mask with a thickness of 1.6 μm to fabricate the Al_2O_3 channel waveguide structures. The resist was deposited onto the Al_2O_3 layer by means of spin-coating and it was patterned using standard lithography. The optimized etching process parameters were ICP power = 1750 W, RF electrode power = 25 W, pressure = 12 mTorr with a total gas flow of 35 sccm. Etching of the Al_2O_3 layers was performed with an Oxford Plasmalab 100 ICP reactive ion etching system. Using the optimized etching process, channel etch depths of up to 530 nm were demonstrated with an Al_2O_3 etch rate of ∼60 nm/min and a selectivity to the resist mask of 0.76. The resulting channel waveguides had minimal sidewall roughness and sidewall angles were typically between 56° and 68°.

Cladding

After the waveguides have been etched, the residual resist mask is removed using an O_2 plasma followed by wet cleaning in 100% HNO_3, in order to prepare the surface for the deposition of the SiO_2 cladding layer in which the Bragg gratings will be etched. The plasma enhanced chemical vapour deposition (PECVD) SiO_2 cladding is deposited using an Oxford PECVD 80 system. The optimized processing parameters are as follows: gas flow rates of 200 sccm and 710 sccm for 2% SiH_4/N_2 and N_2O, respectively, an applied power of 60 W, a chamber pressure of 650 mTorr, and a substrate temperature of 300°C, resulting in a deposition rate of 37 nm/min.

3.2.2 Bragg Gratings

It follows from Equation 2.38 and the typical modal effective refractive index of ∼ 1.6, that the periodicity of Bragg gratings used in this work ranges from ∼ 315 nm to ∼ 485 nm, for Bragg wavelengths at 1020 nm and 1550 nm, respectively. It is not possible to make use of conventional lithography techniques in order to define Bragg grating structures with these dimensions. Consequently, a high-resolution lithography technique, known as laser interference lithography (LIL) has been used to pattern a resist layer, after which the grating pattern was transferred into the SiO_2 cladding by means of reactive-ion etching. Although alternative high-resolution techniques such as electron-beam lithography and nano-imprinting do exist, LIL was chosen due to the large grating regions which can be fabricated, the possibility to adjust the grating period for each new sample, as well as its high production speed and cost effectiveness. The LIL setup in the MESA+ NanoLab which has been used to prepare the Bragg gratings was built and optimized by Henk van

Wolferen and, consequently, all LIL exposure experiments were performed together with him.

Laser Interference Lithography

Laser interference lithography is based on two coherent plane waves which spatially overlap and form a standing wave pattern in the region where they overlap. The standing wave pattern is then exploited by exposing a photosensitive resist layer with it in order to capture the periodic line structure. Instead of using two individual coherent beams, a single light beam can be used in combination with a mirror which is mounted perpendicular to the sample so that half of the beam is folded back onto itself creating a region of interference on the substrate. This is known as a Lloyds mirror interferometer and a schematic of the setup which was used in this work is shown in Figure 3.10. In the case of two interfering plane waves, the period of the standing wave is given by [123]

$$\Lambda = \frac{\lambda_{\mathrm{LIL}}}{2\sin\theta} \tag{3.2}$$

with λ_{LIL} the wavelength of the illuminating source and θ the angle of incidence as shown in Figure 3.10. However, in the case of the Lloyd's mirror setup shown in Figure 3.10, the light beam which passes through the pinhole has a spherical wavefront, resulting in an error of the period of the interfering standing wave as given by Equation 3.2. The error in the grating period is expressed in terms of the divergence angle α of the beam and is given by [124]

$$\epsilon = 100\left[1 - \frac{1}{\cos\left(\frac{\alpha}{2}\right)}\right]\% \tag{3.3}$$

For the LIL setup which was used to fabricate the Bragg gratings in this work, the divergence angle was typically $\alpha \leq 3°$, resulting in an error in the grating period of $\epsilon \simeq -0.03\%$. Consequently, this will result in an error of about 0.5 nm in the Bragg wavelength, which should be taken into consideration.

A fourth harmonic continuous-wave yttrium aluminum garnet MBD 266 laser system (Coherent) with an exposure wavelength of 266 nm was used for the LIL exposure. The laser beam was aligned and focused on a pinhole unit, which creates a Gaussian beam profile that expands uniformly towards the substrate holder over a distance of approximately 2.6 m for the exposure of 100 mm wafers [123]. Before the LIL exposure could be performed, a bottom anti-reflection coating (BARC), a photoresist layer, as well as a top anti-reflection coating (TARC) were spun on top of the PECVD SiO_2 cladding.

The DUV30J (Brewer Science) BARC layer with a thickness of ∼65 nm was spun on top of the PECVD SiO_2 cladding, after which it was cured for 30 s at 90°C, and then for another 60 s at 180°C. The purpose of the BARC layer is to suppress unwanted reflections from the substrate during LIL exposure, which lead to undesirable standing wave ripples in the sidewalls of the developed photoresist. A 120-nm-thick negative photoresist MA-N2403 (Micro Resist Technology) was spun onto the BARC layer and softbaked at 110°C for 90 s. Finally, a TARC layer (Aquatar by Microchemicals) was applied to further prevent standing waves oscillating in the resist, perpendicular to the substrate.

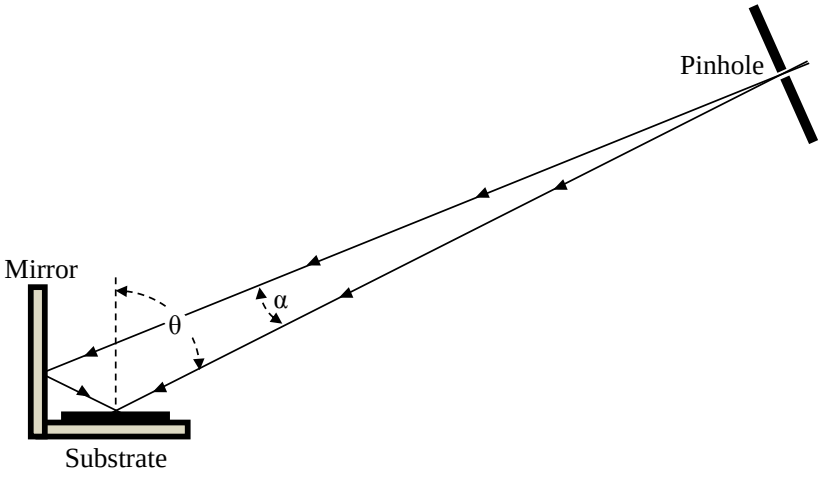

Figure 3.10: Schematic of the laser interference lithography setup in the MESA+ NanoLab. The setup is based on a Lloyd mirror interferometer. (Illustration adapted from [123].)

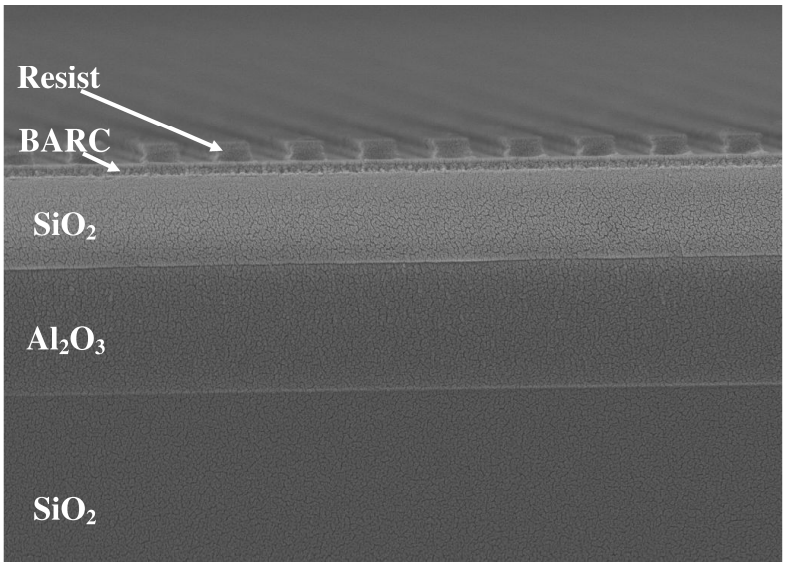

Figure 3.11: Scanning electron microscope (SEM) image of the cross-sectional layer structure showing the developed grating in the resist mask layer before it was etched into the SiO_2 cladding.

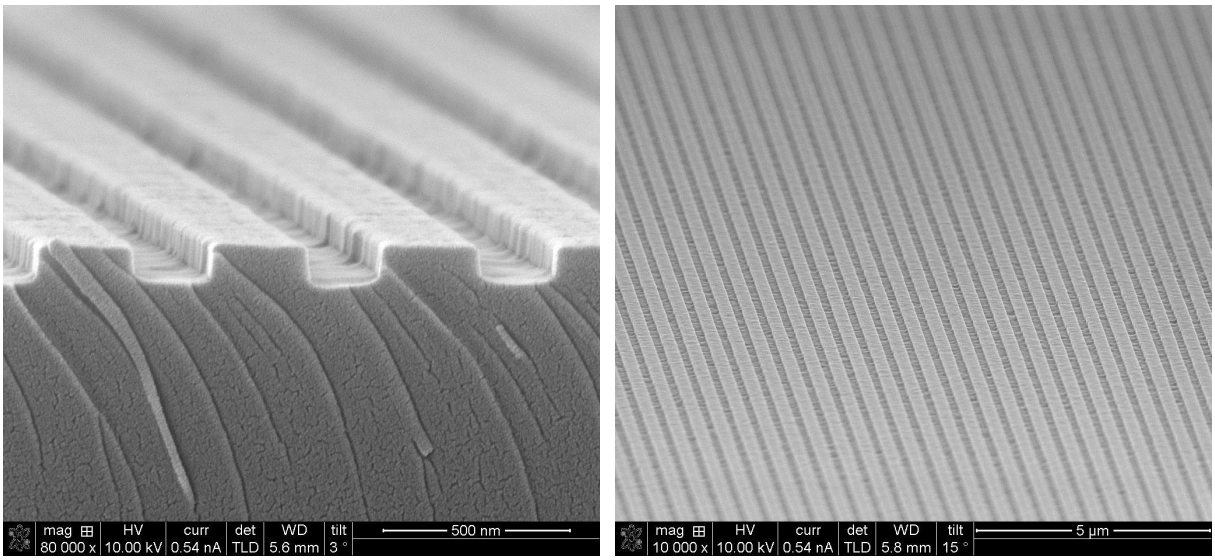

(a) Cross-sectional view. (b) Top-view.

Figure 3.12: Scanning electron microscope (SEM) image of a surface corrugated Bragg grating with a depth of 100 nm that has been etched into a SiO_2 layer. The granular texture is due to a conductive gold layer which was deposited to prevent charging in the SEM.

The Lloyd's mirror was rotated with respect to the incident laser beam so that the angle of incidence θ resulted in the desired grating period according to Equation 3.2. For a typical grating period of 500 nm, the resulting incidence angle is 15.4°. The dose of the LIL exposure was optimized to a value of 2.1 mJ.cm^{-2} (175 μW.cm^{-2} for 12 s) to produce a grating with a 50% duty cycle. For the Bragg grating periods which are of interest in this work, uniform gratings can be fabricated up to a maximum length of approximately 1 cm, which corresponds to a few tens of thousands of grating periods. Since the LIL typically exposes a much larger area than required for the gratings, a subsequent 600-s-long UV exposure with a bright-field mask was performed at a wavelength of 436 nm in order to define the grating regions. After this second exposure, the resist was developed for 30 s by emerging the wafer in a solution of OPD4262 (Fujifilm) which has been diluted with water to 75%, after which the wafers were rinsed in deionized water and spin dried. Figure 3.11 shows a cross-section of the layer stack with the developed grating structure in the photoresist mask layer before the grating pattern was etched into the SiO_2 cladding.

Etching

A reactive ion etching process was used to transfer the Bragg grating structure from the patterned photoresist to the SiO_2 cladding with a PlasmaTherm 790 (Unaxis) reactive ion etcher. However, an initial O_2 reactive ion plasma etch step was performed first in order to etch through the BARC layer and expose the SiO_2 layer underneath. The process parameters for the O_2 etch were 20 sccm gas flow at 100 mTorr, 100 W for 30 s. Subsequently, the grating pattern was etched into the SiO_2 layer using a CHF_3(100 sccm):O_2(5 sccm)

reactive ion plasma with pressure = 40 mTorr, temperature = 10°C, and power = 250 W. These optimized process parameters produced a SiO_2 planar etch rate of 35±2 nm/min. Since the grating region etches at approximately 75% of this rate, the etching time for a 100-nm-deep Bragg grating is around 4 minutes. Finally, the residual BARC and photoresist were removed by another O_2 plasma etch step, using the same parameters as before but for an etch duration of 10 minutes. Scanning electron microscope (SEM) images of a surface corrugated Bragg grating with a depth of 100 nm that has been etched in a SiO_2 layer is shown in Figure 3.12.

4

Passive Cavity Characterization

In this chapter the characterization and application of surface corrugated Bragg gratings which are integrated with Al_2O_3 channel waveguides are described. The Bragg gratings are employed to realize a variety of monolithic DBR and DFB cavities in Al_2O_3 waveguides. The Bragg gratings possess reflectivities higher than 99%, due partly to the waveguide propagation losses (including grating-induced scattering losses) being as low as 0.14 ± 0.07 dB/cm. Measured quality factors (Q-factors) exceed 1.0×10^6 for the DBR cavities, and reach values of up to 1.35×10^6 for the DFB cavities. The performance of the fabricated Bragg gratings and monolithic cavities in Al_2O_3 show good agreement with theoretical models based on coupled mode theory which are described in Chapter 2.

4.1 Waveguide Propagation Losses

For the realization of high-quality monolithic cavities, it is crucial to reduce the waveguide optical propagation losses as much as possible. In the work presented here, the waveguide propagation losses in the absence of integrated Bragg gratings have not been measured explicitly. The measured optical losses in this work include waveguide propagation losses due to sidewall roughness or impurities as well as grating-induced losses. However, in order to determine how much of the losses are grating-induced, it is necessary to have knowledge about the propagation losses in channel waveguides without Bragg gratings.

Wörhoff,Bradley and Yang have each performed extensive loss measurements on Al_2O_3 slab and channel waveguides [62, 93, 125]. By making use of the moving prism method, Wörhoff et al. have measured optical losses for the TE-polarization in Al_2O_3 slab waveguides as low as 0.29 ± 0.04 dB/cm and 0.11 ± 0.02 dB/cm at wavelengths of 633 nm and 1522 nm, respectively [62]. Using the cut-back method, Bradley

measured propagation losses of 0.21 ± 0.05 dB/cm in 2.5-μm-wide Al_2O_3 channel waveguides in the wavelength range 1520-1580 nm [93]. This indicates that the channel waveguide sidewall roughness typically introduce only small additional losses on the order of 0.1 dB/cm. Bradley has also used the moving prism method to determine the losses in Al_2O_3:Er^{3+} slab waveguides, where propagation losses of 0.21 to 0.68 dB/cm at a wavelength of 633 nm, and 0.12 to 0.34 dB/cm at 1320 nm were measured for erbium concentrations ranging from 0.27 to 4.22 $\times$ 10^{20} cm^{-3} [93]. At a wavelength of 1064 nm, Yang has measured propagation losses of TE-polarized light of 0.35 ± 0.06 dB/cm and 0.65 ± 0.06 dB/cm, respectively, for Al_2O_3:Nd^{3+} slab and channel waveguides [125].

4.2 Uniform Bragg Gratings

4.2.1 Waveguide and Grating Fabrication

Al_2O_3 ridge channel waveguides were fabricated in a 1-μm-thick Al_2O_3 layer which was deposited onto a standard thermally oxidized silicon 100 mm wafer using the reactive co-sputtering process as describe in Section 3.2.1. The waveguides supported single-transverse-mode operation and were 1 cm long, 2.5 μm wide, and etched to a depth of 100 nm via the chlorine reactive ion etching process discussed in Section 3.2.1. A 670-nm-thick plasma enhanced chemical vapor deposition (PECVD) SiO_2 cladding layer was deposited on top of the ridge waveguides. The surface-relief Bragg gratings were fabricated on the top surface of the PECVD SiO_2 cladding by means of laser interference lithography (LIL) using a Lloyds mirror interferometer setup and etched into the SiO_2 cladding layer using a CHF_3:O_2 reactive ion plasma (Section 3.2.2). The resultant Bragg gratings had an etch depth of 120 nm with a period of 507 nm and a duty cycle of 50%. The end facets of the sample were prepared by dicing. By choosing such a shallow-ridge waveguide geometry, it is possible to fabricate the grating in the cladding layer without the need to planarize the surface before the grating is written. Another benefit of this geometry is the fact that additional propagation losses due to the roughness in the waveguide sidewalls are minimized. As mentioned in the previous section, reducing the propagation losses is particularly important for the successful realization of monolithic cavities with high Q-factors. Top-view microscope images of the chip containing the integrated Bragg are shown in Figure 4.1.

4.2.2 Grating Transmission Measurements

The effect of the grating on the guided mode can be modeled using coupled mode theory (CMT) as discussed in Section 2.2.1. This allows the grating coupling coefficient to be calculated by a simple overlap integral Γ between the guided waveguide mode and the grating region as given by Equation 2.57. With the calculated mode profiles at the operating wavelength of $\sim$ 1590 nm, the particular grating geometry was calculated to produce a grating coupling coefficient of $\kappa = 6.7$ cm^{-1} (with $\Gamma = 0.146\%$ and effective index $n_{\text{eff}} = 1.57$) for TE polarization and $\kappa = 5.1$ cm^{-1} (with $\Gamma = 0.11\%$ and $n_{\text{eff}} = 1.56$)

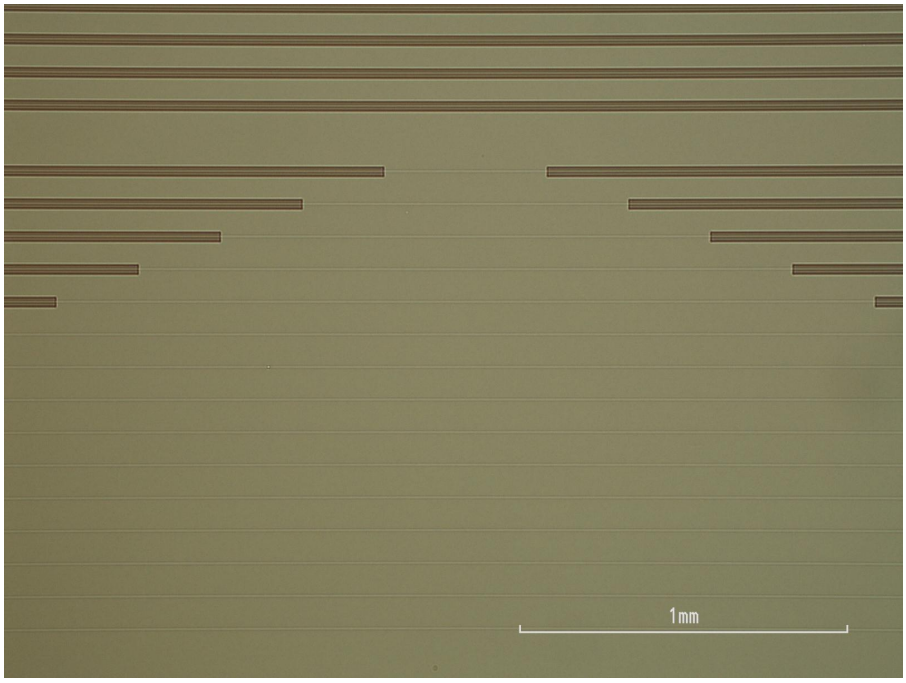

(a) A variety of DFB and DBR structures. The thin light horizontal lines are waveguides, while the thicker dark horizontal lines are the Bragg grating regions.

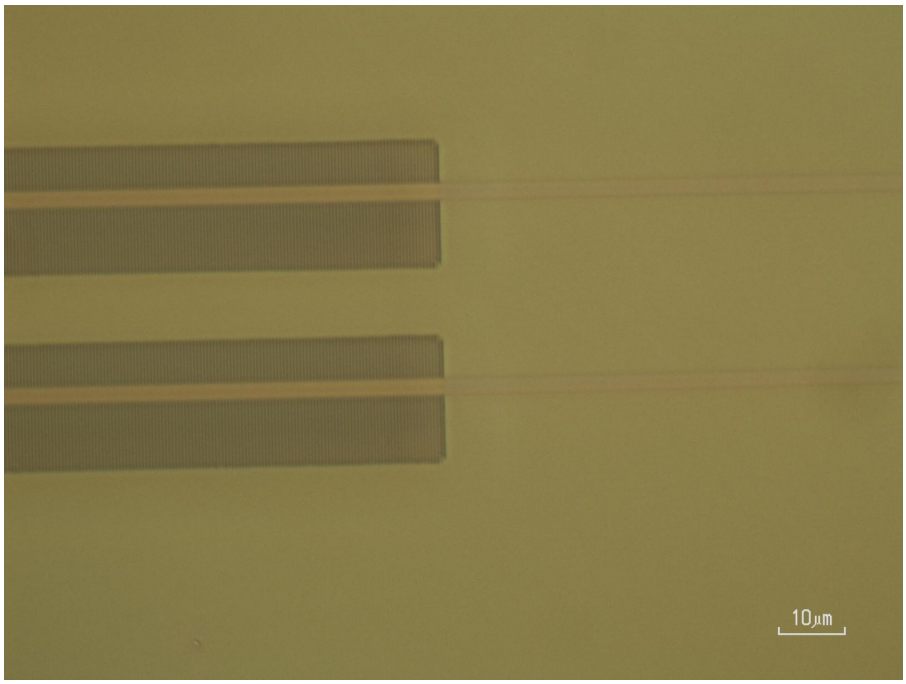

(b) Two 2.5-μm-wide channel waveguides with surface corrugated Bragg gratings.

Figure 4.1: Top-view microscope images of the chip containing the integrated Bragg grating structures.

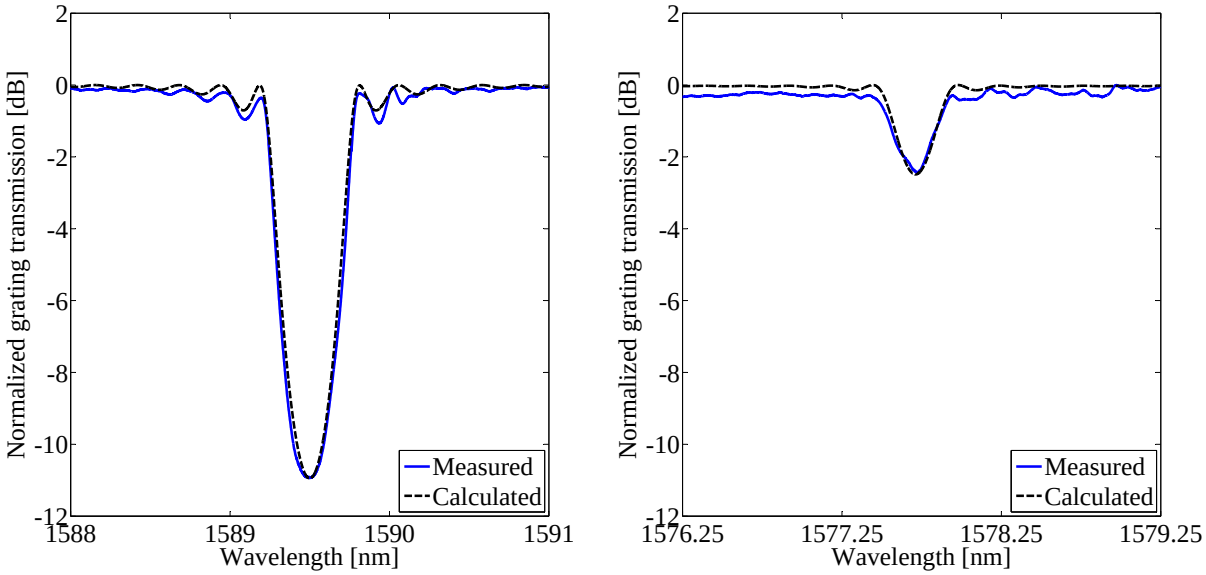

(a) TE-polarization.

(b) TM-polarization.

Figure 4.2: Measured and calculated (Equation 2.52) grating transmission spectra of a 3-mm-long uniform waveguide Bragg grating.

for TM polarization. If the constant grating loss α_T is much smaller than the grating coupling coefficient, i.e., $\alpha_T \ll \kappa$, the reflection R and transmission T at the Bragg wavelength λ_B of a uniform Bragg grating of length L_g with a constant grating period Λ can be approximated using Equations 2.60a and 2.60b. As will be shown later in this section, all the devices in this work have a loss value of $\alpha_T = 0.032$ cm^{-1} ($\alpha_T = 0.014$ dB/cm) and grating coupling coefficient of $\kappa = 6.5$ cm^{-1}, so that the approximations in Equations 2.60a and 2.60b are valid. If L_g is known, the approximation in Equations 2.60a and 2.60b provide an easy way to determine κ by measuring the value of the grating transmission at the Bragg wavelength. Various uniform Bragg gratings as well as DFB and DBR cavities were fabricated.

To characterize the devices, linearly TE- or TM-polarized light from a tunable laser source (Agilent 8164B) with a wavelength range of 1456-1640 nm and 1 pm resolution was coupled into the individual waveguides via a polarization-maintaining (PM) fiber in an end-fire setup. Light transmitted through the waveguide was collected by a fiber with ultra-high numerical aperture (NA = 0.35) and sent to a power meter. Index-matching fluid was used to eliminate Fresnel reflections at the fiber-chip interfaces. Measured TE- and TM-polarized transmission spectra of a single 3-mm-long uniform Bragg grating are shown in Figure 4.2. The wavelength separation of 11.8 nm between the TE and TM Bragg wavelengths agrees well with the calculated modal birefringence of 11.6 nm, suggesting that the birefringence is due primarily to modal birefringence rather than intrinsic material birefringence. For each polarization the depth of the grating transmission dip was used to extract the grating coupling coefficient via the approximations in Equations 2.60a and 2.60b. The measured grating coupling coefficient of $\kappa = 6.5$ cm^{-1} for TE polarization

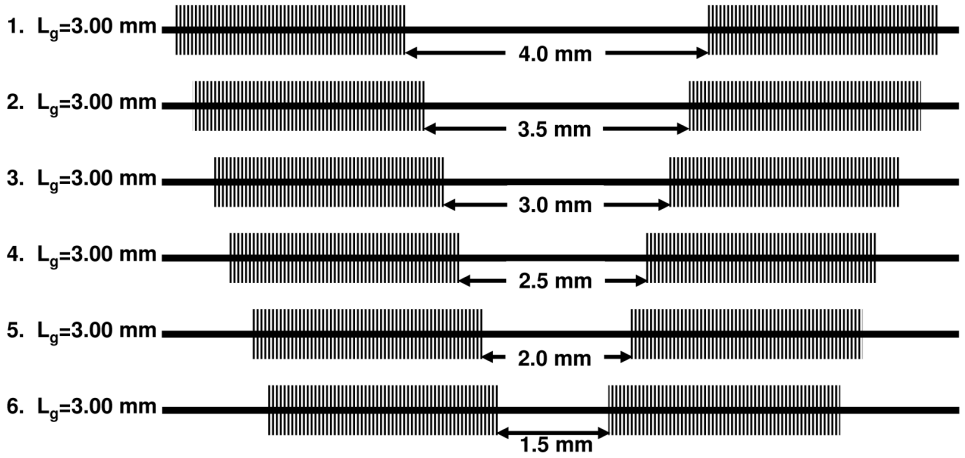

Figure 4.3: A set of six DBR cavities which were fabricated in order to determine the grating-induced loss in these devices.

is consistent with the value of $\kappa = 6.7$ cm^{-1} calculated from Equation 2.57 and, via the approximation in Equation 2.60a, suggests a grating reflectivity of 92% for these 3-mm-long gratings. In contrast, the measured grating coupling coefficient of $\kappa = 2.5$ cm^{-1} for TM polarization is approximately 50% lower than the value calculated from Equation 2.57 and implies a grating reflectivity of only 40%. It is not clear why the grating does not perform as expected for the TM mode, however this behavior has previously been reported for Bragg gratings in silicon-on-insulator ridge waveguides [126]. The calculated grating transmission spectra for both polarizations as predicted by Equation 2.52 agree very well with the measured spectra and are also shown in Figure 4.2.

4.2.3 Grating-Induced Optical Loss

Six DBR cavities were fabricated, each consisting of two 3-mm-long Bragg gratings, with their distance L_d being sequentially decreased from 4.0 mm to 1.5 mm in steps of 0.5 mm Figure 4.3. The finesse of each DBR cavity was determined from the measured transmission spectra as

$$F = \frac{FSR}{\delta\lambda} \tag{4.1}$$

where FSR denotes the cavity free spectral range, which is determined by the wavelength spacing between two successive transmission peaks inside the grating transmission band, while $\delta\lambda$ is the -3 dB width of the transmission peaks. From the three measured transmission peaks which can be observed in the grating transmission band in Figure 4.4(a), the measured FSR of 136 pm and -3 dB width of the transmission peaks of 4.3 pm suggest a finesse of 31.6 for the TE polarization of this particular cavity with $L_\mathrm{d} = 4$ mm. Figure 4.4(b) shows the transmission spectrum for the TM polarization of this DBR cavity. For TE polarization, the finesse was calculated to be between 31.2 and 36.8 for the respective cavities with 3-mm-long Bragg reflectors. For the TM polarization, it was not possible to determine the finesse, since the transmission peaks were not even 3 dB high.

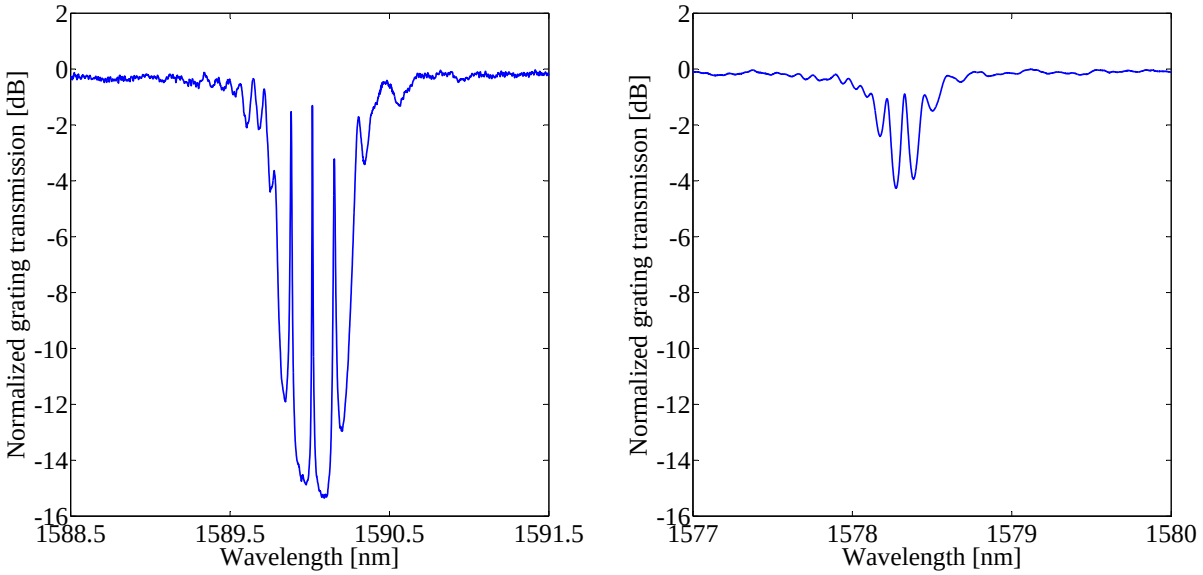

(a) TE-polarization.

(b) TM-polarization.

Figure 4.4: Measured transmission spectra in a DBR cavity with $L_{\mathrm{d}} = 4$ mm and 3-mm-long Bragg reflectors.

The gratings reflect the propagating light in a distributed manner, i.e., light penetrates into the grating region by a distance L_{pen}, resulting in an effective cavity length L_{eff} which is given by [127]

$$L_{\mathrm{eff}} = L_{\mathrm{d}} + 2L_{\mathrm{pen}} = \frac{\lambda^2}{2n_{\mathrm{eff}}FSR} \tag{4.2}$$

where λ is the free-space wavelength. By using Equation 4.2, the measured FSR for the various DBR cavities resulted in $L_{\mathrm{pen}} = 0.93 \pm 0.05$ mm for TE polarization and $L_{\mathrm{pen}} = 1.47 \pm 0.08$ mm for TM polarization. The TM mode penetrates deeper into the gratings, because the measured grating coupling coefficient is 60% smaller for this polarization.

In analogy to a symmetric Fabry-Pérot cavity, R and α_{T} are related to F according to [128]

$$\ln\left[\frac{\cos\left(\frac{\pi}{F}\right)}{1-\sin\left(\frac{\pi}{F}\right)}\right] = \alpha_{\mathrm{T}}L_{\mathrm{eff}} - \ln(R) \tag{4.3}$$

Usually, two of the values of α_{T}, R, and F have to be known in order to determine the third one. However, by measuring the finesse of cavities with different lengths (Figure 4.3) and plotting the left-hand side of Equation 4.3 versus L_{eff}, a straight line is obtained, with its slope and intercept with the ordinate representing α_{T} and R, respectively [129]. This method allows the simultaneous measurement of α_{T} and R. Moreover, it is independent of the amount of light coupled into the waveguide.

A linear fit of the left-hand side of Equation 4.3 versus L_{eff} for the six different DBR cavities suggests $\alpha_{\mathrm{T}} = 0.14$ dB/cm and $R = 92.2\%$ (Figure 4.5). The value of α_{T} is small enough, such that the approximation in Equation 2.60a holds and the reflectivity

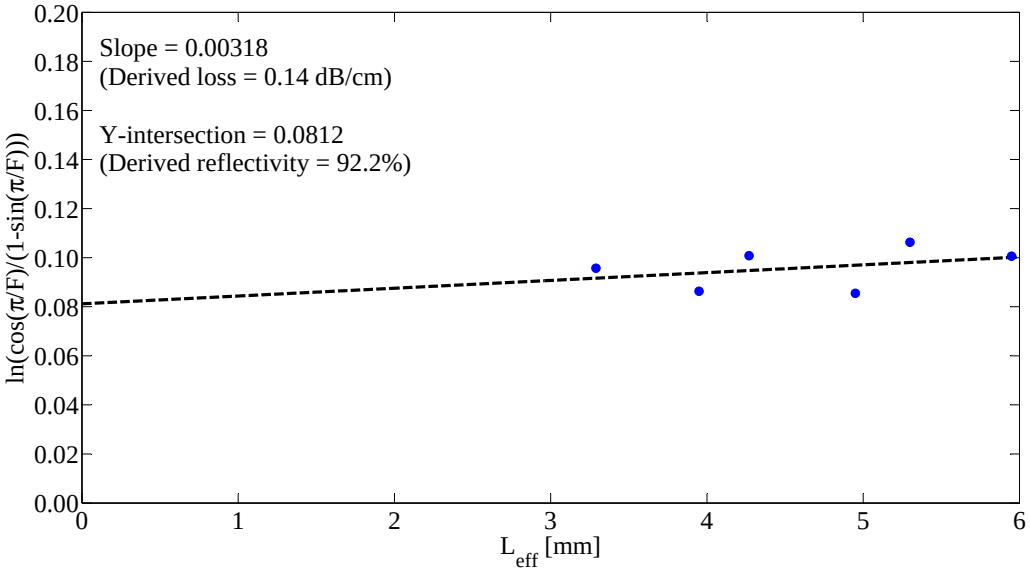

Figure 4.5: Linear fit of the left-hand side of Equation 4.3 versus L_{eff}, suggesting $\alpha_{\text{T}} = 0.14$ dB/cm (via the slope) and $R = 92.2\%$ (via the intercept with the ordinate) for the DBR cavities.

of the 3-mm-long Bragg grating can be calculated to an accuracy of better than 0.5% in comparison to the exact equation in Equation 2.51 which takes the loss into account. The value of R as derived from the linear fit in Equation 4.3 is in excellent agreement with the value derived above from the approximation in Equation 2.60a, i.e., the value of R has been confirmed with two independent methods.

The loss for each DBR cavity was also determined by inserting the finesse from Equation 4.1 and the reflectivity from the approximation in Equation 2.60a into Equation 4.3, resulting in an average loss of $\alpha_{\text{T}} = 0.14 \pm 0.07$ dB/cm, which is consistent with the loss as obtained via the linear fit of Equation 4.3. This loss value includes waveguide propagation losses due to sidewall roughness or impurities as well as grating-induced losses. The losses induced in the Bragg gratings of the DBR cavities can be determined from

$$\alpha_{\text{G}} = \frac{L_{\text{eff}}}{2L_{\text{pen}}}(\alpha_{\text{T}} - \alpha_{\text{U}}) \tag{4.4}$$

where α_{U} is the waveguide propagation loss in the absence of a grating. Previous loss measurements in undoped Al_2O_3 planar waveguides showed that $\alpha_{\text{U}} = 0.11$ dB/cm [62], as discussed in Section 4.1, while the background loss value for 2.5-μm-wide and 220-nm-deep Al_2O_3 ridge waveguides revealed $\alpha_{\text{U}} = 0.21$ dB/cm [122]. This shows that the geometry of the shallow ridge channel waveguides does not induce significant additional background propagation losses in comparison to that of planar waveguide layers, and for the 100-nm-deep ridge waveguide used in this work, the value of α_{U} is expected to be even lower. However, in order to obtain an upper limit of the grating-induced losses, the lower limit of $\alpha_{\text{U}} = 0.11$ dB/cm is assumed, which implies a grating-induced loss value of $\alpha_{\text{G}} = 0.08 \pm 0.01$ dB/cm, via Equation 4.4, for the six DBR cavities. This small value for

the grating-induced loss is evidence of the small overlap ($\Gamma < 0.15\%$) between the guided mode and the grating region.

4.3 High-Q Distributed Bragg Reflector Cavities

The investigated waveguide and grating geometry with its small losses is suitable for the realization of highly reflective monolithic cavities with high Q-factors. Fifteen different DBR cavities were fabricated in order to investigate their grating reflectivity R, finesse F and Q-factor. The length of the Bragg gratings on either side of the DBR cavities was varied from 1.25 mm to 4.75 mm in steps of 0.25 mm, with L_d chosen such that the total physical cavity length was 10 mm in all cases (Figure 4.6).

To characterize the DBR cavities, the same experimental procedure as described in Section 4.2.2 was used. The measured transmission spectra of the cavity with the shortest (1.25 mm) Bragg reflectors and $L_\mathrm{d} = 7.5$ mm are shown in Figure 4.7. This particular cavity has the longest effective cavity length of the entire set of fabricated DBR cavities and, consequently the smallest FSR (Equation 4.2), hence multiple Fabry-Pérot modes are visible inside the stopband of the Bragg reflectors. As discussed before, the effect of the Bragg gratings on the TM polarization is significantly weaker as compared to the TE polarization. The measured FSR of 89 pm for the TE polarization corresponds to an effective cavity length of 9.06 mm, which implies that the light penetrates 0.78 mm into the 1.25-mm-long Bragg reflectors. For the TM polarization with a much smaller grating coupling coefficient, the measured FSR is 83 pm, implying an effective cavity length of 9.59 mm and a light penetration depth of 1.04 mm.

For the DBR cavity with the longest (4.75 mm) Bragg reflectors and $L_\mathrm{d} = 0.5$ mm, the effective cavity is short enough to effectively only have a single Fabry-Pérot resonance inside the stopband of the Bragg reflectors. In the case of the TE polarization the single sharp Fabry-Pérot resonance is clearly visible in the measured transmission spectrum (Figure 4.8(a)). This single resonance has a -3 dB Lorentzian linewdith of 1.56 pm, which represents a Q-factor of 1.02×10^6 according to

$$Q = \frac{\lambda}{\delta\lambda} \tag{4.5}$$

where λ is the free-space wavelength and $\delta\lambda$ is the -3 dB width of the transmission peak. Note that Equation 4.5 is the Fourier-transformed definition. The Q-factor is originally defined as the energy stored in the resonator, E_stored, divided by the energy lost per oscillation cycle, E_lost,

$$Q = 2\pi \frac{E_\mathrm{stored}}{E_\mathrm{lost}}. \tag{4.6}$$

The measured effective cavity length is 3.51 mm, which suggests that the light penetrates ~ 1.5 mm into each Bragg reflector on either side of the cavity. For the TM polarization where the grating coupling coefficient is much weaker, a resonance is hardly visible for this cavity (Figure 4.8(b)).

Since the propagation loss for the TE polarization was determined in the previous section, the grating reflectivity for each cavity could be investigated by measuring the finesse and substituting it into Equation 4.3. The grating reflectivity for TE polarization measured in this way agrees well with the value predicted by substituting the previously measured $\kappa = 6.5$ cm^{-1} into Equation 2.60a (Figure 4.9). The maximum measured reflectivity exceeds 99% and was measured for the DBR cavity with the 4.75-mm-long Bragg reflectors. The finesse of a Fabry-Pérot cavity is given by [130]

$$F = \frac{\pi e^{-\rho L_{\text{eff}}/2}}{1 - e^{-\rho L_{\text{eff}}}} \tag{4.7}$$

where

$$\rho = \alpha_{\text{T}} - \frac{1}{L_{\text{eff}}} \ln(R) \tag{4.8}$$

The measured finesse for each DBR cavity is in very good agreement with that predicted by Equation 4.7 (Figure 4.10), and ranges between 4 up to a maximum value of 147. The measured Q-factors of the DBR cavities correlate well with those predicted by

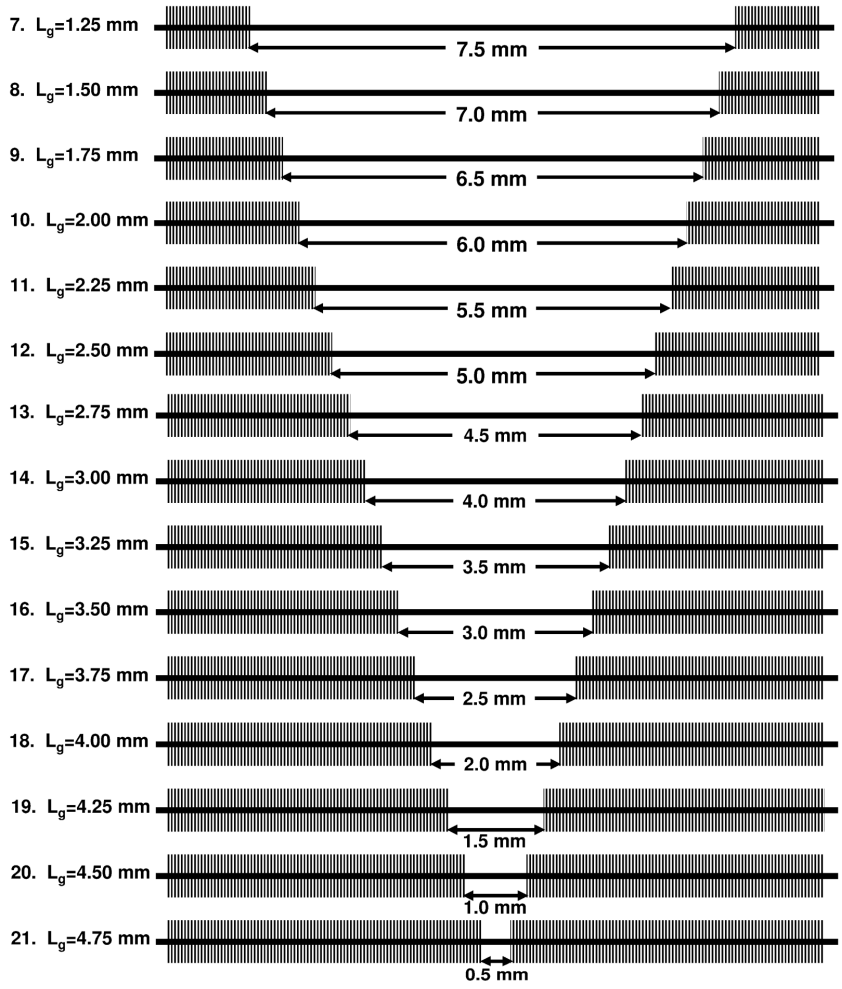

Figure 4.6: Set of fifteen DBR cavities of total length 10 mm, which were investigated to determine their reflectivity, finesse, and Q-factors.

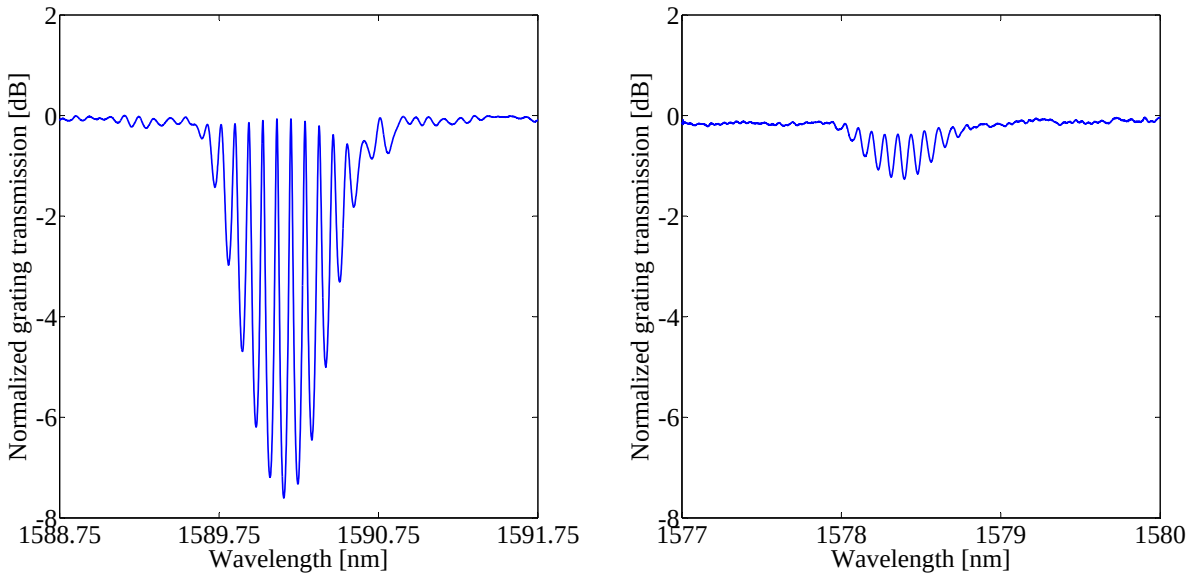

(a) TE-polarization. (b) TM-polarization.

Figure 4.7: Measured transmission spectra in a DBR cavity with $L_{\mathrm{d}} = 7.5$ mm and 1.25-mm-long Bragg reflectors.

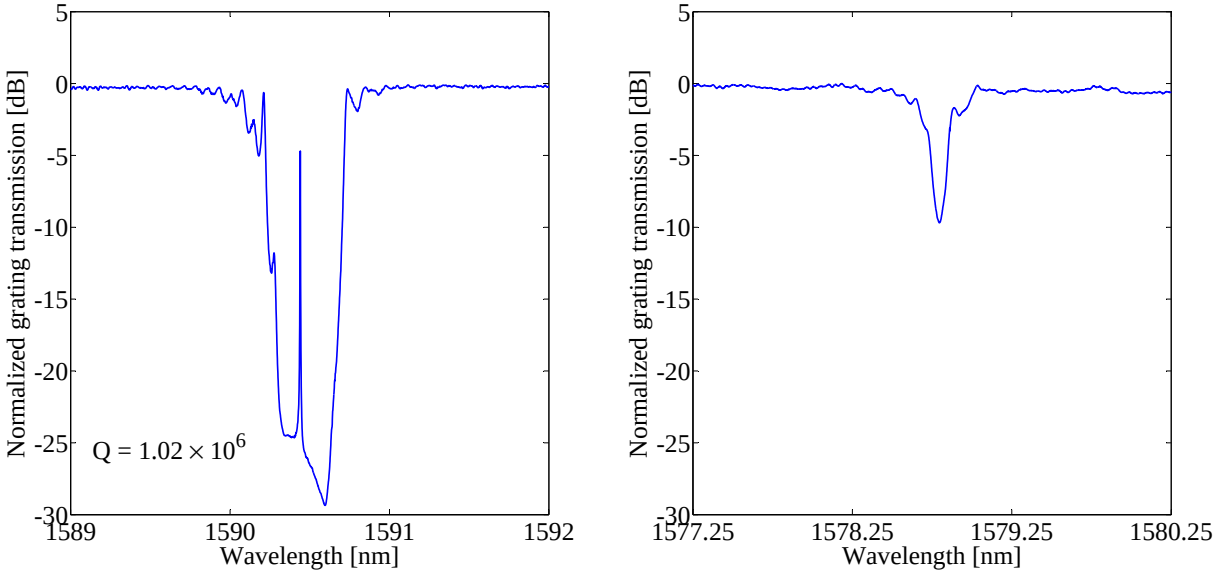

(a) TE-polarization. (b) TM-polarization.

Figure 4.8: Measured transmission spectra in a DBR cavity with $L_{\mathrm{d}} = 0.5$ mm and 4.75-mm-long Bragg reflectors.

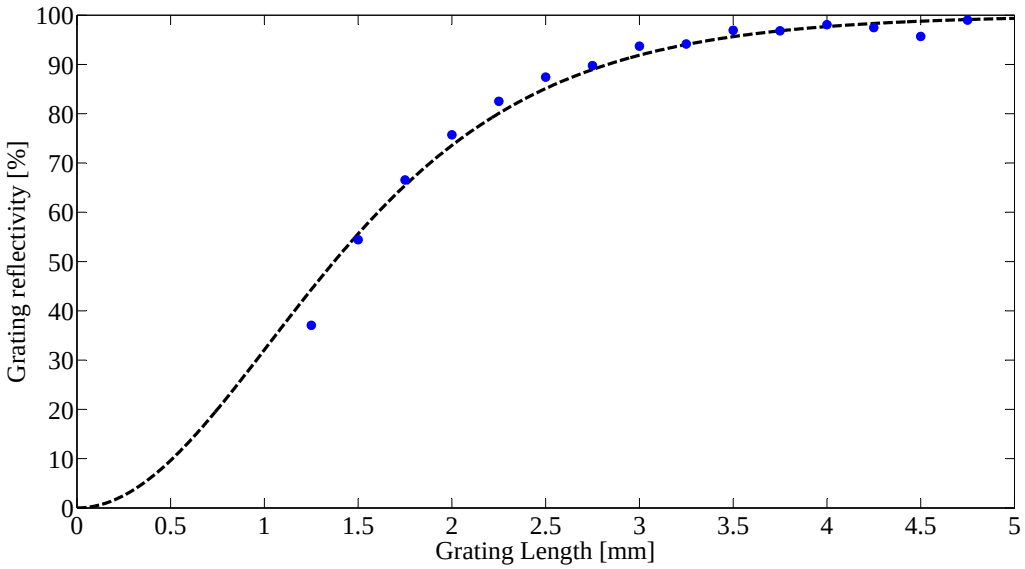

Figure 4.9: Grating reflectivity at the Bragg wavelength for TE polarization as a function of grating length. The blue dots represent the reflectivity as determined from the measured finesse and Equation 4.3, while the dashed line is the predicted reflectivity according to Equation 2.60a.

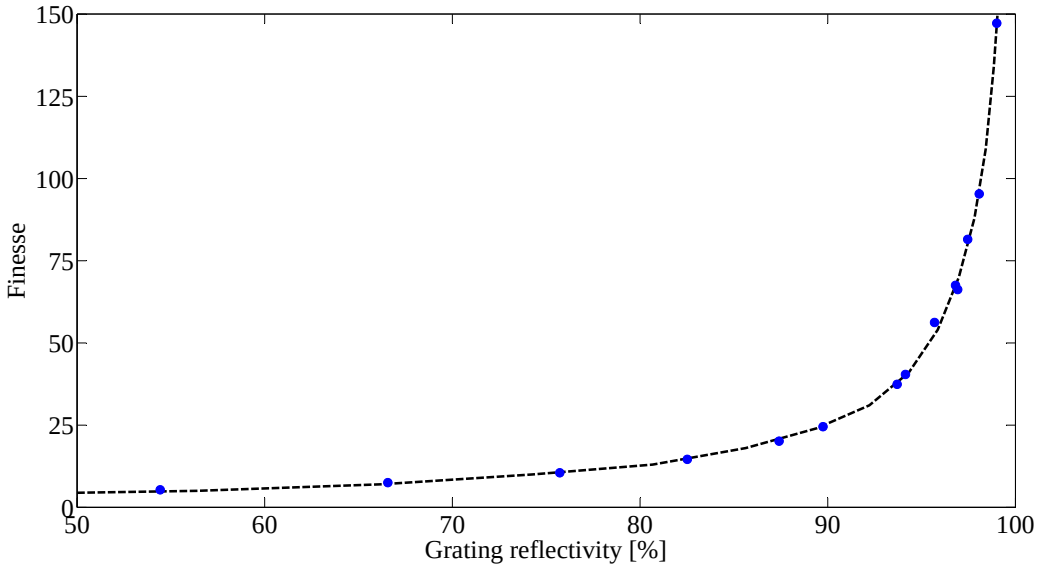

Figure 4.10: Measured finesse (blue points) for each DBR cavity along with the value (dashed line) predicted by Equation 4.7.

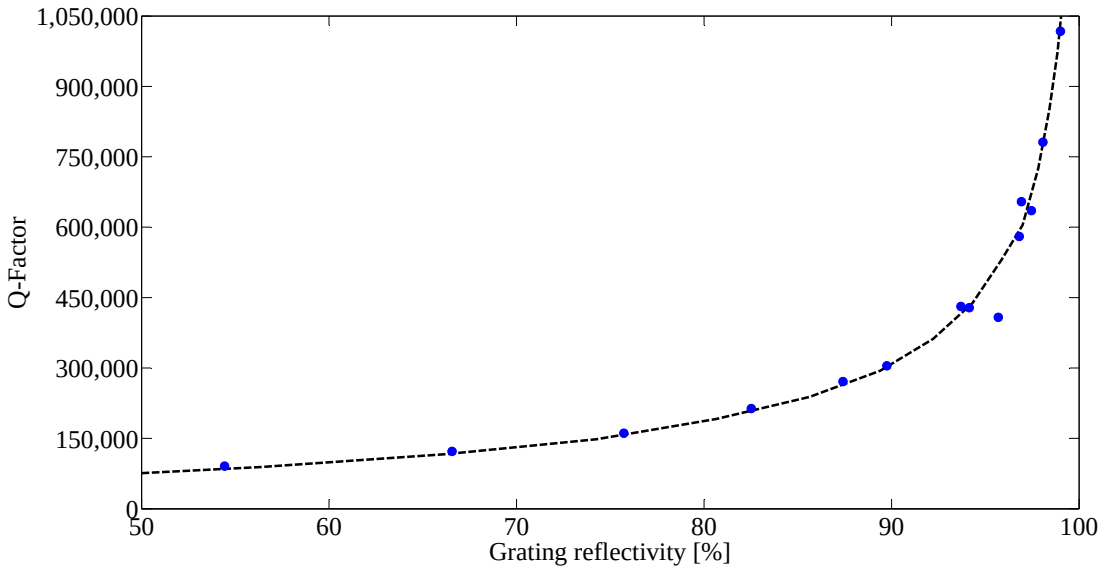

Figure 4.11: The measured Q-factors (blue points) correlate well with the value (dashed line) predicted by $Q = \lambda F/FSR$ [130], where F was calculated from Equation 4.7.

λ_B [nm]	L_d [mm]	L_g [mm]	L_{eff} [mm]	L_{eff} [mm]	FSR [pm]	$\delta\lambda$ [pm]	R [%]	F	Q-factor
1590.212	7.5	1.25	9.06	0.78	89	24.93	37.05	4	6.40×10^4
1590.187	7.0	1.50	8.76	0.88	92	17.50	54.43	5	9.09×10^4
1590.170	6.5	1.75	8.31	0.91	97	13.00	66.56	7	1.22×10^5
1590.209	6.0	2.00	7.75	0.88	104	9.89	75.72	11	1.61×10^5
1590.322	5.5	2.25	7.40	0.95	109	7.44	82.52	15	2.14×10^5
1590.297	5.0	2.50	6.83	0.92	118	5.86	87.41	20	2.71×10^5
1590.384	4.5	2.75	6.30	0.90	128	5.22	89.75	25	3.05×10^5
1590.354	4.0	3.00	5.84	0.92	138	3.69	93.70	37	4.31×10^5
1590.280	3.5	3.25	5.38	0.94	150	3.71	94.14	40	4.28×10^5
1590.385	3.0	3.50	5.01	1.00	161	2.43	96.93	66	6.54×10^5
1590.323	2.5	3.75	4.36	0.93	185	2.74	96.81	67	5.80×10^5
1590.454	2.0	4.00	4.16	1.08	194	2.04	98.07	95	7.81×10^5
1590.368	1.5	4.25	3.95	1.23	204	2.50	97.46	82	6.35×10^5
1590.581	1.0	4.50	3.68	1.34	219	3.90	95.69	56	4.08×10^5
1590.441	0.5	4.75	3.51	1.50	230	1.56	99.01	147	1.02×10^6

Table 4.1: A summary of the measured data in TE polarization for the respective DBR cavities.

$Q = \lambda F/FSR$ [130], with F calculated from Equation 4.7 (Figure 4.11). The measured Q-factors were between 6.40×10^4 for the cavity with the shortest Bragg reflectors, up to a maximum of 1.02×10^6 for the cavity with the longest Bragg reflectors. Table 4.1 presents a summary of all the measured values for the respective DBR cavities.

4.4 High-Q Distributed Feedback Cavities

As an alternative to a DBR cavity configuration, various DFB cavities have also been fabricated by using $\sin^2$-shaped distributed phase shifts as discussed in Section 2.2.4. The cavities were fabricated as described in Section 4.2.1, with a Bragg grating length of 10 mm and a distributed phase shift length of 2 mm for all cavities. The phase shifts were centered at 6 mm, as measured from the end-facet where the light was incident. The phase shifts were offset with respect to the center of the grating to give the cavities a higher outcoupling in the direction of the shorter end of the cavity, for the purpose of realizing laser cavities with a high degree of output power directionality [131].

The channel waveguides were fabricated having a width of $w = 2.5$ μm, while the widest part inside the 2-mm-long distributed phase shift region w_{ps} was varied in order to attain different phase shift values. The value of Δw ranged from 0.1 μm to 0.55 μm, where $\Delta w = w_{\text{ps}} - w$. Mode calculations were performed in order to determine Δn for each cavity, where $\Delta n = n_{\text{eff}}^{\text{ps}} - n_{\text{eff}}$, with $n_{\text{eff}}^{\text{ps}}$ being the effective refractive index in the widest part of the $\sin^2$ distributed phase shift region and n_{eff} the effective refractive index of the waveguide without the phase shift. The calculated values of Δn were used to calculate the amount of phase shift θ of each cavity according to Equation 2.67.

Transmission spectra of the DFB cavities were obtained using the same experimental procedure as described in Section 4.2.2. Figure 4.12 shows the measured TE polarized transmission spectra for DFB cavities with varying amount of phase shift. For small phase shift vales ($\theta = 0.17\pi$), a narrow resonance is visible inside the grating stopband, located towards the short-wavelength edge of the stopband. The measured Q-factor of this resonance is $Q = 3.43 \times 10^5$. As θ increases, the resonance moves towards the center region of the stopband, while the Q-factor increases to a maximum of $Q = 6.28 \times 10^5$ for $\theta = 0.33\pi$. For further increased values of θ, the resonance gradually moves past the center of the stopband, towards the long-wavelength edge of the stopband, while the Q-factor steadily decreases. For the maximum phase shift value of $\theta = 0.87\pi$, the Q-factor has decreased to $Q = 1.91 \times 10^5$. It can be seen that the height of the resonance peak decreases with increasing values of θ. This suggests that there might be additional cavity losses present for large phase shift values. However, it is not clear what such an additional loss mechanism might be and this effect requires further investigation. Figure 4.13 shows the measured Q-factor for the TE polarization as a function of the distributed phase shift value for the various DFB cavities. The maximum Q-factor is expected for a quarter-wavelength phase shift ($\theta = 0.5\pi$) when the resonance should be located exactly in the center of the grating stopband where the reflectivity is highest. However, the highest measured Q-factors were for slightly lower phase shift values ($\theta = 0.33\pi$ to $\theta = 0.5\pi$).

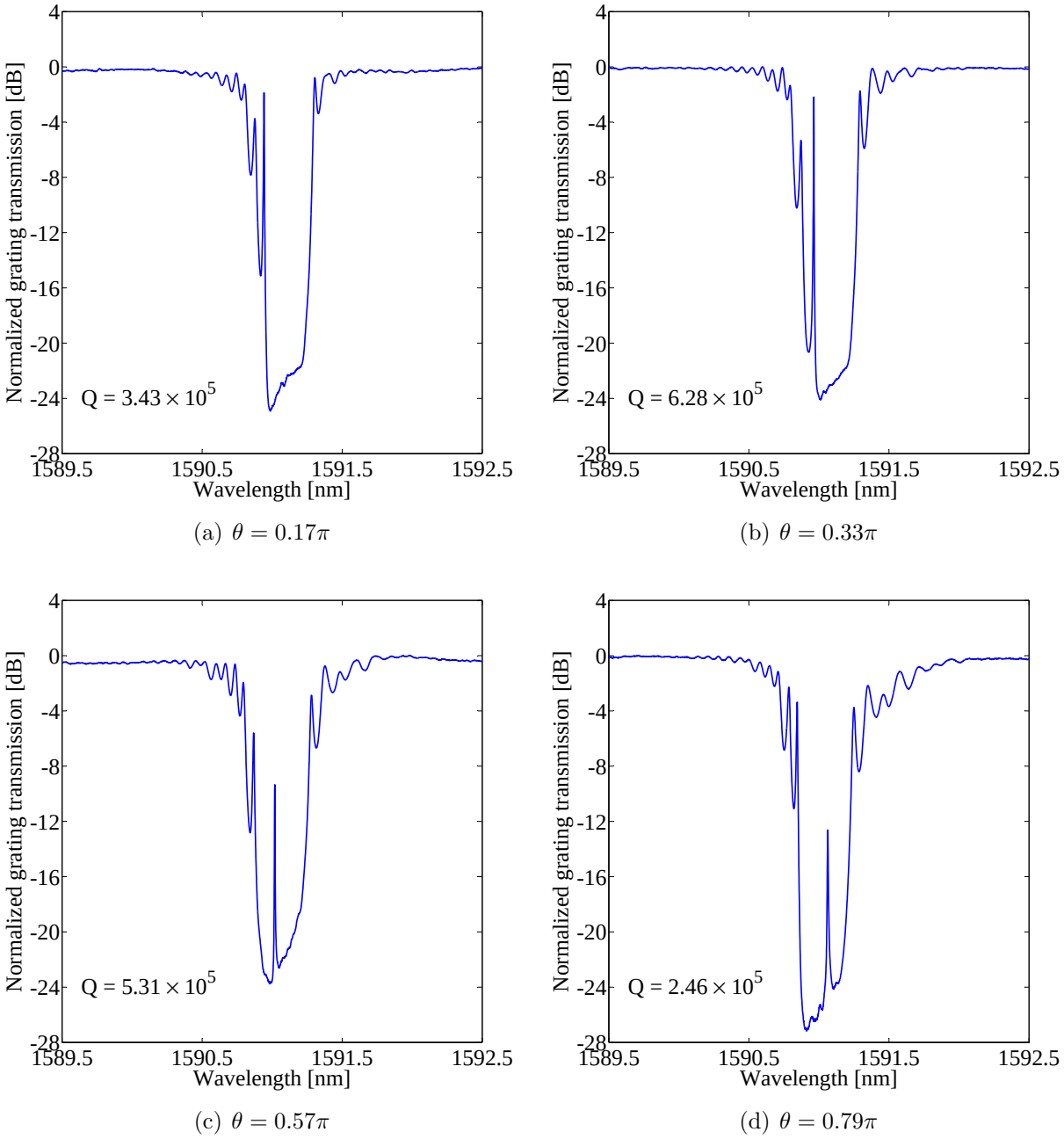

(a) $\theta = 0.17\pi$ (b) $\theta = 0.33\pi$

(c) $\theta = 0.57\pi$ (d) $\theta = 0.79\pi$

Figure 4.12: Measured TE polarized transmission spectra in a 10-mm-long DFB cavity for various values of distributed phase shift θ. The phase shifts were 2-mm-long and centered at 6 mm (as measured from the end-facet where the light was incident).

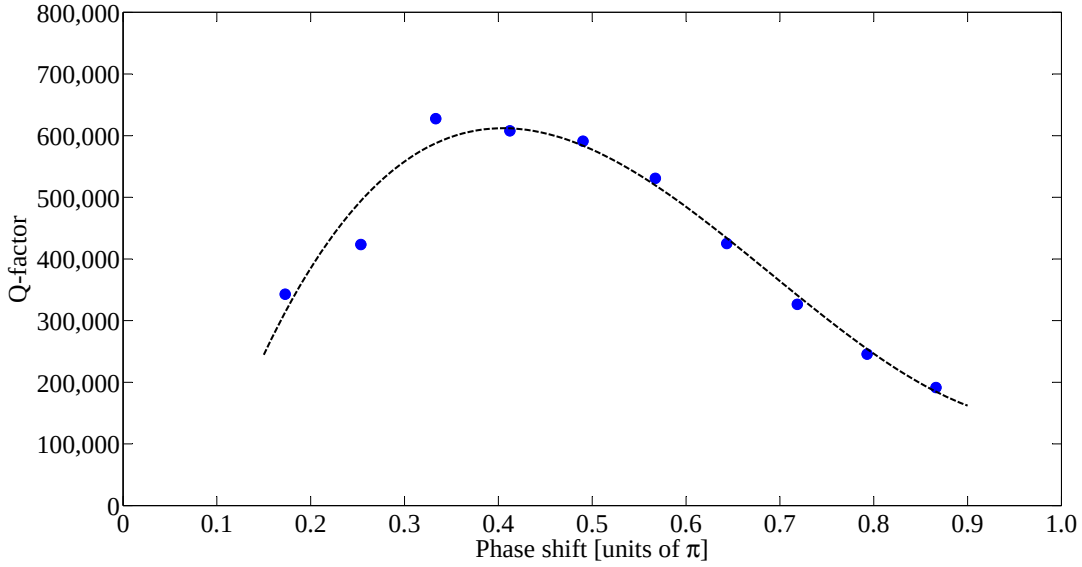

Figure 4.13: Measured Q-factor for the TE polarization as a function of the distributed phase shift value for the various DFB cavities. The dashed black line represents a third order polynomial fit to the measured data.

This might be due to the calculated Δn being slightly underestimated. Alternatively, the suggested additional loss mechanism at large values of θ could also be responsible for the optimum phase shift being slightly lower than expected.

4.5 Applications

Besides the fact that spectral response of the realized DBR and DFB cavities makes then ideal for sophisticated optical add-drop multiplexers, the exceptionally high demonstrated Q-factors make these cavities ideal for the realization of integrated optical sensors based on absorption spectroscopy. The sensitivity of such a high-Q cavity sensor is not determined by the physical length of the device, but rather by the number of oscillations of the light supported by the cavity, which is characterized by the Q-factor. The effective interaction length is given by [132]

$$L_{\text{int}} = \frac{Q\lambda}{2\pi n_{\text{eff}}} \tag{4.9}$$

Since the absorption in such a sensor is an accumulative effect, a longer interaction length will result in a lower detection limit. The DBR cavity in which the highest Q-factor of 1.02×10^6 was realized has an effective interaction length of $L_{\text{int}} = 16.5$ cm. This represents more than a 16-fold improvement over the physical cavity length of 1 cm and a 50-fold increase with respect to the effective cavity length. Once optical gain is introduced to such a cavity by doping the Al_2O_3 waveguides with rare-earth ions, these cavities can be used for the realization of optically pumped, single-longitudinal-mode monolithic waveguide lasers, which is discussed in the next chapter. Because the particular grating

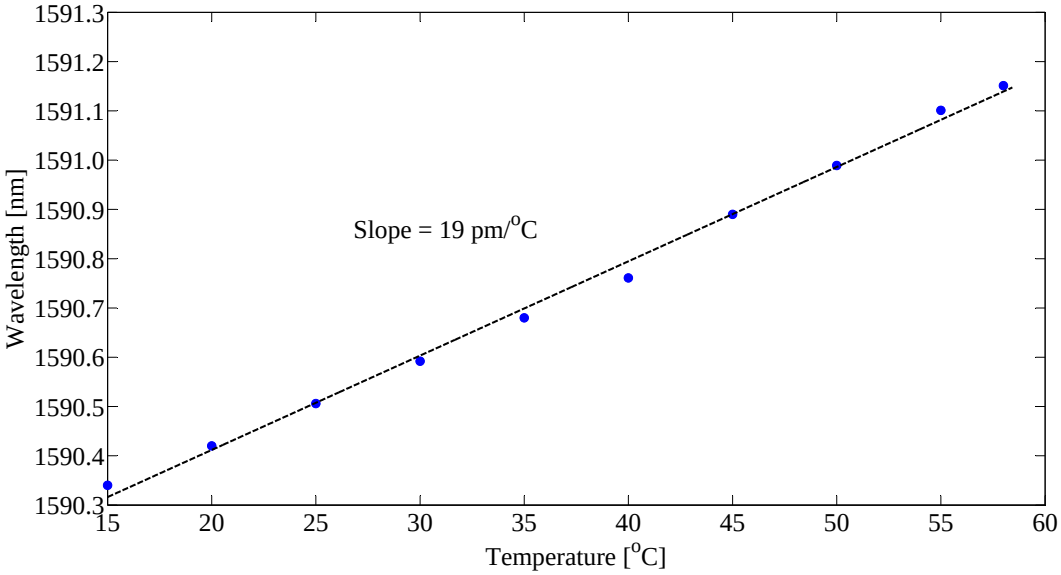

Figure 4.14: Measured temperature dependence of the Bragg wavelength (blue points) over a temperature range from 15°C to 58°C. The linear fit (dashed line) to the measured data revealed the temperature dependence to be 19 ± 1 pm/°C.

geometry which is considered in this work has much better reflection performance for TE polarization than for TM polarization, such a laser should have single polarization output with no mode competition between the respective polarizations, since the TM mode will not reach threshold. Another attribute which makes these devices ideal for the realization of monolithic lasers is their wavelength stability. The temperature drift of the Bragg wavelength was measured over a temperature range of 15-58°C and found to be 19 ± 1 pm/°C, which is equivalent to a frequency change of 2.25 GHz/°C (Figure 4.14). This represents at least five times better environmental temperature stability than that of typical commercially available semiconductor DBR and DFB waveguide lasers.

5 Lasers

Nowadays, monolithic lasers find numerous applications in spectroscopy, optical communications, and optical sensing. These modern-day applications often place stringent requirements with respect to efficiency, output power, spectral characteristics, compactness, robustness, and thermal stability on the laser. Waveguide lasers are of particular importance for the realization of compact, rigid, and robust optical devices, since the entire laser cavity along with the optical feedback elements can be fabricated on the same substrate. Such an integrated solution is desired for combination with other photonic components on the same chip. Besides, when an application requires a laser array, e.g., for simultaneous operation over a specific wavelength range, cost issues strongly favor an on-chip integrated approach. In this chapter the DFB and DBR cavity configurations which have previously been discussed and characterized (Chapter 4) are implemented in erbium- and ytterbium-doped Al_2O_3 thin film layers for the purpose of realizing monolithic waveguide lasers.

5.1 Er^{3+}-Doped Distributed Feedback Laser

Due to their high-quality emission properties in the third telecommunication window (1525-1565 nm), erbium-doped dielectric waveguide lasers have found numerous applications within the telecommunication industry, where they offer a capable and competitive alternative to semiconductor lasers. Bradley et al. have previously demonstrated Al_2O_3:Er^{3+} waveguides with low background losses and an internal net gain over a wavelength range of 80 nm (1500-1580 nm), with a peak gain of 2.0 dB/cm at 1533 nm [60]. Soon thereafter, the broad gain bandwidth of Al_2O_3:Er^{3+} was exploited by demonstrating an Al_2O_3:Er^{3+} integrated ring laser which has been shown to operate on sev-

eral wavelengths in the range 1530-1557 nm [66]. In this section, the fabrication and characterization of a monolithic single-longitudinal-mode DFB channel waveguide laser in Al_2O_3:Er^{3+} is presented. The laser output power surpasses that of the previously demonstrated ring laser by more than two orders of magnitude, while also providing the additional feature of single-polarization, single-longitudinal-mode emission.

5.1.1 Fabrication

The 1-μm-thick channel waveguides were fabricated in an Al_2O_3:Er^{3+} layer with an erbium concentration of 3×10^{20} cm^{-3}, which was deposited onto an 8-μm-thick thermally oxidized, 10-cm-diameter standard silicon wafer by means of the reactive co-sputtering process which has been described in Section 3.2.1 [62]. The ridge waveguides were 1 cm long, 3 μm wide, and were etched 100 nm deep using the standard lithography and reactive ion etching processes discussed in Section 3.2.1 [122]. A 650-nm-thick SiO_2 cladding layer was deposited on top of the ridge waveguides by use of plasma-enhanced chemical vapor deposition. This waveguide geometry was designed to support only single transverse mode operation at the 1545 nm laser wavelength as well as the respective pump wavelengths at 976 nm and 1480 nm, for both TE- and TM-polarized modes. The end facets of the optical chip were prepared by dicing.

Optical feedback in the cavity was provided by a surface corrugated Bragg grating, which extended over the entire 1 cm length of the cavity. Using the laser interference lithography setup and etching process discussed in Section 3.2.2, a 150-nm-deep Bragg grating with a period of 488 nm and a duty cycle of 50% was etched into the SiO_2 cladding layer. Figure 5.1 shows a top-view scanning electron microscope (SEM) image of the realized Bragg grating.

To ensure single-longitudinal-mode laser operation, a quarter-wave phase shift was introduced to the DFB cavity. The phase shift was implemented by means of a 2-mm-long

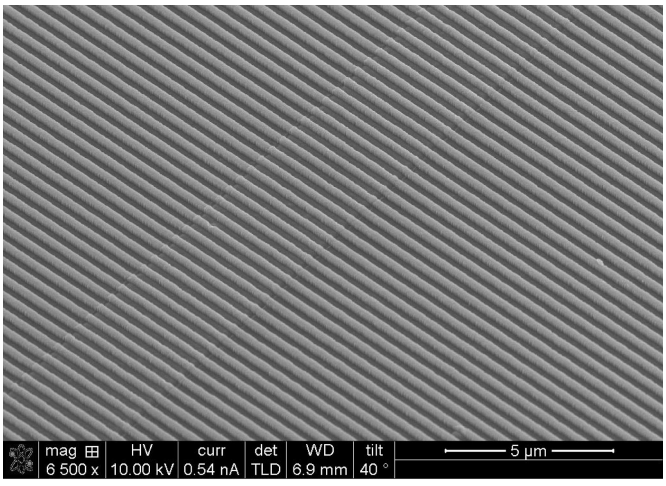

Figure 5.1: Top-view SEM image of the Bragg grating. The 3 μm-wide ridge feature is due to the waveguide below the grating.

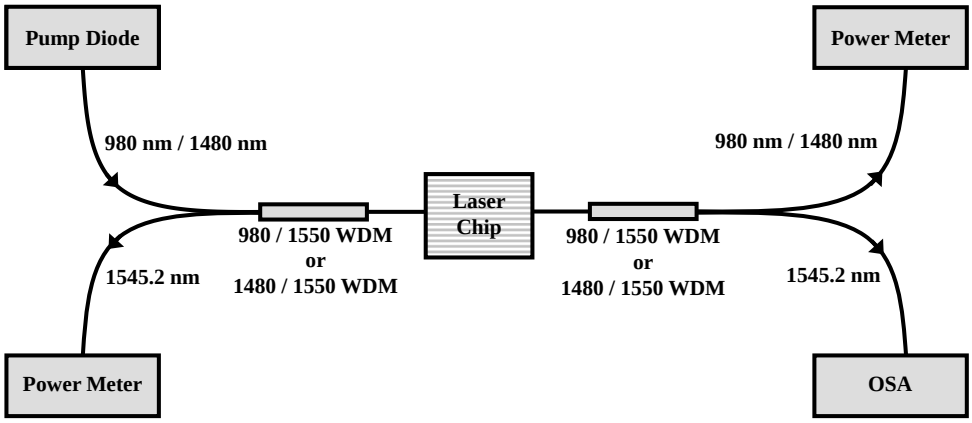

Figure 5.2: Experimental setup used to characterize the Al_2O_3:Er^{3+} DFB laser.

adiabatic sinusoidal tapering of the waveguide width in the center region of the cavity (Section 2.2.4) [96]. Inside the phase-shift region, the waveguide width was increased adiabatically from 3.0 μm to a maximum of 3.45 μm. By placing the phase shift asymmetrically with respect to the center of the cavity, a higher degree of laser outcoupling can be attained in the direction of the shorter end of the cavity. To optimize the laser output power, the phase shift was displaced 1 mm from the center of the cavity. Consequently, by pumping the cavity from the end facet nearer to the phase shift, the majority of the laser power was emitted in the direction of the pumped facet where the gain is highest.

5.1.2 Power Characteristics

The laser was characterized by using respective 976 nm and 1480 nm diode pump lasers, in order to compare the performance. In the experimental setup shown in Figure 5.2, the Al_2O_3:Er^{3+} DFB laser was pumped by a 976 nm laser diode through a 980/1550 nm wavelength division multiplexer (WDM) fiber. The laser emission was collected from the pumped side of the cavity via the 1550 nm port of the WDM, which was connected to a power meter. The input port of a second 980/1550 nm WDM fiber was connected to the unpumped side of the cavity. Its 980 nm port was connected to a second power meter to measure the unabsorbed pump power, while the 1550 nm port was connected to an optical spectrum analyzer (OSA), with a resolution of 0.1 nm, to determine the laser wavelength and to confirm single-longitudinal-mode behavior. In the case of using the 1480 nm pump diode laser, a similar configuration as shown in Figure 5.2 was used, but with the 980/1550 nm WDM fibers being replaced by appropriate 1480/1550 nm WDM fibers. In both cases the WDM fibers were butt coupled to the respective ends of the optical chip by use of index-matching fluid at the fiber-chip interfaces. From insertion loss measurements, a fiber-chip coupling efficiency of 27% was determined for the 1480 nm pump and laser wavelengths, while a coupling efficiency of 35% was calculated for the 976 nm pump, as the waveguide geometry was not particularly optimized for fiber-chip coupling. From mode overlap calculations, it is estimated that the fiber-chip coupling can be improved to $> 90\%$ with optimized horizontal and vertical tapers of the waveguide.

The maximum 976 nm pump power that could be launched into the waveguide with the configuration shown in Figure 5.2 was 96 mW. A slope efficiency of 1.6% versus absorbed pump power was achieved with a maximum laser output power of 0.78 mW for an absorbed pump power of 66 mW; see Figure 5.3(a). Further power scaling was limited by the available pump power. The laser threshold occurred at 17 mW of absorbed pump power. This low threshold is a consequence of the strong light confinement due to the relatively high refractive index of Al_2O_3, which allows for the fabrication of small waveguide cross-sections. The threshold and slope efficiency versus launched pump power are 24 mW and 1.1%, respectively.

A DFB laser model (based on the erbium rate equations described in Section 2.1.3 and the coupled mode equations in Section 2.2.1) was used to simulate the performance of the laser using a discrete quarter-wavelength phase shift and the parameters listed in Table 5.1. The calculated laser output power agrees well with the measured values (Figure 5.3(a)). Note that the estimated background loss at the 976 nm pump wavelength has a rather high value of 4.5 dB/cm. This value was estimated by performing an insertion loss measurement at 976 nm using the calculated fiber-chip coupling of 35%. The high loss is likely due to diffraction at the pump wavelength which has been induced by the grating. Diffraction losses of up to 5.5 dB/cm at a wavelength of 980 nm have been reported for erbium-ytterbium-codoped phosphate glass DFB lasers [133]. Aside from the laser output power, the laser model makes it possible to determine the intra-laser-cavity power (Figure 5.3(b)) and population densities of the respective erbium energy manifolds (Figure 5.3(c)). As seen in Figure 5.3(b), the laser power is strongly confined in the region of the phase shift from where the power decays exponentially into the Bragg gratings on either side of the phase shift. Due to the non-uniform laser power distribution, the subsequent erbium population densities are also highly non-uniform along the length of the laser cavity. In the region of the phase shift, the high laser power in this region induces a high stimulated emission rate, which depopulates the upper laser level ($^4I_{13/2}$) and populates the ground level ($^4I_{15/2}$) (Figure 5.3(c)). As a result, the pump absorption increases in the region of the phase shift due to the increased ground state population, while the amount of optical gain at the laser wavelength is decreased due to the smaller population inversion (Figures 5.3(d) and 5.3(e)).

In comparison to using the 976 nm pump source, the laser has much improved performance when using the 1480 nm pump. With the 1480 nm pump a maximum power of 67 mW could be launched into the waveguide. The laser produced up to 3 mW output power for 10 mW of absorbed pump power with a laser threshold of 2.2 mW and a slope efficiency of 41.3% (Figure 5.4(a)). The threshold and slope efficiency versus launched pump power are 15 mW and 6.2%, respectively. There are three main reasons for the improved laser performance using a 1480 nm pump source. Firstly, there is significantly less grating diffraction of the 1480 nm pump radiation as compared to that at 976 nm. Furthermore, excited state absorption which attenuates the 976 nm pump radiation does not occur at the pump wavelength of 1480 nm [70], and lastly, the relatively long lifetime of the $^4I_{11/2}$ manifold serves as an energy bottleneck when the 976 nm pump is used, since erbium ions are accumulated in this level and, consequently, energy is partially stored

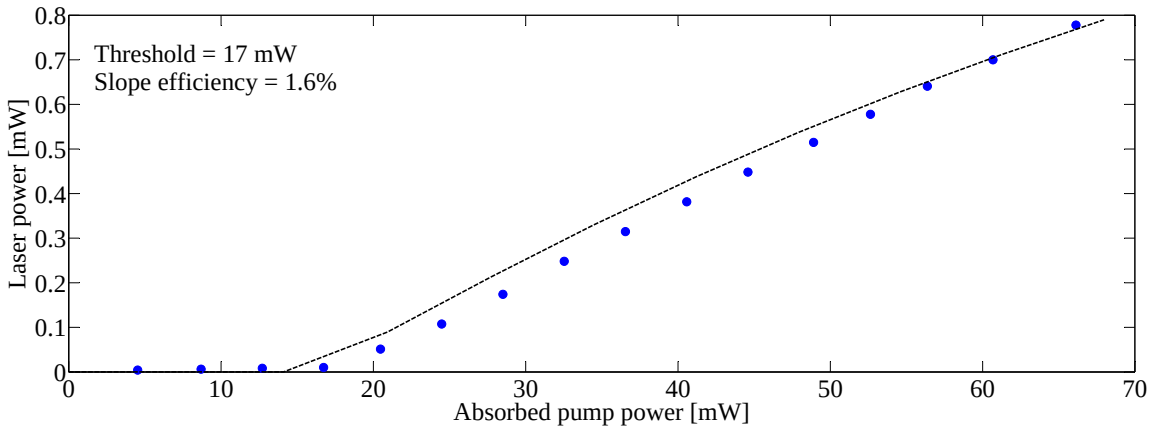

(a) Measured (blue dots) and simulated (dashed line) laser output power as a function of absorbed pump power.

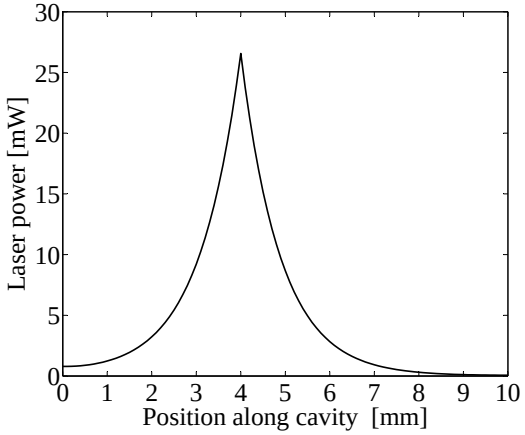

(b) Calculated intra-cavity laser power.

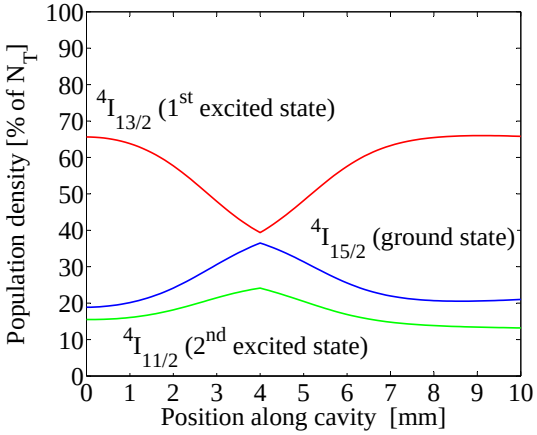

(c) Calculated population densities along the center of the laser mode.

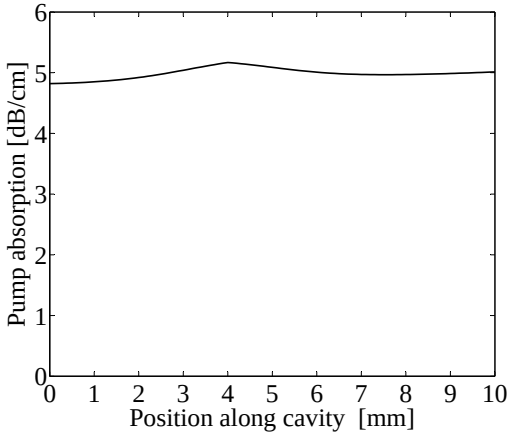

(d) Calculated pump absorption along the cavity.

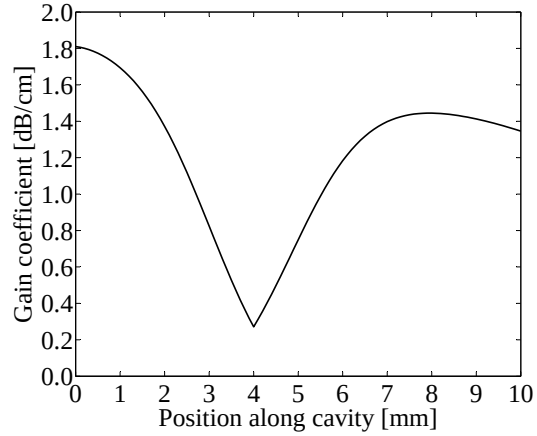

(e) Calculated gain coefficient along the cavity.

Figure 5.3: Power characteristics and population dynamics of the Al_2O_3:Er^{3+} DFB laser using a 976 nm pump. All simulations were performed using parameters listed in Table 5.1.

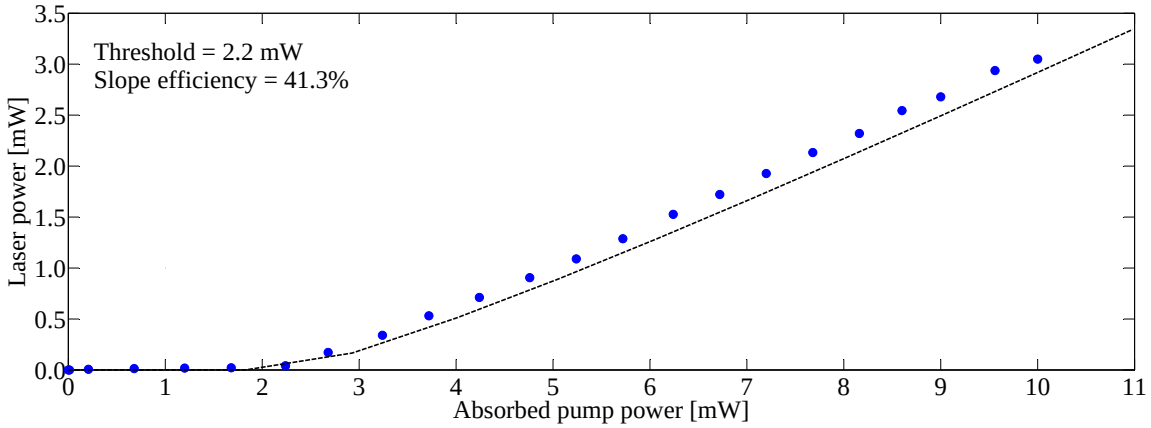

(a) Measured (blue dots) and simulated (dashed line) laser output power as a function of absorbed pump power.

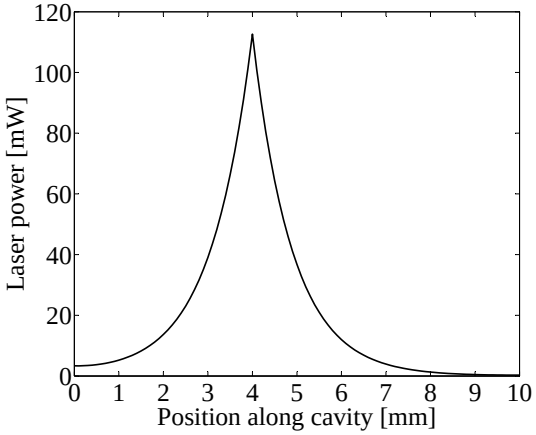

(b) Calculated intra-cavity laser power.

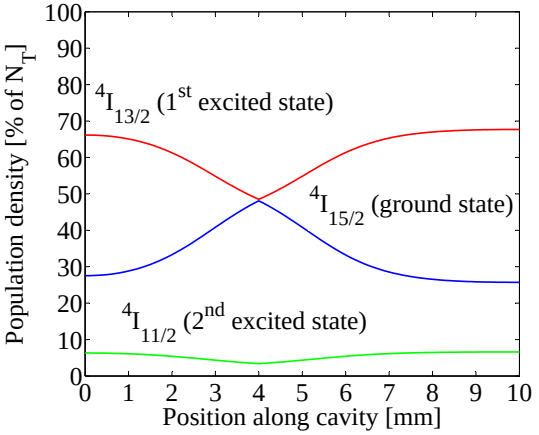

(c) Calculated population densities along the center of the laser mode.

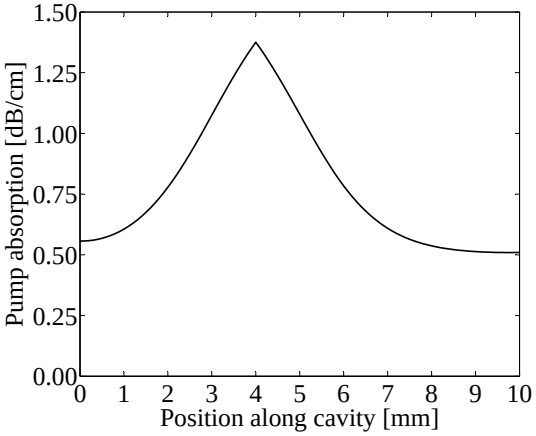

(d) Calculated pump absorption along the cavity.

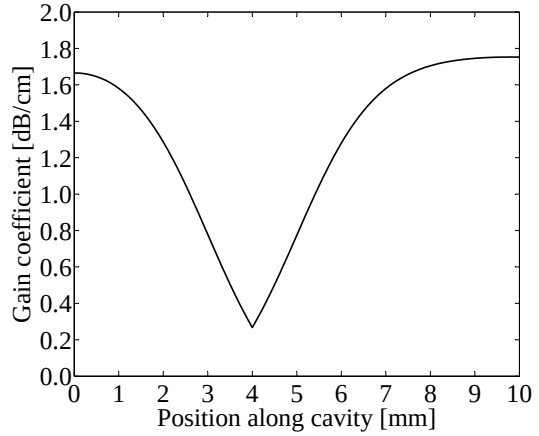

(e) Calculated gain coefficient along the cavity.

Figure 5.4: Power characteristics and population dynamics of the Al_2O_3:Er^{3+} DFB laser using a 1480 nm pump. All simulations were performed using parameters listed in Table 5.1.

Parameter	Value	Reference
Erbium concentration	3.0×10^{20} cm^{-3}	Measured
Absorption cross-section (976 nm)	2.0×10^{-21} cm^2	[93]
Absorption cross-section (1480 nm)	3.3×10^{-21} cm^2	[93]
Absorption cross-section (1545 nm)	3.2×10^{-21} cm^2	[93]
Emission cross-section (976 nm)	2.0×10^{-21} cm^2	[93]
Emission cross-section (1480 nm)	1.1×10^{-21} cm^2	[93]
Emission cross-section (1545 nm)	4.2×10^{-21} cm^2	[93]
Excited state absorption cross-section (976 nm)	0.8×10^{-21} cm^2	[93]
Luminescence lifetime of first excited state	7.6 ms	[70]
Luminescence lifetime of second excited state	60 μs	[70]
Energy transfer upconversion	8.0×10^{-18} cm^3.s^{-1}	[93]
Background loss (976 nm)	4.50 dB/cm	Fitted
Background loss (1480 nm)	0.25 dB/cm	Estimated
Background loss (1545 nm)	0.25 dB/cm	Estimated
Absorbed pump power (976 nm)	66 mW	Measured
Absorbed pump power (1480 nm)	10 mW	Measured
Grating coupling coefficient	5.5 cm^{-1}	Fitted

Table 5.1: Parameters used in Al_2O_3:Er^{3+} DFB laser simulations.

in this level [134]. As erbium ions populate the $^4I_{11/2}$ manifold, stimulated emission and excited state abortion at the wavelength of 976 nm, which are detrimental to the laser performance, become more pronounced. For erbium-doped lithium niobate waveguide lasers, it has been shown that the optimized laser output power for the 1480 nm pump case is expected to be nearly five times higher than for the optimum 980 nm pump case, due to the aforementioned reasons [134]. The calculated population dynamics are shown in Figure 5.4. The calculated laser output power agrees well with the measured values (Figure 5.4(a)). It is interesting to note that in the case of the 976 nm pump, the population density of the $^4I_{11/2}$ manifold is proportional to the population density of the $^4I_{15/2}$ ground manifold due to ground state absorption (Figure 5.3(c)). However, for the 1480 nm pump, the population density of the $^4I_{11/2}$ manifold depends on the population density of the $^4I_{13/2}$ manifold since, in this case, the $^4I_{11/2}$ manifold is populated by upconversion, which occurs from the the $^4I_{13/2}$ manifold (Figure 5.4(c)).

5.1.3 Spectral Characteristics

The laser operated at a wavelength of 1545.2 nm and the emission was TE polarized (Figure 5.5). Characterization of the Bragg gratings showed that the Bragg reflection of the TM mode occurs at $\sim$ 1533 nm. However, the lower grating coupling coefficient for the TM polarization (as discussed in Section 4.2.2) resulted in a grating reflectivity which was too low for this polarization to reach threshold. Although single-longitudinal-mode behavior could be confirmed with the OSA measurement, the linewidth of laser

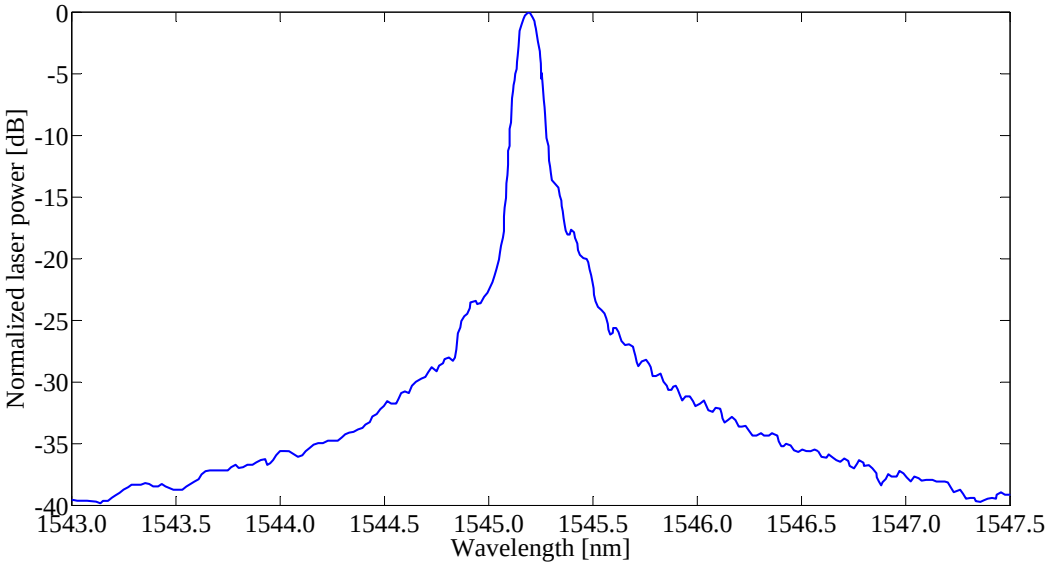

Figure 5.5: Measured Al_2O_3:Er^{3+} DFB laser emission spectrum.

emission was limited by the 0.1 nm resolution. Consequently, a delayed self-heterodyne interferometer [135] was implemented to measure the laser linewidth. The setup was constructed with two 50/50 couplers, an 8.9 km fiber, an 80 MHz acousto-optic modulator (AOM), a photodetector, and an RF spectrum analyzer. The measured radio frequency (RF) beat signal is shown in Figure 5.6. The interference fringes that are observed in the measured RF power spectrum indicate that the coherence length of the DFB laser is considerably longer than the 8.9 km fiber, so that the two optical signals in the respective branches of the interferometer are still highly correlated. The Lorentzian laser linewidth cannot simply be inferred from this measurement because the Lorentzian line shape is distorted by the superimposed interference lobes. Instead, the laser linewidth for such a sub-coherence delay length was extracted by a least-squares fit of the theoretical RF power spectrum (centered at the AOM modulation frequency) given by [136, 137]

$$S_{\mathrm{RF}}(f) = e^{-2\rho}\delta(f) + \frac{\tau_{\mathrm{coh}}}{(1+\pi f\tau_{\mathrm{coh}})^2}\left[1 - e^{-2\rho}\left(\cos(2\pi\rho f\tau_{\mathrm{coh}}) + \frac{\sin(2\pi\rho f\tau_{\mathrm{coh}})}{\pi f\tau_{\mathrm{coh}}}\right)\right] \quad (5.1)$$

where f is the detuning from the AOM modulation frequency, δ the Dirac delta function, τ_{coh} the coherence time of the laser, and $\rho = \tau_0/\tau_{\mathrm{coh}}$ with τ_0 the interferometer delay time ($\tau_0 = 44$ μs in this case). Initial measurements revealed a linewidth of 15 kHz, which was limited by mechanical vibrations in the measurement setup. By mounting the fiber-chip-coupling setup on an air-cushioned platform, the measured linewidth was reduced to a -3 dB Lorentzian laser linewidth of 1.70 kHz, which corresponds to a coherence length of more than 55 km and a Q-factor of 1.14×10^{11}. The fundamental Schawlow-Townes linewidth limit for this laser is estimated to be 0.45 kHz via Equation 2.70. To determine the uncertainty $\delta\nu$ in the laser linewidth, the theoretical RF power spectra corresponding to Lorentzian linewidths of $1.70 \pm \delta\nu$ kHz were calculated, such that they enclose 68% (in analogy to one standard deviation) of the measured data. This method suggests a

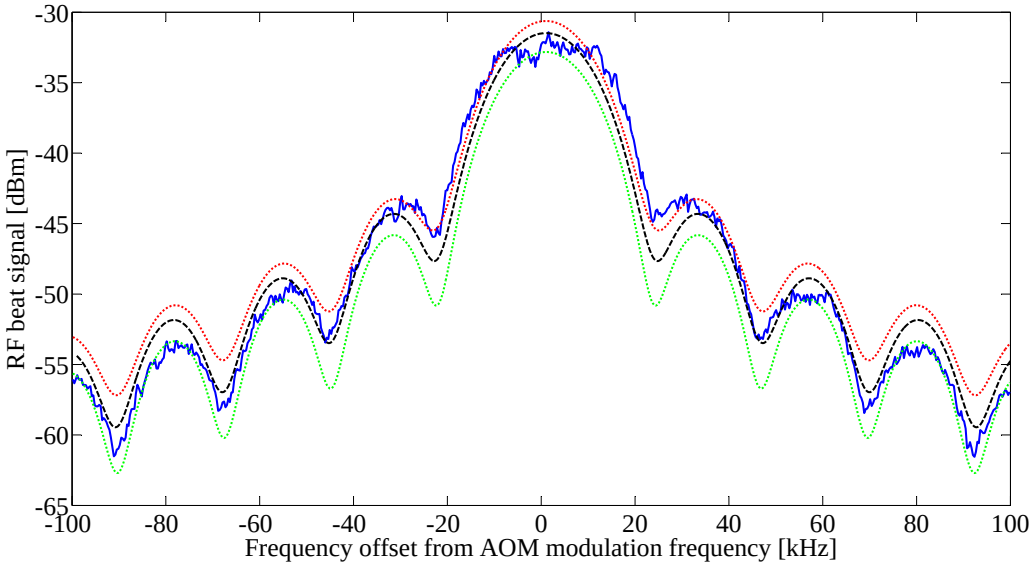

Figure 5.6: Measured RF power spectrum (blue solid curve), along with the best fitted theoretical RF power spectrum of a 1.70 kHz Lorentzian linewidth (dashed black curve). The calculated RF power spectrum curves for Lorentzian linewidths of $1.70 + 0.58$ kHz (red dotted curve) and $1.70 - 0.58$ kHz (green dotted curve) enclose 68% of the measured data.

linewidth uncertainty of $\delta\nu = 0.58$ kHz. The calculated RF power spectra associated with Lorentzian linewidths of $1.70 + 0.58$ kHz and $1.70 - 0.58$ kHz are shown in Figure 5.6. Standard semiconductor DFB lasers typically have linewidths that are a few orders of magnitude larger owing to longitudinal spatial hole burning when carriers are depleted by the nonuniform photon distribution [18]. This induces a refractive-index change, which results in a decreased grating reflectivity and, consequently, linewidth broadening.

Aside from the fundamental laser linewidth being limited by spontaneous emission as described by the generalized Schawlow-Townes relation in Equation 2.70, the linewidth is also limited by fundamental thermal noise, caused by random temperature fluctuations within the laser cavity (Section 2.4.1) [105]. The frequency noise S_ν spectrum resulting from the fundamental temperature fluctuations was calculated using Equation 2.77 and the parameters listed in Table 5.2 (Figure 5.7), with S_ν being the mean square frequency deviation within a 1 Hz band centered at (fluctuation) frequency f and has units of $\text{Hz}^2.\text{Hz}^{-1}$ as discussed in Section 2.4.1. Since fundamental thermal noise generally represents the most significant practical noise limit (even greater than spontaneous emission noise) for compact rare-earth-ion-doped DFB lasers at finite temperature [106, 138], Equations 2.77 and 2.79 provide an easy way to estimate the lower limit for the laser linewidth due to fundamental thermal cavity noise. In this way, the fundamental laser linewidth, limited by fundamental thermal noise, was calculated as a function of the linewidth observation time (Figure 5.8). It is evident that the laser linewidth only becomes limited by fundamental thermal noise fluctuations if the linewidth is observed for periods > 1 ms,

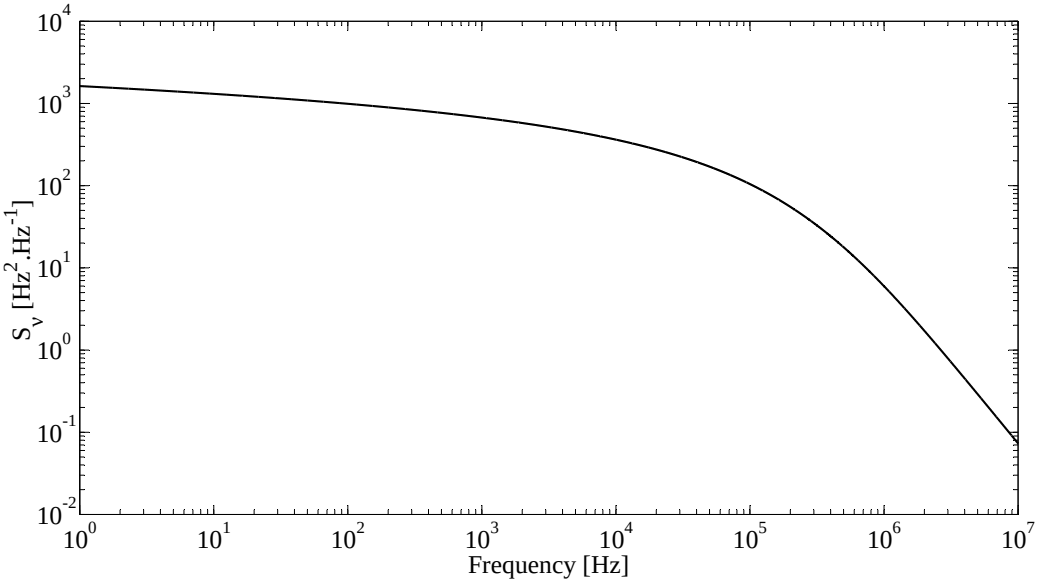

Figure 5.7: Calculated fundamental thermal noise of the Al_2O_3:Er^{3+} DFB laser (determined using the parameters listed in Table 5.2).

and reaches a linewidth limit of 1.2 kHz for an observation time of 1 s. The observation time of 44 μs in the delayed self-heterodyne interferometer is short enough so that there is no fundamental thermal noise contribution to the laser linewidth, implying that the measured laser linewidth is currently limited by other technical noise sources.

This Al_2O_3:Er^{3+} monolithic DFB waveguide laser is, to the best of my knowledge, the first rare-earth-ion-doped DFB laser on a silicon substrate. This result holds many promising opportunities for the integration of such single-frequency lasers with existing waveguide technology on silicon substrates. The low-threshold, single-longitudinal-mode, and single-polarization laser operation, along with the broad emission spectrum of Al_2O_3:Er^{3+} and the wafer-scale deposition process hold great potential for the realization of integrated DFB laser arrays that operate on the International Telecommunication Union Grid throughout the entire telecommunication C band.

Parameter	Value	Reference
Temperature	298.15 K	Estimated
Thermal conductivity	1.37 $W.m^{-1}.K^{-1}$	(Fused silica) [103]
Specific heat capacity	1.67×10^6 $J.m^{-3}.K^{-1}$	(Fused silica) [103]
Thermo-optic coefficient	9.6×10^{-6} K^{-1}	(Fused silica) [103]
Effective cavity length	3.8 mm	Calculated using Equation 2.61
Guided mode radius	1.5 μm	Calculated

Table 5.2: Parameters used in the calculation of the fundamental thermal cavity noise of the Al_2O_3:Er^{3+} DFB laser.

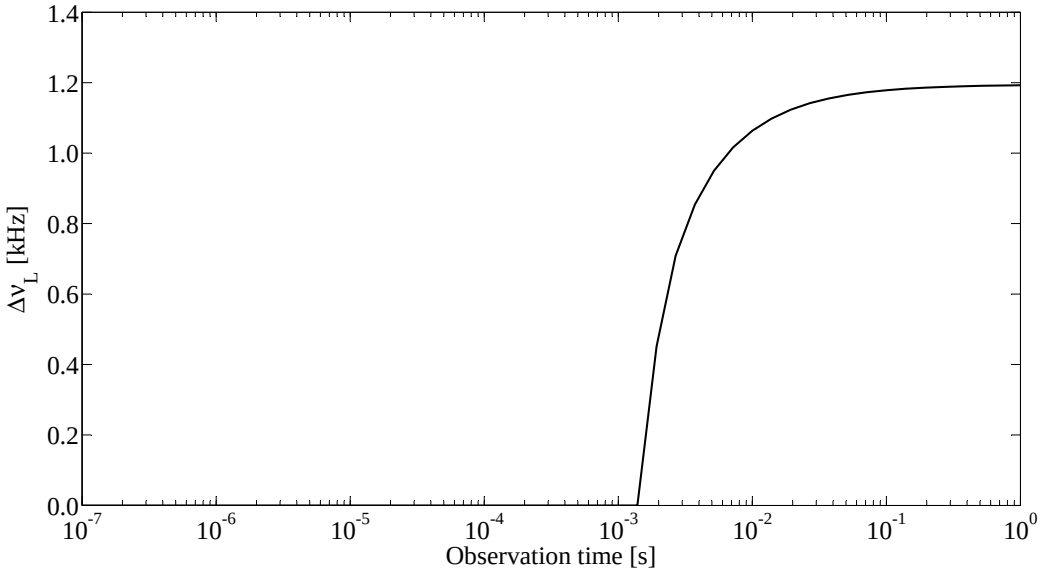

Figure 5.8: Calculated fundamental laser linewidth $\Delta\nu_{\mathrm{L}}$, limited by fundamental thermal noise, as a function of the linewidth observation time.

5.2 Yb^{3+}-Doped Distributed Feedback Laser

Ytterbium-doped waveguides are suitable for realizing compact and highly efficient lasers due to the relatively large absorption and emission cross-sections and high quantum efficiency of ytterbium. Because of the absence of energy-transfer upconversion and excited-state absorption, waveguides can be highly doped with Yb^{3+} ions in order to realize compact devices in which efficient absorption of the pump light is achieved within cavity lengths of a few millimeters. Monolithic, ytterbium-doped channel waveguide lasers have previously been demonstrated in a variety of cavity configurations and materials, which include Fabry-Pérot cavities in YAG [139] and KYW [13], as well as one previous report of a DFB cavity which was realized in phosphate glass [8]. In this section, to the best of my knowledge, the first ytterbium-doped laser in Al_2O_3 is presented, which is also the first ytterbium-doped DFB channel waveguide laser fabricated on a silicon substrate. Above a threshold of 5 mW, the single polarization, single-longitudinal-mode emission at a wavelength of 1022.2 nm produced up to 55 mW of output power, which resulted in a slope efficiency of 67% versus launched pump power.

5.2.1 Fabrication

Using the waveguide layer deposition, photolithography and etching processes described in Section 3.2.1, channel waveguides with a width of 2.5 μm and an etch depth of 90 nm were fabricated in an Al_2O_3:Yb^{3+} layer with an ytterbium concentration of 5.8×10^{20} cm^{-3}. These ridge waveguides supported single-transverse-mode operation at the the 976 nm pump and $\sim$ 1020 nm laser wavelengths. A 490-nm-thick SiO_2 cladding layer was deposited on top of the ridge waveguides using plasma enhanced chemical vapor deposition.

A 1-cm-long surface corrugated Bragg grating was defined with laser interference lithography and etched ~ 120 nm into the SiO_2 cladding as described in Section 3.2.2. Initial optical characterization of the device suggested that the grating coupling coefficient was too weak, after which the SiO_2 layer was etched another 150 nm in order to have the grating structure closer to the guided mode, and hence, creating a larger overlap between the mode and the grating region, resulting in a stronger grating coupling coefficient via Equation 2.57. This second etching step was performed without a resist mask so that both the peaks and troughs of the gratings were etched, resulting in a grating structure with an etch depth of ~ 80 nm and with a period of 316 nm. As with the Al_2O_3:Er^{3+} DFB laser in the previous section, a 2-mm-long distributed quarter-wave phase shift was introduced to the cavity. The distributed phase shift was centered at 4 mm as measured from the pumped end facet, and the waveguide width was tapered to a maximum width of 2.85 μm inside the sinusoidal taper.

5.2.2 Power and Spectral Characteristics

The experimental setup that was used to measure the power characteristics of the laser is shown in Figure 5.9. The laser was optically pumped with a 976 nm laser diode via a 980/1030 nm wavelength division multiplexing (WDM) fiber where a maximum pump power of 91.5 mW was launched into the waveguide. The measured power characteristics of the laser are shown in Figure 5.10(a). The laser emission was collected from the pumped side of the cavity via the WDM fiber and sent to a power meter. The DFB laser threshold occurs at a launched pump power of only 5 mW. The low laser threshold as compared to the threshold performance of a previously realized ytterbium-doped DFB laser in phosphate glass [8] emphasizes the strong light confinement due to the relatively high refractive index of Al_2O_3 as well as the low losses which are present in this waveguide geometry. The maximum laser power emitted from the pumped side of the cavity is more than 55 mW, which results in a slope efficiency of 67% versus launched pump power. No saturation of the output power was observed and further power scaling is only limited by the amount of available pump power. Using the parameters listed in Table 5.3, the laser output power was calculated using the DFB laser model based on the ytterbium rate equations described in Section 2.1.2 and the coupled mode equations in Section 2.2.1. The calculated laser power agrees very well with the measured output power as shown in Figure 5.10(a). The intra-cavity laser power was calculated to reach values as high as 1.3 W inside the region of the phase shift (Figure 5.10(b)). The highly localized laser power depletes the population of the excited state ($^2F_{5/2}$) in the region of the quarter-wavelength phase shift by means of stimulated emission to populate the ground state ($^2F_{7/2}$), as shown in Figure 5.10(c). Consequently, an increase of up to 16 dB in the pump absorption is attained inside the distributed phase shift, due to the highly populated ground state in this region (Figure 5.10(d)). Further, the smaller population inversion inside the phase shift region leads to a reduction in the optical gain which is available at the laser wavelength (Figure 5.10(e)).

The emission spectrum of the laser was measured with an optical spectrum analyzer

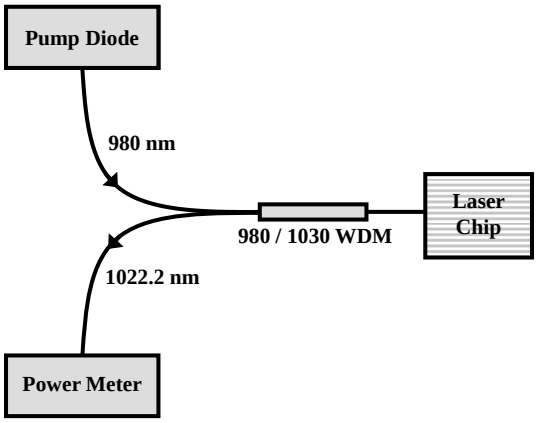

Figure 5.9: Experimental setup used to characterize the Al_2O_3:Yb^{3+} DFB laser.

Parameter	Value	Reference
Ytterbium concentration	5.8×10^{20} cm^{-3}	Estimated
Absorption cross-section (976 nm)	12.70×10^{-21} cm^2	[70]
Absorption cross-section (1022.2 nm)	0.27×10^{-21} cm^2	[70]
Emission cross-section (976 nm)	12.58×10^{-21} cm^2	[70]
Emission cross-section (1022.2nm)	2.87×10^{-21} cm^2	[70]
Luminescence lifetime of the excited state	380 μs	[70]
Background loss (976 nm)	0.25 dB/cm	Estimated
Background loss (1022.2 nm)	0.25 dB/cm	Estimated
Grating coupling coefficient	5.0 cm^{-1}	Fitted

Table 5.3: Parameters used in Al_2O_3:Yb^{3+} DFB and Al_2O_3:Yb^{3+} DBR laser simulations.

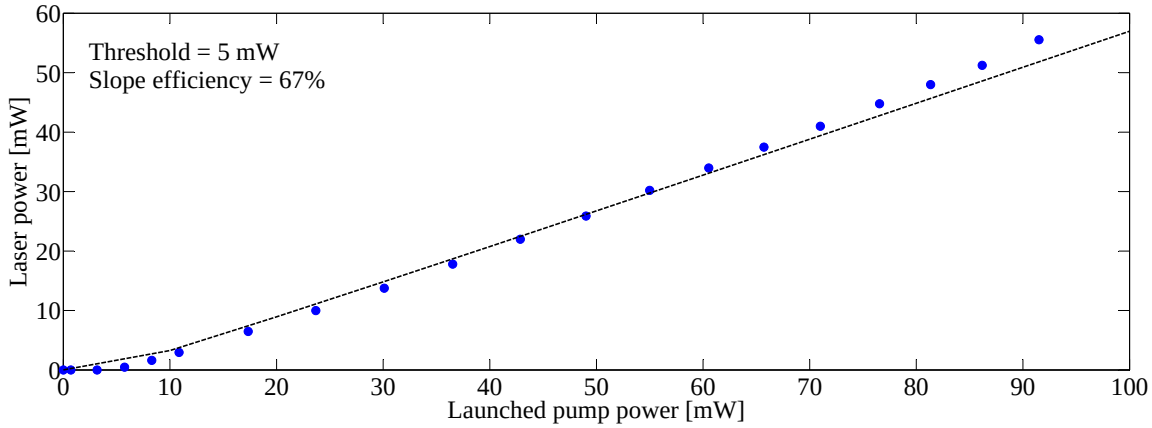

(a) Measured (blue dots) and simulated (dashed line) laser output power as a function of launched pump power.

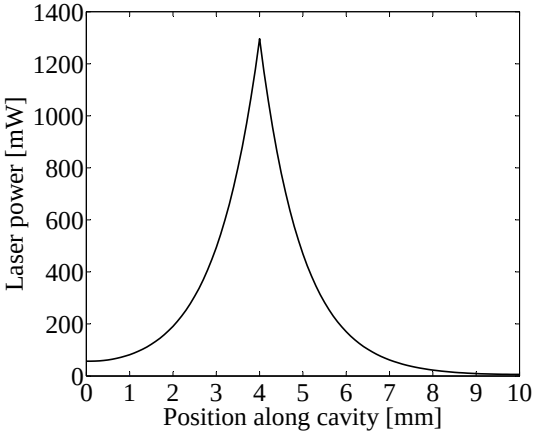

(b) Calculated intra-cavity laser power.

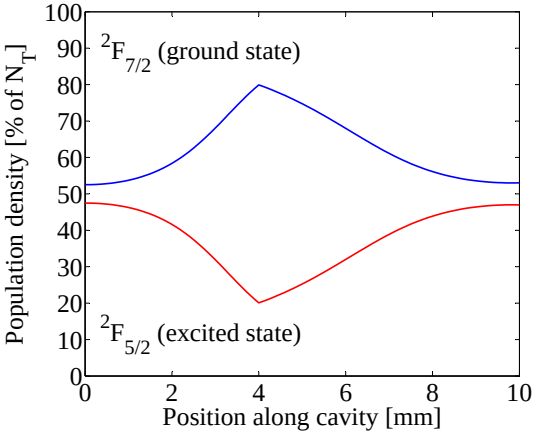

(c) Calculated population densities along the center of the laser mode.

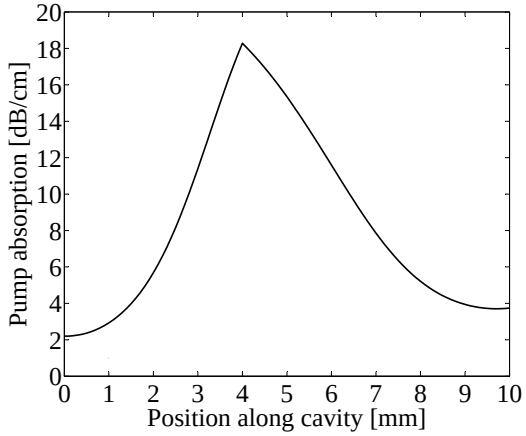

(d) Calculated pump absorption along the cavity.

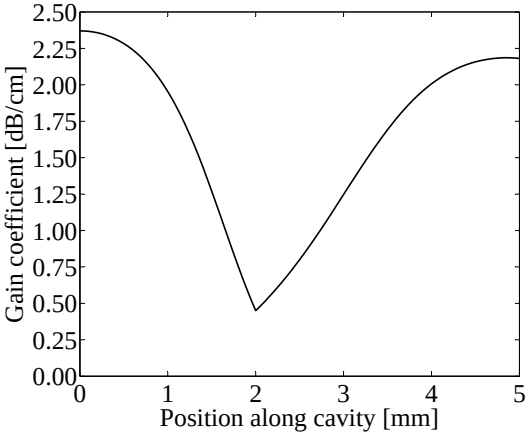

(e) Calculated gain coefficient along the cavity.

Figure 5.10: Power characteristics and population dynamics of the Al_2O_3:Yb^{3+} DFB laser at a launched pump power of 100 mW. All simulations were performed using parameters listed in Table 5.3.

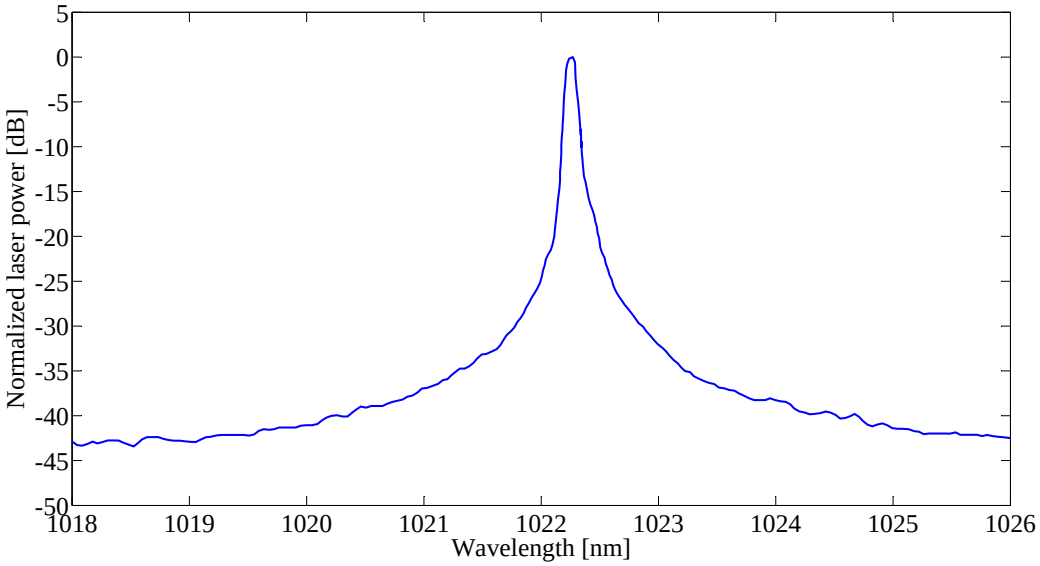

Figure 5.11: Measured Al_2O_3:Yb^{3+} DFB laser emission spectrum.

(OSA) which has a resolution of 0.1 nm. The laser operated at a wavelength of 1022.2 nm and exhibits an emission peak with an optical signal-to-noise ratio of more than 40 dB (see Figure 5.11). Although single-longitudinal-mode behavior could be confirmed with this measurement, the measured linewidth was limited by the resolution of the OSA. Since mode calculations and measurements of passive gratings (Chapter 4) showed that the grating coupling coefficient for the TM mode is significantly weaker compared to the TE polarization (so that the reflectivity is not sufficient to reach threshold), it was concluded that the laser emission was TE polarized at all times.

This laser shows more than one order-of-magnitude improvement in output power as compared to the demonstrated 1.7 kHz linewidth of the Al_2O_3:Er^{3+} channel waveguide DFB laser in the previous section. Since the fundamental laser linewidth is inversely proportional to the laser output power (Equation 2.70), the linewidth according to the generalized Schawlow-Townes limit is estimated to be 30 Hz. However, the laser wavelength of 1022.2 nm makes it rather difficult to characterize the linewidth, since the standard optical modulators and long fiber delays which are used in a delayed self-heterodyne interferometer are designed to operate at typical telecommunication wavelengths around 1.5 μm.

The high output power and high efficiency as well as the absorption coefficient of water which is about 50 times smaller at a wavelength of $\sim$ 1020 nm compared to erbium emission wavelengths around $\sim$ 1550 nm [35], make such monolithic Al_2O_3:Yb^{3+} waveguide lasers ideal for biosensing applications, as will be shown in Chapter 6.

5.3 Yb^{3+}-Doped Distributed Bragg Reflector Laser

Aside from the Al_2O_3:Yb^{3+} DFB laser which has been described in the previous section, in this section a monolithic Al_2O_3:Yb^{3+} DBR laser is demonstrated. Although a DFB cavity configuration is considered to be more suitable for single-longitudinal-mode laser operation, the realization of the DBR laser emphasizes the versatility of this technology.

The 2.5-μm-wide ridge waveguide and surface corrugated Bragg grating were fabricated as described in Section 5.2.1. The realized DBR cavity consisted of two integrated Bragg reflectors with a length of 3.75 mm on either side of a 2.5-mm-long, grating-free waveguide region, to form a total DBR cavity length of 1 cm.

Based on coupled-mode theory (Section 2.2.2), where the grating reflectivity at the Bragg wavelength is given by Equation 2.60a, each of the Bragg reflectors was designed to have a grating coupling coefficient $\kappa = 6$ cm^{-1}, which yields a reflectivity of 96% with a 48 GHz FWHM reflection bandwidth. Although the interaction between the guided laser mode and the grating region is very weak per unit length ($\sim 0.1\%$ transversal overlap), the Bragg reflectors are sufficiently long to accumulate this high reflectivity.

The experimental setup for characterization of the DBR waveguide laser performance is shown in Figure 5.12. Two 980/1030 nm wavelength division multiplexing (WDM) fibers were butt-coupled to the respective waveguide end facets of the optical chip by use of an index-matching fluid to match the effective refractive index of the waveguide mode. With this configuration, up to 92 mW of diode pump power could be launched into the channel waveguide via the 976 nm port of one of the WDM fibers. The laser emission was collected from both sides of the cavity through the 1030 nm ports of the respective WDM fibers, each of which was connected to a separate power meter. In order to investigate the emission spectrum of the laser, the power meter which was connected to the WDM on the pumped side of the cavity was interchanged by an optical spectrum analyzer with a resolution of 0.1 nm.

The measured power characteristics of the laser is shown in Figure 5.13(a). DBR laser oscillation commenced at 10 mW launched pump power. The laser delivered a maximum

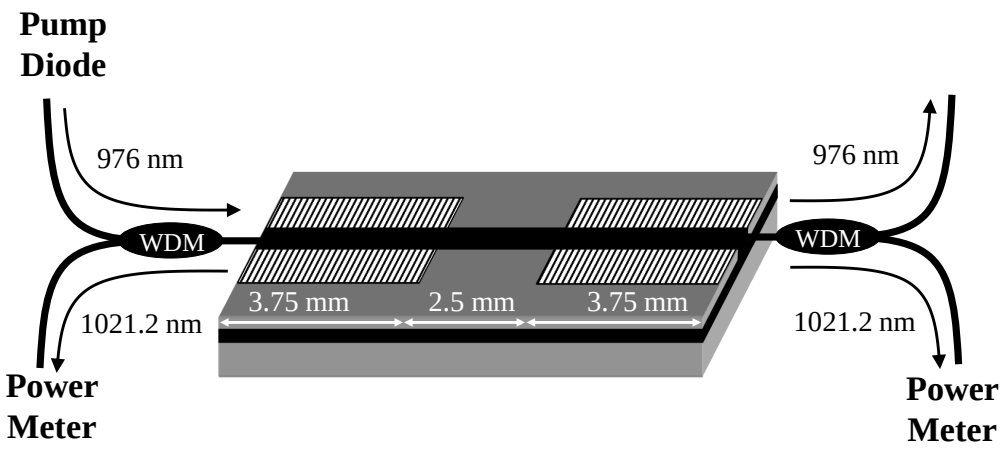

Figure 5.12: Experimental setup used to characterize the Al_2O_3:Yb^{3+} DBR laser.

bidirectional output power of 47 mW at 92 mW of launched pump power, resulting in a slope efficiency of 67% with respect to launched pump power. Since the DBR cavity was fabricated to be symmetric, one would expect nearly equal powers emanating from each side of the cavity. However, the laser power measured on the unpumped side of the cavity was 1.4 times higher than that measured on the pumped side. This is likely caused by a slightly higher outcoupling of the Bragg reflector on the unpumped side of the cavity and is consistent with a reflectivity difference of $\sim 2\%$ between the two respective ends of the cavity according to the theory of Rigrod given by [140, 141]

$$\frac{P_2}{P_1} = \frac{1 - R_2}{1 - R_1}\sqrt{\frac{R_1}{R_2}} \tag{5.2}$$

where P_1 and P_2 are the output powers at the pumped and unpumped ends of the cavity, respectively, while R_1 and R_2 are the respective reflectivities of the Bragg reflectors on the pumped and unpumped sides of the cavity.

The laser output power was calculated using the ytterbium rate equations described in Section 2.1.2 and the coupled mode equations in Section 2.2.1. In order to achieve the 1.4 times higher output power on the unpumped side, a good fit was obtained by using a grating coupling coefficient of 5 cm^{-1} for the Bragg reflector on the pumped side, and 4.55 cm^{-1} for the Bragg reflector on the unpumped side. Although the calculated slope efficiencies agree very well with the measured values, the calculated laser threshold is about 5 mW lower than the measured value (Figure 5.13(a)). From the calculated intra-cavity laser power it can be seen that the region between the two Bragg reflectors has a constant power of $\sim$ 500 mW, while the laser power decays exponentially into each of the grating regions (Figure 5.13(b)). The localized laser power in-between the two Bragg reflectors depletes the population of the excited state ($^2F_{5/2}$) via stimulated emission to populate the ground state ($^2F_{7/2}$), as shown in Figure 5.13(c). As with the Al_2O_3:Yb^{3+} DFB laser, the non-uniform laser power distribution also affects the pump absorption and gain coefficient significantly (Figures 5.10(d) and 5.10(e)).

The measured laser emission spectrum at the maximum output power is shown in Figure 5.14. The laser operated at a wavelength of 1021.2 nm with a measured linewidth which was limited by the 0.1 nm resolution of the optical spectrum analyzer. The emission peak had a signal-to-noise ratio of more than 45 dB. Characterization of passive Bragg gratings in undoped Al_2O_3 with a similar geometry showed that the measured grating coupling coefficient for the TM mode is approximately 60% lower than that of the TE mode, which results in a reflectivity of less than 50% for the TM polarization. With such a high outcoupling it is not possible to reach threshold, which led us to conclude that the laser was operating TE-polarized at all times. Because of the distributed nature of light reflection in a Bragg reflector, the incident light penetrates a finite depth into the grating. The penetration depth at the Bragg wavelength is given by Equation 2.61. Since light penetrates into the Bragg reflectors on either side of the cavity, an effective cavity length of 4.13 mm is estimated (assuming $\kappa = 6$ cm^{-1}), which implies a cavity free spectral range of about 22.4 GHz. This suggests that up to three longitudinal modes could potentially exist within the estimated Bragg reflector bandwidth of 48 GHz (Figure 5.15). In order to

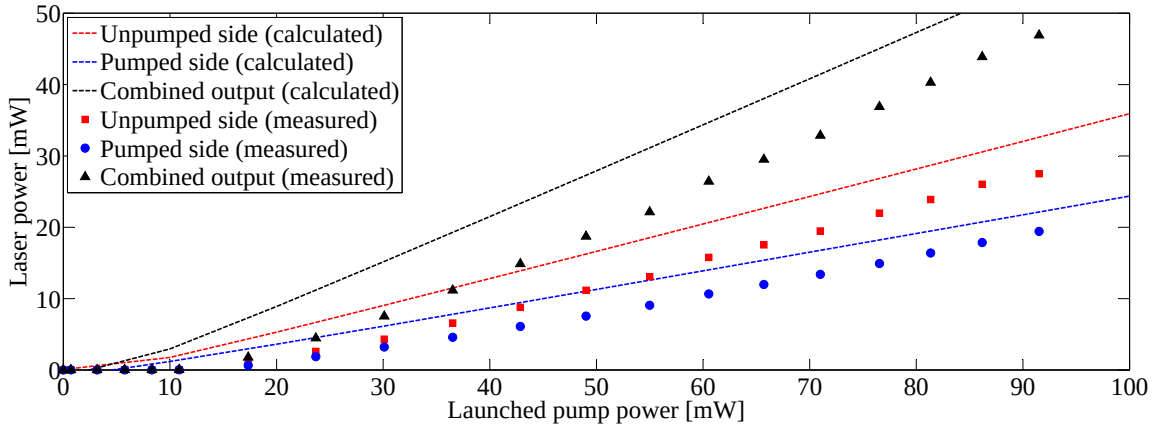

(a) Measured and simulated laser output power as a function of launched pump power.

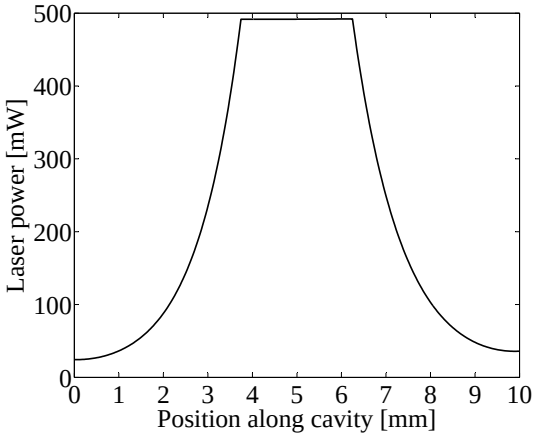

(b) Calculated intra-cavity laser power.

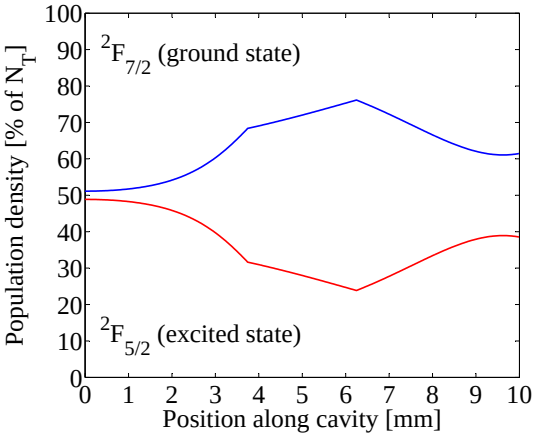

(c) Calculated population densities along the center of the laser mode.

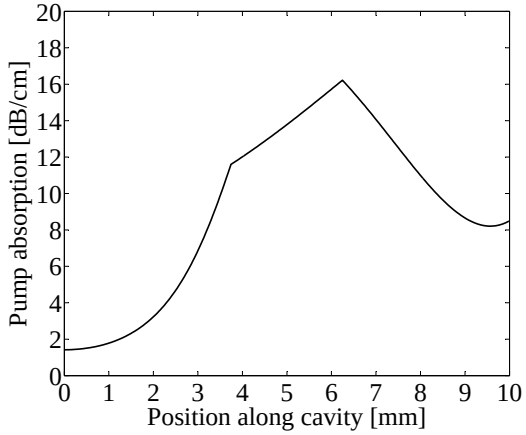

(d) Calculated pump absorption along the cavity.

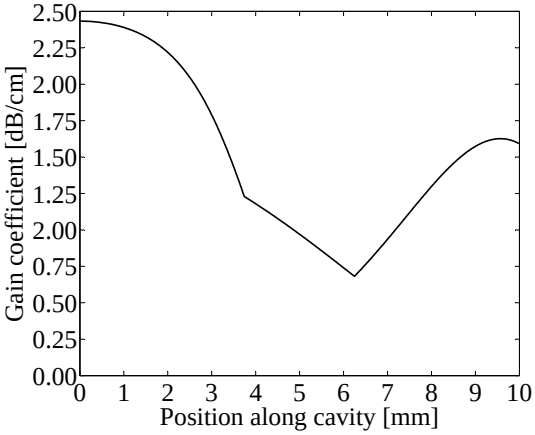

(e) Calculated gain coefficient along the cavity.

Figure 5.13: Power characteristics and population dynamics of the Al_2O_3:Yb^{3+} DBR laser at a launched pump power of 100 mW. All simulations were performed using parameters listed in Table 5.3.

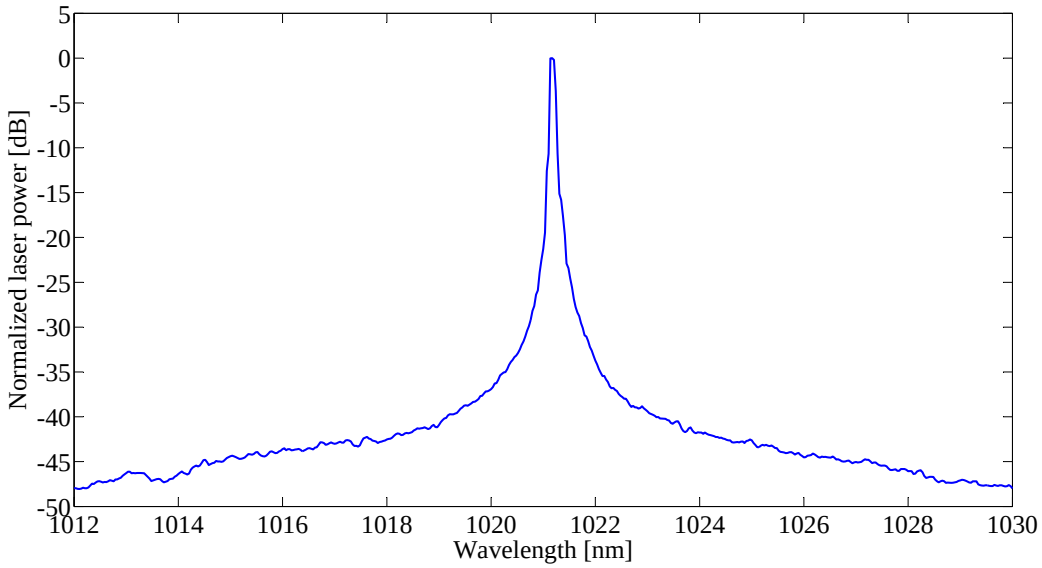

Figure 5.14: Measured Al_2O_3:Yb^{3+} DBR laser emission spectrum.

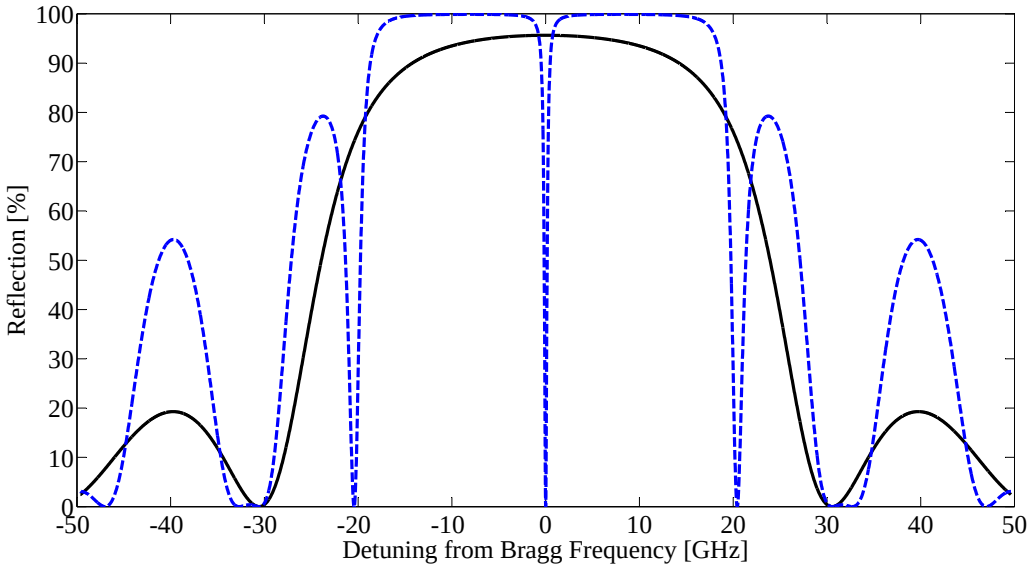

Figure 5.15: Calculated reflection spectrum of a single Bragg reflector (solid black curve) along with the reflection spectrum of the entire DBR cavity (dashed blue curve) showing the three potential longitudinal modes (assuming $\kappa = 6$ cm^{-1}).

confirm single-longitudinal-mode laser operation, the laser output from the pumped side of the cavity was sent to a 40 GHz photodetector which was connected to a 26.5 GHz RF spectrum analyzer. With such a measurement, it would have been possible to observe a beat signal at 22.4 GHz as a result of the presence of two longitudinal modes. However, the absence of any such beat signal was evidence that the laser was indeed operating on a single longitudinal mode. The single-longitudinal-mode operation is most likely due to one of the three modes being located in the center of the reflection bandwidth where the reflectivity is maximum, which results in a low threshold, while the two other modes are located close to the reflection band edge. By use of a rate-equation model, it was confirmed that the reflectivities near the edges of the reflection band are indeed insufficient for these modes to reach laser threshold. To my knowledge, this device represents the first DBR waveguide laser in Al_2O_3.

6 Applications

Where the previous chapter was about the development and characterization of monolithic single-longitudinal-mode Al_2O_3 waveguide lasers, this chapter concerns the realization of monolithic dual-wavelength, or dual-longitudinal-mode, Al_2O_3 waveguide lasers. The main purpose for using dual-wavelength lasers in this work, is to create a stable electrical beat signal at the output of a photodetector, with the frequency of the beat signal corresponding to the wavelength spacing of the two optical waves. Here, a dual-wavelength laser is used to create microwave signals, or millimeter-wave signals, for use in phase array antennas. The second application of the dual-wavelength DFB laser design is the realization of a novel and highly sensitive intra-laser-cavity integrated optical particle sensor which, as a proof of principle, is able to detect single borosilicate glass microspheres with diameters as small as 1 μm.

6.1 Radio Frequency Generation

An advantage of using a dual-wavelength laser to generate microwave signals is the fact that the system does not require an additional microwave reference source, like with other photonic microwave generation techniques which rely on the external modulation of the optical signal. Free-running dual-wavelength lasers for the purpose of microwave-signal generation have been demonstrated in various configurations, including rare-earth-ion-doped fibers [142–145], as well as semiconductor-based devices [146]. However, there are several drawbacks associated with these previously demonstrated dual-wavelength lasers. Fiber lasers often require long cavities and cannot be integrated monolithically with existing silicon-compatible photonic waveguide platforms, such as silicon-on-insulator waveguides. The intrinsic linewidth of free-running semiconductor lasers is typically a few

MHz, which results in microwave signals that are inadequate for use in microwave systems where high-purity, very-narrow-line-shape signals are required [21].

6.1.1 Operation Principle

The operation of the dual-wavelength cavity is based on two localized quarter-wavelength phase shifts in a DFB cavity [147]. When two phase shifts are induced in a uniform waveguide Bragg grating, two resonance peaks appear in the transmission stop-band of the device. The two resonances share a common cavity which consists of both phase-shift regions, and the wavelength spacing between these resonances depends on the spatial separation and values of the respective phase shifts. For two discrete quarter-wavelength phase shifts the frequency spacing between two resonances is given by [148]

$$\Delta\nu = \frac{c}{8n_{\text{eff}}\Delta L} \tag{6.1}$$

where c is the speed of light in vacuum, n_{eff} the effective refractive index of the guided mode, and ΔL the distance between the two phase shifts.

The operation principle can be clearly illustrated by first considering the spectral response of a passive dual-phase-shift DFB cavity. Making use of the waveguide and grating fabrication processes described in Section 4.2.1, a 10-mm-long passive DFB cavity with two 2-mm-long distributed quarter-wavelength phase shifts were fabricated, with the phase shifts centered at 3.5 mm and 5.5 mm (as measured from the end-facet from where the light is launched).

Transmission spectra of the cavity were measured by coupling linearly TE-polarized light from a tunable laser source (Agilent 8164B) with a 0.2 pm resolution into the waveguide via a polarization-maintaining (PM) fiber in an end-fire setup. Light transmitted through the waveguide was collected by an ultra-high numerical aperture fiber (NA = 0.35) and sent to a power meter. Index-matching fluid was used to eliminate Fresnel reflections at the fiber-chip interfaces. Due to the two quarter-wavelength phase shifts, there are two resonances which can be observed inside the stopband of the grating (Figure 6.1). Since the two longitudinal modes share the same cavity, the relative fluctuations between the two resonant wavelengths are low, since they experience the same environmental and temperature perturbations. Consequently, much improved temperature stability is expected for the wavelength difference (between the two longitudinal modes), as compared to the temperature stability of the individual longitudinal modes.

By mounting the optical chip on a copper mount which was in contact with a temperature controlled Peltier device, the temperature of the DFB cavity could be tuned with an accuracy of 0.1°C. Using this setup, the temperature was varied from 20°C to 35°C with a 1°C increment, while the TE-polarized transmission was measured for each temperature. Figure 6.2 shows the temperature dependence of the two resonances inside the grating stopband. While each of the individual resonances varies with $\sim$ 1.97 GHz/°C, the frequency difference between the two resonances varies with 1.3 MHz/°C, resulting in a $\sim$1500-fold improvement in the temperature stability.

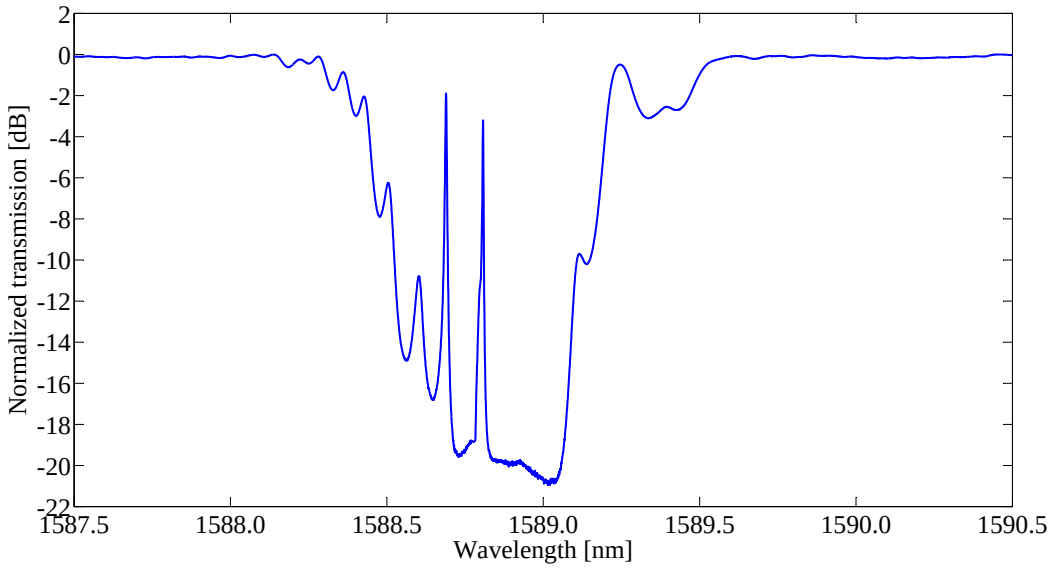

Figure 6.1: Measured TE polarized transmission spectrum in a 10-mm-long DFB cavity with two distributed quarter-wavelength phase shifts located at 3.5 mm and 5.5 mm (as measured from the end-facet from where the light is launched).

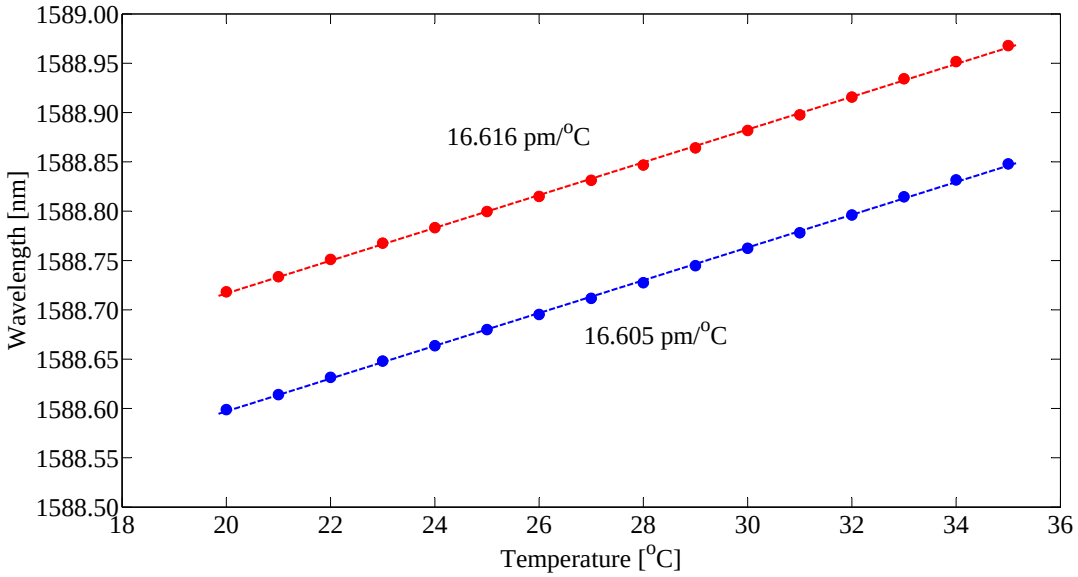

Figure 6.2: Temperature dependence of the two resonances in the TE polarized transmission spectra in a 10-mm-long DFB cavity with two distributed quarter-wavelength phase shifts located at 3.5 mm and 5.5 mm (as measured from the end-facet from where the light is launched).

When both phase shifts are varied symmetrically from a quarter-wavelength phase-shift $\pi/2$, such that one has a value of $\pi/2 - \Delta\theta$ and the other $\pi/2 + \Delta\theta$, then the two resonant wavelengths separate symmetrically from each other with respect to the Bragg wavelength, while they remain equivalent in terms of their amplitude and line width [147]. In other words, the value of $\Delta\theta$ can be used to increase the frequency spacing between the two resonances as compared to the frequency spacing given by Equation 6.1. This is clearly illustrated in Figures 6.3(a) to 6.3(d) where the measured TE-polarized transmission spectra of various dual-phase-shift DFB cavities with different values of $\Delta\theta$ are shown. The frequency spacing $\Delta\nu$ has a linear dependence on the $\Delta\theta$, which would allow $\Delta\nu$ to be tuned over a range of approximately 20 GHz for a single cavity. Such dynamic tuning of $\Delta\theta$ can be obtained by making use of thermo-optic tuning via electrodes for instance. Note that it is not only the spectral characteristics of the device which change as $\Delta\theta$ is varied, but also the spatial distribution of the resonances. As the value of the phase detuning $\Delta\theta$ increases, the shorter wavelength oscillates more around the $\pi/2 - \Delta\theta$ phase shift, while the longer wavelength concentrates around the $\pi/2 + \Delta\theta$ phase shift, instead of both wavelengths concentrating equally around both phase-shift regions simultaneously, as in the case of $\Delta\theta = 0$. This dual-phase-shift dual-wavelength DFB cavity approach has been used to realize a dual-wavelength laser in Al_2O_3:Yb^{3+}.

6.1.2 Fabrication

Using the fabrication processes discussed in Section 5.2.1, 2.5-μm-wide waveguides with 10-mm-long Bragg gratings were fabricated in an Al_2O_3:Yb^{3+} waveguide layer with an ytterbium concentration of 5.8×10^{20} cm^{-3}. In order to induce the two required phase shifts in the waveguide Bragg grating in each of the ten cavities, two sections with 2-mm-long adiabatic sinusoidal widening of the waveguide width were fabricated. The two phase shifts in each cavity were centered at 3.5 mm and 5.5 mm (as measured from the pumped end facet) and had values of $\pi/2 - \Delta\theta$ and $\pi/2 + \Delta\theta$, respectively, where the value of $\Delta\theta$ was systematically increased from 0.0π to 0.34π for each subsequent cavity.

6.1.3 Power and Spectral Characteristics

In order to characterize the various laser cavities, a 980/1030 nm wavelength-division-multiplexing (WDM) fiber was butt-coupled to the optical chip by use of an index-matching fluid. The 976 nm diode pump light was launched into the waveguides via the 980 nm port of the WDM fiber, while the laser emission was collected through the 1030 nm port, which also contained an isolator to prevent optical back-reflections into the laser cavities. The laser emission was then sent to either an optical spectrum analyzer (OSA), a power meter, or a 40 GHz photodetector (PD) connected to an electrical spectrum analyzer (ESA).

By measuring the laser emission of each cavity with the PD, it was confirmed that eight of the ten cavities produced a microwave beat signal. It is not clear why the particular cavity with $\Delta\theta = 0\pi$ did not produce a beat signal. However, the cavity with $\Delta\theta = 0.19\pi$,

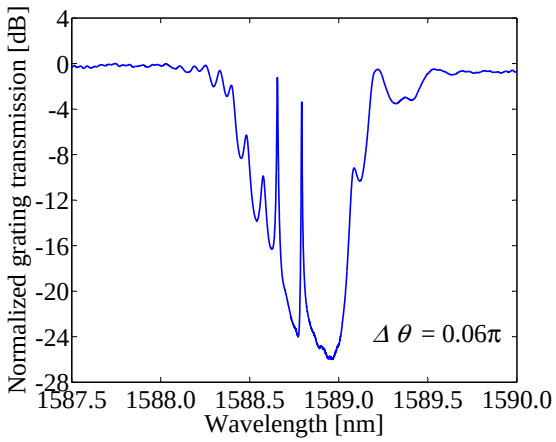

(a) $\Delta\theta = 0.06\pi$

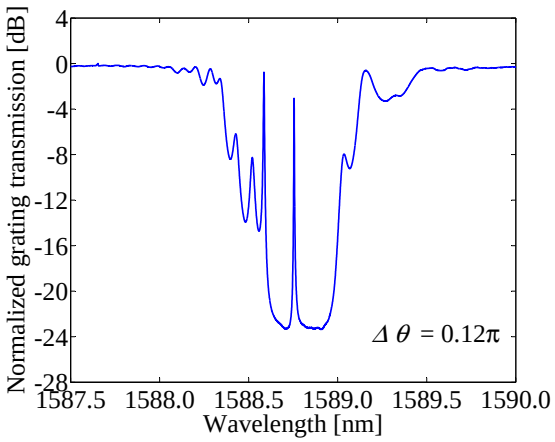

(b) $\Delta\theta = 0.12\pi$

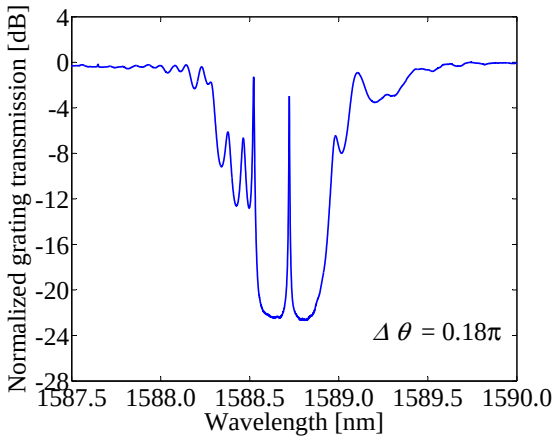

(c) $\Delta\theta = 0.18\pi$

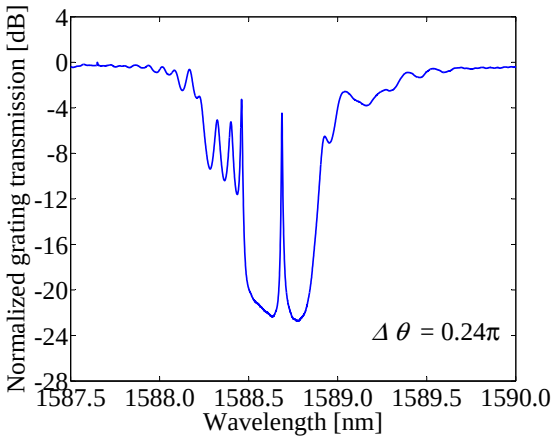

(d) $\Delta\theta = 0.24\pi$

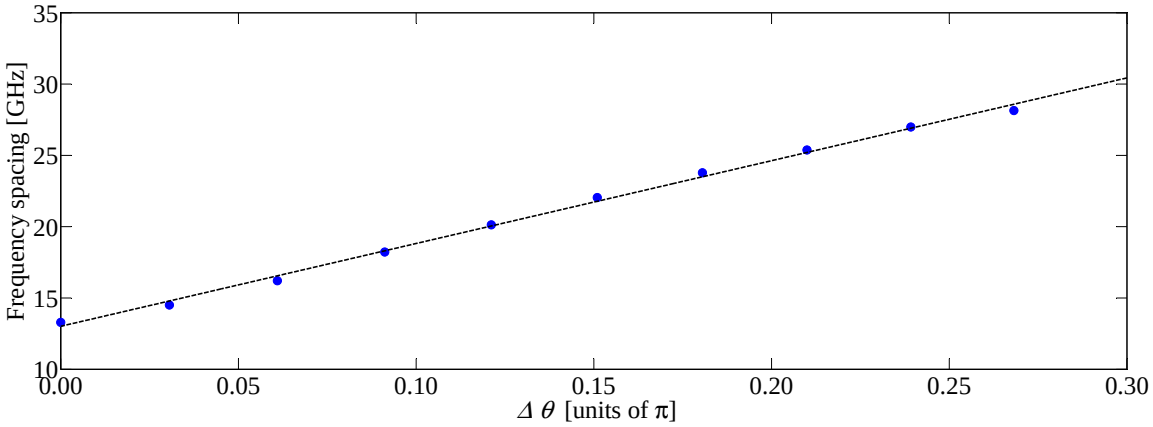

(e) Measured frequency spacing (blue dots) between the two narrowband resonances inside the grating stopband as a function of $\Delta\theta$. The black dashed line represents a linear fit to the data.

Figure 6.3: TE-polarized transmission characteristics of various dual-phase-shift DFB cavities.

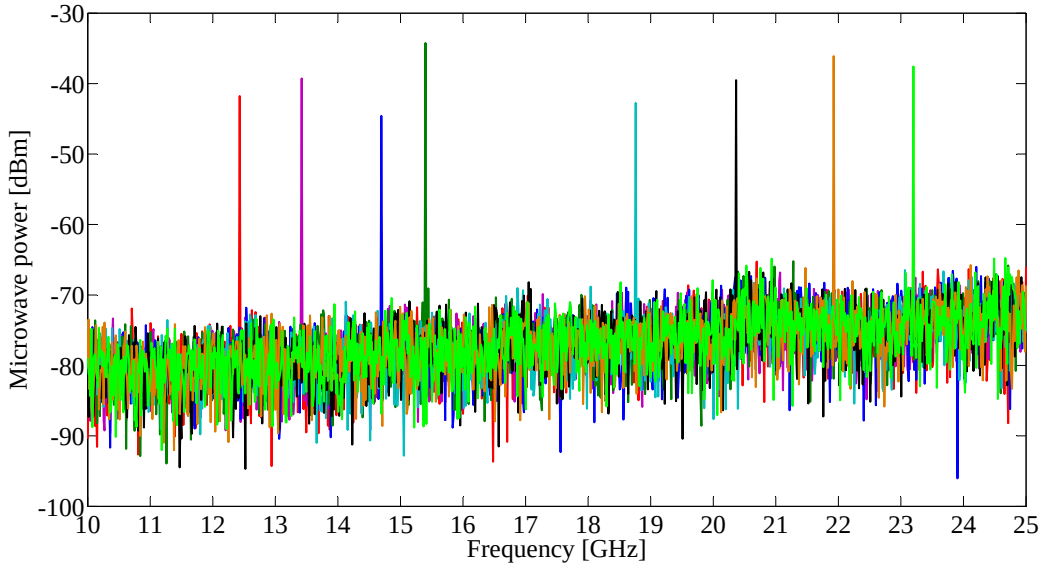

Figure 6.4: Measured microwave beat signals of dual-phase shift cavities with different values of $\Delta\theta$.

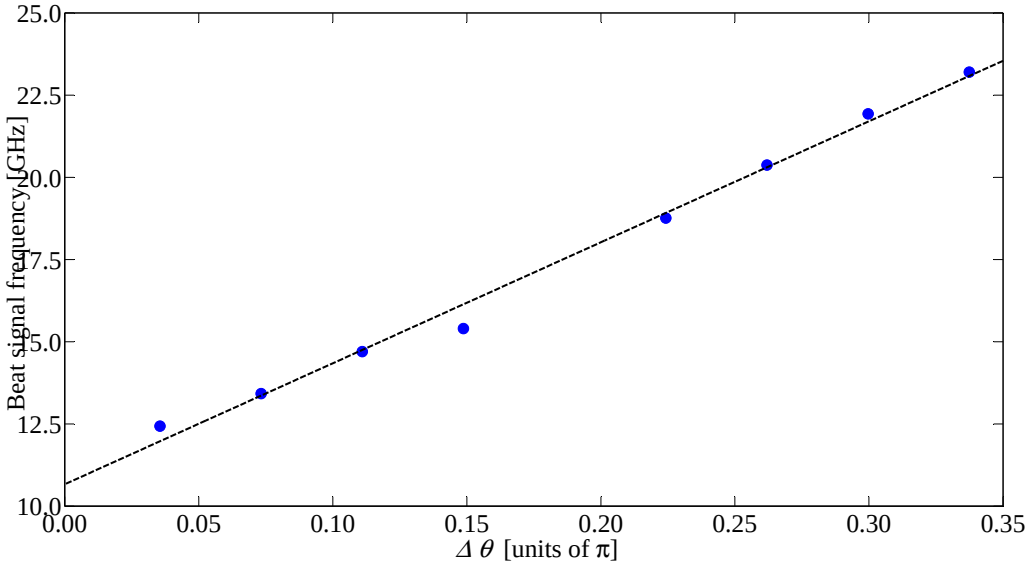

Figure 6.5: Measured microwave beat frequency (blue dots) as a function of $\Delta\theta$. The dashed black line represents a linear fit to the data.

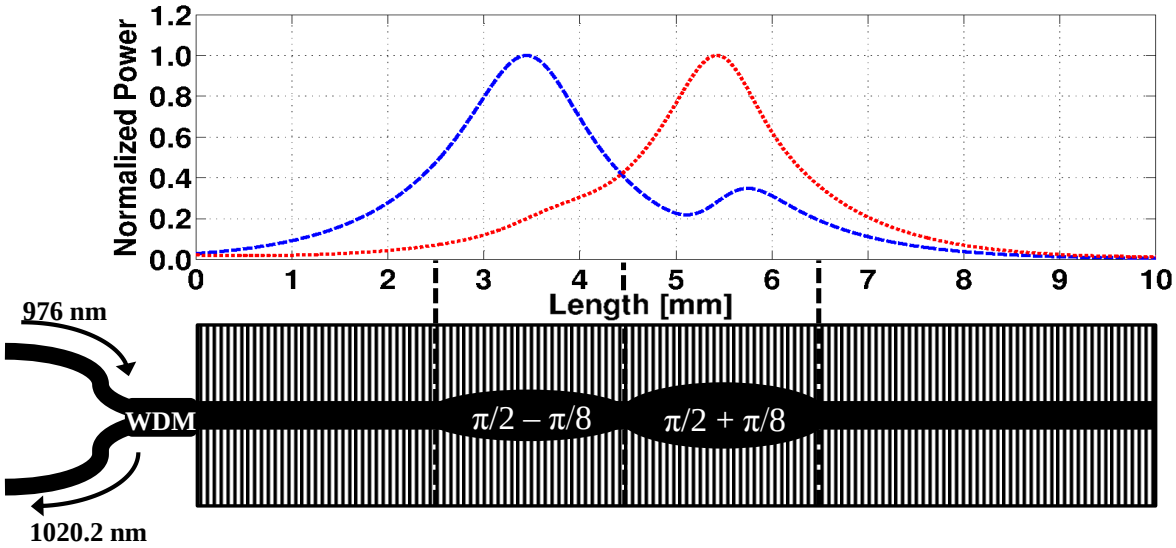

Figure 6.6: Schematic of the dual-wavelength Al_2O_3:Yb^{3+} DFB cavity, along with the calculated longitudinal field distribution of the two respective laser wavelengths.

which did also not produce a microwave beat signal, had a damaged end-facet hindering the coupling of pump power and most likely explains why this particular cavity did not operate. The measured microwave beat signals of the remaining eight cavities are shown in Figure 6.4, and range between 12.43 GHz and 23.2 GHz. As expected from the passive cavity characterization in Section 6.1.1, the microwave beat frequency increases linearly as a function of $\Delta\theta$ (Figure 6.5).

Further characterization was performed on the particular cavity which produced the strongest microwave beat frequency. This cavity had a value of $\Delta\theta \approx \pi/8$, and a schematic of the laser cavity, along with the calculated longitudinal field distribution of the two laser wavelengths as calculated with the transfer-matrix method (Section 2.2.1), is shown in Figure 6.6. Laser oscillation commenced at a launched pump power of 5 mW, after which the laser output power increased linearly with a slope efficiency of 41% to produce a pump-power-limited output power of 28 mW for a launched pump power of 75 mW (Figure 6.7). The laser emission spectrum was centered at 1020.2 nm, however the two individual laser emission peaks could not be resolved due to the limited 0.1 nm resolution of the OSA. In order to confirm that the laser was operating on two longitudinal modes, the laser output was measured with the PD and ESA, which confirmed a microwave beat signal at 15 GHz.

Initially, the generated microwave signal demonstrated erratic behavior in the form of excess jitter and coherence collapse, where the microwave signal randomly and abruptly increased up to 3 orders of magnitude in linewidth for a few seconds. This behavior is consistent with that produced by excess back-reflections into the laser cavity [110]. The back-reflections mainly originated from Fresnel reflections on the 1030 nm fiber facet and caused instabilities despite the use of a 22 dB optical isolator and an 8 degree angled fiber facet. From the parameters listed in Table 6.1 and Equation 2.89, coherence collapse is

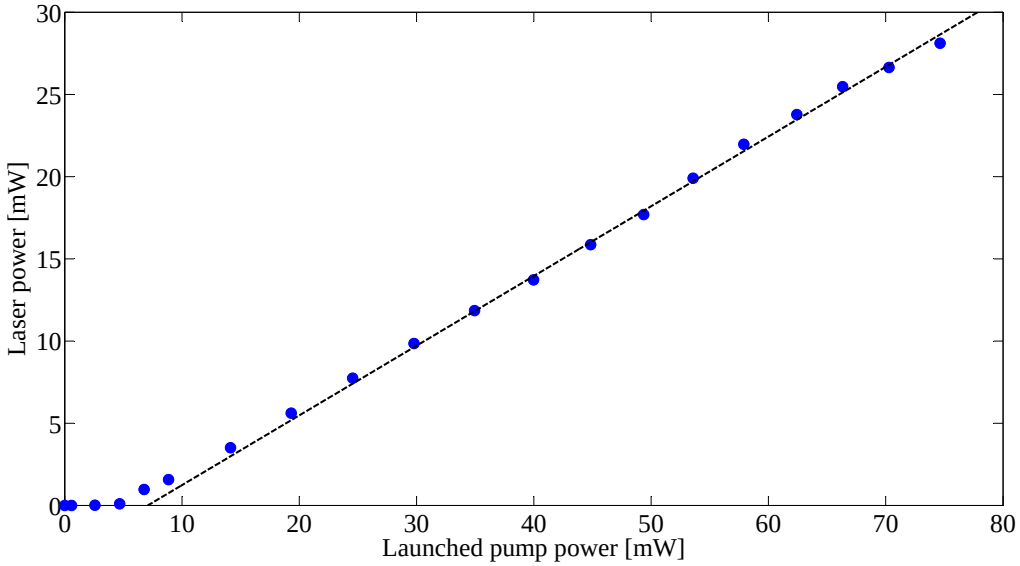

Figure 6.7: Measured output power (blue dots) of the dual-wavelengthAl_2O_3:Yb^{3+} waveguide laser as a function of launched pump power. The fitted black dashed line represents a 41% slope efficiency.

expected to persist until the laser is operated at a pump power of more than 30 times the laser threshold. In order to decrease the back-reflections which couple into the laser cavity, the WDM fiber was slightly misaligned with respect to the waveguide and fixed into position with UV-curable glue. The estimated fiber-chip-coupling with this configuration was $\sim$ 10%. This solution resulted in much improved stability, and from Equation 2.89 it was confirmed that the coherence collapse should cease when the laser is operated at pump powers beyond $\sim$ 3.0 times the laser threshold value.

The resulting microwave beat signal ($\sim$ 4 times above threshold) was centered at 15.0426 GHz and is shown in Figure 6.8. The beat signal frequency implies a wavelength separation of 52 pm between the two individual longitudinal laser modes. The two side-

Parameter	Value	Reference
Ytterbium concentration	5.8×10^{20} cm^{-3}	Estimated
Absorption cross-section (1020.2 nm)	0.32×10^{-21} cm^2	[70]
Effective luminescence lifetime of the excited state	41 μs	Calculated
Cavity lifetime	0.24 ns	Calculated
Fiber-chip coupling efficiency	0.35	Calculated
Fresnel reflection (fiber-air interface)	0.03	Calculated
Effective refractive index	1.62	Calculated
Linewidth enhancement factor	1.0	Assumed [138]
Grating coupling coefficient	5.0 cm^{-1}	Estimated

Table 6.1: Parameters used for the dual-wavelength Al_2O_3:Yb^{3+} DFB calculations.

bands on either side of the main microwave peak are produced by relaxation oscillations from the two respective longitudinal modes (Figure 6.8(a)). The relaxation oscillation frequencies f_{ro} were measured as a function of pump power and by comparing the onset of the respective relaxation oscillations it became apparent that one of the longitudinal modes had a 20% higher pump threshold than the other (Figure 6.9). The shorter wavelength most likely reaches threshold first, since it oscillates around the phase shift nearer to the pumped side of the chip where it receives more pump power than the longer wavelength.

The two relaxation-oscillation frequencies were used to calculate the Lamb's coupling constant given by [149]

$$C_{\mathrm{lamb}} = \left[\frac{1-(f_{\mathrm{L}}/f_{\mathrm{R}})^2}{1+(f_{\mathrm{L}}/f_{\mathrm{R}})^2}\right]^2 \tag{6.2}$$

where f_{L} and f_{R} are the relaxation oscillation frequencies of the two respective longitudinal modes with $f_{\mathrm{L}} < f_{\mathrm{R}}$. The value of C_{lamb} indicates whether there exists weak ($C \approx 0$) or strong ($C \approx 1$) mode competition between the two oscillating wavelengths. By using the measured relaxation oscillation frequencies as shown in Figure 6.9, the value of C_{lamb} could be determined. Just above threshold of the second mode, $C_{\mathrm{lamb}} > 0.5$, indicating a relatively strong interaction and mode competition between the two longitudinal laser modes close to threshold. However, with increasing pump power C_{lamb} converges to a value of $C_{\mathrm{lamb}} = 0.23$, indicating that the mode competition is rather weak, since each longitudinal mode was being amplified mostly by separate sections of the active medium (Figure 6.10). The weak longitudinal mode interaction was confirmed by the longitudinal field overlap between the two modes (Figure 6.6), which was calculated to be 0.34.

6.1.4 Frequency Stability

The long-term frequency stability of the microwave beat signal was measured over a period of 45 minutes with a 100 ms interval. The standard deviation of the microwave frequency during this period was found to be ±2.5 MHz, see Figure 6.11(a). During the same period the power of the microwave signal was stable within ±0.35 dB (Figure 6.11(b)). From the power stability measurement, three events are observed during which the RF power was decreased by 2.5-5.0 dB for a duration of 2 minutes each. These three events correspond to times during which the laser still entered into coherence collapse.

In order to investigate the short-term frequency stability, the microwave signal at the output of the photodiode was mixed with a high-purity, stable electrical reference signal with a sub-Hz line width, which was produced by a microwave signal generator (Agilent E8267D). This reference signal was set within a few hundred kHz of the ∼15 GHz microwave beat signal produced by the laser. Since the reference signal was much narrower than the laser beat signal, mixing of the two signals produced a convoluted signal which was nearly identical in shape to the original microwave beat signal produced by the laser, but shifted to the kilohertz range, so that a time trace of this down-converted signal could be measured with an oscilloscope. A short-time Fourier transformation using a Hamming window function with a frequency resolution of 20 kHz (time span of 64.8 μs)

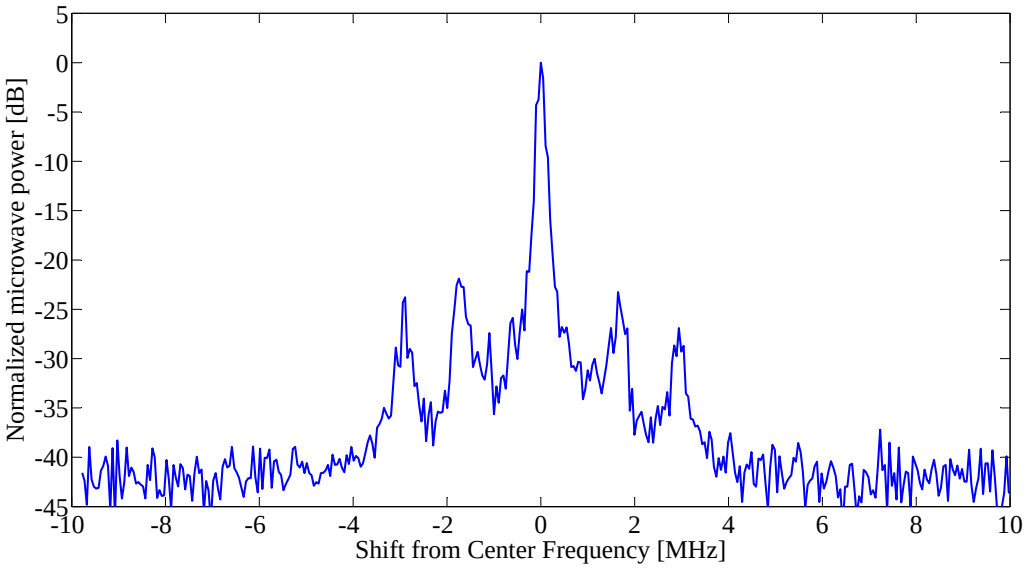

(a) Logarithmic power scale.

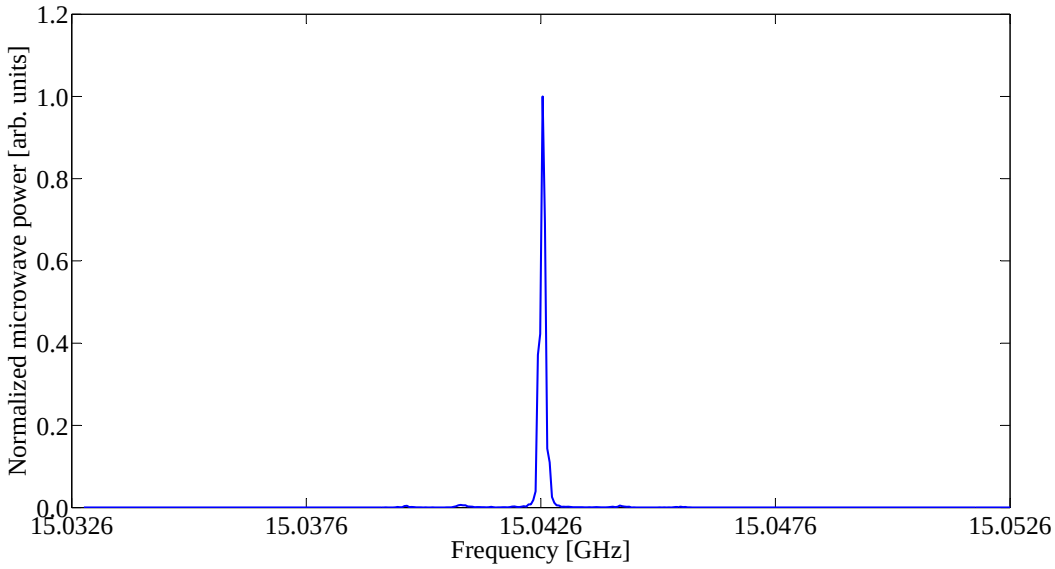

(b) Linear power scale.

Figure 6.8: Electrical spectrum of the microwave beat signal centered at 15.0426 GHz measured with a resolution bandwidth of 50 kHz.

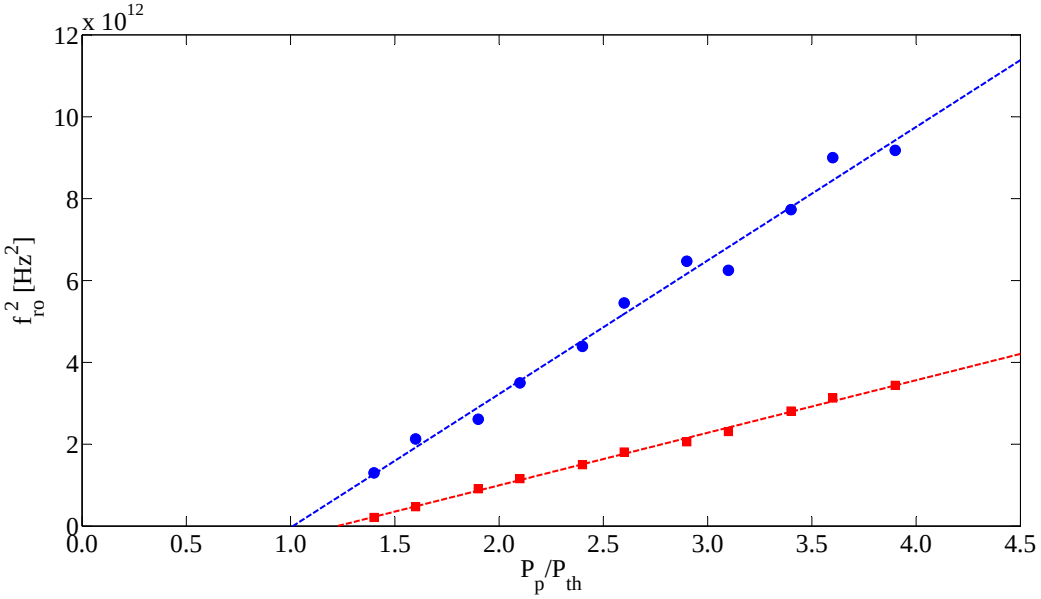

Figure 6.9: Square of the relaxation oscillation frequency (f_{ro}) of the two longitudinal laser modes as a function of $P_{\mathrm{P}}/P_{\mathrm{th}}$, with P_{P} the pump power and P_{th} the threshold pump power of the lowest threshold mode.

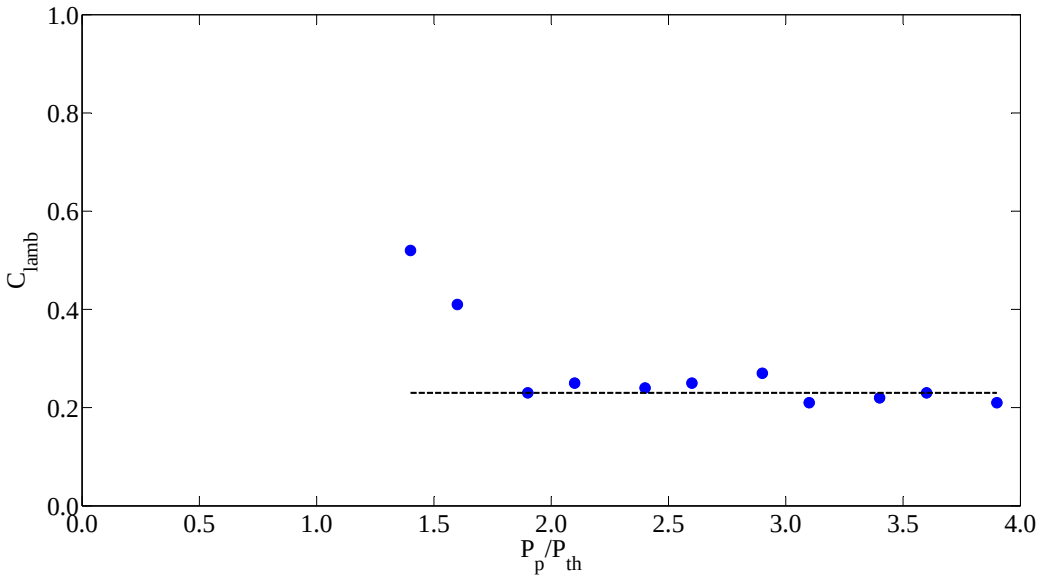

Figure 6.10: Lamb's coupling constant C_{lamb} as a function of $P_{\mathrm{P}}/P_{\mathrm{th}}$, with P_{P} the pump power and P_{th} the threshold pump power of the lowest threshold mode. The black dashed line represents a value of $C_{\mathrm{lamb}} = 0.23$.

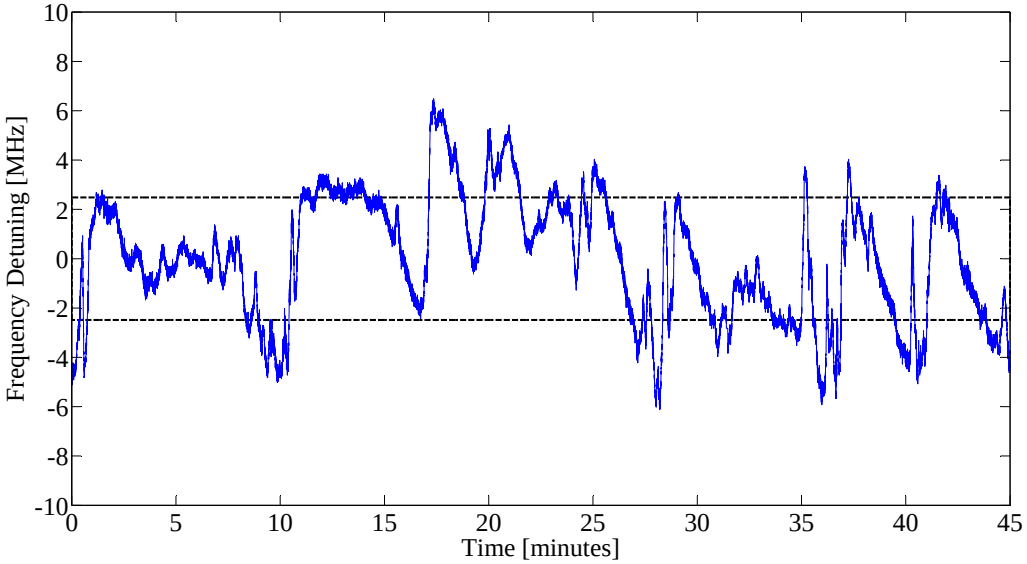

(a) Frequency stability. The standard deviation of the center frequency during this period was ±2.5 MHz, indicated by the black horizontal dashed lines.

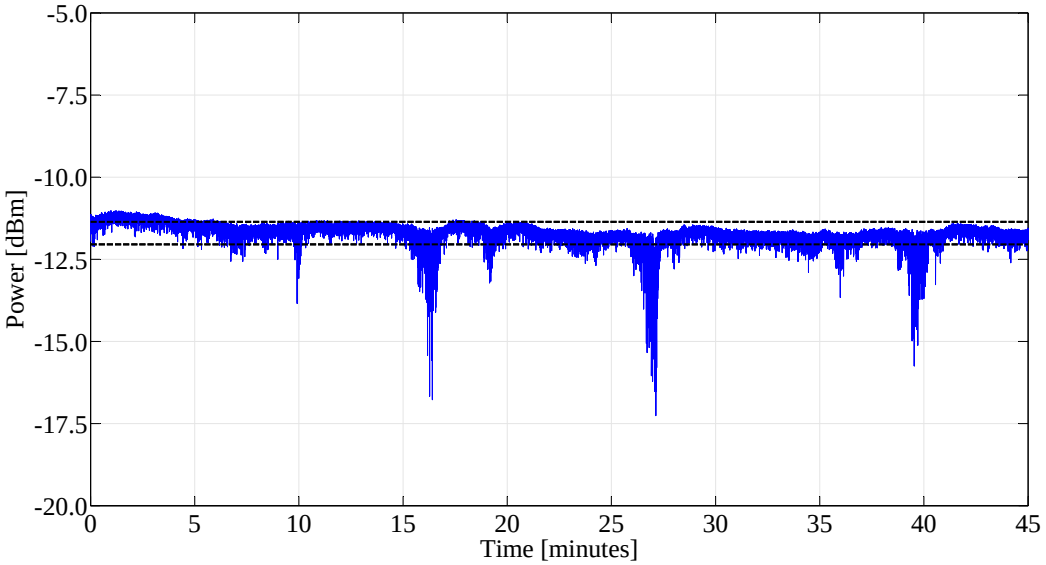

(b) Power stability. The standard deviation of the RF power during this period was ±0.35 dB, indicated by the black horizontal dashed lines.

Figure 6.11: Measured stability of the microwave signal during a period of 45 minutes.

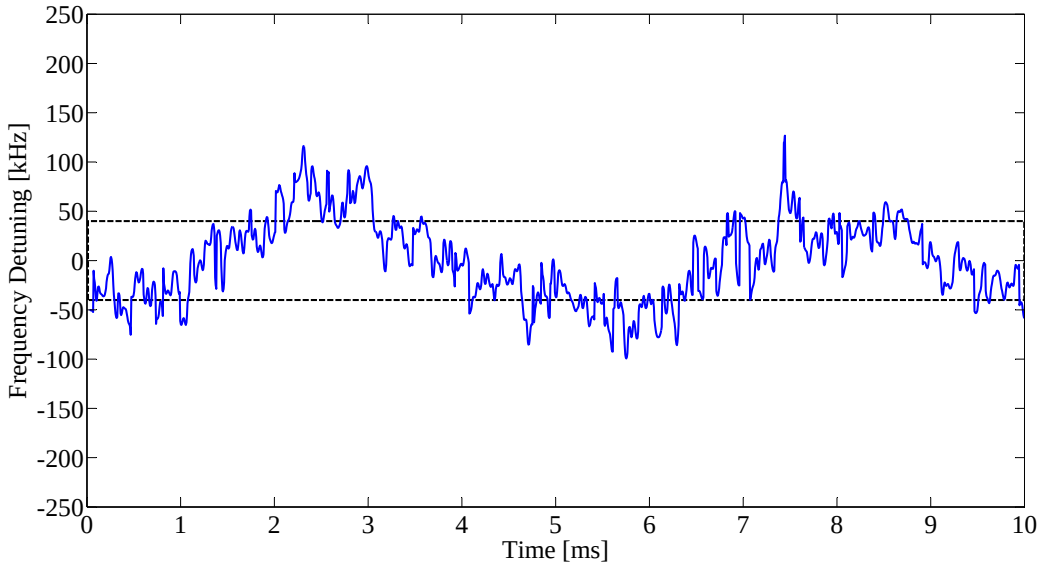

Figure 6.12: Measured short-term frequency stability of the RF beat signal. The standard deviation of the RF center frequency during this period was ±40 kHz, indicated by the black horizontal dashed lines.

was performed on the time trace of the down-converted signal to obtain a spectrogram (successive measurements of the signal spectrum versus time) over a duration of 10 ms. By noting the center frequency of each spectrum in the spectrogram, the short-term frequency stability of the microwave signal during the 10 ms period was found to be ±40 kHz, see Figure 6.12.

In order to determine the line width of the laser, a single temporal slice was extracted from a spectrogram with a frequency resolution of 8 kHz (time span of 162.4 μs), see Figure 6.13. This confirmed that the microwave signal produced by the laser was below 9.0 kHz. With the assumption that the two longitudinal modes have equal powers, it follows that the individual laser line width is half of the RF linewidth, suggesting an individual laser linewidth below 4.5 kHz, close to the 1.7 kHz previously demonstrated in the Al_2O_3:Er^{3+} single-wavelength DFB laser (Section 5.1). Both the long- and short-term frequency stability are believed to be limited by pump-power fluctuations, since a change in pump power induced a frequency shift of approximately -60 MHz/mW in the microwave beat signal. The stability performance and narrow linewidth of the free-running laser shows the great potential of using rare-earth-ion-doped monolithic waveguide lasers for the photonic generation of stable microwave signals.

In collaboration with the Telecommunication Engineering group at the University of Twente, Reza Khan has implemented an optical frequency locked loop in which the center frequency of the microwave signal of a similar dual-wavelength Al_2O_3:Yb^{3+} waveguide laser was stabilized to $\sim$ 50 kHz for a measurement time of 1000 s, while the power stability of the beat signal was improved from ±0.35 dB to ±0.11 dB [150]. The feedback loop relied on slightly tuning the pump power which, in turn, changes the thermally induced

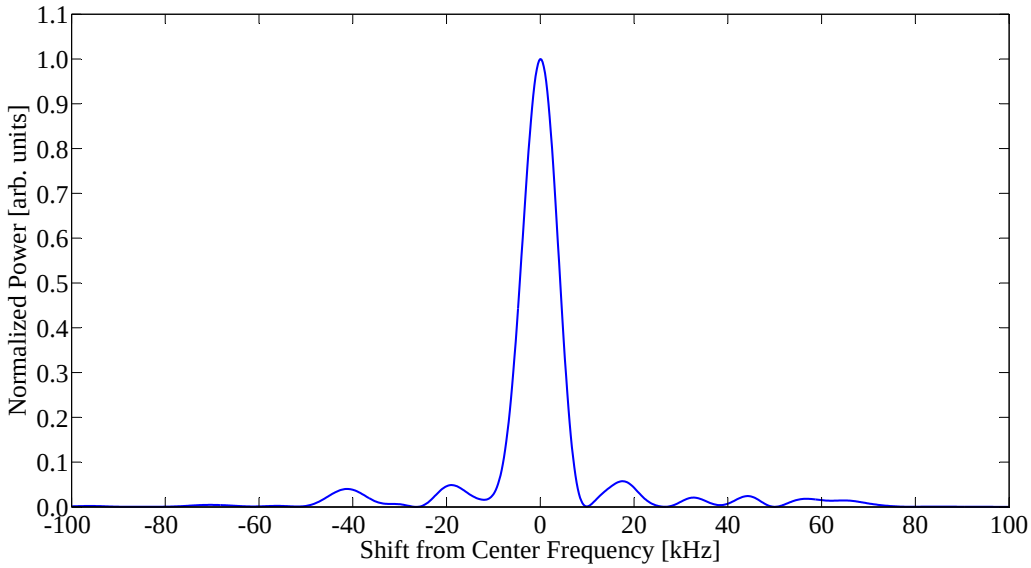

Figure 6.13: The RF beat signal spectrum which was extracted from a single temporal slice in a spectrogram (8 kHz resolution). The FWHM of the microwave signal was below 9.0 kHz, which implies an individual laser line width below 4.5 kHz.

chirp in the Bragg grating and, consequently, the frequency separation between the two laser modes.

6.2 Optical Sensing

High-quality passive whispering-gallery-mode (WGM) resonators are particularly prominent in the field of label-free integrated optical sensing [55–57]. WGM fused-silica microspheres with Q-factors as high as 8×10^9 have previously been demonstrated [151]. However, these devices have not been integrated on a chip and require bulky glass prisms in order to couple light into them [151, 152]. As an alternative to the high-Q microspheres, toroid-shaped silica WGM resonators with Q-factors in excess of 1×10^8 have been integrated on a silicon chip, where tapered fibres were used to couple light [153]. A disadvantage of these devices is that during fabrication, each cavity has to be selectively reflowed using CO_2 laser radiation, which makes wafer-scale fabrication impractical and time-consuming. Very recently, integrated WGM wedge-shaped resonators, which do not require the individual reflow fabrication step, demonstrated record-high Q-factors of up to 8.75×10^8 in a silica-on-silicon platform [154]. The maximum achievable Q-factors of typical passive WGM silica resonators are limited to $< 10^{10}$, due to the intrinsic material loss of silica [155], which also limits the sensitivity of these passive cavities for sensing applications.

By exploiting laser operation in which optical gain partially compensates the losses in the cavity, the laser Q-factor [100] exhibits several orders of magnitude improvement over the passive cavity Q-factor (in other words, the line width narrows by several orders of

magnitude), through which much higher sensitivity for such a laser-cavity-based sensor is achieved [156]. This Q-factor enhancement is clearly illustrated in an erbium-doped silica micro-toroid laser where a linewidth of 4 Hz was demonstrated, corresponding to a laser Q-factor of $\sim 5 \times 10^{13}$ [48]. Subsequently, laser-based sensors have been used to detect particles which are too small to be detected by sensors based on passive optical resonators [157]. Rare-earth-ion-doped micro-lasers have been particularly successful for the realization of particle sensors and have demonstrated the detection of individual 15-nm-radius polystyrene nanoparticles, 10 nm gold nanoparticles and influenza A virions in air, as well as 30 nm polystyrene nanoparticles in water [155]. Even though the rare-earth-ion-doped WGM toroid lasers have the ability to detect particles on the order of a few tens of nanometers, each individual cavity requires fiber-taper or prism alignment alignment, which makes it susceptible to mechanical and acoustic vibrations and impractical to realize arrays of simultaneously operating sensors on the same substrate. Since the typical diameters of the WGM resonators are on the order of 20-40 μm [155], it requires that the particles which need to be detected should be placed very accurately within a relatively small volume in order to interact with the cavity, which places stringent requirements on the measurement setup.

In the previous section, an integrated Al_2O_3:Yb^{3+} DFB channel waveguide laser operating at 1020 nm, achieving a laser Q-factor of 6.54×10^{10} (4.5 kHz linewidth) was demonstrated, while Q-factors as high as 1.14×10^{11} (1.7 kHz linewidth) for the Al_2O_3:Er^{3+} laser operating at 1545 nm was achieved (Chapter 5). These devices have much narrower linewidths as compared to semiconductor-laser-based sensors with linewidths ranging between 1.8 MHz and 7.5 MHz, which have demonstrated a refractive index sensitivity of 6×10^{-6} [22, 158].

In this section, the ultra-high Q-factors of the rare-earth-ion-doped Al_2O_3 monolithic laser cavities is exploited by demonstrating the capability of a dual-wavelength Al_2O_3:Yb^{3+} DFB channel waveguide laser as a highly sensitive particle sensor, which enables the detection of individual borosilicate microspheres ranging between 1 μm and 20 μm in diameter. The Al_2O_3 waveguide technology has wafer-scale fabrication potential and the waveguides can be deposited on a number of substrates, including thermally oxidized silicon [62]. Constituting a significant advantage over the WGM cavities, this waveguide technology allows the parallel fabrication of arrays of on-chip integrated resonators that can easily be pumped and read out via a single integrated waveguide.

6.2.1 Fabrication

The optically pumped dual-wavelength laser was realized in a 2.5-μm-wide, 1.0-μm-high, 90-nm-etched straight channel waveguide in an Al_2O_3:Yb^{3+} layer deposited onto a thermally oxidized silicon wafer (Section 3.2.1), with a uniform surface corrugated Bragg grating inscribed to its SiO_2 top cladding by laser interference lithography and reactive ion etching as described in Section 5.2.1. Two localized quarter-wavelength phase shifts, each comprising a 2-mm-long adiabatic sinusoidal widening of the waveguide width (Section 2.2.4), were centered at distances of 4 mm and 6 mm from the pumped end-facet of

the 10-mm-long cavity. These phase shifts induce two resonances that form two longitudinal lasing modes. Each mode is spatially distributed over both phase-shift regions, so that the two modes share a common cavity. Since the two lasing modes share the same optical gain, they exhibit similar gain fluctuations, i.e., the relative fluctuations between these two frequencies owing to environmental perturbations are several orders of magnitude weaker than the absolute ones. Consequently, the two emitted laser lines can be used to generate a low-noise microwave signal by measuring the frequency of the corresponding heterodyne beat signal with a photodetector. In addition, the dual-wavelength-laser approach reduces the relative frequency fluctuations arising from pump-power variations, since both laser modes are pumped by the same pump source, as opposed to two individual laser cavities being pumped by two separate pump sources.

6.2.2 Micro-Particle Detection

The sensing principle is based on the interaction between the evanescent field of the laser modes and a microparticle on the top surface of the grating in one of the two phase-shift regions to which the laser modes are mostly confined; the induced light-scattering loss evokes a change in the frequency spacing between the two emission lines, which manifests itself in a frequency shift of the measured heterodyne beat signal. The laser self-compensates the higher intra-cavity loss by an accordingly higher optical gain, i.e., an increase in the ytterbium population inversion. If for simplicity it is assumed that a constant fraction η of the absorbed pump radiation is converted to heat, then the power per unit volume dissipated as heat along the laser cavity is given by [159]

$$h(y) = \eta \left(\sigma_{\mathrm{P}}^{\mathrm{abs}} N_0(y) - \sigma_{\mathrm{P}}^{\mathrm{em}} N_1(y) \right) I_{\mathrm{P}}(y) \tag{6.3}$$

where y is the position along the waveguide, while $\sigma_{\mathrm{P}}^{\mathrm{abs}}$ and $\sigma_{\mathrm{P}}^{\mathrm{em}}$ are the absorption and emission cross-sections at the pump wavelength, respectively. N_0 and N_1 represent the population density of the ground state and first excited state, respectively, with I_{P} being the pump intensity. Due to the approximately exponential absorption of pump intensity I_{P} propagating along the waveguide a temperature and consequent refractive-index increase of the material with a similar axial profile is formed. Hence a thermal chirp is imposed on the Bragg grating by the absorption of pump light, so that the two phase shift regions receive slightly different grating optical periods and resonance frequencies. If due to the particle-induced scattering of laser power the population inversion increases, $h(y)$ and, thus, the temperature and refractive index of the waveguide decrease, thereby altering the thermal chirp of the Bragg grating, which accordingly affects the frequency spacing between the two emitted laser lines. Observing the heterodyne signal generated at the output of the photodetector allows the frequency difference between the two optical waves to be measured within 1 Hz accuracy in the electrical domain by use of an electronic spectrum analyzer. This provides a convenient, real-time and high-resolution sensor readout signal.

A (980/1030)±10 nm wavelength-division-multiplexing (WDM) fiber was butt-coupled to the optical chip and fixed into position with UV-curable glue. Continuous-wave 976 nm

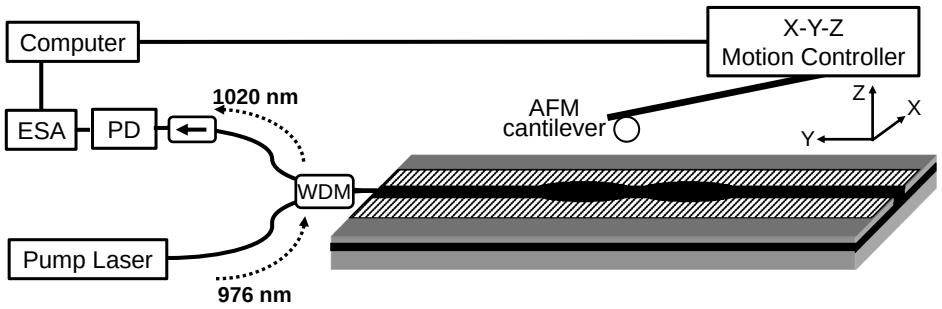

Figure 6.14: Experimental setup used to characterize the intra-laser-cavity microparticle dual-wavelength laser sensor. ESA: Electronic spectrum analyzer;PD: Photodetector; WDM: Wavelength division multiplexing fiber; AFM: Atomic force microscope.

diode pump light was launched into the waveguide via the 980 nm port of the WDM fiber, while the 1020 nm laser emission was collected through the 1030 nm port, which also contained a 22 dB optical isolator to prevent optical back-reflections into the laser cavity (Figure 6.14). The free-running laser emission was monitored with a 40 GHz photodetector (PD) which was connected to an electrical spectrum analyzer. A microwave beat signal was observed, whose frequency of $\sim$ 13.5 GHz or free-space wavelength of $\sim$ 2.2 cm corresponds to a wavelength separation of 47 pm between the two longitudinal laser modes.

Optical sensing has been demonstrated by systematically probing the intra-cavity evanescent laser- and pump fields with various borosilicate glass microspheres of diameters ranging between 1 μm and 20 μm. Each microsphere was attached to a low-stiffness (spring constant 0.01-0.02 N/m) atomic force microscope (AFM) cantilever. The cantilever was mounted on a 3-dimensional computer-controlled translation stage (Figure 6.14). This experimental setup allowed the microspheres to be scanned in contact mode across the top surface of the waveguide laser with a lateral resolution of 25 nm, while recording the center frequency of the microwave beat signal for each position of the microsphere. A similar experimental setup has previously been used to probe the intra-cavity field of a photonic crystal microcavity via the interaction with an AFM cantilever [160]. Figure 6.15 shows top views of the AFM cantilever, with a 20-μm-diameter microsphere attached, as it is scanned perpendicular across the waveguide top surface in the center of the phase shift located at the pumped side of the cavity. A bright scattering point is clearly visible as the microsphere interacts with the intra-laser-cavity evanescent fields (Figure 6.15(b)). This scattering event induces a decrease of $\sim$ 8% in the laser output power, as can be seen from the laser power measurement shown in Figure 6.16. By simply observing a decrease in laser power a single 5-μm-diameter microsphere, which induced a $\sim$ 3% decrease in the laser power, could still be detected, while a 1-μm-diameter microsphere did not induce any measureable change in the laser power. Although semiconductor lasers have previously been employed as microparticle sensors where single 1-μm-diameter latex spheres were detected by observing the particle-induced decrease in laser power due to scattering [161], the overlap between the laser field and the micro-particle was approxi-

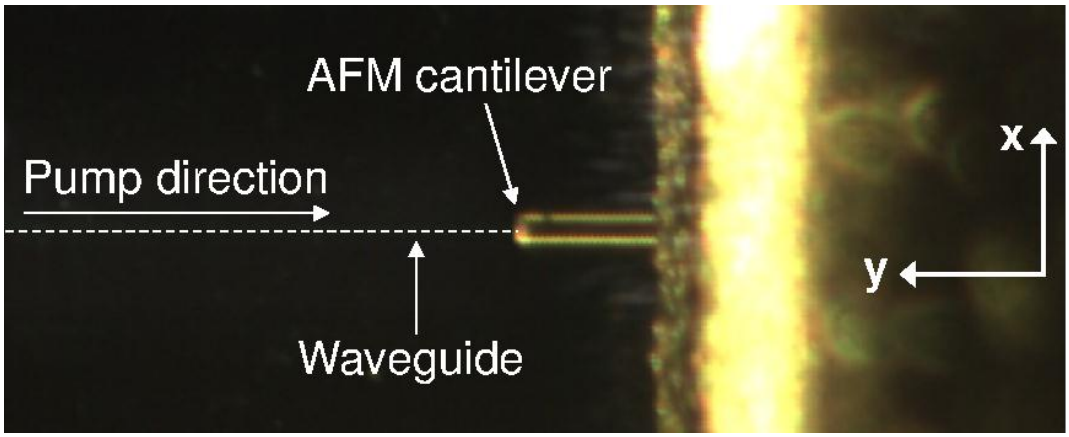

(a) Top-view of the AFM cantilever with a 20-μm-diameter microsphere attached to it.

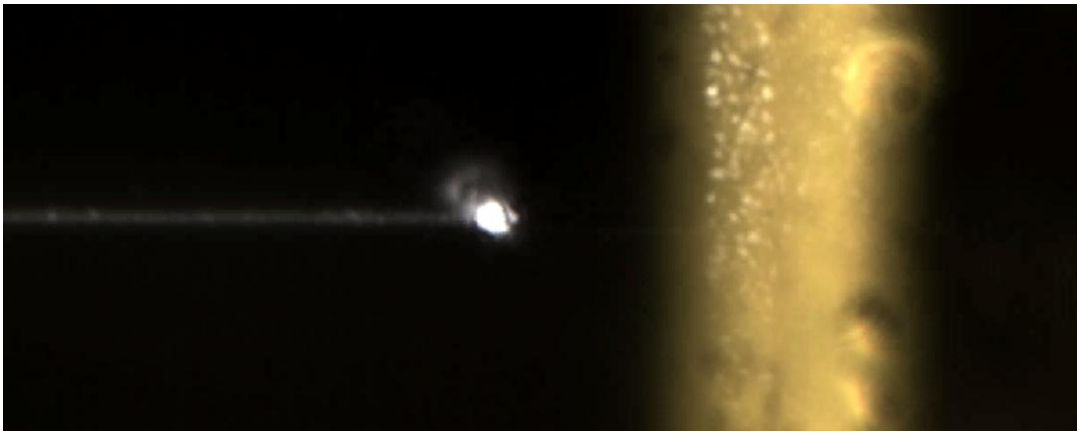

(b) The microsphere in contact with the surface, on top of the waveguide.

Figure 6.15: Top-view of the AFM cantilever with a 20-μm-diameter microsphere attached to it, while it is scanned across the waveguide surface.

mately 40 times larger than in our waveguide geometry. Optimizing our waveguide and grating geometry in order to increase the overlap between the laser field and the particle is expected to result in a significant improvement in the sensitivity of our device.

Instead of exploiting information about the decrease in laser power as a measure of the microparticle size, the frequency difference between the two longitudinal laser modes, as measured via the heterodyne beat frequency, was used as an alternative. To illustrate the impact of such a particle-induced scattering loss on the microwave beat frequency, a 10-μm-diameter borosilicate glass microsphere was scanned on the waveguide top surface along a 4-mm-long section of the laser cavity, covering both distributed phase shift regions (Figure 6.17). Surprisingly, inside the phase shift region located on the pumped side of the cavity, a negative detuning of the beat signal is observed, while probing the other phase shift with the microsphere resulted in a positive detuning of the beat signal. The opposite signs of frequency detuning can qualitatively be justified by the following explanation. The thermally induced grating chirp, where the grating optical period in the first phase

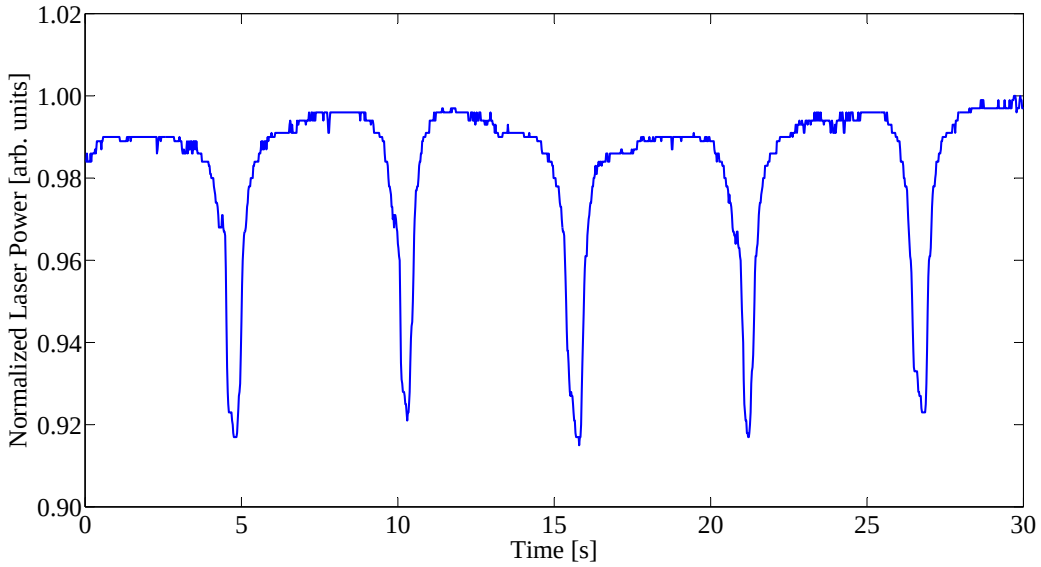

Figure 6.16: Normalized laser output power as a function of time, when the 20-μm-diameter microsphere is repeatedly scanned across the waveguide surface in the center of the phase shift located at the pumped side of the cavity.

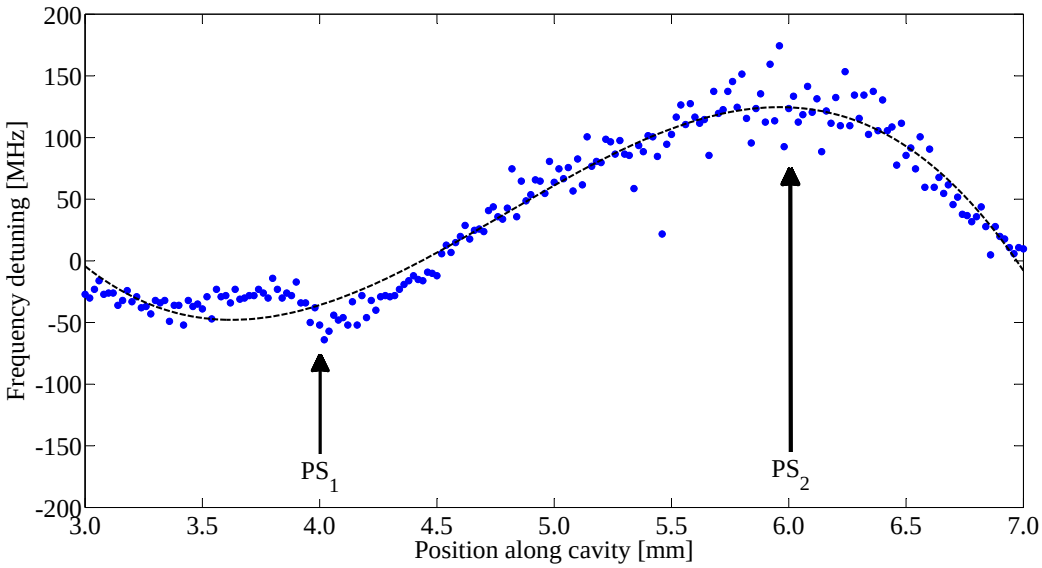

Figure 6.17: Measured beat frequency detuning (blue dots) as a 10-μm-diameter borosilicate glass microsphere is scanned on the waveguide top surface along the length of the laser cavity. The dashed line represents a third order polynomial fit to the data and serves as a guide for the eye. PS_1: center of the distributed phase shift on the pumped side of the cavity; PS_2: center of the distributed phase shift on the unpumped side of the cavity

shift (pumped side) is larger than that of the second phase shift (unpumped side), causes the laser mode with the longer wavelength to be confined primarily to the phase shift on the pumped side, while the other laser mode becomes primarily confined to the second phase shift region. By creating a scattering loss inside the first phase shift, the population inversion is increased, hence the pump absorption, generated heat, temperature, and refractive index are decreased in this region of the waveguide. Consequently, the grating optical period in the first phase shift is reduced due to the reduction in waveguide temperature. This implies that the difference in Bragg wavelength of the two phase shift regions is reduced, thereby decreasing the microwave beat signal frequency. On the contrary, if a scattering loss is induced inside the second phase shift, the population inversion increases and the waveguide temperature and refractive index decrease in this region, which further enhances the difference in grating optical period (and Bragg wavelength) of the two phase shift regions, so that the observed microwave beat frequency is also increased.

The interaction between the intra-laser-cavity light fields and the microspheres was further analyzed by performing a 2-dimensional scan on the waveguide surface inside the center of each of the two respective phase shift regions, using a 5-μm-diameter borosilicate glass microsphere. Evidently, the scattering loss caused by this microsphere in the phase shift on the pumped side induces a negative frequency detuning of the microwave signal of ~ 40 MHz (Figure 6.18(a)), while a positive frequency detuning of ~ 70 MHz is induced by the scattering loss in the phase shift on the unpumped side of the laser cavity (Figure 6.18(b)). It can clearly be seen that, via the interaction between the intra-laser-cavity fields and the microsphere, the beat frequency detuning of the beat signal maps out the structure of the channel waveguide (Figures 6.18(a) and 6.18(b)). By averaging along the y-direction (along the length of the waveguide), a single curve could be constructed for each of the two 2-dimensional surface scans, representing the beat frequency detuning as the microsphere is scanned perpendicular across the waveguide (Figure 6.19).

In order to investigate the size-measurement capability of our dual-wavelength laser sensor, the effect of various sizes of microspheres on the microwave beat frequency was measured. Each microsphere, attached to an AFM cantilever, was scanned across the waveguide laser in the center region of each of the two respective phase shifts, while the frequency detuning of the microwave beat signal was observed. The results of these measurements are shown in Figure 6.20. Inside the first phase shift, the largest investigated microsphere with a diameter of 20 μm induced a 94 MHz decrease in the microwave beat signal, while the smallest microsphere, with a diameter of 1 μm, induced a frequency decrease of 6 MHz. In the second phase shift region, the largest and smallest microspheres induced an increase in the microwave beat signal of 212 MHz and 9 MHz, respectively. Assuming that the frequency detuning of the laser-generated beat signal has a linear dependence on microsphere size, as shown in Figure 6.20, the resolution of the sensor is currently limited to particles of $\sim$ 500 nm diameter. This size limitation is due to the free-running frequency stability of the laser of $\sim$ 5 MHz, which is most likely due to fluctuations in the pump power as well as some optical back-reflections into the laser cavity. By use of a power-stabilized pump laser and further isolating the back-reflected laser power, this device has the potential to detect sub-100-nm particles.

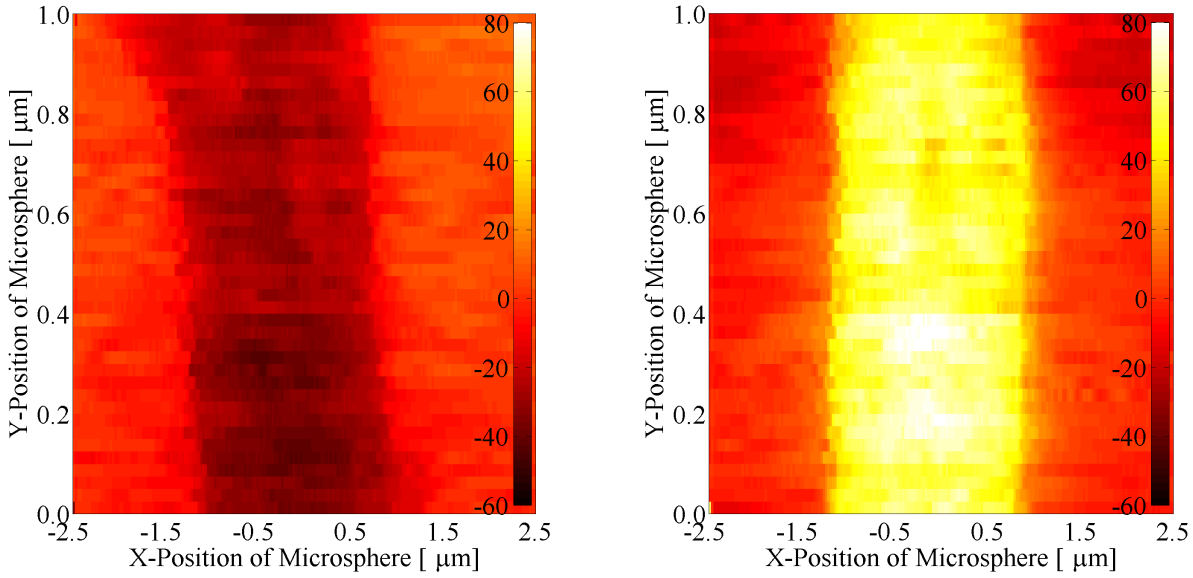

(a) Phase shift on the pumped side of the cavity. (b) Phase shift on the unpumped side of the cavity.

Figure 6.18: Frequency detuning (in MHz) of the microwave beat signal, as a 5-μm-diameter microsphere is scanned across a 2-dimensional area of the waveguide laser surface in the center region of the respective phase shift regions.

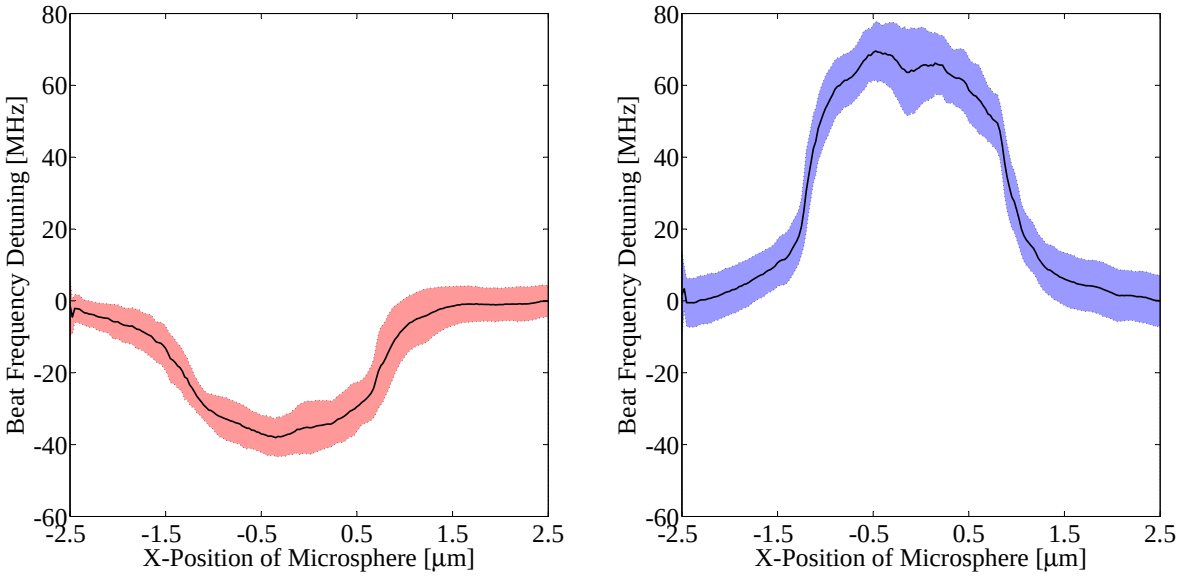

(a) Phase shift on the pumped side of the cavity. (b) Phase shift on the unpumped side of the cavity.

Figure 6.19: By averaging along the y-direction (along the length of the waveguide) of Figures 6.18(a) and 6.18(b), a single curve was constructed for the two 2-dimensional surface scans in the respective phase shift regions. The colored regions in the graphs represent the standard deviation.

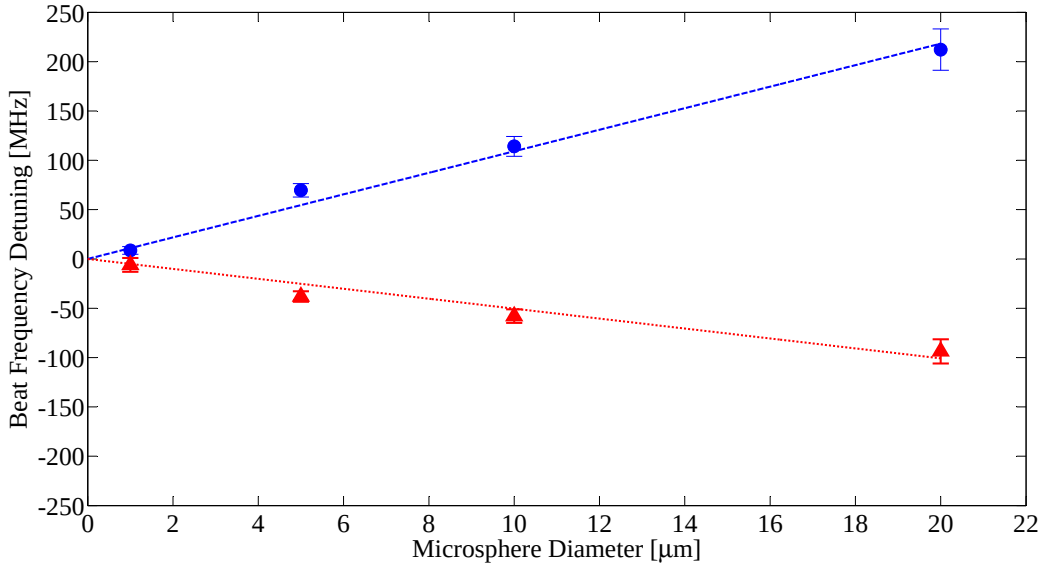

Figure 6.20: Laser microwave beat frequency detuning as a function of the diameter of the microspheres. The red triangles were measured in the center of the phase shift on the pumped side, while the blue circles were measured in the center of the phase shift on the unpumped side of the laser cavity. The red and blue lines represent linear fits through the origin with slopes of -5 MHz/μm and 11 MHz/μm, respectively.

With this particular configuration, the refractive index of the microspheres and the position of interaction on the waveguide were known, while the size of the microparticles was the quantity which was determined via the detuning of the microwave beat signal frequency. However, if the size and refractive index of the microparticles are known, the waveguide section between the two phase shift regions, i.e., between 4 and 6 mm from the pumped waveguide end, where the beat frequency detuning as a function of axial waveguide position is approximately linear (Figure 6.20), can be used to obtain information regarding the position of the microparticle. In other words, depending on the particular sensing application, this dual-wavelength laser can be used to obtain information about the size, refractive index, or position of a microparticle.

In this section, an integrated optical particle sensor based on an Al_2O_3:Yb^{3+} dual-wavelength DFB channel waveguide laser was demonstrated. Borosilicate glass microspheres with diameters as small as 1 μm were detected. With changes to the sample geometry and experimental set-up, the detection of sub-100-nm particles is feasible, which will make this device performance comparable to the WGM toroid laser sensors, but with the added benefit of a silicon-compatible wafer-scale fabrication process and the prospect of integrating the sensor with microfluidic channels. This result holds great potential for the detection of single fungal and bacterial pathogens and even single molecules. A situation comprising a Bragg-grating-based channel waveguide laser and a biological object alighted by its evanescent field is illustrated in Figure 6.21, while an artist's impression of the dual-wavelength laser being probed by a glass microsphere in shown in Figure 6.22.

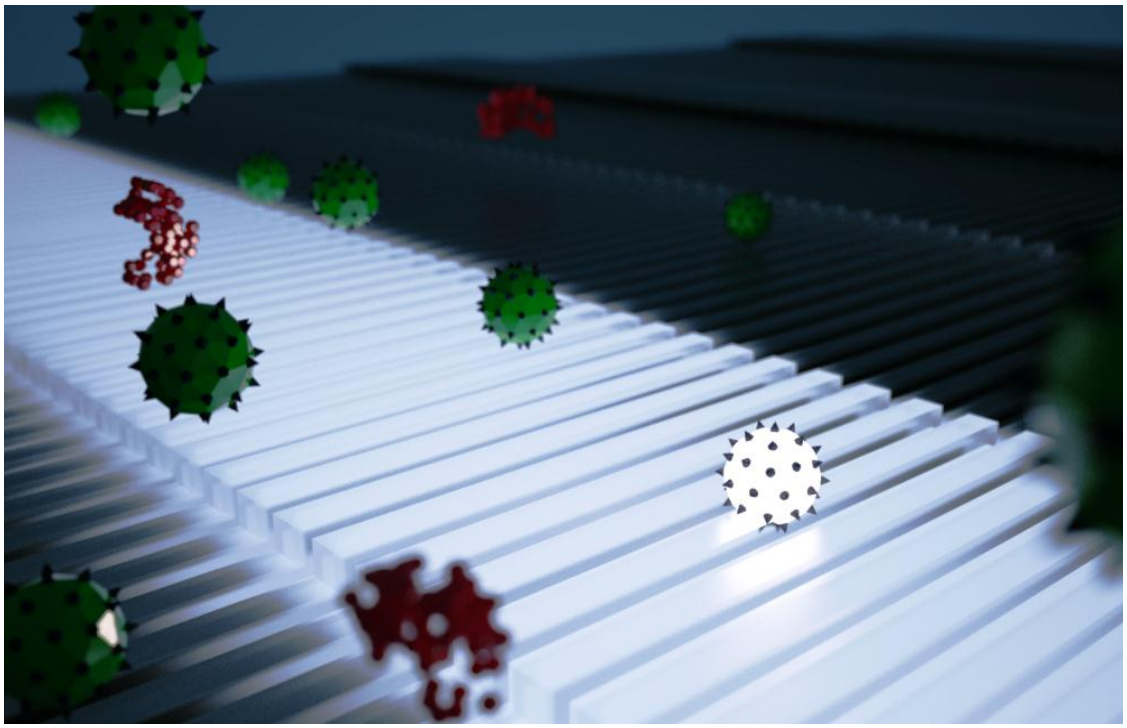

Figure 6.21: Illustration of the Bragg-grating-based channel waveguide laser microparticle sensor.

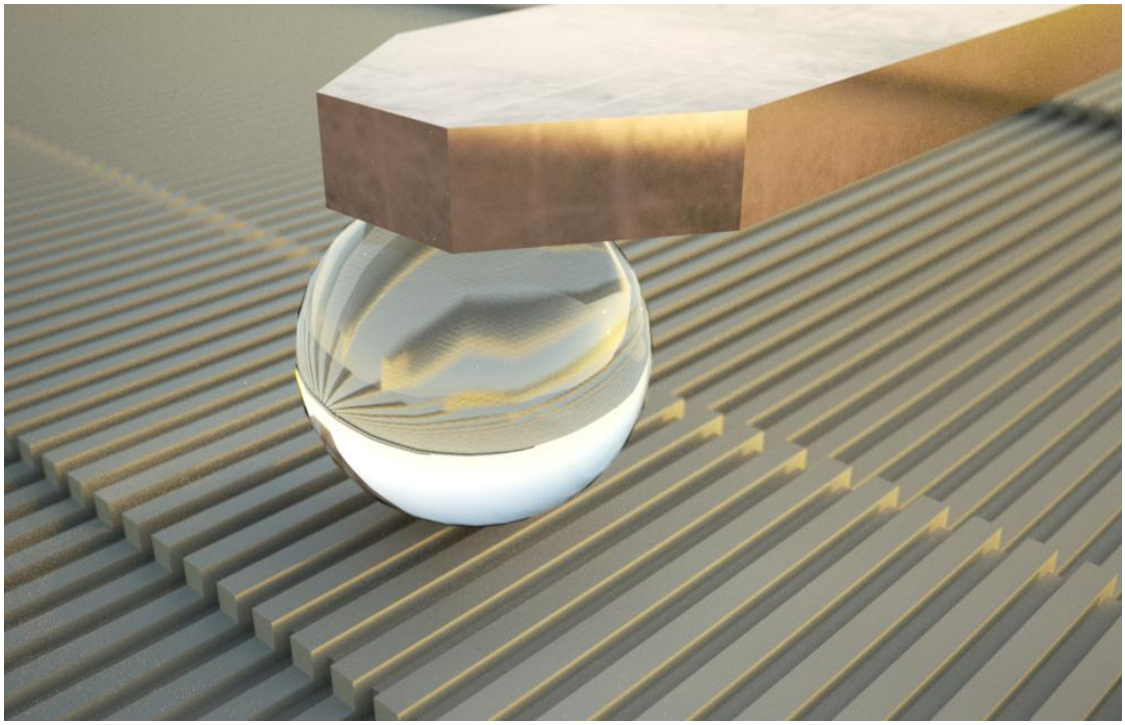

Figure 6.22: An artist's impression of the dual-wavelength laser microparticle sensor.

7 Conclusions

7.1 Summary

This thesis concerns the investigation and development of Bragg-grating-based integrated cavities for the Al_2O_3 waveguide platform, both from a theoretical and an experimental point of view, with the primary purpose of realizing narrow-linewidth, monolithic rare-earth-ion-doped channel waveguide lasers. Prior to this work, the only monolithic laser which has been demonstrated in the Al_2O_3 waveguide platform, was a multi-longitudinal-mode ring laser.

The theoretical foundation and the governing rate equations which describe the energy transitions and population dynamics of the quasi-three-level ytterbium- and erbium-ions have been presented and discussed. Coupled mode equations along with the transfer matrix method have been implemented in order to describe the operation of a typical waveguide Bragg grating as would be required for the interpretation of the performance of a distributed feedback (DFB) or a distributed Bragg reflector (DBR) waveguide laser. The theoretical description of a distributed quarter-wavelength phase shift in a DFB cavity has also been given. In such a cavity the phase shift have been implemented by means of a localized adiabatic variation in the waveguide dimensions, as opposed to the conventional discrete phase shift where the phase of the Bragg grating corrugation itself is altered. The distributed phase shift has been considered to be a more elegant solution, since the phase shift is defined with the same lithographic step in which the waveguide is defined. Although the concept of a distributed phase shift has previously been used in a variety of semiconductor lasers, it has only been demonstrated in integrated rare-earth-ion lasers in the form of a discrete step in the waveguide width. In this work, a local adiabatic sinusoidal variation of the waveguide width was used instead, in order to reduce

unwanted optical losses and reflections. Furthermore, the fundamental laser linewidth as predicated by the generalized SCHAWLOW-TOWNES equation has been discussed, where it was shown that a four-level laser has the ability to achieve significantly narrower linewidths as compared to a (quasi-)three-level laser, due to the absence of laser reabsorption. The laser stability in the presence of environmental noise and optical feedback has also been discussed.

After the optimized waveguide and grating geometries have been determined, the necessary fabrication techniques were described. These include the reactive co-sputtering process which has been used to deposit the rare-earth-ion-doped Al_2O_3 waveguide layers and has been primarily developed by Dr. Wörhoff, as well as the reactive ion etching process which has been developed by Dr. Bradley to etch the channel waveguides. Particular attention has been given to the laser interference lithography technique which were used to define the Bragg grating structures.

The characterization of integrated uniform Bragg gratings, as well as DBR and DFB cavities in Al_2O_3 ridge waveguides has been presented. The measured performance of the gratings agrees well with that predicted by the model based on coupled mode theory. Due to the low total waveguide propagation losses of 0.14 ± 0.07 dB/cm and grating-induced losses of 0.08 ± 0.01 dB/cm which have been measured, it was possible to realize Bragg gratings with reflectivities exceeding 99%. This enabled the demonstration of DBR cavities with a finesse of more than 147 and a Q-factor as high as $1.02 \pm 0.01 \times 10^6$. This is, so far as could be established, the highest demonstrated Q-factor of any passive monolithic DBR cavity on a silicon chip.

Using the established waveguide and grating technology, various rare-earth-ion-doped integrated channel waveguide lasers have been demonstrated. An Al_2O_3:Er^{3+} DFB waveguide laser has been presented which, so far as could be ascertained, represents the first rare-earth-ion-doped DFB laser on a silicon substrate. The low-threshold laser demonstrates single longitudinal mode, single polarization emission at a wavelength of 1545.2 nm with a linewidth of 1.7 kHz. A maximum output power of more than 3 mW is achieved. The first ytterbium-doped distributed feedback channel waveguide laser in Al_2O_3 has also been presented. The laser operates in a single longitudinal mode and single polarization at a wavelength of 1022.2 nm. The laser exhibits a low threshold of 5 mW launched pump power and emits a maximum laser output power of more than 55 mW, resulting in a slope efficiency of 67%. In addition to the Al_2O_3:Yb^{3+} DFB laser, a low-threshold, monolithic Al_2O_3:Yb^{3+} DBR waveguide laser operating at a wavelength of 1021.2 nm has been realized, emphasizing the versatility of the technology. The laser exhibited a pump-power-limited output power of 47 mW and a slope efficiency of 67%. The achieved laser power, efficiency, and spectral characteristics of these devices make the rare-earth-ion-doped Al_2O_3 waveguide platform an excellent competitor against other well-established optical waveguide technologies. The wafer-scale deposition of Al_2O_3 and the diversity of the devices which are demonstrated with this waveguide technology hold great potential for large-scale fabrication of complex photonic circuits on a single chip.

To demonstrate a novel application of the narrow-linewidth monolithic waveguide lasers, dual-wavelength Al_2O_3:Yb^{3+} DFB waveguide lasers have been used to generate

stable microwave signals ranging between 12.43 GHz and 23.2 GHz, for use in phased array antennas. In particular, a 4.5 kHz-wide microwave signal at $\sim$ 15 GHz has been demonstrated. The stability performance and narrow linewidth of the free-running laser show the great potential of using rare-earth-ion-doped monolithic waveguide lasers for the photonic generation of stable microwave signals. An innovative application of the photonic generation of stable microwave signals is the demonstration of an integrated intra-laser-cavity microparticle optical sensor. It enables convenient, real-time detection and accurate size measurement of single micro-particles with diameters ranging between 1 μm and 20 μm, which represents the typical size of many fungal and bacterial pathogens. This sensitivity is remarkable considering that no stabilization of the pump power nor the temperature was performed.

The Bragg-grating-based monolithic cavities and waveguide lasers which have been developed in this work establish a solid foundation for complex integrated optical circuits in which their functionality can fulfill the ever-growing requirements of innovative photonic applications. Instead of considering these rare-earth-ion-doped DFB and DBR waveguide lasers as competitors to the well-established semiconductor lasers in the telecommunication industry, the Bragg-grating-based rare-earth-ion-doped Al_2O_3 lasers should rather be established in the optical sensing market segment, in which the semiconductor lasers cannot compete in terms of their linewidth or stability.

7.2 Outlook

Three main aspects have been identified toward which future work in this field could be directed to. In the following sections each of these aspects is discussed briefly, which can be considered as a basis for future work.

7.2.1 Alternative Laser Cavities

Although the dual-wavelength lasers for microwave signal generation which are demonstrated in the previous chapter were designed to reduce gain competition between the respective longitudinal laser modes, it cannot be eliminated completely in the dual phase shift DFB cavity. An alternative design is to make use of two individual quarter-wavelength phase shift single-longitudinal-mode DFB cavities arranged in a Mach-Zehnder configuration as shown in Figure 7.1. The waveguide geometries in the two respective branches of the Mach-Zehnder design are slightly different in order to have different effective refractive indices and, consequently, different Bragg wavelengths. This allows an elegant way to tune the wavelength difference between the two cavities and the subsequent beat signal. This layout would still allow both cavities to be pumped with a single pump laser in order to reduce the pump-power-induced frequency fluctuations of the generated microwave signal. The TE-polarized transmission spectrum (measured from port 1 to port 3 as indicated in Figure 7.1) of such a device realized in an undoped Al_2O_3 waveguide layer is shown in Figure 7.2. Here, the widths of the respective branches of the Mach-Zehnder

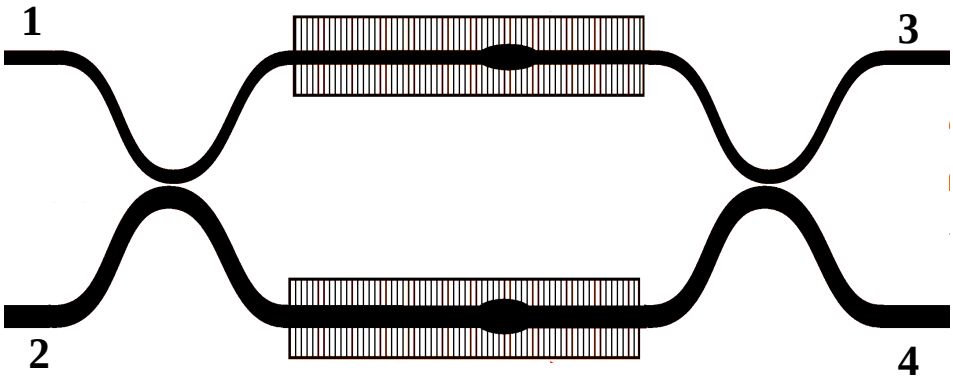

Figure 7.1: Schematic of two individual DFB cavities in the Mach-Zehnder design.

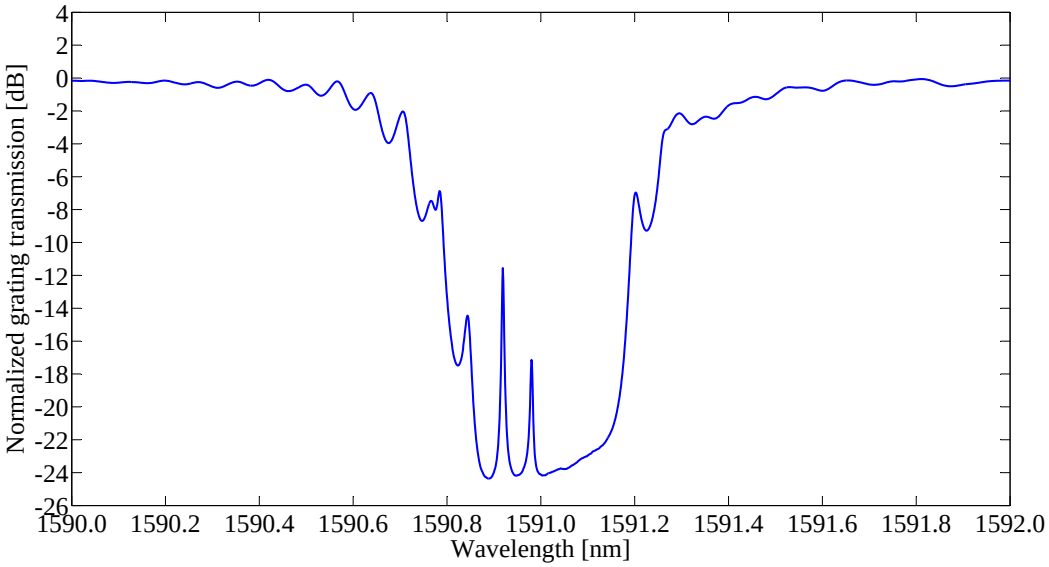

Figure 7.2: Normalized TE-polarized grating transmission spectrum of the two individual DFB cavities in the Mach-Zehnder design (measured from port 1 to port 3 as indicated in Figure 7.1).

were 2.5 μm and 2.55 μm, respectively, resulting in a wavelength difference of 7.23 GHz between the two respective resonances.

7.2.2 Alternative Grating Geometries

Instead of using the laser interference lithography technique to define Bragg gratings on the top surface of the cladding layer as shown throughout this thesis, a surface corrugated Bragg grating could be defined in a layer which is embedded below the waveguide. The benefit of such a waveguide/grating geometry is that the grating is not exposed to the environment where is can be damaged or have its optical performance degraded due to the presence of dust or other impurities.

As an alternative to grating fabrication based on laser interference lithography, waveg-

uide sidewall gratings, which are defined in the same lithographic step in which the waveguides are defined, could be considered. Since ~ 0.8 μm is the minimum feature size that can be defined using standard lithography in the MESA+ cleanroom, this approach will likely require a third-order Bragg grating to be used.

7.2.3 Other Rare-Earth-Ions

The incorporation of different rare-earth ions will expand the possibilities of the monolithic lasers in Al_2O_3 even further, from remote sensing and trace-gas detection using thulium-doped lasers operating around 2 μm, to integrated laser sources which emit in the visible region of the electromagnetic spectrum. Neodymium-doped integrated lasers operating on the $\sim$ 1060 nm laser transition, occurring from the $^4F_{3/2}$ to the $^4I_{11/2}$ manifold, hold great potential for the realization of ultra-narrow linewidths, due to the four-level-laser scheme in which no reabsorption loss occurs.

Appendix

```
%DESCRIPTION:   Spatially resolved rate-equation model
%               for a Yb-doped DFB waveguide laser
%AUTHOR:        E.H. Bernhardi (IOMS - University of Twente)

%==========Imported data from PhoeniX FieldDesigner=======================
%Refractive index profile as exported from Phoenix
refractive_index_dist=dlmread('yb_index_2.5um.txt');
%Transverse pump intensity profile
pump_dist=dlmread('yb_980nm_2.5um.txt');
%Transverse laser intensity profile
laser_dist=dlmread('yb_1020nm_2.5um.txt');
%==========================================================================

%==========Constructs refractive index and mode profiles==================
%X-discretiztion as exported from Phoenix
x=refractive_index_dist(2:size(refractive_index_dist,1),1).*1e-6;
%Y-discretiztion as exported from Phoenix
y=refractive_index_dist(1,1:size(refractive_index_dist,2)-1).*1e-6;
refractive_index_dist=refractive_index_dist...
(2:size(refractive_index_dist,1),2:size(refractive_index_dist,2));
pump_dist=pump_dist(2:size(pump_dist,1),2:size(pump_dist,2));
laser_dist=laser_dist(2:size(laser_dist,1),2:size(laser_dist,2));
gain_n=max(max(refractive_index_dist));
norm_pump_dist=pump_dist;
norm_laser_dist=laser_dist;
[xx,yy]=meshgrid(x,y);
%==========================================================================

%===============Grating parameters (All in SI Units)=======================
%Effective refractive index of the mode
neff=1.61;
%Peak reflectivity wavelegth
lambdab=1020.2e-9;
%The required grating period to acheive maximum reflection
%at the given wavelength
period=lambdab/2/neff;
%Grating coupling coefficient
kappa=500;
%Propagation constant of wavelength Lambda
```

```
beta=2*pi*neff/lambdab;
%Propagation constant of Bragg wavelength
beta0=pi/period;
 %Detuning parameter (wavelength deviation from Bragg wavelength)
dbeta=beta-beta0;
%=========================================================================

%===============Input parameters (All in SI Units)=======================
%Speed of light
c=299792458;
%Planck's constant
h=6.626068e-34;
%Pump wavelength
lambda_p=976e-9;
%Laser wavelength
lambda_l=lambdab;
%Pump light frequency
nu_p=c/lambda_p;
%Laser light frequency
nu_l=c/lambda_l;
 %Total Density of active ions
NT=5.8.*1e26;
%Effective absorption and emission cross-section data
cross=dlmread('Yb_Al2O3_cross_sections.dat');
%Effective absorption cross-section at pump wavelength
sigma_abs_p=interp1(cross(:,1),cross(:,2),lambda_p);
%Effective emission cross-section at pump wavelength
sigma_em_p=interp1(cross(:,1),cross(:,3),lambda_p);
%Effective absorption cross-section at laser wavelength
sigma_abs_l=interp1(cross(:,1),cross(:,2),lambda_l);
%Effective emission cross-section at laser wavelength
sigma_em_l=interp1(cross(:,1),cross(:,3),lambda_l);
%Propagation loss at pump wavelength
loss_int_p=0.25/4.34*100;
%Propagation loss at laser wavelength
loss_int_l=0.25/4.34*100;
%Lifetime of upper laser level
tau1=polyval([-0.075426 0.8187],5.8).*1e-3;
%Incident pump power
Pp0=100e-3;
%Fraction of pump power incident
P_inc_fract=1.0;
%Fraction of pump power from left
P_left_fract=1.0;
%Pump Power Incident on the gain medium from the left
P_left=Pp0*P_inc_fract*P_left_fract;
%Pump Power Incident on the gain medium from the right
P_right=Pp0*P_inc_fract*(1-P_left_fract);
%Number of roundtrips before considered converged
RT=2;
%Gain medium length
```

```
Z=10e-3;
%Number of discrete elements along the X-direction
Xnum=size(x,1);
%Number of discrete elements along the Y-direction
Ynum=size(y,2);
%Number of discrete elements along the Z-direction
Znum=101;
%Vector containing all the Z-elements
ZZ=linspace(0,Z,Znum);
%Size of a Z-element
dZ=Z/Znum;
%Population density of ground level
N0=ones(Xnum,Ynum,Znum).*NT;
%Polulation density of first excited level
N1=zeros(Xnum,Ynum,Znum);
%Initialize vector containing pump powers (incident from left)
%along the Z-direction
Ppf=zeros(1,Znum);
%Initialize vector containing all pump powers (incident from right)
%along the Z-direction
Ppr=zeros(1,Znum);
%All pump powers (incident from left) for which calculations are performed
ppf=linspace(0e-3,P_left,11);
%All pump powers (incident from right) for which calculations are performed
ppr=linspace(0,P_right,11);
%=========================================================================

%======================Main Simulation====================================
%Main loop for incrementing launched pump power and solving
%population densities and for laser power
for p=1:size(ppf,2)
    Plf=ones(1,Znum).*1e-8;
    Plr=ones(1,Znum).*1e-8;
    A=Plf;
    B=Plr;
    B0=sqrt(ppf(p));
    counter=1;
    %Loop executed until convergence criteria are met
    while ((Plr(1,Znum)*1e3≥1e-8) && (B0≥0))
        disp(num2str(Plr(1,Znum)));
        fac=sqrt(200*Plr(1,Znum)*(abs(0.6-0.5)/4+0.1251)/(kappa*10));
        B0=B0-fac;
        %Loop which propagates the optical fields RT times through the
        %cavities while updating the population densities
        %of the respective levels
        for r=1:RT
            %Loop for solving rate equations along laser length
            %by propagating in Z direction and solving population
            %density equations at each Z step:
            for j=1:Znum
                %Loop for solving rate equations along X-direction
```

```
%and solving population density equations at each X step:
for k=1:Xnum
    %Loop for solving rate equations along Y-direction
    %and solving population density equations
    %at each Y step:
    for l=1:Ynum
        if refractive_index_dist(k,l)==gain_n
            %Calculate absorption and gain coefficients
            %for all positions inside the gain medium
            alpha(k,l)=norm_pump_dist(k,l)*...
            (sigma_em_p*N1(k,l,j)-...
            sigma_abs_p*N0(k,l,j)-loss_int_p);
            gain(k,l)=norm_laser_dist(k,l)*...
            (sigma_em_l*N1(k,l,j)-sigma_abs_l*N0(k,l,j)...
            -loss_int_l);
        else
            %Calculate absorption and gain coefficients
            %for all positions outside the gain medium
            alpha(k,l)=norm_pump_dist(k,l)*(-loss_int_p);
            gain(k,l)=norm_laser_dist(k,l)*(-loss_int_l);
            N0(k,l,j)=0;
            N1(k,l,j)=0;
        end
    end
end
AA(j)=trapz(y,(trapz(x,alpha)));
GG(j)=trapz(y,(trapz(x,gain)));
%Calculating optical fields for first Z-element
if j==1
    a=trapz(y,(trapz(x,alpha)));
    g=trapz(y,(trapz(x,gain)));
    Ppf(1,j)=ppf(p);
    Ppr(1,j)=Ppr(1,j+1)*exp(a.*dZ);
    Plf(1,j)=0;
    B(1,j)=B0;
    Plr(1,j)=abs(B(1,j))^2;
%Calculating optical fields for last Z-element
elseif j==Znum
    a=trapz(y,(trapz(x,alpha)));
    g=trapz(y,(trapz(x,gain)));
    Ppf(1,j)=Ppf(1,j-1)*exp(a.*dZ);
    A(1,j)=A(1,j-1)+(-1i.*kappa*B(1,j-1)...
    .*exp(+i.*2.*dbeta.*ZZ(j-1)-i*pi)+g/2*A(1,j-1)).*dZ;
    B(1,j)=B(1,j-1)+(1i.*kappa*A(1,j-1)...
    .*exp(-i.*2.*dbeta.*ZZ(j-1)+i*pi)-g/2*B(1,j-1)).*dZ;
    Plf(1,j)=abs(A(1,j))^2;
    Plr(1,j)=abs(B(1,j))^2;
else
    %Calculating optical fields for all other Z-elements
    a=trapz(y,(trapz(x,alpha)));
    g=trapz(y,(trapz(x,gain)));
```

```
                    Ppr(1,j)=Ppr(1,j+1)*exp(a.*dZ);
                    Ppf(1,j)=Ppf(1,j-1)*exp(a.*dZ);
                    % Implement quarter-wavelength phase shift
                    if ZZ(j-1)>=Z*0.4
                        g=trapz(y,(trapz(x,gain)));
                        A(1,j)=A(1,j-1)+(-1i.*kappa*B(1,j-1).*exp(+i.*...
                        2.*dbeta.*ZZ(j-1)-i*pi)+g/2*A(1,j-1)).*dZ;
                        B(1,j)=B(1,j-1)+(1i.*kappa*A(1,j-1).*exp(-i.*...
                        2.*dbeta.*ZZ(j-1)+i*pi)-g/2*B(1,j-1)).*dZ;
                        Plf(1,j)=abs(A(1,j))^2;
                        Plr(1,j)=abs(B(1,j))^2;
                    else
                        g=trapz(y,(trapz(x,gain)));
                        A(1,j)=A(1,j-1)+(-1i.*kappa*B(1,j-1).*exp(+i.*...
                        2.*dbeta.*ZZ(j-1))+g/2*A(1,j-1)).*dZ;
                        B(1,j)=B(1,j-1)+(1i.*kappa*A(1,j-1).*exp(-i.*...
                        2.*dbeta.*ZZ(j-1))-g/2*B(1,j-1)).*dZ;
                        Plf(1,j)=abs(A(1,j))^2;
                        Plr(1,j)=abs(B(1,j))^2;
                    end
                end
                P(:,:,j)=((Ppf(1,j).*norm_pump_dist + ...
                Ppr(1,j).*norm_pump_dist))./(h*nu_p);
                L(:,:,j)=(Plf(1,j).*norm_laser_dist + ...
                Plr(1,j).*norm_laser_dist)./(h*nu_l);
                edd(j)=trapz(y,(trapz(x,L(:,:,j)*g)));
            end
            %Update population densities according to
            %calculated optical fields
            if r<=RT-1
                N1=NT.*(P.*sigma_abs_p + L.*sigma_abs_l)./(P.*...
                (sigma_abs_p+sigma_em_p) + L.*(sigma_abs_l+sigma_em_l) ...
                + 1/tau1);
                N0=NT-N1;
            end
        end
    end
%==========Plotting graphs=============================================
%Laser output power vs launched pump power
figure(80);
plot(ppf(p).*1e3,Plr(1,1).*1e3,'ob','linewidth',2)
hold on;
plot(ppf(p).*1e3,Plf(1,Znum).*1e3,'or','linewidth',2)
xlabel('Launched pump power [mw]')
ylabel('Laser power [mW]')
grid on
figure(82);
%Intra-cavity pump power
subplot(2,2,1)
plot(ZZ.*1000,Ppf.*1e3,'r','linewidth',2)
hold on;
```

```
    plot(ZZ.*1000,Ppr.*1e3,'b','linewidth',2)
    hold on;
    disp(['Transmitted pump power [mW]: ',num2str((Ppf(1,Znum).*1e3))])
    plot(ZZ.*1000,(Ppf(1,1)-Ppf).*1e3,':b','linewidth',2)
    xlabel('Gain Medium Length [mm]')
    ylabel('Pump Power [mW]')
    grid on;
    drawnow
    hold off;
    %Intra-cavity laser power
    subplot(2,2,2)
    plot(ZZ.*1000,(Plf).*1e3,'-r','linewidth',2)
    hold on;
    plot(ZZ.*1000,(Plr).*1e3,'-b','linewidth',2)
    plot(ZZ.*1000,(Plr+Plf).*1e3,':k','linewidth',2)
    xlabel('Gain Medium Length [mm]')
    ylabel('Laser Power [mW]')
    grid on;
    drawnow
    hold off;
    %Absorption coeff
    subplot(2,2,3)
    plot(ZZ.*1e3,abs(AA).*4.34/100,'b','linewidth',2)
    xlabel('Waveguide Length [mm]')
    ylabel('Absorption Coefficient [dB/cm]')
    grid on;
    drawnow;
    %Gain coeff
    subplot(2,2,4)
    plot(ZZ.*1e3,GG.*4.34/100,'b','linewidth',2)
    xlabel('Waveguide Length [mm]')
    ylabel('Gain Coefficient [dB/cm]')
    grid on;
    drawnow;
 end
%=========================================================================

%=========================================================================
```

Bibliography

[1] A. Einstein, "The quantum theory of radiation", *Physikalische Zeitschrift* **18**, 121 (1917).

[2] A. L. Schawlow and C. H. Townes, "Infrared and optical masers", *Physical Review* **112**, 1940 (1958).

[3] T. H. Maiman, "Stimulated optical radiation in ruby", *Nature* **187**, 493 (1960).

[4] T. Kitagawa, F. Bilodeau, B. Malo, S. Theriault, J. Albert, D. C. Jihnson, K. O. Hill, K. Hattori, and Y. Hibino, "Single-frequency Er^{3+}-doped silica-based planar waveguide laser with integrated photo-imprinted Bragg reflectors", *Electronics Letters* **30**, 1311 (1994).

[5] S. Blaize, L. Bastard, C. Cassagnètes, and J. E. Broquin, "Multiwavelengths DFB waveguide laser arrays in Yb-Er codoped phosphate glass substrate", *IEEE Photonics Technology Letters* **15**, 516 (2003).

[6] L. Bastard, S. Blaize, and J. E. Broquin, "Glass integrated optics ultranarrow linewidth distributed feedback laser matrix for dense wavelength division multiplexing applications", *Optical Engineering* **42**, 2800 (2003).

[7] G. D. Marshall, P. Dekker, M. Ams, J. A. Piper, and M. J. Withford, "Directly written monolithic waveguide laser incorporating a distributed feedback waveguide-Bragg grating", *Optics Letters* **33**, 956 (2008).

[8] M. Ams, P. Dekker, G. D. Marshall, and M. J. Withford, "Monolithic 100 mW Yb waveguide laser fabricated using the femtosecond-laser direct-write technique", *Optics Letters* **34**, 247 (2009).

[9] B. K. Das, H. Suche, and W. Sohler, "Single-frequency Ti:Er:$LiNbO_3$ distributed Bragg reflector waveguide laser with thermally fixed photorefractive cavity", *Applied Physics B* **73**, 439 (2001).

[10] B. K. Das, R. Ricken, and W. Sohler, "Integrated optical distributed feedback laser with Ti:Fe:Er:$LiNbO_3$ waveguide", *Applied Physics Letters* **82**, 1515 (2003).

[11] B. K. Das, R. Ricken, V. Quiring, H. Suche, and W. Sohler, "Distributed feedback-distributed Bragg reflector coupled cavity laser with a Ti:(Fe:)Er:$LiNbO_3$ waveguide", *Optics Letters* **29**, 165 (2004).

[12] D. Geskus, S. Aravazhi, E. Bernhardi, C. Grivas, S. Harkema, K. Hametner, D. Günther, K. Wöorhoff, and M. Pollnau, "Low-threshold, highly efficient Gd^{3+}, Lu^{3+} co-doped $KY(WO_4)_2$:Yb^{3+} planar waveguide lasers", *Laser Physics Letters* **6**, 800 (2009).

[13] D. Geskus, S. Aravazhi, C. Grivas, K. Wörhoff, and M. Pollnau, "Microstructured $KY(WO_4)_2$:Gd^{3+}, Lu^{3+}, Yb^{3+} channel waveguide laser", *Optics Express* **18**, 8853 (2010).

[14] K. van Dalfsen, S. Aravazhi, D. Geskus, K. Wörhoff, and M. Pollnau, "Efficient $KY_{1-x-y}Gd_xLu_y(WO_4)_2$:$Tm^{3+}$ channel waveguide lasers", *Optics Express* **19**, 5277 (2011).

[15] J. J. Zayhowski and A. Mooradian, "Single-frequency microchip Nd lasers", *Optics Letters* **14**, 24 (1989).

[16] J. L. Zyskind, J. W. Sulhoff, Y. Sun, J. Stone, L. W. Stulz, G. T. Harvey, D. J. Digiovanni, H. M. Presby, A. Piccirilli, U. Koren, and R. M. Jopson, "Singlemode diode-pumped tunable erbium-doped fibre laser with linewidth less than 5.5 kHz", *Electronics Letters* **27**, 2148 (1991).

[17] I. D. Henning, L. D. Westbrook, A. W. Nelson, and A. W. Fiddyment, "Measurements of the linewidth of ridge-guide DFB Lasers", *Electronics Letters* **20**, 885 (1984).

[18] T. Kunii and Y. Matsui, "Narrow spectral linewidth semiconductor lasers", *Optical and Quantum Electronics* **24**, 719 (1992).

[19] C. Laperle, M. Svilans, M. Poirier, and M. Têtu, "Frequency multiplication of microwave signals by sideband optical injection locking using a monolithic dual-wavelength DFB laser device", *IEEE Transactions on Microwave Theory and Techniques* **47**, 1219 (1999).

[20] P. Signoret, M. Myara, J. P. Tourrenc, B. Orsal, M. H. Monier, J. Jacquet, P. Leboudec, and F. Marin, "Bragg section effects on linewidth and lineshape in 1.55-μm DBR tunable laser diodes", *IEEE Photonics Technology Letters* **16**, 1429 (2004).

[21] A. J. Seeds and K. J. Williams, "Microwave photonics", *Journal of Lightwave Technology* **24**, 4628 (2006).

[22] J. A. Nolde, J. W. Raring, and L. A. Coldren, "Increased modal overlap for improved sensitivity in a monolithic intracavity chemical sensor", *IEEE Photonics Technology Letters* **19**, 1051 (2007).

[23] K. Paschke, S. Spießberger, C. Kaspari, D. Feise, C. Fiebig, G. Blume, H. Wenzel, A. Wicht, and G. Erbert, "High-power distributed Bragg reflector ridge-waveguide diode laser with very small spectral linewidth", *Optics Letters* **35**, 402 (2010).

[24] C. H. Henry, "Theory of the linewidth of semiconductor lasers", *IEEE Journal of Quantum Electronics* **QE-18**, 259 (1982).

[25] M. Okai, T. Tsuchiya, K. Uomi, N. Chinone, and T. Harada, "Corrugation-pitch-modulated MQW-DFB laser with narrow spectral linewidth (170 kHz)", *IEEE Photonics Technology Letters* **2**, 529 (1990).

[26] T. Kunii, Y. Matsui, H. Horikawa, T. Kamijoh, and T. Nonaka, "Narrow linewidth (85 kHz) operation in long cavity 1.5 μm-MQW DBR Laser", *Electronics Letters* **27**, 691 (1991).

[27] M. Okai, M. Suzuki, and T. Taniwatari, "Strained multiquantum-well corrugation-pitch-modulated distributed feedback laser with ultranarrow (3.6 kHz) spectral linewidth", *Electronics Letters* **29**, 1696 (1993).

[28] P. Dowd, I. H. White, M. R. T. Tan, and S. Y. Wang, "Linewidth narrowed vertical-cavity surface-emitting lasers for millimeter-wave generation by optical heterodyning", *IEEE Journal of Selected Topics in Quantum Electronics* **3**, 405 (1997).

[29] L. Hsu, A. Mooradian, and R. L. Aggarwal, "Spectral linewidth of a free-running continuous-wave single-frequency external-cavity quantum-well InGaAs/AlGaAs diode laser", *Optics Letters* **20**, 1788 (1995).

[30] D. Erni, M. M. Spüler, and J. Fröhlich, "Evolutionary optimization of non-periodic coupled-cavity semiconductor laser diodes", *Optical an Quantum Electronics* **30**, 287 (1998).

[31] G. Adolfsson, J. Bengtsson, and A. Larsson, "Spectral engineering of semiconductor Fabry-Perot laser cavities in the weakly and strongly perturbed regimes", *Journal of the Optical Society of America B* **27**, 118 (2010).

[32] R. M. Lammert, J. S. Hughes, S. D. Roh, M. L. Osowski, A. M. Jones, and J. J. Coleman, "Low-threshold narrow-linewidth InGaAs-GaAs ridge-waveguide DBR lasers with first-order surface gratings", *IEEE Photonics Technology Letters* **9**, 149 (1997).

[33] R. K. Price, J. J. Borchardt, V. C. Elarde, R. B. Swint, and J. J. Coleman, "Narrow-linewidth asymmetric cladding distributed Bragg reflector semiconductor lasers at 850 nm", *IEEE Photonics Technology Letters* **18**, 97 (2006).

[34] B. Kelly, R. Phelan, D. Jones, C. Herbert, J. O'Carroll, M. Rensing, J. Wendelboe, C. B. Watts, A. Kaszubowska-Anandarajah, P. Perry, C. Guignard, L. P. Barry, and J. O'Gorman, "Discrete mode laser diodes with very narrow linewidth emission", *Electronics Letters* **43**, 1282 (2007).

[35] G. M. Hale and M. R. Querry, "Optical constants of water in the 200-nm to 200-μm wavelength region", *Applied Optics* **12**, 555 (1973).

[36] K. Iwatsuki, H. Okamura, and M. Saruwatari, "Wavelength-tunable single-frequency and single-polarization Er-doped fibre ring-laser with 1.4 kHz linewidth", *Electronics Letters* **26**, 2033 (1990).

[37] G. A. Ball, W. W. Morey, and W. H. Glenn, "Standing-wave monomode erbium fiber laser", *IEEE Photonics Technology Letters* **3**, 613 (1991).

[38] W. H. Loh, B. N. Samson, L. Dong, G. J. Cowle, and K. Hsu, "High performance single frequency fiber grating-based erbium:ytterbium-codoped fiber lasers", *Journal of Lightwave Technology* **16**, 114 (1998).

[39] C. Spiegelberg, J. Geng, Y. Hu, Y. Kaneda, S. Jiang, and N. Peyghambarian, "Low-noise narrow-linewidth fiber laser at 1550 nm (June 2003)", *Journal of Lightwave Technology* **22**, 57 (2004).

[40] J. Sun, Y. Dai, X. Chen, Y. Zhang, and S. Xie, "Stable dual-wavelength DFB fiber laser with separate resonant cavities and its application in tunable microwave generation", *IEEE Photonics Technology Letters* **18**, 2587 (2006).

[41] B. Wu, Y. Liu, Z. Dai, and S. Liu, "Stable narrow linewidth Er-doped fiber laser at 1550 nm", *Microwave and Optical Technology Letters* **49**, 1453 (2007).

[42] A. C. L. Wong, D. Chen, H.-J. Wang, W. H. Chung, H.-Y. Tam, C. Lu, and B.-O. Guan, "Extremely short distributed Bragg reflector fibre lasers with sub-kilohertz linewidth and ultra-low polarization beat frequency for sensing applications", *Measurement Science and Technology* **22**, 045202 (2011).

[43] G. J. Simonis and K. G. Purchase, "Optical generation, distribution, and control of microwaves using laser heterodyne", *IEEE Transactions on Microwave Theory and Techniques* **38**, 667 (1990).

[44] P. Laporta, S. Taccheo, S. Longhi, and O. Svelto, "Diode-pumped microchip Er-Yb:glass laser", *Optics Letters* **18**, 1232 (1993).

[45] I. Baumann, S. Bosso, R. Brinkmann, R. Corsini, M. Dinand, A. Greiner, K. Schäfer, J. Söchtig, W. Sohler, H. Suche, and R. Wessel, "Er-doped integrated optical devices in $LiNbO_3$", *IEEE Journal of Selected Topics in Quantum Electronics* **2**, 355 (1996).

[46] D. L. Veasey, D. S. Funk, N. A. Sanford, and J. S. Hayden, "Arrays of distributed-Bragg-reflector waveguide lasers at 1536 nm in Yb/Er codoped phosphate glass", *Applied Physics Letters* **74**, 789 (1999).

[47] L. Xiao, S. Trebaol, Y. Dumeige, Z. Cai, M. Mortier, and P. Féron, "Miniaturized optical microwave source using a dual-wavelength whispering gallery mode laser", *IEEE Photonics Technology Letters* **22**, 559 (2010).

[48] L. Yang, T. Lu, T. Carmon, B. Min, and K. J. Vahala, "A 4-Hz fundamental linewidth on-chip microlaser", *Conference on Lasers and Electro-Optics/Quantum Electronics and Laser Science Conference and Photonic Applications Systems Technologies* **CMR2** (2007).

[49] A. Meijerink, C. G. H. Roeloffzen, R. Meijerink, L. Zhuang, D. A. I. Marpaung, M. J. Bentum, M. Burla, J. Verpoorte, P. Jorna, A. Hulzinga, and W. van Etten, "Novel ring resonator-based integrated photonic beamformer for broadband phased array receive antennas-part I: design and derformance analysis", *Journal of Lightwave Technology* **28**, 3 (2010).

[50] D. Marpaung, C. Roeloffzen, W. Beeker, B. Noharet, J. Verpoorte, and R. Baggen, "Development of a broadband and squint-free Ku-band phased array antenna system for airborne satellite communications", In S. Plass, editor, *Future Aeronautical Communications*. InTech (2011).

[51] J. Yao, "Microwave photonics", *Journal of Lightwave Technology* **27**, 314 (2009).

[52] J. Capmany and D. Novak, "Microwave photonics combines two worlds", *Nature Photonics* **1**, 319 (2007).

[53] A. M. Armani, R. P. Kulkarni, S. E. Fraser, R. C. Flagan, and K. J. Vahala, "Label-free, single-molecule detection with optical microcavities", *Science* **317**, 783 (2007).

[54] S. Mandal and D. Erickson, "Nanoscale optofluidic sensor arrays", *Optics Express* **16**, 1623 (2008).

[55] F. Vollmer, S. Arnold, and D. Keng, "High sensitivity nanoparticle detection using optical microcavities", *Proceedings of the National Academy of Sciences of the United States* **105**, 20701 (2007).

[56] J. Zhu, S. K. Özdemir, Y. F. Xiao, L. Li, L. He, D. R. Chen, and L. Yang, "On-chip single nanoparticle detection and sizing by mode splitting in an ultrahigh-Q microresonator", *Nature Photonics* **4**, 46 (2009).

[57] T. Lu, H. Lee, T. Chen, S. Herchak, J. H. Kim, S. E. Fraser, R. C. Flagan, and K. J. Vahala, "High sensitivity nanoparticle detection using optical microcavities", *Proceedings of the National Academy of Sciences of the United States* **108**, 5976 (2011).

[58] S. V. Pham, M. Dijkstra, A. J. F. Hollink, L. J. Kauppinen, R. M. de Ridder, M. Pollnau, P. V. Lambeck, and H. J. W. M. Hoekstra, "On-chip bulk-index concentration and direct, label-free protein sensing utilizing an optical grated-waveguide cavity", submitted (2012).

[59] G. N. van den Hoven, E. Snoeks, A. Polman, J. W. M. van Uffelen, Y. S. Oei, and M. K. Smit, "Photoluminescence characterization of Er-implanted Al_2O_3 films", *Applied Physics Letters* **62**, 3065 (1993).

[60] J. D. B. Bradley, L. Agazzi, D. Geskus, F. Ay, K. Wörhoff, and M. Pollnau, "Gain bandwidth of 80 nm and 2 dB/cm peak gain in Al_2O_3:Er^{3+} optical amplifiers on silicon", *Journal of the Optical Society of America B* **27**, 187 (2010).

[61] A. Polman, D. C. Jacobson, D. J. Eaglesham, R. C. Kistler, and J. M. Poate, "Optical doping of waveguide materials by MeV Er implantation", *Applied Physics* **70**, 3778 (1991).

[62] K. Wörhoff, J. D. B. Bradley, F. Ay, D. Geskus, T. P. Blauwendraat, and M. Pollnau, "Reliable low-cost fabrication of low-loss aler waveguides with 5.4-dB optical gain", *IEEE Journal of Quantum Electronics* **45**, 454 (2009).

[63] L. Agazzi, J. D. B. Bradley, M. Dijkstra, F. Ay, G. Roelkens, R. Baets, K. Wörhoff, and M. Pollnau, "Monolithic integration of erbium-doped amplifiers with silicon-on-insulator waveguides", *Optics Express* **18**, 27703 (2010).

[64] J. D. B. Bradley, M. C. Silva, M. Gay, L. Bramerie, A. Driessen, K. Wörhoff, J. C. Simon, and M. Pollnau, "170 Gbit/s transmission in an erbium-doped waveguide amplifier on silicon", *Optics Express* **17**, 22201 (2009).

[65] J. D. B. Bradley, R. Stoffer, A. Bakker, L. Agazzi, F. Ay, K. Wörhoff, and M. Pollnau, "Integrated Al_2O_3:Er^{3+}zero-loss optical amplifier and power splitter with 40-nm bandwidth", *IEEE Photonics Technology Letters* **22**, 278 (2010).

[66] J. D. B. Bradley, R. Stoffer, L. Agazzi, K. Wörhoff, and M. Pollnau, "Integrated Al_2O_3:Er^{3+} ring lasers on silicon with wide wavelength selectivity", *Optics Letters* **35**, 73 (2010).

[67] J. Yang, K. van Dalfsen, K. Wörhoff, F. Ay, and M. Pollnau, "High-gain Al_2O_3:Nd^{3+}channel waveguide amplifiers at 880 nm, 1060 nm, and 1330 nm", *Applied Physics B* **101**, 119 (2010).

[68] J. Yang, T. Lamprecht, K. Wörhoff, A. Driessen, F. Horst, B. J. Offrein, F. Ay, and M. Pollnau, "Integrated optical backplane amplifier", *IEEE Journal of Selected Topics in Quantum Electronics* **17**, 609 (2011).

[69] A. Polman, "Erbium as a probe of everything?", *Physica B* **300**, 78 (2001).

[70] L. Agazzi, *Spectroscopic excitation and quenching processes in rare-earth-ion-doped Al_2O_3 and their impact on amplifier and laser performance*, PhD thesis University of Twente (2012).

[71] H. M. Pask, R. J. Carman, D. C. Hanna, A. C. Tropper, C. J. Mackechnie, P. R. Barber, and J. M. Dawes, "Ytterbium-doped silica fiber lasers: versatile sources for the 1-1.2 μm region", *IEEE Journal of Selected Topics in Quantum Electronics* **1**, 2 (1995).

[72] X. Zou and T. Izumitani, "Spectroscopic properties and mechanisms of excited state absorption and energy transfer upconversion for Er^{3+}-doped glasses", *Journal of Non-Crystalline Solids* **162**, 68 (1993).

[73] J. M. Castro, D. F. Geraghty, S. Honkanen, C. M. Greiner, D. Iazikov, and T. W. Mossberg, "Optical add-drop multiplexers based on the antisymmetric waveguide Bragg grating", *Applied Optics* **45**, 1236 (2006).

[74] C. J. Brooks, G. L. Vossler, and K. A. Winick, "Integrated-optic dispersion compensator that uses chirped gratings", *Optics Letters* **20**, 368 (1995).

[75] S. Yliniemi, J. Albert, Q. Wang, and S. Honkanen, "UV-exposed Bragg gratings for laser applications in silver-sodium ion-exchanged phosphate glass waveguides", *Optics Express* **14**, 2898 (2006).

[76] G. D. Marshall, M. Ams, and M. J. Withford, "Direct laser written waveguide-Bragg gratings in bulk fused silica", *Optics Letters* **31**, 2690 (2006).

[77] H. Kogelnik and C. V. Shank, "Coupled-wave theory of distributed feedback lasers", *Journal of Applied Physics* **43**, 2327 (1972).

[78] A. Yariv, "Coupled-mode theory for guided-wave optics", *IEEE Journal of Quantum Electronics* **QE-9**, 919 (1973).

[79] A. Yariv and H. W. Yen, "Bragg amplification and oscillation in periodic optical media", *Optics Communications* **10**, 120 (1974).

[80] W. P. Huang, "Coupled-mode theory for optical waveguides: an overview", *Journal of the Optical Society of America A* **11**, 963 (1994).

[81] A. Yariv and M. Nakamura, "Periodic structures for integrated optics", *IEEE Journal of Quantum Electronics* **QE-13**, 233 (1977).

[82] M. Yamada and K. Sakuda, "Analysis of almost-periodic distributed feedback slab waveguides via a fundamental matrix approach", *Applied Optics* **26**, 3474 (1987).

[83] M. A. Rodriguez, M. S. Malcuit, and J. J. Butler, "Transmission properties of refractive index-shifted Bragg gratings", *Optics Communications* **177**, 251 (2000).

[84] C. L. Chen, *Foundations for guided wave optics*, John Wiley and Sons (2007).

[85] M. G. Dyndgaard, *Ytterbium- and erbium-doped silica for planar waveguide lasers and amplifiers*, PhD thesis Technical University of Denmark (2001).

[86] M. A. Muriel, A. Carballar, and J. Azaña, "Field distributions inside fiber gratings", *IEEE Journal of Quantum Electronics* **35**, 548 (1999).

[87] T. E. Murphy, *Design, fabrication and measurement of integrated Bragg grating optical filters*, PhD thesis Massachusetts Institute of Technology (2001).

[88] T. Erdogan, "Fiber grating spectra", *Journal of Lightwave Technology* **15**, 1277 (1997).

[89] J. I. Kinoshita and K. Matsumoto, "Yield analysis of SLM DFB lasers with an axially-flattened internal field", *IEEE Journal of Quantum Electronics* **25**, 1324 (1989).

[90] J. E. A. Whiteaway, B. Garrett, G. H. B. Thompson, A. J. Collar, C. J. Armistead, and M. J. Fice, "The static and dynamic characteristics of single and multiple phase-shifted DFB laser structures", *IEEE Journal of Quantum Electronics* **28**, 1277 (1992).

[91] S. W. Løvseth and E. Rønnekleiv, "Fundamental and higher order mode thresholds of DFB fiber lasers", *Journal of Lightwave Technology* **20**, 494 (2002).

[92] D. I. Babic and S. W. Corzine, "Analytic expressions for the reflection delay, penetration depth, and absorptance of quarter-wave dielectric mirrors", *IEEE Journal of Quantum Electronics* **28**, 514 (1992).

[93] J. D. B. Bradley, *Al_2O_3:Er^{3+} as a gain platform for integrated optics*, PhD thesis Integrated Optical MicroSystems (IOMS) Group, Faculty of Electrical Engineering, Mathematics and Computer Science, MESA+ Institute for Nanotechnology (2009).

[94] H. A. Haus and C. V. Shank, "Antisymmetric taper of distributed deedback lasers", *IEEE Journal of Quantum Electronics* **QE-12**, 532 (1976).

[95] S. L. McCall and P. M. Platzman, "An optimized $\pi/2$ distributed feedback laser", *IEEE Journal of Quantum Electronics* **QE-21**, 1899 (1985).

[96] K. Tada, "Proposal of a distributed feedback laser with nonuniform stripe width for complete single-mode oscillation", *Microelectronic Engineering* **2**, 157 (1984).

[97] K. Utaka, S. Akiba, K. Sakai, and Y. Matsushima, "$\lambda/4$-shifted InGaAsP/InP DFB lasers by simultaneous holographic exposure of positive and negative photoresists", *Electronics Letters* **20**, 1008 (1984).

[98] M. Lax, "Classical noise. V. Noise in self-sustained oscillators", *Physical Review* **160**, 290 (1967).

[99] H. Haken, "Laser Theory", In S. Flügge, editor, *Encyclopedia of Physics* volume XXV 2C. Springer-Verlag (1970).

[100] M. Eichhorn and M. Pollnau, "The theory of continuous-wave lasers in the spot light of the vacuum photon", submitted (2012).

[101] H. A. Kramers, "La diffusion de la lumiére par les atomes", *Atti del Congresso Internazionale dei Fisici* **2**, 545 (1927).

[102] R. L. Kronig, "On the theory of the dispersion of X-rays", *Journal of the Optical Society of America* **12**, 547 (1926).

[103] E. Rønnekleiv, "Frequency and intensity noise of single frequency fiber Bragg grating lasers", *Optical Fiber Technology* **7**, 206 (2001).

[104] S. W. Løvseth, J. T. Kringlebotn, and E. Rønnekleiv, "Fiber distributed-feedback lasers used as acoustic sensors in air", *Applied Optics* **38**, 4821 (1999).

[105] S. Foster, A. Tikhomirov, and M. Milnes, "Fundamental thermal noise in distributed feedback fiber lasers", *IEEE Journal of Quantum Electronics* **43**, 378 (2007).

[106] S. Foster, G. A. Cranch, and A. Tikhomirov, "Experimental evidence for the thermal origin of 1/f frequency noise in erbium-doped fiber lasers", *Physical Review A* **79**, 053802 (2009).

[107] N. Bucalovic, V. Dolgovskiy, C. Schori, P. Thomann, G. Di Domenico, and S. Schilt, "Experimental validation of a simple approximation to determine the linewidth of a laser from its frequency noise spectrum", *Applied Optics* **51**, 4582 (2012).

[108] K. Petermann, "External optical feedback phenomena in semiconductor lasers", *IEEE Journal of Selected Topics in Quantum Electronics* **1**, 480 (1995).

[109] G. A. Acket, D. Lenstra, A. den Boef, and B. H. Verbeek, "The influence of feedback intensity on longitudinal mode properties and optical noise in index-guided semiconductor lasers", *IEEE Journal of Quantum Electronics* **QE-20**, 1163 (1984).

[110] D. Lenstra, B. H. Verbeek, and A. J. den Boef, "Coherence collapse in single-mode semiconductor lasers due to optical feedback", *IEEE Journal of Quantum Electronics* **QE-21**, 674 (1985).

[111] R. W. Tkach and A. R. Chraplyvy, "Regimes of feedback effects in 1.5-μm distributed feedback lasers", *Journal of Lightwave Technology* **LT-4**, 1655 (1986).

[112] C. H. Henry and R. F. Kazarinov, "Instability of semiconductor lasers due to optical feedback from distant reflectors", *IEEE Journal of Quantum Electronics* **QE-22**, 294 (1986).

[113] F. Favre, "Theoretical analysis of external optical feedback on DFB semiconductor lasers", *IEEE Journal of Quantum Electronics* **QE-23**, 81 (1987).

[114] H. Li, J. Ye, and J. G. McInerney, "Detailed analysis of coherence collapse in semiconductor lasers", *IEEE Journal of Quantum Electronics* **29**, 2421 (1993).

[115] E. Rønnekleiv, O. Hadeler, and G. Vienne, "Stability of an Er-Yb-doped fiber distributed-feedback laser with external reflections", *Optics Letters* **24**, 617 (1999).

[116] A. Tikhomirov and S. Foster, "DFB FL sensor cross-coupling reduction", *Journal of Lightwave Technology* **25**, 533 (2007).

[117] T. Hirono, T. Kurosaki, and M. Fukuda, "Transition from the lowest linewidth mode operation to coherence collapse in a semiconductor laser with feedback from a distant reflector", *IEEE Journal of Quantum Electronics* **32**, 829 (1996).

[118] K. Kikuchi and T. Okoshi, "Simple formula giving spectrum-narrowing ratio of semiconductor-laser output obtained by optical feedback", *Electronics Letters* **18**, 10 (1982).

[119] J. O. Binder and G. D. Cormack, "Mode selection and stability of a semiconductor laser with weak optical feedback", *IEEE Journal of Quantum Electronics* **25**, 2255 (1989).

[120] N. Schunk and K. Petermann, "Numerical analysis of the feedback regimes for a single-mode semiconductor laser with external feedback", *IEEE Journal of Quantum Electronics* **24**, 1242 (1988).

[121] L. Agazzi, E. H. Bernhardi, K. Wörhoff, and M. Pollnau, "Impact of luminescence quenching on relaxation-oscillation frequency in solid-state lasers", *Applied Physics Letters* **100**, 011109 (2012).

[122] J. D. B. Bradley, F. Ay, K. Wörhoff, and M. Pollnau, "Fabrication of low-loss channel waveguides in Al_2O_3 and Y_2O_3 layers by inductively coupled plasma reactive ion etching", *Applied Physics B* **89**, 311 (2007).

[123] R. Luttge, H. A. G. M. van Wolferen, and L. Abelmann, "Laser interferometric nanolithography using a new positive chemical amplified resist", *Journal of Vacuum Science and Technology B* **25**, 2476 (2007).

[124] H. van Wolferen and L. Abelmann, "Laser interference lithography", In T. C. Hennessy, editor, *Lithography: Principles, Processes and Materials*. Nova Science Publichers, Inc. (2011).

[125] J. Yang, *Neodymium-doped waveguide amplifiers and lasers for integrated optical applications*, PhD thesis Integrated Optical MicroSystems Group, University of Twente (2010).

[126] T. E. Murphy, J. T. Hastings, and H. I. Smith, "Fabrication and characterization of narrow-band Bragg-reflection filters in silicon-on-insulator ridge waveguides", *Journal of Lightwave Technology* **19**, 1938 (2001).

[127] S. Legoubin, M. Douay, P. Bernage, P. Niay, S. Boj, and E. Delevaque, "Free spectral range variations of grating-based Fabry-Perot filters photowritten in optical fibers", *Journal of the Optical Society of America A* **12**, 1687 (1995).

[128] G. Tittelbacht, B. Richter, and W. Karthe, "Comparison of three transmission methods for integrated optical waveguide propagation loss measurement", *Pure and Applied Optics* **2**, 683 (1993).

[129] S. Taebi, M. Khorasaninejad, and S. S. Saini, "Modified Fabry-Perot interferometric method for waveguide loss measurement", *Applied Optics* **47**, 6625 (2008).

[130] B. A. E. Saleh and M. C. Teich, *Fundamentals of photonics*, John Wiley & Sons New York (1991).

[131] V. C. Lauridsen, J. H. Povlsen, and P. Varming, "Design of DFB fibre lasers", *Electronics Letters* **34**, 2028 (1998).

[132] R. K. Chang and A. J. Campillo, *Optical processes in microcavities*, World Scientific Singapore (1996).

[133] A. Blaize, L. Bastard, C. Cassagnetes, G. Vitrant, and J. E. Broquin, "Ion-exchanged glass DFB Lasers for DWDM", In *SPIE - Photonics West* volume 4640 pages 218–225 San Jose, CA, USA (2002).

[134] D. L. Veasey, J. M. Gary, J. Amin, and J. A. Aust, "Time-dependent modeling of erbium-doped waveguide lasers in lithium niobate pumped at 980 and 1480 nm", *IEEE Journal of Selected Topics in Quantum Electronics* **33**, 1647 (1997).

[135] T. Okoshi, K. Kikuchi, and A. Nakayama, "Novel method for high resolution measurement of laser output spectrum", *Electronics Letters* **16**, 630 (1980).

[136] L. E. Richter, H. I. Mandelberg, M. S. Kruger, and P. A. McGrath, "Linewidth determination from self-heterodyne measurements with subcoherence delay times", *IEEE Journal of Quantum Electronics* **QE-22**, 2070 (1986).

[137] C. Lennartz, W. van Etten, T. van Osch, and F. Huijskens, "Laser spectra measured with the recirculating self heterodyne technique", *Journal of Optical Communications* **17**, 138 (1996).

[138] S. Foster, "Dynamical noise in single-mode distributed feedback fiber lasers", *IEEE Journal of Quantum Electronics* **40**, 1283 (2004).

[139] J. Siebenmorgen, T. Calmano, K. Petermann, and G. Huber, "Highly efficient Yb:YAG channel waveguide laser written with a femtosecond-laser", *Optics Express* **18**, 16035 (2010).

[140] W. W. Rigrod, "Saturation effects in high-gain lasers", *Journal of Applid Physics* **36**, 2487 (1965).

[141] D. L. Veasey, D. S. Funk, P. M. Peters, N. A. Sanford, G. E. Obarski, N. Fontaine, M. Young, A. P. Peskin, W. Liu, S. N. Houde-Walter, and J. S. Hayden, "Yb/Er-codoped and Yb-doped waveguide lasers in phosphate glass", *Journal of Non-Crystalline Solids* **263&264**, 369 (2000).

[142] J. Sun, Y. Dai, Y. Zhang, X. Chen, and S. Xie, "Dual-wavelength DFB fiber laser based on unequalized phase shifts", *IEEE Photonics Technology Letters* **18**, 2493 (2006).

[143] D. Chen, H. Fu, W. Liu, Y. Wei, and S. He, "Dual-wavelength single-longitudinal-mode erbium-doped fibre laser based on fibre Bragg grating pair and its application in microwave signal generation", *Electronics Letters* **44**, 459 (2008).

[144] Y. Yao, X. Chen, Y. Dai, and S. Xie, "Dual-wavelength erbium-doped fiber laser with a simple linear cavity and its application in microwave generation", *IEEE Photonics Technology Letters* **18**, 187 (2006).

[145] J. Sun, Y. Huang, H. Li, and C. Jiang, "Photonic generation of microwave signals using dual-wavelength single-longitudinal-mode fiber lasers", *Optik* **122**, 764–768 (2011).

[146] R. K. Price, V. B. Verma, K. E. Tobin, V. C. Elarde, and J. J. Coleman, "Y-Branch surface-etched distributed Bragg reflector lasers at 850 nm for optical heterodyning", *IEEE Photonics Technology Letters* **19**, 1610 (2007).

[147] G. E. Villanueva, P. Pérez-Millán, J. Palací, J. L. Cruz, M. V. Andrés, and J. Martí, "Dual-wavelength DFB erbium-doped fiber laser with tunable wavelength spacing", *IEEE Photonics Technology Letters* **22**, 254 (2010).

[148] L. Xia, P. Shum, Y. Wang, and T. H. Cheng, "Stable triple-wavelength fiber ring laser with ultranarrow wavelength spacing using a triple-transmission-band fiber Bragg grating filter", *IEEE Photonics Technology Letters* **18**, 2162 (2006).

[149] M. Brunel, A. Amon, and M. Vallet, "Dual-polarization microchip laser at 1.53 μm", *Optics Letters* **30**, 2418 (2005).

[150] M. R. H. Khan, E. H. Bernhardi, D. A. I. Marpaung, M. Burla, R. M. de Ridder, K. Wörhoff, M. Pollnau, and C. G. H. Roeloffzen, "Dual-frequency distributed feedback laser with optical frequency locked loop for stable microwave signal generation", *Photonics Technology Letters* **24**, 1431 (2012).

[151] M. L. Gorodetsky, A. A. Savchenkov, and V. S. Ilchenko, "Ultimate Q of optical microsphere resonators", *Optics Letters* **21**, 453 (1996).

[152] L. Collot, V. Levèvre-Sequin, M. Brune, R. J. M, and S. Haroche, "Very high-Q whispering-gallery mode resonances observed on fused silica", *Europhysics Letters* **23**, 327 (1993).

[153] D. K. Armani, T. J. Kippenberg, S. M. Spillane, and K. J. Vahala, "Ultra-high-Q toroid microcavity on a chip", *Nature* **421**, 925 (2003).

[154] H. Lee, T. Chen, J. Li, K. Y. Yang, S. Jeon, O. Painter, and K. Vahala, "Chemically etched ultrahigh-Q wedge-resonator on a silicon chip", *Nature Photonics* **6**, 369 (2012).

[155] L. He, S. K. Özdemir, J. Zhu, W. Kim, and L. Yang, "Detecting single viruses and nanoparticles using whispering gallery microlasers", *Nature Nanotechnology* **6**, 428 (2011).

[156] J. Yang and L. J. Guo, "Optical sensors based on active microcavities", *IEEE Journal of Selected Topics in Quantum Electronics* **12**, 143 (2006).

[157] L. He, S. K. Özdemir, J. Zhu, and L. Yang, "Ultrasensitive detection of mode splitting in active optical microcavities", *Physical Review A* **82**, 053810 (2010).

[158] D. A. Cohen, J. A. Nolde, A. T. Pedretti, C. S. Wang, E. J. Skogen, and L. A. Coldren, "Sensitivity and scattering in a monolithic heterodyned laser biochemical sensor", *IEEE Journal of Selected Topics in Quantum Electronics* **9**, 1124 (2003).

[159] W. A. Clarkson, "Thermal effects and their mitigation in end-pumped solid-state lasers", *Journal of Physics D: Applied Physics* **34**, 2381 (2001).

[160] W. C. L. Hopman, K. O. van der Werf, A. J. F. Hollink, W. Bogaerts, V. Subramaniam, and R. M. de Ridder, "Modeling and experimental verification of the dynamic interaction of an AFM-Tip with a photonic crystal microcavity", *IEEE Photonics Technology Letters* **20**, 57 (2008).

[161] D. A. Cohen, C. S. Wang, J. A. Nolde, D. D. Lofgreen, and L. A. Coldren, "A monolithic evanescent field spore detector", *OSA Integrated Photonics Research Conference* **IthB3** (2004).

Acknowledgements

The last few years have been a wonderful journey, which would not have been possible without the involvement and support of so many people.

I would like to thank my promoter, Markus Pollnau, for the opportunity to pursue my Ph.D. as a member of the Integrated Optical MicroSystems (IOMS) group. I am grateful for his guidance as well as the countless discussions and suggestions which helped me to benefit from his experience as a great laser physicist. I truly appreciate his continuous confidence in me.

I also want to express my deepest gratitude to my assistant promoter, Kerstin Wörhoff for always encouraging and motivating me. Her friendship and good sense of humour supported me through some difficult times. Additionally, I would like to thank her for the good quality Al_2O_3 layers which were used in this work. Kerstin is also one of only three people who can understand the "Nederkaans" language, which I have developed since my arrival in the Netherlands.

I am very grateful to René de Ridder for his great interest in my work and for his constructive recommendations, which often helped me to put the last pieces of the puzzle together. His open-door-policy gave me the liberty to often turn to him for advice.

I would like to thank my graduation committee: Prof. Jean-Emmanuel Broquin from the Grenoble Institute of Technology, Dr. Bart Verbeek chairman of IOP Photonic Devices, as well as Prof. Klaus Boller, Prof. Vinod Subramaniam, Dr. Kerstin Wörhoff and Prof. Markus Pollnau from the University of Twente for their valuable input and effort in reviewing this thesis.

A special thanks to all present and past IOMS members with whom I have worked during the last few years, each contributing to the IOMS group in a unique way:

I thank Feridun Ay, Jonathan Bradley and Jing Yang for the many valuable discussions and for their contributions to the establishment and development of the Al_2O_3 waveguide technology.

A kind word of thanks to my first officemates in Hogekamp, Dimitri Geskus, Laura Agazzi and Chaitanya Dongre for some great memories. I can probably write a book about my adventures with the three of them. Dimitri: a true and compassionate friend, an absolute genius in the lab and an excellent laser physicist. Dimitri is also the second person who understands "Nederkaans". Laura: always very patiently explaining the numerous dynamics of rare-earth-ions to me, extremely good with mathematics, smiling at all times, and bakes the most awesome Italian delicacies. Chaitanya: a cultural chameleon, keen adventurer, and master of many languages, making me realize how important it is to

maintain a good balance in life.

I thank Marko van Dalfsen, a close friend and officemate in Carré, for his positive attitude, attention to detail, for many discussions about lasers and physics, and for being my forex partner. I also thank Marko for his help with the design of this thesis cover and for translating the abstract to Dutch. Thanks to Imran Akca, colleague and old neighbour, for sharing and understanding the challenges of being far away from home and for introducing me to Turkish cuisine.

I thank my other fellow IOMS students: Fehmi Civitci, Lantian Chang, Mustafa Sefünc, Sergio Vázquez-Córdova, Yean-Sheng Yong, So Van Pham, Nur Ismail, Saara-Maarit Reijn, Lasse Kauppinen and Marcel Hoekman for creating an enjoyable working environment and for teaching me about the diversity of their respective cultures.

Thanks to Anton Hollink for being a great role model, for always immediately assisting me in the lab, and for so many conversations about football, rugby, politics, family, and life. To Meindert Dijkstra, for his vast experience and knowledge about the required fabrication processes, his guidance in the cleanroom, and for always thinking seven steps ahead. To Henk van Wolferen, for being an awesome cleanroom partner, for his great contribution to the Bragg-grating fabrication, and for taking beautiful photographs of my devices. I also thank Gabriël Sengo for assisting in the fabrication of some devices.

I am thankful to Hugo Hoekstra, Manfred Hammer, Sonia García-Blanco and Abu (Shanmugam) Aravazhi for valuable discussions and great suggestions concerning my work.

I would like to express my appreciation to the IOMS secretaries: Rita ter Weele-Stokkers, Annitta David, and Brigit Binkhorst-Reinshagen for always ensuring that IOMS runs like a well-oiled machine. In particular, I want to thank Rita for all her assistance when I just arrived in the Netherlands: fetching me from the train station, arranging my accommodation, providing my first bicycle and for encouraging me during the first three difficult months.

I am grateful to Kees van der Werf for performing the AFM measurements and for great suggestions to the sensor related part of the work. I am still amazed at how quickly Kees can make 3-D drawings by hand, according to scale, with shadows, everything.

A kind word of thanks to Chris Roeloffzen, Reza Khan, Maurizio Burla and David Marpaung from the Telecommunication group for many shared publications and a fruitful collaboration within the Memphis project.

I also want to thank Peter Maat (Astron), Arne Leinse (Lionix), Jaco Verpoorte (NLR) and Peter de Hek (TNO) for their collaboration within the Memphis project.

Many thanks to Arjen Bakker, Sesilia Kriswandhi and Remco Stoffer from PhoeniX Software for providing very useful PhoeniX training and for always responding to my software related questions straightaway.

A special acknowledgement goes to my teammates at the Enschedese rugby club. In particular I want to thank Peter Ploeger (Guus), Patrick Slottje, Tonny ter Braak, Chuck Sterk, Nutte Dijkstra, Ruud Stolk, Wilfred van den Berg and Ben Jansen for being great mates, both on and off the field. Guus and Nutte, thanks for saving me many times when the big guys wanted a piece of me.

I would like to thank Astrid Brunnekreef and Piet Scipio for their friendship and support and for welcoming me and Michelle into their home as family. Astrid is also the third person who understands "Nederkaans".

I want to acknowledge Christoph Bollig, Andrew Forbes and Daniel Esser, my scientific mentors during my M.Sc. at the CSIR in South Africa. I am grateful for their guidance and encouragement to pursue a Ph.D.

I would like to mention my great friends in South Africa, in particular Carel, Sanette, Wian, Lena, Deon and Corlia.

I want to thank my family for their continuous love and support: my parents Edward and Jenny, my brother Christopher, my parents-in-law Pierre and Wilma as well as my sister-in-law Chantál.

Finally, I want to thank Michelle, my amazing wife, for her unconditional love, patience and encouragement. Thank you for sharing this adventure with me. Dankie dat jy my liefhet net soos wat ek is.

Thank you all,

Edward

"Onze wegen zullen kruisen
Ergens ooit wie weet misschien
Want het licht heeft zoveel kleuren
Er kan zoveel gebeuren
En er is zoveel te zien"

-*De Ruimtevaarder*, Stef Bos-

List of Publications

Peer-Reviewed Journal Articles

[1] E. H. Bernhardi, K. O. van der Werf, A. J. F. Hollink, K. Wörhoff, R. M. de Ridder, V. Subramaniam, and M. Pollnau, "Evanescent-field intra-cavity sensing with a dual-wavelength distributed-feedback waveguide laser", ***in preparation*** (2012).

[2] M. R. H. Khan, E. H. Bernhardi, D. A. I. Marpaung, M. Burla, R. M. de Ridder, K. Wörhoff, M. Pollnau, and C. G. H. Roeloffzen, "Dual-frequency distributed feedback laser with an optical frequency locked loop for stable microwave signal generation", *Photonics Technology Letters*, **24**, 1431 (2012).

[3] L. Agazzi, E. H. Bernhardi, K. Wörhoff, and M. Pollnau, "Impact of luminescence quenching on relaxation-oscillation frequency in solid-state lasers", *Applied Physics Letters*, **100**, 011109 (2012).

[4] E. H. Bernhardi, M. R. H. Khan, C. G. H. Roeloffzen, H. A. G. M. van Wolferen, K. Wörhoff, R. M. de Ridder, and M. Pollnau, "Photonic generation of stable microwave signals from a dualwavelength Al_2O_3:Yb^{3+} distributedfeedback waveguide laser", *Optics Letters*, **37**, 181 (2012).

[5] E. H. Bernhardi, Q. Lu, H. A. G. M. van Wolferen, K. Wörhoff, R. M. de Ridder, and M. Pollnau, "Monolithic distributed Bragg reflector cavities in Al_2O_3 with quality factors exceeding 10^6", *Photonics and Nanostructures - Fundamentals and Applications*, **9**, 225 (2011).

[6] E. H. Bernhardi, H. A. G. M. van Wolferen, K. Wörhoff, R. M. de Ridder, and M. Pollnau, "Highly efficient, low-threshold monolithic distributed Bragg reflector channel waveguide laser in Al_2O_3:Yb^{3+}", *Optics Letters*, **36**, 603 (2011).

[7] E. H. Bernhardi, H. A. G. M. van Wolferen, L. Agazzi, M. R. H. Khan, C. G. H. Roeloffzen, K. Wörhoff, M. Pollnau, and R. M. de Ridder, "Ultra-narrow-linewidth, single-frequency distributed feedback waveguide laser in Al_2O_3:Er^{3+} on silicon", *Optics Letters*, **35**, 2394 (2010).

[8] D. Geskus, S. Aravazhi, E. Bernhardi, C. Grivas, S. Harkema, K. Hametner, D. Günther, K. Wörhoff, and M. Pollnau, "Low-threshold Gd^{3+}, Lu^{3+} co-doped $KY(WO_4)_2$:Yb^{3+} planar waveguide lasers", *Laser Physics Letters*, **6**, 800 (2009).

Contributions to International Conferences

[9] Edward H. Bernhardi, René M. de Ridder, Kerstin Wörhoff, and Markus Pollnau, "Rare-earth-ion-doped ultra-narrow-linewidth lasers on a silicon chip and applications to intra-laser-cavity optical sensing", Photonics West, San Francisco, USA, ***accepted*** (2013)

[10] M. Pollnau, C. Dongre, S. V. Pham, E. H. Bernhardi, K. Wörhoff, R. M. de Ridder, and H. J. W. M. Hoekstra (2012), "Optical bio-sensors in microfluidic chips", *Materials Research Society Fall Meeting, Symposium XX "Materials and Concepts for Biomedical Sensing"*, Boston, USA, paper XX9.01, ***invited paper*** (2012).

[11] M. Pollnau, K. van Dalfsen, E. H. Bernhardi, D. Geskus, K. Wöhoff, R. M. de Ridder, and S. M. García-Blanco, "Fabrication, operation, and applications of efficient dielectric waveguide lasers", *International Conference on Advanced Laser Technologies*, Thun, Switzerland, paper Tu-1B-2-IN, ***invited paper*** (2012).

[12] M. R. H. Khan, E. H. Bernhardi, D. A. I. Marpaung, M. Burla, R. M. de Ridder, K. Wörhoff, M. Pollnau, and C. G. H. Roeloffzen (2012), "Highly stable microwave carrier generation using a dual-frequency distributed feedback laser", *IEEE International Topical Meeting on Microwave Photonics*, Noordwijk, The Netherlands, ***Accepted*** (2012).

[13] K. van Dalfsen, H. A. G. M. van Wolferen, M. Dijkstra, S. Aravazhi, E. H. Bernhardi, S. M. García-Blanco, and M. Pollnau, "Towards integrated channel waveguide lasers in monoclinic double tungstates", *EPS-QEOD Europhoton Conference on Solid-State, Fibre, and Waveguide Coherent Light Sources*, Stockholm, Sweden, Europhysics Conference Abstract **34C**, paper ThP.30 (2012).

[14] M. Pollnau, J. D. B. Bradley, E. H. Bernhardi, L. Agazzi, D. Geskus, K. van Dalfsen, J. Yang, A. Driessen, S. M. García-Blanco, K. Wörhoff, and R. M. de Ridder, "On-chip integrated amplifiers and lasers utilizing rare-earth-ion activation", *Nano-TR-VIII Nanoscience and Nanotechnology Congress*, Ankara, Turkey, ***plenary lecture*** (2012).

[15] E. H Bernhardi, H. A. G. M. van Wolferen, K. Wörhoff, R. M. de Ridder, and M. Pollnau, "Waveguide Bragg gratings for the realization of high-quality monolithic cavities", *Conference on Bragg Gratings, Photosensitivity and Poling in Glass Waveguides*, Colorado Springs, USA, paper BM3D.1, ***invited paper*** (2012).

[16] L. Agazzi, E. H. Bernhardi, K. Wörhoff, and M. Pollnau, "Luminescence quenching in rare-earth-ion-doped Al_2O_3 lasers and its influence on relaxation oscillation frequency", *Advanced Solid-State Photonics Conference*, San Diego, USA, (Optical Society of America, Washington, DC), paper AT4A.18 (2012).

[17] E. H. Bernhardi, K. Wörhoff, R. M. de Ridder, and M. Pollnau, "Stable microwave generation in a dual-phase-shifted Al_2O_3:Yb^{3+} distributed-feedback waveguide laser", *Advanced Solid-State Photonics Conference*, San Diego, USA, (Optical Society of America, Washington, DC), paper AM5A.6 (2012).

[18] M. Pollnau, D. Geskus, E. H. Bernhardi, K. van Dalfsen, K. Wörhoff, and R. M. de Ridder, "Highly efficient solid-state waveguide lasers", *Advanced Solid-State Photonics Conference*, San Diego, USA, (Optical Society of America, Washington, DC), paper AM5A.1, ***invited paper*** (2012) .

[19] L. Agazzi, E. H. Bernhardi, K. Wörhoff, and M. Pollnau, "The impact of lifetime quenching on relaxation oscillations in solid-state lasers", *Conference on Lasers and Electro-Optics: Science and Innovations (CLEO: S and I)*, San José, USA, (Optical Society of America, Washington, DC), paper CTu1D.6 (2012).

[20] E. H. Bernhardi, K. O. van der Werf, A. J. F. Hollink, K. Wörhoff, R. M. de Ridder, V. Subramaniam, and M. Pollnau, "Evanescent-field intra-cavity sensing with a dual-wavelength distributed-feedback waveguide laser", *Conference on Lasers and Electro-Optics: Science and Innovations (CLEO: S and I)*, San José, USA, paper CM3B.5 (2012).

[21] E. H. Bernhardi, M. R. H. Khan, C. G. H. Roeloffzen, H. A. G. M. van Wolferen, K. Wörhoff, R. M. de Ridder, and M. Pollnau, "Optical generation of microwave signals with a dual-phase-shifted Al_2O_3:Yb^{3+} distributed-feedback laser", *Conference on Lasers and Electro-Optics: Science and Innovations (CLEO: S and I)*, San José, USA, paper JW2A.36 (2012).

[22] D. Geskus, S. Aravazhi, E. H. Bernhardi, L.Agazzi, S. M. García-Blanco, and M. Pollnau, "150 dB/cm gain over 55 nm wavelength range near 1 μm in an Yb-doped waveguide amplifier", *Conference on Lasers and Electro-Optics: Science and Innovations (CLEO: S and I)*, San José, USA, paper CM1A.6 (2012).

[23] E. H. Bernhardi, M. R. H. Khan, C. G. H. Roeloffzen, H. A. G. M. van Wolferen, K. Wörhoff, R. M. de Ridder, and M. Pollnau, "Dual-wavelength Al_2O_3:Yb^{3+} distributed feedback waveguide laser for microwave signal generation", *European Conference on Integrated Optics*, Sitges, Spain, (Insitut de Ciències Fotòniques), paper 69 (2012).

[24] D. Geskus, S. Aravazhi, E. H. Bernhardi, L. Agazzi, S. M. García-Blanco, and M. Pollnau, "Ultra-high, broadband gain in a lattice-engineered, Yb-doped double tungstate channel waveguide", *European Conference on Integrated Optics*, Sitges, Spain, (Insitut de Ciències Fotòniques), paper 109 (2012).

[25] E. H. Bernhardi, H. A. G. M. van Wolferen, K. Wörhoff, R. M. de Ridder, and M. Pollnau, "Ultra-narrow-linewidth distributed feedback lasers in Al_2O_3:Er^{3+} and

Al_2O_3:Yb^{3+}", *International Quantum Electronics Conference and Conference on Lasers and Electro-Optics Pacific Rim*, Sydney, Australia, paper 5420-CT-6 (2011).

[26] E. H. Bernhardi, H. A. G. M. van Wolferen, K. Wörhoff, R. M. de Ridder, and M. Pollnau (2011), "Monolithic distributed Bragg reflector cavities in Al_2O_3 with quality factors exceeding one million", *International Quantum Electronics Conference and Conference on Lasers and Electro-Optics Pacific Rim*, Sydney, Australia, paper 4240-CT-6 (2011).

[27] E. H. Bernhardi, H. A. G. M. van Wolferen, K. Wörhoff, R. M. de Ridder, and M. Pollnau, "Efficient and ultra-narrow-linewidth integrated waveguide lasers in Al_2O_3:Yb and Al_2O_3:Er", *International Laser Physics Workshop*, Sarajevo, Bosnia and Herzegovina, paper 4.5.3, ***invited paper*** (2011).

[28] K. Wörhoff, E. H. Bernhardi, J. D. B. Bradley, J. Yang, F. Ay, R. M. de Ridder, and M. Pollnau, "Rare-earth-ion doped amplifiers and lasers integrated on silicon", *International Conference on Transparent Optical Networks*, Stockholm, Sweden, paper Tu.C1.1, ***invited paper*** (2011).

[29] M. R. H. Khan, D. A. I. Marpaung, M. Burla, C. G. H. Roeloffzen, E. H. Bernhardi, and R. M. de Ridder (2011), "Investigation on the performance of an optically generated RF local oscillator signal in Ku-band DVB-S systems", *General Assembly and Scientific Symposium of the International Union of Radio Science*, Istanbul, Turkey (2011).

[30] E. H. Bernhardi, H. A. G. M. van Wolferen, K. Wörhoff, R. M. de Ridder, and M. Pollnau (2011), "High-Q distributed-Bragg-grating laser cavities", *International Conference on Luminescence and Optical Spectroscopy of Condensed Matter*, Ann Arbor, USA, paper MI2 (2011).

[31] E. H. Bernhardi, H. A. G. M. van Wolferen, K. Wörhoff, R. M. de Ridder, and M. Pollnau (2011), "Distributed Bragg reflector high-Q cavities and lasers in Al_2O_3 on silicon", *Conference on Lasers and Electro-Optics Europe*, Munich, Germany, paper CE5.2 (2011).

[32] E. H. Bernhardi, H. A. G. M. van Wolferen, K. Wörhoff, R. M. de Ridder, and M. Pollnau, "Distributed feedback channel waveguide lasers in erbium- and ytterbium-doped Al_2O_3 on silicon", *Conference on Lasers and Electro-Optics Europe*, Munich, Germany, paper CJ10.4 (2011).

[33] E. H. Bernhardi, H. A. G. M. van Wolferen, K. Wörhoff, R. M. de Ridder, and M. Pollnau, "High-Q monolithic distributed Bragg reflector cavities in Al_2O_3 channel waveguides", *Conference on Lasers and Electro-Optics*, Baltimore, Maryland, (Optical Society of America, Washington, DC), paper CME4, (2011).

[34] E. H. Bernhardi, K. Wörhoff, R. M. de Ridder, and M. Pollnau, "Highly efficient distributed feedback waveguide laser in Al_2O_3:Yb^{3+} on silicon", *Advanced Solid-State Photonics Conference*, Istanbul, Turkey, paper ATuD7 (2011).

[35] E. H. Bernhardi, H. A. G. M. van Wolferen, K. Wörhoff, M. Pollnau, and R. M. de Ridder, "1.7-kHz-linewidth distributed feedback laser in Al_2O_3:Er^{3+}, *EPS-QEOD Europhoton Conference on Solid-State, Fibre, and Waveguide Coherent Light Sources*, Hamburg, Germany, Europhysics Conference Abstract **34C**, paper FrB7 (2011).

[36] M. Pollnau, J. D. B. Bradley, J. Yang, E. H. Bernhardi, R. M. de Ridder, and K. Wörhoff, "Rare-earth-ion doped waveguide amplifiers and lasers in alumina and polymers", *Frontiers in Optics/Laser Science, Annual Meeting of the Optical Society of America*, Rochester, USA, paper FWD1, ***invited paper*** (2011).

[37] M. Pollnau, J. D. B. Bradley, E. H. Bernhardi, F. Ay, R. M. de Ridder, and K. Wörhoff (2010), "Integrated amplifiers and lasers in Al_2O_3:Er^{3+} thin films on a silicon chip", *IV International Workshop on Photonic and Electronic Materials*, San Sebastian, Spain, Scientific Program and Workshop Abstracts, p. 44, ***invited paper*** (2010).

[38] E. H. Bernhardi, K. Wörhoff, J. D. B. Bradley, R. M. de Ridder, and M. Pollnau, "Integrated Al_2O_3:Er^{3+} microring and distributed feedback lasers on silicon", *European Materials Research Society Meeting, Symposium K: "Rare Earth Doped Materials for Optical Based Technologies*, Strasbourg, France, session 1, paper 4 (2010).

[39] E. H. Bernhardi, H. A. G. M. van Wolferen, K. Wörhoff, M. Pollnau, and R. M. de Ridder, "High-quality, distributed phase-Shift, distributed feedback cavities in Al_2O_3 waveguides", *Conference on Bragg Gratings, Photosensitivity and Poling in Glass Waveguides*, Karlsruhe, Germany, (Optical Society of America, Washington, DC 2010), paper BMB5 (2010).

[40] E. H. Bernhardi, H. A. G. M. van Wolferen, L. Agazzi, M. R. H. Khan, C. G. H. Roeloffzen, K. Wörhoff, M. Pollnau, and R. M. de Ridder, "Low-threshold, single-frequency distributed-feedback waveguide laser in Al_2O_3:Er^{3+} on silicon", *Conference on Lasers and Electro-Optics*, San José, USA, (Optical Society of America, Washington, DC), paper CTuU4 (2010).

[41] F. Ay, E. H. Bernhardi, L. Agazzi, J. D. B. Bradley, K. Wörhoff, M. Pollnau, and R. M. de Ridder, "Characterization of Bragg gratings in Al_2O_3 waveguides fabricated by focused ion beam milling and laser interference lithography", *Conference on Lasers and Electro-Optics*, San José, USA, (Optical Society of America, Washington, DC), paper CMQ4 (2010).

[42] M. Pollnau, J. D. B. Bradley, F. Ay, E. H. Bernhardi, R. M. de Ridder, and K. Wörhoff, "On-chip integrated lasers in Al_2O_3:Er^{3+} on silicon", *Optoelectronic Integrated Circuits XII*, edited by L.A. Eldada and E.H. Lee, *Proceedings of the SPIE*, **7605**, paper 76050M (2010).

[43] E. H. Bernhardi, H. A. G. M. van Wolferen, L. Agazzi, M. R. H. Khan, C. G. H. Roeloffzen, K. Wörhoff, M. Pollnau and R. M. de Ridder, "Single-frequency, narrow-linewidth distributed feedback waveguide laser in Al_2O_3:Er^{3+} on silicon", *European Conference on Integrated Optics*, Cambridge, UK, paper ThE1 (2010).

[44] Dimitri Geskus, Shanmugam Aravazhi, Edward Bernhardi, Christos Grivas, Kerstin Wörhoff, Markus Pollnau, "Low-threshold and highly efficient Gd^{3+}, Lu^{3+} co-doped $KY(WO_4)_2$:Yb^{3+} planar waveguide lasers", *Advanced Solid-State Photonics Conference*, San Diego, USA, (Optical Society of America, Washington, DC), paper ATuB2 (2010).

[45] Dimitri Geskus, Shanmugam Aravazhi, Edward Bernhardi, Christos Grivas, Kerstin Wörhoff, and Markus Pollnau, "Highly efficient Gd, Lu co-doped $KY(WO_4)_2$:Yb^{3+} planar waveguide laser", *European Optical Society Topical Meeting on Lasers*, Capri, Italy, On-site Programme, p. 27 (2009).

[46] M. Pollnau, J. D. B. Bradley, L. Agazzi, E. Bernhardi, F. Ay, K. Wörhoff, and R. M. de Ridder, "Al_2O_3:Er^{3+} as a new platform for active integrated optics", *International Conference on Transparent Optical Networks*, São Miguel, Azores, Portugal, paper We.D2.1, ***invited paper*** (2009).

Contributions to National Conferences

[47] E. H. Bernhardi, M. R. H. Khan, C. G. H. Roeloffzen, H. A. G. M. van Wolferen, K. Wörhoff, R. M. de Ridder, and M. Pollnau, "Photonic generation of microwave signals using dual-wavelength distributed-feedback waveguide lasers", *Annual Symposium of the IEEE Benelux Chapter*, Mons, Belgium, ***accepted***, (2012).

[48] E. H. Bernhardi, K. Wörhoff, R. M. de Ridder, and M. Pollnau, "High-quality distributed Bragg reflector cavities and lasers in alumina on silicon", *Annual Symposium of the IEEE Benelux Chapter*, Ghent, Belgium, pp. 41-44 (2011).

[49] M. Pollnau, E. H. Bernhardi, J. D. B. Bradley, R. M. de Ridder, K. Wörhoff, J. Yang, M. B. J. Diemeer, and A. Driessen, "Rare-earth-ion-doped lasers integrated on a silicon chip", *Joint Annual Meeting of the Swiss Physical Society and Austrian Physical Society*, Lausanne, Switzerland, Bulletin SPG/SSP **28**, paper 214, (2011).

[50] E. H. Bernhardi, L. Agazzi, H. A. G. M. van Wolferen, K. Wörhoff, R. M. de Ridder, and M. Pollnau, "Monolithic channel waveguide lasers in rare-earth-ion-doped alumina", *Fotonica Evenement*, Nieuwegein, The Netherlands (2011).

[51] E. H. Bernhardi, L.Agazzi, K. Wörhoff, R. M. de Ridder, and M. Pollnau, "Narrow-linewidth distributed feedback channel waveguide laser in Al_2O_3:Er^{3+}", *Annual Symposium of the IEEE Benelux Chapter*, Delft, The Netherlands, pp. 85-88 (2010).

[52] E. H. Bernhardi, H. A. G. M. van Wolferen, L. Agazzi, M. R. H. Khan, C. G. H. Roeloffzen, K. Wörhoff, M. Pollnau, and R. M. de Ridder, "Ultra-narrow-linewidth, single-frequency distributed feedback waveguide laser in Al_2O_3:Er^{3+} on silicon, Fotonica Evenement, Nieuwegein, The Netherlands, (2009).

[53] E. H. Bernhardi, H. A. G. M. van Wolferen, M. Dijkstra, L. Agazzi, K. Wörhoff, M. Pollnau, and R. M. de Ridder, "Designing an integrated Al_2O_3:Er^{3+} distributed feedback laser", *Annual Symposium of the IEEE Benelux Chapter*, Brussels, Belgium, pp. 197-200 (2009).

[54] D. Geskus, S. Aravazhi, E. Bernhardi, C. Grivas, K. Wörhoff, and M. Pollnau, "Highly efficient waveguide lasing in Gd^{3+}, Lu^{3+} co-doped $KY(WO_4)_2$:Yb^{3+}", *IEEE Photonics Society Workshop*, Eindhoven, The Netherlands (2009).